5-2007

The Geologic History of Subsurface Arkosic Sedimentary Rocks in the San Andreas Fault Observatory at Depth (SAFOD) Borehole, Central California

Sarah D. Draper
Utah State University

2007

The Geologic History of Subsurface Arkosic Sedimentary Rocks in the San Andreas Fault Observatory at Depth (SAFOD) Borehole, Central California

Sarah D. Draper

THE GEOLOGIC HISTORY OF SUBSURFACE ARKOSIC SEDIMENTARY ROCKS IN THE SAN ANDREAS FAULT OBSERVATORY AT DEPTH (SAFOD) BOREHOLE, CENTRAL CALIFORNIA

by

Sarah D. Draper

A thesis submitted in partial fulfillment
of the requirements for the degree

of

MASTER OF SCIENCE

in

Geology

Approved:

UTAH STATE UNIVERSITY
Logan, Utah

2007

ABSTRACT

The Geologic History of Subsurface Arkosic Sedimentary Rocks in the San Andreas Fault Observatory at Depth (SAFOD) Borehole, Central California

by

Sarah D. Draper, Master of Science

Utah State University, 2007

Major Professor: Dr. James P. Evans
Department: Geology

The aim of the San Andreas Fault Observatory at Depth (SAFOD) project, a component of the NSF Earthscope Initiative, is to directly observe active fault processes at seismogenic depths through the drilling of a 3 km deep (true vertical depth) inclined borehole across San Andreas fault. Preliminary subsurface models based on surface mapping and geophysical data predicted different lithologies than were actually encountered. At 1920 meters measured depth (mmd), a sequence of well-indurated, interbedded arkosic conglomerates, sandstones, and siltstones was encountered. We present a detailed lithologic and structural characterization as a step toward understanding the complex geologic history of this fault-bounded block of arkosic sedimentary rocks. We divide the arkosic section into three lithologic units with different

compositional, structural, and sedimentary features: the upper arkose, 1920-2530 mmd, the clay-rich zone, 2530-2680 mmd, and the lower arkose, 2680-3150 mmd. We interpret the section to have been deposited in a Salinian transtensional basin, in either a subaqueous or subaerial fan setting. We suggest four different possibly equivalent sedimentary units to the SAFOD arkoses, the locations of which are dependent on how the San Andreas fault system has evolved over time in the vicinity of the SAFOD site. Detailed analysis of three subsidiary faults encountered in the arkosic section at 1920 mmd, 2530 mmd, and 3060 mmd, shows that subsurface faults have similar microstructures and composition as exhumed faults at the surface, with less evidence of alteration from extensive fluid flow.

(200 pages)

ACKNOWLEDGMENTS

This project was made possible through funding provided by NSF Earthscope grant # EAR-0454527, and the Drilling and Observation of the Earth's Continental Crust (DOSECC) student internship program. Scholarships from the Chevron Corporation, the J.S. Williams Fellowship, and the Beryl and Tura Springer scholarship fund were fundamental in the successful completion of this master's project.

I want to thank my advisor, Jim Evans, who has taught me so much about the various aspects of the geologic world. He has been an incredible teacher, mentor, and friend. His consistently positive outlook on life has been an inspiration to me. Jim makes the whole master's experience relatively stress-free and downright fun. My committee members, Susanne Janecke and John Shervais, have also been instrumental to my success. I couldn't possibly have asked for a better, more supportive committee.

My thesis project has been an incredible experience. Steve Hickman, Mark Zoback, and Bill Ellsworth, the co-principal investigators of the SAFOD project, need to be especially commended not only for making the SAFOD project possible but also accessible to students, professors, industry professionals, and interested parties of all educations. Their friendly, supportive, and open-door approach to the project made it possible for me and all the other members of the "SAFOD Science Team" to spend our summers learning a ton. The friends I made at the SAFOD site are very important to me and they contributed significantly to my success as well. These friends include: Naomi Boness, Amy Day-Lewis, Rafael Almeida, Sonata Wu, Simona Pierdominici,

Thomas Wiersberg, Fermin Fernandez-Ibanez, Kelly Mitchell, Dave Kirschner, Alexander MacQuitty, and Sean and Jessica Mitchell.

USU alum John Solum and his wife, Marie, very kindly opened their home to me for the month of May and other short trips to Menlo Park, CA. As a result of all the time I spent with these two generous people we've become very good friends. I also learned a lot from John with regards to clay mineralogy and the mineralogy of the SAFOD borehole specifically.

Lori Hirschi has been a great, supportive friend. Lori really cares about the students at Utah State, and I think we usually fail to appreciate her the way she deserves. All of the people with whom I have shared an office over the last 2.5 years, Joe Jacobs, Alex Steely, Angela Isaacs, Ben Belgarde, Adam Majeski, and Dave Forand also deserve my thanks for all I have learned from them and their friendship. Corey Barton and Kelly Bradbury have worked with me as a part of the USU SAFOD team and they taught me a ton about microscopy methods and our interesting science discussions have often found their way into this thesis. Finally, I want to thank my fiancé, Kellen Springer, who has been nothing but incredibly supportive this whole time, from moving to Utah with me to calming me down when I get especially panicked about whatever stresses me out at the moment. Thanks everyone.

Sarah D. Draper

CONTENTS

LIST OF TABLES

LIST OF FIGURES

CHAPTER 1

INTRODUCTION

One of the most studied faults in the world, the 1100 km long San Andreas fault (SAF) in California provides a unique opportunity to make direct observations of a tectonically active transform plate margin. Despite significant advances in our understanding of fault processes, answers to questions about the behavior of the SAF remain elusive. The San Andreas Fault Observatory at Depth (SAFOD) project, located north of Parkfield in central California, stemmed from the desire to more fully understand the processes that occur within seismogenic fault zones (Hickman et al., 2004). SAFOD, a component of the National Science Foundation's Earthscope project, is a collaborative geoscientific experiment aimed at directly observing fault processes at seismogenic depths. In August 2005 the SAFOD main hole was completed at a total measured depth of 3.99 km, approximately 3.0 km true vertical depth (Hickman et al., 2005). The drilling target is a patch of regularly repeating microearthquakes, which occur 2.5-12 km below the surface (Nadeau et al., 2004; Hickman et al., 2004). Ultimately, the SAFOD borehole will serve as a long-term subsurface observatory by monitoring strain, fluid pressure and composition, and other seismic parameters associated with both near-field and far-field seismic activity (Hickman et al., 2004; Ellsworth et al., 2005).

There is a strong geologic component to the SAFOD project; it is paramount that we gain a firm understanding of the rocks through which the SAFOD borehole was

drilled. Without this geologic framework, it is impossible to construct the velocity models needed for seismic studies. Also, when studying fluid pressures and composition, a knowledge of the rocks from which those fluids originate and/or flow is a crucial first step in understanding how those fluids affect the seismic cycle and fault behavior (i.e. Sibson, 1981; Hickman, 1991). This thesis characterizes the lithology and structural geology of subsurface sedimentary lithologies in the SAFOD borehole through analysis of cuttings, core, and wireline and image logs as a contribution to the SAFOD project and the overall study of the San Andreas fault system.

Tectonic Setting of the SAFOD Site

The SAFOD drilling site is located 5 km northwest of Parkfield, California at the northern end of the Parkfield segment of the San Andreas Fault (Fig. 1.1). This segment is the most heavily instrumented fault segment in the world and is characterized by regular M_w 6.0 earthquakes. The most recent event occurred on September 28, 2004 (see http://www.cisn.org/special/evt.04.09.28). The fault segment north of the drill site, the creeping segment, moves continuously through right-lateral aseismic creep approximately 25-39 mm/year (Argus and Gordon, 2001; Titus et al., 2005). The SAFOD borehole is targeting the transition zone between the two segments where M_w 1.0-2.0 repeatedly occur at a regular interval (Nadeau et al., 2004).

The major faults of the right-lateral San Andreas fault system accommodate approximately two-thirds of the northwest-southeast motion between the North American and Pacific plates (Wallace, 1990). In central California the majority of past and present

slip has been taken up on the modern trace of the SAF (Wright, 2000). Since approximately 8 Ma, when plate motion vectors rotated significantly (Atwater and Stock, 1998), the central Coast Ranges, where the SAFOD site is located, has been in a state of transpression (Page et al., 1998). Evidence for compression is found in the numerous fault-parallel folds and thrust faults along the SAF system in central California (i.e. Jennings and Strand, 1958; Dibblee, 1971; Sims, 1990). This combination of right-lateral plate motion and compression results in a unique state of stress along the SAF system. Maximum horizontal stresses have been consistently shown to be oriented at a high angle to the plane of the SAF (Zoback et al., 1987). Andersonian fault mechanics indicate that a strike-slip fault system should be active when horizontal stresses are oriented 30-45º to the vertical fault plane (Anderson, 1951). The fact that the maximum horizontal stress is oriented nearly 90º to the SAF plane indicates the fault moves under particularly low shear stresses. Furthermore, the lack of a frictional heat anomaly across the plane of the fault also indicates low fault strength (Lachenbruch and Sass, 1992; Saffer et al., 2003). These factors have led to extensive study of the paradoxical nature of the San Andreas fault and are large motivations in the inception of the SAFOD project (Hickman et al., 2004).

The SAFOD drill site was chosen not only for the ideal repeating low magnitude earthquakes but also because the subsurface geology was hypothesized to be distinctly different on either side of the fault (Hickman et al., 2004). Presumably, the noticeable lithologic change would make it immediately clear when the SAF had been encountered. At the surface, Jurassic/Cretaceous Franciscan Formation crops out on the east side of the

fault, rising 305 m above the valley in rolling hills (Jennings and Strand, 1958; Dibblee, 1971; Sims, 1990; Rymer et al., 2003). In this area the Franciscan is composed primarily of blueschist facies metamorphosed ocean floor rocks such as hydrothermally altered pillow basalts, ribbon cherts, and serpentinized ultramafics (Dickinson, 1966; Dibblee, 1971; Sims 1990). Although Salinian granitic basement is rarely exposed at the surface (Jennings and Strand, 1958; Dibblee, 1971; Sims, 1990; Rymer et al., 2003), it has been encountered in oil wells on the west side of the fault (Graham et al., 1989; Cummings, 1999). The Salinian block is composed of Upper Cretaceous plutonic and older metamorphic rocks (Barbeau et al., 2005; Barth et al., 2003), the plutonics range from tonalite to granite to gabbro in some localities (Dickinson, 1981); the metamorphic rocks are moderate to high grade, similar to metamorphic rocks found in the San Gabriel range to the south (Ross, 1970, 1984; Irwin, 1990). The basement on both sides of the fault is covered in late Tertiary and Quaternary marine and fluvial sedimentary rocks, with different formations on either side (Rymer et al., 2003; Thayer and Arrowsmith, 2005).

The SAFOD Drilling Strategy

Due to a variety of factors such as weather conditions and land access, the SAFOD project has been split into three phases following a successful preliminary study. In 2002, a pilot hole was drilled as a precursor to the main project phases at the site chosen for the SAFOD project, approximately 5 km northwest of Parkfield, California (Figure 1.1). Phase one, completed in the summer of 2004, drilled from the surface to 3049 meters measured depth (mmd), at 1436 mmd the borehole deviated from vertical

toward the SAF at a 55° angle. Drilling ended for phase one nearly half a kilometer horizontal distance from the surface trace of the SAF; drill casing was set, followed by a coring run at the bottom of the borehole. Phase two began June 2005, drilling from 3048 mmd to the total depth of 3989 mmd, which is approximately 3.05 km vertical depth. The final depth of the borehole corresponds to a surface distance meters east of the surface expression of the San Andreas fault. After drilling ended the geophysical observatory was set in place along the casing and at the bottom of the borehole (Ellsworth et al., 2005). Phase three will commence in summer 2007 when the project will endeavor to core the fault zone and initiate a longer term seismological observatory in the main borehole (Hickman et al., 2004, 2005).

Results of Drilling

Drilling of the SAFOD borehole proved to be a difficult task, frought with complications but still successful in the end. One of the more surprising complications were the lithologies encountered in the borehole. The subsurface model created from seismic surveys (Hole et al., 2001; Catchings and Rymer, 2002; Rymer et al., 2003; Thurber et al., 2004), magnetic and gravity surveys (McPhee et al., 2004) and geologic maps (Dibblee, 1971; Sims, 1990; M. Rymer, pers comm.) of the region near the SAFOD site, predicted Salinian granite on the southwest side of the fault would be juxtaposed against the Franciscan Formation on the northeast. However, shortly after the borehole began to whipstock toward the fault, at 1920 mmd, a series of arkosic sedimentary rocks were encountered. At 3150 mmd, the arkosic sandstone abruptly gave way to dark gray,

fine-grained mudstones, interpreted to be the Cretaceous Great Valley Sequence (Evans et al., 2005). The mudstones persisted until the final depth of the SAFOD borehole, without the expected transition into Franciscan blueschists or serpentinites. Without a clear lithology change, it was, at first, difficult to ascertain where the borehole had intercepted the San Andreas fault plane. This difficulty was compounded by the fact that the newly encountered lithologies necessitated a reevaluation of earthquake locations (Roecker et al., 2005) and velocity models (Hole et al., 2006). Fortuitously, 40-arm caliper measurements taken after casing in Fall, 2005, revealed a zone from 3295-3313 mmd where the borehole is being progressively deformed in a right-lateral sense (Hickman et al., 2005). This has been interpreted to be a creeping strand of the SAF (Hickman et al., 2005) possibly with a component of afterslip from the 2004 Parkfield earthquake, which when correlated to the surface trace of the SAF indicates a dip of 83º to the southwest (Bradbury et al., in review).

Description of Project and Motivation for Work

The presence of the arkosic rocks to the southwest of the SAF and the Great Valley Sequence to the northeast present a challenge to geologists wishing to understand the tectonic evolution of the SAFOD site. To this point, there is little known about the nature, origin, and age of the arkosic rocks. The rocks are unlike most of the Tertiary marine sedimentary rocks found at the surface of the SAFOD site as well as in the hills surrounding the site. Interesting questions generated by the discovery of these arkosic rocks in the subsurface include:

1) What was the original tectonic and geographic position of the arkosic rocks? Are they a remnant fault sliver resulting from offset along extinct strands of the San Andreas fault system? Are they depositionally related to the Salinian granite encountered in the SAFOD borehole?
2) The arkoses are at 2 km vertical depth, what is the mechanism for this deep burial? What is the exhumation and burial history of these rocks and is it similar to other subsurface rocks in the borehole?
3) The arkosic rocks are nearly adjacent to the SAF, how has the deformational history of the San Andreas fault zone been recorded in the rocks? What can we learn about subsurface subsidiary fault zones in the arkosic rocks? Is fault structure and composition in the subsurface different than after exhumation?

The purpose of this thesis is to address these questions and to a) determine if they are answerable within the scope of the data collected to date by the SAFOD project b) to apply results to the larger study of the tectonic evolution of the SAF in the vicinity of the SAFOD site. Furthermore, this thesis also serves as a test of methodology. One of the purposes of the SAFOD project is to gain a better understanding of how to relate geophysical properties to physical properties in subsurface rocks. Here, we combine hard rock data derived from cuttings and core microscopy with borehole-based geophysical logs and electrical micro-resistivity image logs in order to characterize the arkosic section.

In Chapter 2 we present a thorough lithologic characterization of the arkosic section. We use those results to interpret the depositional and diagenetic history of the

rocks and in combination with external fission-track studies a preliminary exhumation and burial history as well. Using the geologic history of the rocks we suggest possible correlations to sedimentary rocks found at the surface in other localities.

Chapter 3 is a structural characterization of the arkosic section and focuses on three major subsidiary fault zones within the arkosic section. Each fault zone is distinctly different in composition and structure. We use this characterization to work towards a better understanding of how fault zones in the subsurface differ from those studied at the surface.

Chapter 4 summarizes chapters 2 and 3 while making conclusions about the nature of the SAFOD arkoses and implications for future work.

References

Anderson, E.M., 1951, The Dynamics of Faulting, 2nd edition, Edinburgh, Oliver and Boyd, 206 p.

Argus, D.F., and Gordon, R.G., 2001, Present tectonic motion across the Coast Ranges and San Anderas fault system in Central California: Geological Society of America Bulletin, v. 113, p. 1580-1592.

Atwater, T., and Stock, J., 1998, Pacific North American plate tectonics of the Neogene southwestern United States: An update: International Geological Review, v. 40, p. 375-402.

Barbeau, D.L., Ducea, M.N., Gehrels, G.E., Kidder, S., Wetmore, P.H., and Saleeby,J.B., 2005, U-Pb detrital-zircon geochronology of northern Salinian basement and cover rocks: Geological Society of America Bulletin, v. 117, no. 3/4, p. 466-481.

Barth, A.P., Wooden, J.L., Grove, M., Jacobson, C.E., Pedrick, J.N., 2003, U-Pb zircon geochronology of rocks in the Salinas Valley region of California: A reevaluation of the crustal structure and origin of the Salinian block: Geology, v. 31, no. 6, p. 517-520.

Catchings, R.D., and Rymer, M., 2002, High-resolution seismic velocities and shallow structure of the San Andreas fault zone at Middle Mountain, Parkfield, California: Bulletin of the Seismological Society of America, v. 92, p. 2493-2503.

Cummings, M.F., ed., 1999, Northern California Oil and Gas Fields Annual Production and Well Data 1977-1998, California Division of Oil, Gas and Geothermal Resources.

Dibblee, T.W., Jr., 1971, Geologic maps of 17 15-minute quadrangles along the San Andreas fault in the vicinity of King City, Coalinga, Panoche Valley and Paso Robles, with index map: U.S. Geological Survey Open-File Report 71-87, scale 1:62,500.

Dickinson, W.R., 1966, Table Mountain serpentinite extrusion in California Coast Ranges: Geological Society of America Bulletin, v. 77, p. 451-472.

Dickinson, W.R., 1981, Plate tectonics and the continental margin of California: *in* Ernst, W.G., ed., The Geotectonic Development of California: Englewood Cliffs, New Jersey, Prentice-Hall, p. 1-28.

Ellsworth,W., Hickman, S., Zoback, M., Davis, E., Gee, L., Huggins, R., Krug, R., Lippus, C., Malin, P., Neuhauser, D., Paulsson, B., Shalev, E., Vajapeyam, B., Weiland, C., Zumberge, M., 2005, Observing the San Andreas Fault at depth: EOS Trans. AGU, vol. 86(52), Fall Meeting Supplement, Abstract T24B-04.

Evans, J.P., Moore, D.E., Kirschner, D., and Solum, J.G., 2005, Lithologic characterization of the deep portion of the SAFOD drillhole: EOS Trans., AGU, 86(52), Fall Meeting Supplement, Abstract T21A-0450.

Graham, S.A., Stanley, R.G., Bent, J.V., and Carter, J.B., 1989, Oligocene and Miocene paleogeography of central California and displacement along the San Andreas fault: Geological Society of America Bulletin, vol. 101, pp. 711-730.

Hickman, S.H., 1991, Stress in the lithosphere and the strength of active faults: Reviewof Geophysics, Supplement, v. 29, p. 759-775.

Hickman, S., Zoback, M.D., and Ellsworth, W., 2004, Introduction to special sections: Preparing for the San Andreas Fault Observatory at Depth: Geophysical Research Letters, v. 31, no. 12, L12S01.

Hickman, S., Zoback, M., Ellsworth, B., 2005, Structure and composition of the San Andreas Fault Zone at Parkfield: Initial results from SAFOD Phases 1 and 2: EOS Trans. American Geophysical Union, 86(52), Fall Meeting Supplement, Abstract T23E-05.

Hole, JA, Catchings, RD, St Clair, KC, Rymer, MJ, Okaya, DA, and Carney, BJ, 2001, Steep-dip seismic imaging of the shallow San Andreas Fault near Parkfield: Science, v. 294, p. 1513-1515.

Hole, J.A., Ryberg, T., Fuis, G.S., Bleibinhaus, F., and Sharma, A.K., 2006, Structure of the San Andreas fault zone at SAFOD from a seismic refraction survey: Geophysical Research Letters, v. 33, no. 7, doi: 10.1029/2005GL025194.

Irwin, W.P., 1990, Geology and plate-tectonic development: *in* Wallace, R.E. ed., The San Andreas Fault System, USGS Professional Paper 1515, p. 61-80

Jennings, C.W., and Strand, R.G., 1958, Geologic Map of California, San Luis Obisbo sheet, Cal. Division of Mines and Geology, scale 1:250,000.

Lachenbruch, A.H., and Sass, J.H., 1992, Heat flow from Cajon Pass, fault strength, and tectonic implications: Journal of Geophysical research, v. 97, no. B4, p. 4995-5015.

McPhee, D.K., Jachens, R.C., and Wentworth, C.M., 2004, Crustal structure across the San Andreas fault at the SAFOD site from potential field and geologic studies: Geophysical Research Letters, vol. 31, L12S03.

Nadeau, R.M., Michelini, A., Uhrhammer, R.A., Dolenc, D., and McEvilly, T.V., 2004, Detailed kinematics, structure and recurrence of micro-seismicity in the SAFOD target region: Geophysical Research Letters, v. 31, L12S08.

Page, B.M., Thompson, G.A., and Coleman, R.G., 1998, Late Cenozoic tectonics of the central and southern Coast Ranges of California: Geological Society of America Bulletin, v. 110, no. 7, p. 846-876.

Roecker, S., Thurber, C., Shuler, A., Liu, Y., Zhang, H., and Powell, L., 2005, Refined images of the crust around the SAFOD drill site derived from active and passive seismic experiment data: EOS trans. American Geophysical Union, 86(52), Fall Meeting Supplement, Abstract T24B-05.

Ross, D.C., 1970, Quartz gabbro and anorthositic gabbro: Markers of offset along the San Andreas fault in the California Coast Ranges: Geological Society of America Bulletin, v. 81, no. 12, p. 3647–3661.

Ross, D. C., 1984, Possible correlations of basement rocks across the San Andreas, San Gregorio-Hosgri, and Rinconada-Reliz-King City faults, California: U.S. Geological Survey Professional Paper 1317, 37 p.

Rymer, M. J., R. D. Catchings, and M. R. Goldman, 2003, Structure of the San Andreas fault zone as revealed by surface geologic mapping and high-resolution seismic profiling near Parkfield, California: Geophysical Research Abstracts, v. 5, 13523.

Saffer, D.M., Bekins, B.A., and Hickman, S., 2003, Topographically driven groundwater flow and the San Andreas heat flow paradox revisited: Journal of Geophysical Research, vol. 108, no. B5, p. 2274.

Sibson, R.H., 1981, Fluid flow accompanying faulting: Field evidence and models: *in* Simpson, D.W., and Richards, P.G., eds., Earthquake Prediction: An International Review, Maurice Ewing Series, vol. 4, Washington D.C., American Geophysical Union, p 593-603.

Sims, J.D., 1990, Geologic map of the San Andreas Fault in the Parkfield 7.5-minute Quadrangle, Monterey and Fresno counties, California: Miscellaneous Field Studies Map 2115, MF-2115, scale 1:62,500.

Thayer, M., and Arrowsmith, R., 2005, Fault zone structure of Middle Mountain, Central California: EOS trans. AGU, 86(52), Fall Meeting Supplement, Abstract T21A-0458.

Thurber, C. Roecker, S., Zhang, H., Baher, S., and Ellsworth, W., 2004, Fine-scale structure of the San Andreas fault zone and location of the SAFOD target earthquakes: Geophysical Research Letters, v. 31, doi: 10.1029/2003GL019398.

Titus, S., DeMets, C., and Tikoff, B., 2005, New slip rate estimates for the creeping segment of the San Andreas Fault, California: Geology, v. 33, no. 3, p. 205-208.

Wallace, R.E., 1990, General Features: *in* Wallace. R.E. ed, The San Andreas Fault System,
California, United States Geological Survey Professional Paper no. 1515, p. 3-15.

Wright, T.A., 2000, The evolving San Andreas fault system: Nascent tectonic succession of California?: *in* Bokelmann, G., and Kovach, R.L., eds., Proceedings of the 3rd Conference on Tectonic Problems of the San Andreas Fault System, Stanford University Publications, p. 144-149.

Zoback, M.D., Zoback, M.L., Mount, V.S., Suppe, J., Eaton, J.P., Healy, J.H., Oppenheimer, D., Reasenberg, P., Jones, L., Raleigh, C.B., Wong, I.G., Scotti, O., and Wentworth, C., 1987, New evidence on the state of stress of the San Andreas fault system: Science, v. 238, p. 1105-1111.

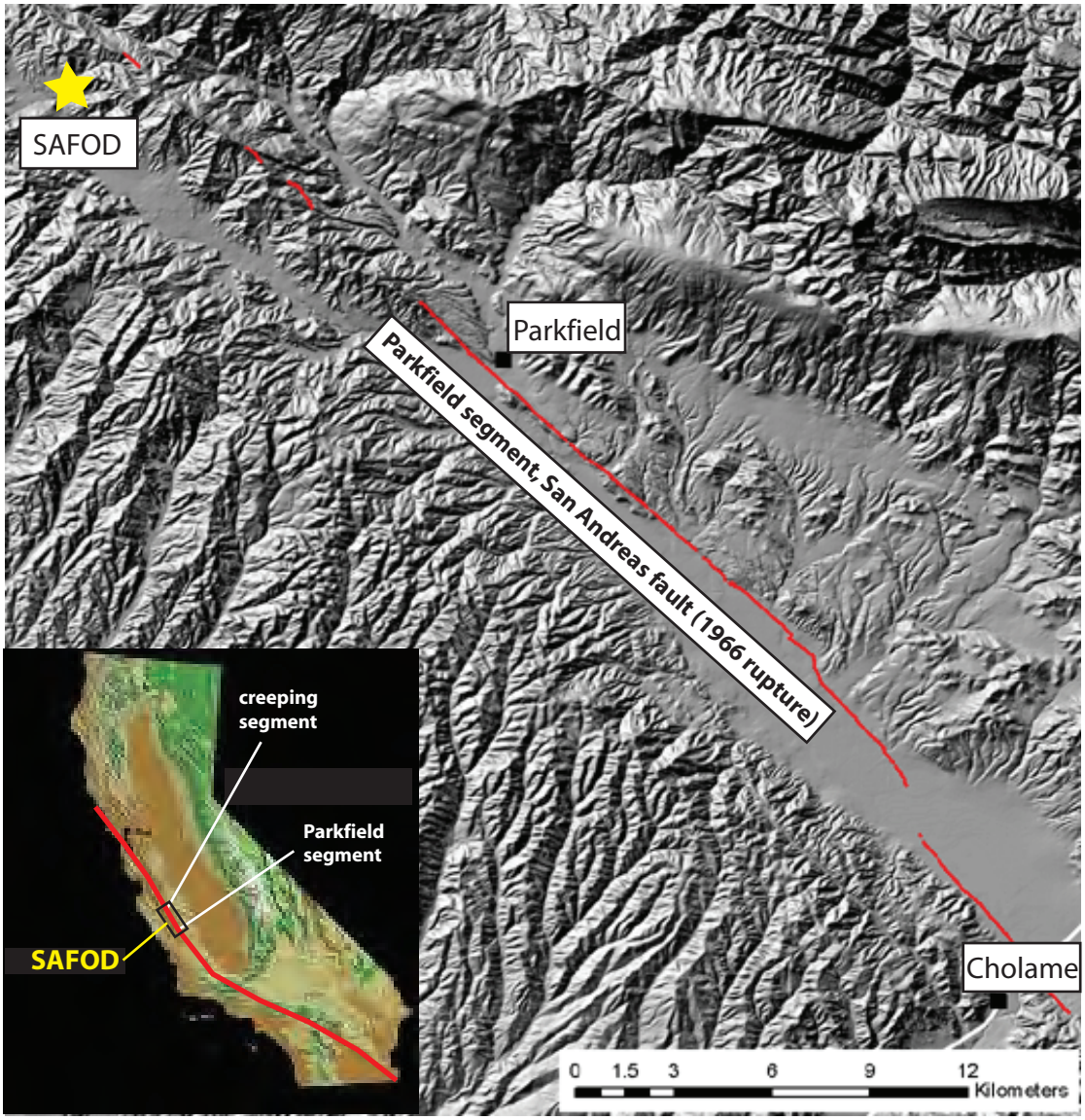

Figure 1.1: DEM of SAFOD area southeast of SAFOD site. The SAFOD site is located in central California at the transition between the creeping and Parkfield segments of the San Andreas fault. The town of Parkfield is approximately 5 km southeast of the SAFOD site. Red fault trace is the surface rupture of the 1966 Parkfield earthquake. DEM map is modified from work done by C.Crosby, Arizona State University, written communication.

CHAPTER 2

SYSTEMATIC CHARACTERIZATION OF SUBSURFACE ARKOSIC ROCKS FROM THE SAN ANDREAS FAULT OBSERVATORY AT DEPTH (SAFOD) BOREHOLE, CENTRAL CALIFORNIA

ABSTRACT

A sequence of well-indurated arkosic sedimentary rocks was encountered in the deviated San Andreas Fault Observatory at Depth (SAFOD) main borehole in central California. Preliminary subsurface models of the SAFOD site predicted Salinian granitic basement on the southwest side of the San Andreas fault. We characterize in detail the lithologic features of this sequence of rocks in order to more fully understand their depositional, diagenetic and deformational history. Characterization is carried out through a combination of petrographic microscopy of cuttings and core, image log analysis, and integration of borehole-based geophysical logs such as neutron porosity, density, gamma ray, resistivity and compressional velocity. The arkosic section is a deformed fault-bound block between the modern strand of the San Andreas fault to the northeast and the Buzzard Canyon fault to the southwest with at least 10 intraformational faults and two major block-bounding faults identified. The arkosic section is composed of three lithologic units: the upper arkose, 1920 - 2530 meters measured depth (mmd), the clay-rich zone, 2530 - 2680 mmd, and the lower arkose, 2680 - 3150 mmd. The upper arkose is a 156.4 m - 381.4 m thick feldspathic unit rich in iron-oxides composed of five distinct structural blocks with different bedding orientations. We infer the

presence of intraformational faults that separate dip domains within the upper arkose. The clay-rich zone is 28.7 m - 121.3 m thick, composed of three structural blocks and has a high abundance of clay-sized particles and clay minerals and is characterized by low compressional velocities and poor borehole stability. The lower arkose is 224 m - 331 m thick, composed of three structural blocks with different bedding orientations, and is finer grained than the upper arkose with more clay minerals and less feldspar. Feldspars are more progressively altered with near complete replacement by muscovite in the lower arkose than the upper arkose, indicating that diagenesis in the lower arkose has taken place under higher temperatures with different fluid compositions, perhaps as a result of fluid compartmentalization. Zircon fission-track cooling ages indicate a maximum age of earliest Paleocene for the arkoses. Different hypotheses for the evolution of the San Andreas fault system in the vicinity of the SAFOD site lead us to identify sedimentary rock units which may be equivalent to the SAFOD arkoses both to the northwest and the southeast of the SAFOD site.

2-1 INTRODUCTION

The San Andreas Fault Observatory at Depth (SAFOD) is a collaborative project aimed at observing fault processes at seismogenic depths. The project has drilled a 3 km deep borehole across the San Andreas fault zone, 5 km northwest of Parkfield in central California (Hickman et al., 2004, 2005) (Figure 2.1). As the project progresses, a variety of questions about fault behavior, structure, composition, physical properties and fluid parameters are being addressed by many different geoscientists (i.e. Boness and Zoback,

2006; Solum et al., 2006; Erzinger et al., 2006; Hole et al., 2006; Schleicher et al., submitted; Bradbury et al., in review). These questions cannot be adequately addressed without first gaining a strong understanding about the subsurface lithologies at the SAFOD site.

Prior to drilling of the pilot hole in 2002, comprehensive suites of geophysical data were collected in order to characterize the drill site fully (see Geophysical Research Letters special volume 31, no. 12 and 15, 2004). These data, in combination with numerous surface geological studies (i.e. Dibblee, 1971; Sims, 1990; Page et al., 1998) were used to construct a subsurface model which predicted Salinian granite on the southwestern side of the SAF juxtaposed against the blueschist facies Franciscan Formation on the northeast (Hickman et al., 2004). This model appeared to be verified by the lithologies encountered in the vertical pilot hole where drilling revealed an approximately 1 km thick Tertiary sedimentary cover overlying Salinian granite (Bradbury et al., in review). In the main hole, at 1920 m measured depth (mmd), not long after the borehole began to whipstock towards the SAF, the borehole crossed abruptly from Salinian granodiorite into a fault-bound block of arkosic sedimentary rocks (Figure 2.2). This section of arkose spans 1237.5 m in the measured depth dimension, from 1920 mmd to 3157 mmd, 735.06 m in true vertical depth (tvd) from 1876.80 m tvd to 2611.86 m tvd and 995.5 m in the horizontal dimension. At 3157 mmd the arkose sits adjacent to fine-grained sandstones and mudstones now identified as Cretaceous Great Valley Sequence (i.e. Evans et al., 2005). The presence of arkosic sedimentary rocks on the southwestern side of the fault against Great Valley sedimentary rocks on the northeastern

side of the fault was not predicted by the subsurface geophysical modeling or surface mapping and poses several geological and tectonic questions not envisioned prior to SAFOD drilling.

Study of the arkosic rocks by on-site geologists at SAFOD reveals that the rocks are indurated feldspathic conglomerates, sandstones and siltstones. While the arkosic rocks are rich in granitic clasts, the arkosic rocks display mesoscopic and microscopic sedimentary characteristics which show that they are sedimentary rather than highly fractured granite. The rocks at the surface immediately above the arkoses are Upper Tertiary conglomerates and sandstones (Thayer and Arrowsmith, 2005) (Figure 2.3), which are very unlike the arkoses at depth. The boundary between the Tertiary rocks at the surface and the arkosic rocks in the subsurface is unclear, but the SAFOD arkoses are likely older than the rocks which lie above them.

The unexpected presence of the arkosic sedimentary rocks has interesting implications for the evolution of the SAF in central California. Geologic and tectonic questions regarding these rocks include: What is the origin of the arkosic sedimentary rocks, are they a part of the Salinian Block which has been buried deeply? Have these rocks been transported a far distance along older strands of the San Andreas fault? The offset of the Salinian block has been shown to be distributed over several different parallel strike-slip fault systems (Graham, 1978; Dickinson and Butler, 1998; Whidden et al., 1998; Dickinson et al., 2005), which accounts for the apparent offset of approximately 500 km from the Sierra Nevada plutonic complex. In the vicinity of the SAFOD site there is at least one SAF parallel fault, the Buzzard Canyon Fault, with an

unknown amount of slip (Rymer et al., 2003; Thayer and Arrowsmith, 2005) (Figure 2.3). Bradbury et al., (in review) show good evidence for the correlation of the Buzzard Canyon Fault at the surface to the fault which separates the granodiorite from the arkosic rocks in the SAFOD borehole. Significant offset of >10 km on the Buzzard Canyon Fault could result in a less than straightforward offset history for the granitic and arkosic rocks in the SAFOD borehole. In this region of California it is assumed that the majority of past and present slip has been accommodated on the modern trace of the SAF (Sims, 1993; Wright, 2000). Is this true, or are other SAF-parallel faults such as the Buzzard Canyon fault (Figures 2.2 and 2.3) (Rymer, 2003; Thayer and Arrowsmith, 2005), which likely separates the granodiorite from the arkosic rocks (Bradbury et al., in review), is responsible for some of the accumulated slip in this part of central California?

This paper focuses on the nature and origin of the arkosic sedimentary rocks. Broader studies of the other lithologies found in the SAFOD pilot and main holes can be found in Solum et al. (2006) and Bradbury et al. (in review). We present detailed lithologic characterization as a first step toward understanding the geologic history of these rocks. We use a variety of subsurface datasets to fully evaluate the composition of the arkosic rocks in order to interpret provenance, depositional environment and diagenetic history. Understanding these features is necessary to compare the SAFOD arkoses to other sedimentary rocks in California. We use our compositional observations and interpretations to identify surface units which may be equivalent to the SAFOD arkoses. A correlation between the arkoses and another formation in California can help constrain the geometry and evolution of the SAF in the area of the SAFOD site.

The four datasets utilized in the characterization of the arkosic sedimentary rocks are: drill cuttings samples, spot and sidewall core samples, wireline logs, and Formation Micro-Imaging (FMI) © Logs. Drill cuttings are small pieces of rock which are the byproducts of the drilling process. Cuttings are circulated through drilling mud to the surface where they emerge as a mix of engineered drilling mud and rock ranging from millimeters to microns in size. Spot core ranges from centimeters to meters in length, 10-15 cm in diameter, and are collected using a specific coring tool at the end of the drilling string. Spot core is collected from rock which has not yet been drilled; it is generally collected directly before or after the borehole has been cased. Sidewall cores are small (2.5-5 cm in length, 2 cm in diameter) rock cores collected using a percussive side-wall core tool which shoots a hollow bullet-style core collector laterally into the borehole wall at specified depths. Wireline logs are a comprehensive suite of borehole-based geophysical logs which measure various physical properties such as velocity, density and porosity. Image logs are collected using an FMS tool which measures the microresistivity of the borehole wall. The product of the FMS measurements is a dynamically normalized resistivity map which can be interpreted with regards to lithological and structural characteristics of the rocks of the borehole wall.

Each data set has inherent limitations which would provide an incomplete picture of the structure and lithology of the fault-bound sedimentary block if evaluated alone. The methodologies involved with the processing, investigation and interpretation of each of these data sets will be discussed separately below. We report the methods used and results obtained using those methodologies in the following sections.

2-2 METHODS

Wireline Logs

A comprehensive suite of borehole-based, industry standard, geophysical wireline logs were collected at the SAFOD site during all phases of drilling (see: www.safod.icdp-online.org). The wireline logs are processed and corrected by the contracted service companies and the final products were delivered to the SAFOD project are .las, .ascii, or text files. The primary logs we used for this study are p-wave velocities (Vp) derived from the sonic monopole velocity log, resistivity, neutron porosity and density, caliper, gamma ray, and spectral gamma ray (Plate 1).

With a nearly continuous sampling rate (every 15.24 cm), wireline logs can fill in the gaps where the resolution of physical samples is low. There are limitations inherent in the use of wireline logs for geological analysis, however. Wireline logs produce nonunique results, for example both a shale layer and a fine-grained fault zone may have similar log signatures. Thus, combining optical microscopy with wireline logs provides a more complete analysis of the presence and nature of cataclasite, foliations and fluid alteration.

The log used most often to interpret lithological characteristics of sedimentary rocks is the gamma ray log. The gamma ray log is collected using a tool which acts as a natural radiation detector, collecting information about the amount of natural radioactivity in the surrounding sedimentary rocks of a borehole. The majority of the radioactivity in the Earth's crust comes from three elements: potassium, thorium and uranium. In the oil industry, the gamma ray log is often used to predict the volume of

shale present. Higher gamma ray values indicate larger amounts of radioactive elements which are preferentially included in clay minerals. Shales have consistently been shown to be the most radioactive lithology, generally due to the larger amount of clay minerals in shales. If the gamma ray values are low, the rocks are usually interpreted to have less clay mineral: sandstone. Different reservoirs have different criteria for what constitutes "sand" vs. "shale," but a sand cutoff gamma ray value is usually stipulated in order to place rocks in either category.

The problem with this simplification is that radioactive elements are not necessarily an indication of clay minerals. Arkoses are part of a category called radioactive sands, due to the high content of potassium in the k-feldspars. Detrital and authigenic micas are also radioactive minerals and thus coarse grained rocks with a large mica component will also have high gamma ray values (Rider, 1996). Through cuttings analyses we can determine if there are a large amount of feldspars and micas present and proceed with the gamma ray log analyses by filtering out the signals from radioactive sands.

At the SAFOD site, a spectral gamma ray log was collected using a Hostile Environment Gamma Ray Neutron Sonde (HNGS) tool which resolves the gamma ray signature into Potassium, Uranium, and Thorium concentrations. We use these data to determine which element is the dominant influence in the overall gamma ray signature. It is important to understand which element is affecting the gamma ray the most because it will help us interpret whether a high gamma ray value is indicative of shales or radioactive sands.

Cuttings

Drill cuttings ranging from millimeters to microns in size were nearly continuously sampled through phase one and two drilling (Figure 2.4), providing the most complete lithologic record of subsurface rocks in the SAFOD borehole. However, using cuttings alone to evaluate the characteristics of the rocks is far from ideal for several reasons:

1) Although circulation times from the bottom of the borehole to the surface are well constrained through methods used in the oil industry, mixing of cuttings through the 3 meter interval where they are collected serves as an "average" composition in that interval. Small-scale lithologic changes can not be seen within the resolution of the cuttings samples.

2) The stability of the SAFOD main hole was often questionable through the deviated portion; breakouts and caving were common, as seen in the caliper log (Plate 1). This can cause cuttings from higher in the hole to fall and mix with the cuttings lower in the hole. Therefore, it is difficult to have high confidence that the cuttings being examined from one specific depth all actually represent that depth.

3) At the drill site, careful washing and handling of cuttings samples involved drilling mud being gently washed with water through small mesh-size sieves. However, formation mud and shale grains still may have been washed away during this process, causing the cuttings composition to not be a representative sampling.

4) The very nature of drill cuttings is a limitation. Cuttings samples are small pieces of rock which are cut by the diamond-carbide tipped drill bit. They are circulated to the surface in a drilling mud mixture that flows along the side of the hole and drill pipe to the surface. Therefore, these small pieces of rock only provide nonoriented puzzle pieces to what rock is actually present in the subsurface.

With these limitations in mind, cuttings can be effective in the characterization of subsurface lithologies (Winter et al., 2002; Solum et al., 2006; Bradbury et al., in review). By using a systematic optical microscopic technique, we can quantify components of the system such as mineralogy, deformation textures and degree and nature of alteration.

Samples were prepared to provide a statistically accurate subsample from the larger volumes of cuttings collected. At a depth of every 15.3 meters measured depth (mmd), we used a riffle splitter to split an ~1 cc subsample of cuttings from the archives cuttings samples, ensuring that the sub-sample is representative with regards to grain size and composition. The dry subsample was passed over a magnetic plate to remove drill bit material that was mixed with the cuttings. The magnetic material was examined in a binocular microscope and if magnetic rock fragments were in the separates, the separates were integrated back into the sample to maintain the representative nature of the sub-sample. After magnetic separation, samples were very lightly washed and decanted using distilled water to remove drilling mud additives such as walnut shells. After the sub-samples were split, magnetically separated and decanted they were sent to National Petrographic, a thin section production company, to be made into petrographic thin

sections. A total of 83 thin sections from these sub-samples spaced 15.3 m apart were analyzed for this study.

A modified petrographic point count method was used to quantify the composition of the cuttings and core. This point count method uses the Gazzi-Dickinson method (Dickinson, 1970) as a base: counting 300 grains per sample, each grain that lands randomly under the cross-hairs of the microscope is counted as a framework grain. However, the classification of grains was modified to account for the limitations of cuttings. Bradbury et al. (in review) used the Gazzi-Dickenson method to count the bulk composition of the entire borehole at 33 m intervals, quantifying the ratio of quartz to feldspar to lithics, dividing lithics into several categories. We tailored this method specifically to the characteristics of the arkosic section in order to understand the diagenetic and deformational history as well as provenance of these rocks. We classify grains which land under the cross hairs based on the dominant characteristic of that grain. For example, if the grain is composed primarily of large quartz crystals it is counted as quartz but if the grain contains more clay minerals than quartz, it is classified as clay-rich. This is to ensure that features which will help us to understand the history of the rocks such as degree of cementation, deformation, or alteration are not overlooked. Therefore, we divided the grains into classification categories which include alteration and damage characteristics, cement/matrix composition, and primary and accessory minerals or features. The total point counts sum to greater than 100% as we examined compositional and textural aspects of the rocks in conjunction. For more detail regarding the traditional composition of the rocks, please see Bradbury et al. (in review).

The primary features category includes quartz, unaltered feldspar, opaque minerals, and accessory detrital minerals such as muscovite and fuchsite (a chromium bearing muscovite), and various igneous minerals such as amphiboles or pyroxenes. Diagenetic features are those that form cements or matrix (these are usually grouped together as it is sometimes difficult to differentiate between cement and matrix in cuttings); they are divided into secondary quartz overgrowth, veins, calcite, clay minerals, zeolites and iron oxides (which can also be considered an alteration feature derived from the alteration of mafic minerals). Alteration and deformational features are cataclasite, altered feldspar, and biotite replaced by chlorite. We will discuss the criteria for each division.

Primary features are straightforward in their definition. If the cross-hairs of the microscope lands on a discrete grain of one of the primary features named above it is counted in the counting method. Each mineral has different characteristics in different parts of the borehole which will be discussed individually. Igneous minerals are grouped together for purposes of bulk composition, but individual minerals were noted for provenance studies. Fuchsite is commonly observed and is assigned its own category due to the possible significance of the presence of the mineral. Rock fragments such as volcanic groundmass or chert are also included in the primary features group.

The wide range of diagenetic features observed include clay minerals, calcite, secondary quartz formation and iron oxides. The only clay minerals counted as diagenetic features are those that show evidence of being either matrix or cement. An example of this can be seen in Figure 2.5a, where larger crystals are surrounded by the

clay minerals. It is difficult to determine whether this is a depositional matrix or a secondary cementation. Therefore clays similar to this are counted in this category. The other category of clay minerals are those that form from feldspar alteration, these are categorized as alteration features rather than matrix or cement (Figure 2.5b). This division of clay minerals is different from that of Solum et al. (2006), who used X-Ray diffraction methods to quantify clay minerals in the subsidiary fault zones and the country rock of the SAFOD main hole. Iron-oxides include free hematite grains and fine-grained material that is red in both plane-polarized as well as cross-polarized light (Figure 2.5c).

Altered feldspar may fall into three categories. The most commonly observed is the sericitized and vacoulized phase of alteration (Figure 2.5b). Sericite is often referred to as fine-grained muscovite, but is also synonymous with the clay mineral illite (Moore and Reynolds, 1989). Within the scope of the cuttings petrography we define the alteration product of the first category to be illitic material, a phrase Moore and Reynolds (1989) use to encompass illite, mixed-layer phases and other minerals such as sericite. The second altered feldspar category includes feldspars which are altering directly to muscovite (Figure 2.5d). In some of the altered feldspar grains the alteration material is too coarse grained to be referred to as sericite, without additional SEM characterization we will consider these grains to be altering to muscovite. The third category of alteration is feldspars which have been almost completely replaced by calcite, the grains still display feldspar twinning but with characteristic calcite birefringence (Figure 2.5e).

Damage characteristics are generally confined to cataclasites in this study. An example of what we have labeled cataclasite can be found in Figure 2.5f. Cataclasite grains are so fine-grained as to be nearly opaque in cross polars, but are still transparent in plane-polars. Often included in a cataclastic matrix are quartz or feldspar porphyroclasts reduced in size and rounded as a result from grain-scale rotation (Engelder, 1974).

Core Analysis

The amount of core successfully recovered from the SAFOD borehole to date is volumetrically small compared to the amount of cuttings collected over the duration of the project. The advantage in studying core, however, is core samples are whole rock samples rather than small pieces of rock. At the end of phase one 12 m of non-oriented 10.16 cm diameter core was recovered from 3055mmd to 3067 mmd (approximately 2.5 km vertical depth) in the arkosic section (Figure 2.6). During phase two, two 1.9cm diameter, approximately 2.5-3 cm long percussive sidewall cores were collected at 3084.6 mmd and 3121.2 mmd in the arkosic section (Figure 2.7). We analyzed 14 petrographic thin sections prepared from representative intervals in the spot core and two thin sections from the sidewall cores.

We used the small amount of core from phases one and two to fill the holes in our understanding from the study of the cuttings. It is difficult to precisely ascertain what features of the cuttings grains are a result of the cuttings process. If we see similar damage features in the core as in cuttings from the same interval, it is likely that those

features are actually part of the rocks and not drill induced. For example, the majority of quartz observed in the cuttings is extensively concoidally fractured (Figure 2.8a) but the quartz in the phase one spot core, while still damaged and fractured (Figure 2.16 a and b), is not damaged to the extent of the quartz in cuttings. We interpret the concoidal fractures in the cuttings to be damage resulting from the drilling process.

Core provides an opportunity to study features not observable in cuttings which provide clues about the depositional and diagenetic history of the arkosic rocks. These features include: sedimentary structures such as graded bedding or paleohorizontal indicators, cross-cutting relationships, and diagenetic features such as cementation, compaction structures, and mineral authigenesis. It is easier to separate detrital from authigenic minerals in core than cuttings because the rock is intact and relationships between individual grains can be directly observed rather than inferred. Understanding the origin of minerals such as muscovite or calcite can constrain temperature and pressure conditions as well as fluid flow histories.

Core is also used to evaluate the deformational history of the rocks. With whole rock samples from core we can directly asses the extent and character of deformation through observation of meso- and microstructures. Deformation caused by the coring process and subsequent unloading resulting from bringing the core to the surface is readily apparent to the eye (Almeida et al., 2005). Samples chosen for thin section analysis are located in portions of the core not obviously affected by coring-related deformation. We assume that microstructures observed in thin section are features which are inherent to the arkose.

Electrical Image Log Analysis

Formation Micro-Imaging (FMI) logs, or electrical image logs, are especially helpful for providing information about bedding orientation and character, formation thickness, sedimentary structures, fault and fracture orientations and character, and general lithologic characteristics such as grain size, shape, and sorting (Thompson, 2000). During Phase One of drilling at the SAFOD site, prior to the setting of the second string of drill casing, electrical image logs were collected in the arkosic section from 1920 mmd to 3050 mmd. These data were collected using the Schlumberger Formation Microresistivity Sonde (FMS) tool, first developed in 1986 from traditional dipmeter tools (Ekstrom et al., 1986).

The FMS tool measures minute changes in the electrical resistivity of the borehole wall through electrode arrays embedded in pads on each of the tool's four arms (Ekstrom et al., 1986). Because boreholes often become enlarged in an oval shape due to borehole breakouts, the FMS tool was designed to have two arms record the microresistivity in the long axis orientation and two in the short axis orientation. While having four arms only covers approximately 20% of an 8.5 in diameter borehole, by measuring in the four orientations it is possible to extract pertinent fracture and bedding orientations from the rock volume (Ekstrom et al., 1986). The resolution of the FMS electrical arrays is on the millimeter scale, or nearly continuous sampling of the borehole lithologies.

The SAFOD electrical image logs are dynamically normalized so that the scale is set to the maximum and minimum amounts of resistivity found in a certain volume. Therefore, the image shows resistivity values which are greater than, equal to, or less than the maximum and minimum resistivity values in those rocks rather than an arbitrary numerical scale. We use a white/orange/black color scale to examine our image logs so that white areas show zones with the most electrical resistivity and black areas are zones where the electrical resistivity is the lowest, or the most conductive (Figure 2.9). Orange zones are those that fall somewhere in the middle of the dynamic scale.

We used Geomechanics International (GMI) Imager software to examine the electrical image logs and to plot bedding and fracture orientations. Linear features in a circular or oval borehole will appear as sinusoids with amplitude dependent on the angle at which that linear feature intersects the borehole (Figure 2.9). The GMI software allows us to calculate the dip and dip direction of sinusoidal features. The two most common sinusoidal features are strata, or bedding, and fractures (Figure 2.9). Fractures can be conductive or resistive features depending on whether the fractures are open-mode (conductive), healed fractures (resistive), or filled with minerals such as calcite (resistive), quartz (resistive), clay minerals (conductive) or iron oxides (conductive). The width and clarity of fracture boundaries can also vary widely. Bedding planes can be either conductive or resistive depending on lithology.

Using electrical image logs would be ideal for understanding the depositional and structural characteristics of the arkosic section, but the poor quality of the SAFOD data provides a significant limitation. By the time the electrical image logs were collected, the

borehole wall integrity had degraded significantly. There are many intervals where the borehole had become so enlarged through breakouts and cave-ins (Plate 1) that the pads on the arms of the FMS tool were not in contact with the borehole wall and the tool could not collect data properly. These areas appear blurry and unclear in the logs (Figure 2.10) whereas areas with good data have very high resolution; features on the millimeter scale can be identified. However, even with the gaps in clear data, the Image logs still provide the most complete picture of small scale structural and depositional changes throughout the arkosic section. These data can be interpreted in combination with the lithologic information from the cuttings and core to produce a comprehensive characterization of the arkosic rocks at SAFOD (Figure 2.11).

2-3 RESULTS

Wireline Logs and Cuttings Microscopy

Plate 1 shows the velocity, caliper, porosity, density and gamma ray logs for the phase one arkoses plotted against lithology, composition, and fracture densities in the orientation of the deviated borehole, 55° deviated from vertical. By examining the logs at the same scale, we can identify zones where physical properties of the rocks result in changes in the log response. We incorporate the geophysical signatures from wireline logs with observations of rock samples to form a more complete picture about the nature of these arkosic rocks. Before the combination of these datasets, however, we need to ascertain what certain logs, such as the gamma ray log, are measuring.

Cross-plots of the concentration of natural radioactive elements potassium, thorium, and uranium obtained from the spectral gamma ray log against the general gamma ray signature allow us to determine which elements contribute to the gamma ray signature. We assume that the abundance of an element is what most controls the gamma ray signature; a linear increase in the concentration of that element will correspond to a similar linear increase in the gamma ray signature. The potassium log exhibits little variation with increases or decreases in gamma radiation (Figure 2.12a), which indicates that its contribution is nearly constant through the arkosic interval. The strongest correlation in the cross-plots is the thorium log with correlation coefficients of 0.702 (Figure 2.12b). The most common source of measurable thorium are shales because thorium is often incorporated in clay minerals structure (Rider, 1996). Here, uranium is also strongly correlated to the gamma ray log (Figure 2.12c), but uranium could come from several different sources and is not often utilized in gross lithologic interpretations (Rider, 1996). We interpret these results to show that while the presence of feldspars and micas may elevate the base-level of the gamma ray log, the actual variations in the log are a result of presence of clay minerals and/or shale. This will be considered in subsequent interpretations of the gamma ray logs in combination with lithologic data.

Based on the results detailed below, we have divided the arkosic section into three distinct zones and will discuss the results of cuttings petrography and wireline logs analysis for each zone separately. Each zone has unique characteristics, the implications of which will be discussed in the Discussion portion of this paper. The zones are referred to here as: 1) the "upper arkose" which extends from 1920 mmd to 2530 mmd, 2) the

"clay-rich zone" from 2530 mmd to 2680 mmd, 3) the "lower arkose" from 2680 mmd to 3157 mmd. We describe the lithology and structure of each of these zones within the larger arkosic section below.

The Upper Arkose

The upper arkose zone (1920-2530 mmd) has a porosity range of 0.01 to 0.44, with an average porosity of 0.10, or 10% (Table 2.1). The average density of the upper arkose is 2.56 g/cm3 with a range of 2.13-2.72 g/cm3. Compressional velocities range from 3.2-5.76 km/sec with an overall average velocity of 4.57 km/sec (Table 2.1). Velocities generally increase with depth, although there are some low velocity zones through the middle portions of the upper arkose.

The rocks of the upper arkose are quartz and feldspar rich with 1-10% clay minerals present as cement or matrix (Figure 2.13). The clays of the upper arkose tend to be chlorite or kaolinite minerals, the chlorite generally replaces biotite, a feature often seen in plutonic source rocks (Dapples, 1979), and is very rarely observed as a fine-grained constituent of the matrix. The seemingly anomalous gamma ray signatures averaging 129.08 API is a value typically associated with finer grained rocks, however the arkosic nature of the rocks makes base-level of the gamma ray log signature inherently higher. In comparison with the lower arkose, the gamma ray signature in the upper arkose stays reasonably consistent, with shallow peaks and troughs. We interpret this to be due to the relative homogeneity of the upper arkose.

Quartz grains are generally undeformed aside from the brittle fracturing which we interpret to have occurred as a result of the drilling process (Figure 2.8a). Undulatory extinction and other plastic deformation of the quartz crystal lattice are rarely observed in cuttings from this upper arkose interval. Discrete quartz is the largest component of the system, samples range from 45% - 60% quartz (Figure 2.13).

Feldspar concentrations as a whole are higher in the upper arkose than in the other zones. The amount of unaltered feldspar is constant (4-10% of sample), similar to trends in the lower arkose, with ratios of plagioclase to K-feldspar approximately equal. The K-feldspar component is primarily microcline, displaying classic microcline tartan twinning. Orthoclase is also present, identifiable by its distinct cleavage.

The amount of iron-oxide cements and staining are generally higher than in the rest of the arkosic section, although the proportions vary within this zone; amounts range 5-30% iron-oxide (Figure 2.13). Some iron-oxides may be fracture fill or grain coatings, but the majority of iron-oxide present forms cements and matrix of the grains (Figure 2.5c).

Detrital micas such as muscovite, fuchsite, and biotite are rare, as are igneous minerals; none ever compose more than 1% of the sample (Figure 2.14). Rock fragments other than granitics are rarely observed.

Altered feldspars compose 12-20% of the sample (Figure 2.13). The feldspars range from slightly altered with small amounts of illite forming to highly altered where the feldspar is almost indistinguishable. Feldspar altered to muscovite is very rarely

observed in the upper arkose, the majority of altered feldspars are altered to fine-grained sericite and clay.

Throughout the upper arkose, wireline logs and cuttings composition are generally invariable, reflecting homogeneous physical properties. One noted exception to the homogeneity is 2022 mmd to 2045 mmd where the compressional velocity drops to a range of 3.20 to 4.6 km/sec, corresponding to an increase in porosity to 18%. This zone provides an excellent example of how cuttings microscopy can be combined with wireline logs to more fully characterize the rocks. The two cuttings thin sections evaluated at that depth (2026.92 mmd and 2042.16 mmd) show a marked increase in iron-oxide rich grains (17.00-24.67% of sample) from the samples above and below. There are relatively small amounts of cataclasite in this zone, however, only 4.00-8.00% of sample, less than most of the other upper arkose samples. We believe this is a high porosity; high permeability zone that has acted as a fluid conduit for oxidizing fluids, but the small amount of cataclasite implies that it is not an intraformational fault.

The Clay-rich Zone

A clay-rich zone (2530-2680 mmd) with up to 60% clay minerals and clay-sized particles, anomalously high gamma ray, high porosity, and low velocity is observed from 2530 mmd to 2680 mmd (with the exception of a small block from 2565-2595 mmd which has different characteristics than the rest of the clay-rich zone). Clays cannot be fully characterized optically due to the small grain size. To best understand the composition and morphology of the clay particles in this zone, a combination of X-ray

diffraction (XRD) and Scanning Electron Microscopy (SEM) is needed. There are plans underway to more fully characterize the clays of this zone with J. Solum in the future. However, we can combine our optical analyses with wireline logs to deduce some fundamental characteristics of the clay-rich zone.

The clay-rich zone was initially identified by the wireline logging company at the SAFOD site by the dramatic increase in gamma ray and porosity with a dramatic decrease in velocity. The lowest velocity in the clay-rich zone is 2.69 km/sec with an average velocity of 4.00-4.27 km/sec (Table 2.1); considerably lower than in the upper and lower arkoses. The average neutron porosity is 0.18-0.27, higher than the average porosities of 0.10 and 0.08 in the upper and lower arkoses respectively. Usually, these dramatic peaks and troughs in the wireline logs would indicate a fault zone, but the lithologic evidence does not clearly point to fault zone characteristics, aside from the advanced clay development. Cataclasite values are the lowest in the clay-rich zone than in the upper and lower arkoses, averaging 3.66% of sample (Figure 2.14). It is possible that typical damage characteristics may be overprinted by the large amounts of clay minerals present.

Clay minerals range in composition from illite to smectite to mixed layer illite-smectite (I-S), which are high birefringence clay minerals (Figure 2.8b), to chlorite, which often gives the clay grains a greenish color in cross- and plane-polars, to muscovite. There are more iron-oxide rich grains observed in the clay-rich zone (8.26%) than in the lower arkose but less than in the upper arkose (Figures 2.13 and 2.15). This could be reflecting a decreasing gradation in oxidation with increasing depth. More

calcite also occurs in the clay-rich zone than in either of the arkoses, 5.13 % as opposed to 3.56% in the upper arkose and 1.31% in the lower arkose (2.13).

Additionally, the chromium-bearing muscovite mineral fuchsite is commonly present in the lower arkose and clay-rich zone but is very rarely seen in the upper arkose (Figure 2.14). Fuchsite is very similar to muscovite in cross-polarized light (Figure 2.8c) and can easily be mistakenly identified; however the mineral is a light translucent green in plane-polarized light (Figure 2.8d). It should be noted that sometimes mica minerals are added to drilling mud to maintain the physical properties required to drill successfully but at the SAFOD site walnut shells are the additive used consistently. Fuchsite was also found in core thin sections, confirming that it is in fact a true feature of the rock. There is up to 1.26% fuchsite in the clay-rich zone, a larger amount than in the upper or lower arkoses (Figure 2.14).

Within the larger clay-rich zone an interval from 2565 mmd to 2595 mmd contains 27.33% clay but with quartz and feldspar abundances (37.66% and 10% respectively) similar to the composition of the lower arkose (Figure 2.13). The ability to identify more discrete quartz and feldspar in this zone indicates an increase in grain size from the rest of the clay-rich zone. Wireline logs are also indicative of coarser grained sediment in this interval (Table 2.2). Velocity increases to 4.48 km/sec and porosity decreases to 0.12 with a corresponding increase in density from 2.48 g/cm3 to 2.58 g/cm3. This small interval likely represents a different lithology than the rest of the clay-rich interval and is not considered in the physical property calculations of the rest of the clay-rich lithological unit.

The Lower Arkose

The lower arkose, from 2680 mmd to 3157 mmd is characterized by variable wireline log signatures, with a wider range of values for porosity, gamma ray, velocity and density than the upper arkose (Table 2.1, Plate 1). Porosity is generally less than in the upper arkose and clay-rich zone, with an average porosity of 0.08. The average density is similar to that of the clay-rich zone, 2.53 g/cm3. The average gamma ray value is 112.48 API, less than the upper arkose, and the shape of the gamma ray curve has more peaks and trough overall than the homogeneous curve of the upper arkose.

The lower arkose is generally finer-grained than the upper arkose. Clay-sized particles and minerals compose on average 15.5% of the samples, as opposed to the 3.8% average of the upper arkose (Figure 2.13 and 2.15). Clays are generally illitic and smectitic with almost no kaolin minerals present. There are similar amounts of chlorite present in the lower arkose than in the upper arkose, although altered biotite is rarer in the lower arkose.

There are also distinct compositional differences between the upper and lower arkoses. Quartz is the dominant component of the system in the lower arkose, as in the upper arkose, but the concentration is less than the upper arkose. In the lower arkose the average amount of quartz in samples is 48.12% with a range of 33%-60% (Figure 2.13). The majority of quartz in the lower arkose is plastically deformed (Figure 2.8e), in places full sub-grains have developed in the crystal structure. The quartz is similarly fractured as in both the upper arkose and the clay-rich zone.

There are generally fewer feldspar grains overall (both altered and unaltered) in the lower arkose than the upper arkose, although the ratio of plagioclase to k-feldspar remains equal (Figure 2.13). While the upper arkose contains more grains of altered feldspars, the altered feldspars of the lower arkose are generally altered to a greater degree. Feldspars alter directly to muscovite in the lower arkose; there are some instances of nearly complete replacement by muscovite (Figure 2.5d).

There are fewer iron-oxide rich grains in the lower arkose than the upper arkose, ranging from 2%-15%, averaging 5% of sample (Figures 2.13 and 2.15). The characteristics of the iron-oxides are similar to those in the upper arkose and clay-rich zone, at times dark red in plane and cross polarized light, at other times opaque under both forms of light but red in reflected light. Iron-oxide composes fracture fill, grain coatings and fine-grained matrix.

Volcanic clasts are present in the lower arkose but not in the upper arkose. There is only one sample in the upper arkose that contains fragments of volcanics (1966 mmd) whereas volcanic clasts are present in every lower arkose sample (Figure 2.14). Volcanics clasts comprise an average of 1.79% of sample, but their presence is significant nonetheless. The presence of volcanic lithics may be an indication of a different provenance than the upper arkose. The volcanics are all similar: porphyritic with very fine-grained, often devitrified groundmass which looks distinctly different than the grains designated clay-rich or cataclastic (Figure 2.8f).

Fuchsite concentrations range from 0.14% - 2.00% of sample in the lower arkose. In the lower arkose, fuchsite occurs as small grains within a larger fine-grained, clay-rich grain and rarely as discrete grains.

In the lower arkose there is an average of 0.76% of the zeolite mineral laumontite while the upper arkose average is 0.11% laumontite. The average value for the upper arkose is inflated due to a sample at 1921 mmd which is 2.67% laumontite. The sample at 1921 mmd is in a transition zone from Salinian granodiorite to the arkosic rocks; the large amount of laumontite in sample 1921 mmd may be due to an input from the laumontite-rich granodiorite. Solum et al. (2006) also detected relatively large amounts of laumontite through XRD analysis in the lower arkose with little to no laumontite in the upper arkose; evidence which led them to define two distinct arkosic units similar to our designations.

Core Analysis

The spot core collected during phase one drilling intersected a small clay-rich shear zone at 3067 mmd, the deepest part of the spot core. Numerous studies have examined the composition and frictional properties of this shear zone (Tembe et al., 2005; Shleicher et al., 2006; Solum et al., 2006) and recent revisions of earthquake locations based on the newest velocity models suggest that this shear zone may be a southwestern strand of the SAF (Hickman et al., 2005, Solum et al., 2006). Obtaining whole rocks samples through this interval was sheer luck, but fortuitous nonetheless because this spot core provides the unique opportunity to study fault rocks from

seismogenic depths. The sedimentary rocks in the spot core are thoroughly damaged and deformed (Figure 2.16 a and b), perhaps as a result of the faulting that has occurred in the cored shear zone. The structure and deformation of these rocks are discussed in more detail in Chapter 3 of this thesis. Here, we examine compositional and diagenetic features seen in the spot core to compare to findings in the cuttings samples detailed above while briefly discussing the microstructural features of the core.

The core samples are arkosic, composed primarily of feldspar and quartz. Over the 12 m of core grain size grades abruptly from coarse pebble/cobble conglomerate to coarse sandstone, to fine sandstone to siltstone (Figure 2.6). The pebbles and cobbles of the conglomerate are granitic and volcanic, with significantly more granite than volcanics.

Volcanic clasts are porphyritic, similar to those observed in the lower arkose cuttings, with large plagioclase crystals enmeshed in a fine-grained devitrified groundmass (Figure 2.16c). In some cases, phenocrysts are oriented in a primary flow texture. Granitic clasts are commonly altered (Figure 2.16d), composed of quartz, feldspar, amphiboles and chloritized biotite. The majority of laumontite observed in the core is found in granitic clasts where it has been mobilized into veins or cements (Figure 2.16e).

Macroscopically, the core appears to be stained in many places with iron-oxides and microscopic analysis verifies this (Figure 2.16f). Iron-oxide staining is a common feature found in arkosic rocks resulting from the alteration of unstable mafic minerals (Dapples, 1979). The core is highly indurated, in most cases samples did not need to be

epoxied to maintain integrity when prepared for thin section. Paradoxically, in thin section the arkose is highly damaged, riddled with microfractures with little evidence of healed fractures (Figure 2.16g). Grain-size reduction is common and grains are broken apart in place (Figure 2.16b). Evidence for cementation mechanisms such as quartz overgrowth are not commonly observed. Also absent are indications of extensive fluid flow. There are rare veins filled with laumontite, calcite (Figure 2.16g), secondary quartz or muscovite (Figure 2.16h) observed and feldspars are generally unaltered through the core. The lack of significant amounts of laumontite, calcite and secondary quartz correspond to what has been observed in the cuttings sample. However, more grains of altered feldspar were found in the cuttings than in the core, although the amount varies throughout the cuttings (ranging from 6-20%). It is unlikely that feldspar alteration occurs post-drilling, so the logical interpretation is that the core was collected in an interval where little fluid flow occurred.

Authigenic muscovite was observed as vein material in several locations in the core samples (Figure 2.16h). These veins, no more than 0.10 millimeters in width, cut across several grains which is evidence that they are post-depositional features. The implications of the formation of authigenic muscovite will be discussed in the interpretation section of this chapter.

The fine-grained portions of the spot core look similar to grains counted as clay-rich in the cuttings (Figure 2.16i). The fine-grained rocks are composed primarily of texturally immature quartz and feldspar with a matrix of high birefringence clay minerals. In most areas of the core it is evident that clay minerals are a depositional feature rather

than a secondary cementation. Small angular mica grains similar to those seen in the finer grained cuttings are also observed in the spot core samples, some of these mica grains are muscovite and some are fuchsite, both in the cuttings and core. The clay minerals are not oriented in any of the core samples. No microfossils were observed at all in either cuttings or core, even in the finest grained intervals. This is unfortunate, as will be discussed later in this report.

Electrical Image Logs

Following the designations established in the cuttings and wireline log analysis section, we report our results for the upper arkose, clay-rich zone and lower arkose separately. Image logs also show distinctly different characteristics between the three lithologic units, further verifying our interpretation that the upper arkose, clay-rich zone and lower arkose are separate units.

The Upper Arkose

Based on the analysis of image logs, the upper arkose section can be divided into five blocks with distinctly different sedimentary and structural characteristics including wirleine logs response (Table 2.2). Each block is referred to by a number (Figure 2.17). The map of the different blocks in Figure 2.17 is exclusively in the context of SAFOD borehole and has not been extrapolated out into the formation. True thicknesses of each block were calculated using the following calculation (Figure 2.18):

$x = y (\cos\alpha)$

where x equals the true thickness, y equals the apparent thickness and α is the angle between the trend and plunge of the borehole and the pole to bedding of the block. While there were minor variations in the bearing of the borehole these were too small to significantly alter the true thickness result. We used an average bearing of 35/045 for the borehole in our calculations. An average pole to bedding was determined using the statistical methods of a stereonet program. A complete catalogue of stereonets and calculations for each block can be found in Table 2.3.

Block One, from 1920 mmd to 2145 mmd, is composed of poorly bedded sandstone and conglomerate. The sandstones are fine to coarse grained, represented by a "speckled" texture in the image logs seen frequently throughout the entire arkosic section image logs (Figures 2.9 and 2.10). The rocks are highly fractured in some portions of the block but lightly fractured in others. We define a fracture density of >15 fractures per 10 meters to be highly fractured, 5-15 fractures per 10 meters to be moderately fractured and 0-5 fractures per 10 meters to be lightly fractured. These designations are based on comparisons within the arkosic section as a whole so that each block can be related to other blocks within the section. Much like the dynamically normalized resistivity scale of the image logs, the fracture density scale is based on where the highest fracture density in the arkosic section is and where the lowest fracture density is; these are the maximum and minimum fracture density values. The distribution and nature of fractures are discussed in more detail in the context of structural characterization, in Chapter 3 of this thesis.

There is one small interval of soft sediment deformation in Block 1 at 1955 mmd. Bedding was measured in three different orientations with both shallow and steep dip magnitudes over 10 m, but only in this limited interval. If trends like that were observed over a larger area, it could be interpreted to be a zone of post-lithification tectonic folding, but in an isolated occurrence we interpret it as a soft sediment slump fold. That interval is the only bedding observed in block one.

In block two, the rocks are well-bedded conglomeratic sandstones dipping between 0º and 30º to the northwest, striking south/southwest. Block two extends from 2145 mmd to 2220 mmd, an apparent thickness of 75 m. With beds dipping so shallowly, we assume that the beds are upright and lying nearly flat, rather than completely overturned. With that assumption, we calculate a true thickness for block two of 44.9 m (Table 2.3).

The separation between block one and block two is not easily interpreted due to gaps in the quality of the FMI data. Through the rest of the section, dramatic dip magnitude or direction changes are inferred to be faults (Figure 2.17), but in this instance the change from block one to block two is less clear. With little bedding observed in block one, the boundary between the two blocks is based on a change in rock characteristic at 2145 mmd than in a change in bedding orientation. The transition could be depositional, with blocks one and two representing a fining downward sequence, grading from massive pebble conglomerates in block one to the sandier block two which is more distinctly bedded.

At the interface between blocks two and three there is an abrupt dip change from shallow northwest dipping beds to variably southwest dipping beds (Figure 2.17). Block three is a small block, from 2220-2250 mmd, with a stratigraphic thickness of 20.1 m of sandy and silty beds which dip between 30-90º to the southwest. Block four extends from 2250 to 2290 mmd, with a thickness of 18.8 m, and is nearly identical to block two. Like block two, the bedding in block four is nearly horizontal, or shallowly dipping to the northwest. The relationships between blocks two, three, and four are unclear. We interpret this section either to be 1) faulted, with block three being a fault-bound block which has been rotated relative to blocks two and four or 2) a tight asymmetric fold (Figure 2.19). The bedding of block three is very coherent, with clear bedding trends throughout the block, which is not consistent with soft sediment deformation. The transitions from block two to block three to block four are abrupt but not easily interpreted as discrete fault planes in the image logs. Abrupt bedding changes are also associated with some tight folds and the lack of fault characteristics observed may be an indication of folding. Because the rocks in the SAFOD borehole are heavily fractured and faulted (Bradbury et al., in review; Hickman et al., 2005; Solum et al., 2006; Boness and Zoback, 2006), our favored interpretation is that intraformational faults separate the blocks, but we cannot rule out the possibility that the rocks may be folded as well.

Block five, from 2470 mmd to 2529 mmd with true thickness of 72.6 m, is coarse sandstone with zones of laminated bedding dipping 60º to 90º to the northeast. The coarse sandstones appear as the speckled texture in the image logs, with a combination of conductive and resistive spots and clasts. It is difficult to resolve the spots into lithologic

versus breakout features through much of block five, due to the poor quality of the data. Throughout block five, bedding parallel fractures are common although as the borehole approaches the clay-rich zone, fracture density increases with fractures oriented in all directions. The last 30 meters (measured dimension) of block five is poorly bedded with a high fracture density.

Without considering the thickness of block one, the total measured thickness of the Upper Arkose is 156.4 m. If we consider block one to be oriented similarly to block two, interpreting it to be a fining downward sequence, then the thickness of block one would be 134.78 m. Adding the thickness of block one to the Upper Arkose sequence, the total thickness of the Upper Arkose is 291.18 m.

The Clay-rich Zone

The clay-rich zone is characterized by poor data quality. The borehole was often enlarged elliptically putting the caliper in this unit rarely in gauge. The short axis of the caliper stayed approximately even, at 10-12 inches in diameter but the long axis often maxed out beyond the 20 inch maximum reach of the caliper tool (Plate 1). The result of this drastic loss of borehole integrity is that the image logs appear blurry through nearly the entire clay-rich zone. Few fractures and no bedding were recorded in the more clay-rich portions of this zone, although bedding was observed and noted in block 7, which we believe is a block of more coherent rock within the clay-rich zone. Block 7 strikes southeast, dipping shallowly to the southwest from 2565 mmd to 2595 mmd with a true thickness of 28.7 m (Table 2.3). The image logs in Block 7 are blurry but some

interpretations can be made about grain size from the wireline logs and cuttings analysis. Wireline logs in block seven also changed in character, gamma ray and porosity decreased while density and velocity increased compared to the rest of the clay-rich zone (Plate 1). Cuttings point counts show a decrease in the amount of clay-rich grains. These data indicate that block 7 is coarser grained than blocks 6 and 8, significantly different than the rest of the clay-rich zone.

Few fractures were measured in block 8 and those that are observed are oriented in all directions. The caliper log records as much hole enlargement as in block 6 which is why the Image logs were not useful in observing the lithologic characteristics of block 8 (Plate 1). No bedding was observed in blocks 6 and 8 so no thicknesses could be calculated.

The Lower Arkose

For the sake of simplicity, the lower arkose has been divided into three blocks (Figure 2.17). Block 11 is the last block in the sequence drilled during phase two drilling and image logs are not available for that block at this time. In the absence of FMI data, however, we assume that block 11 is one block. The fault separating blocks 10 and 11 was cored at the end of phase one (location of coring marked on Figure 2.17)

Block 9 extends from 2680 mmd to 2880 mmd with a true thickness of 158.9 m (Table 2.3). The bedding of block 9 dips shallowly to the south/southwest, at a slightly different orientation than that of block 7. The rocks of block 9 are homogeneous fine-grained sandstones with fractures primarily oriented in two directions, bedding parallel

and bedding perpendicular. These fracture orientations are often observed in sandstone outcrops (Narr and Suppe, 1991).

Block 10 is lithologically very similar to block 9 consisting of well-bedded, and in some places laminated, fine-grained sandstone and siltstones. At 2880 mmd there is an abrupt change in dip magnitude and direction (bedding dips steeply to the northeast) which stays consistent until the end of the FMS measurements at 3010 mmd (the borehole extended to 3050 mmd, but due to the tool configuration we were unable to collect image log data to the bottom of the borehole). The core collected at the end of phase one was not oriented so bedding of the core could not be measured. We consider the apparent thickness of block 10 to be 170 m, assuming that the block continues to the shear zone encountered in the phase one spot core. The calculated thickness is 65.1 m, smaller than block 9 (Table 2.3). An example of representative image logs from block 10, along with the corresponding composition can be seen in Figure 2.11; here we see that the bedding in block 10 is centimeters thick.

We do not have bedding or fracture data for block 11, but the apparent thickness is 107 mmd. The extent of block 11 ends at the abrupt lithology change seen at 3157 mmd where the cuttings character changes from arkosic to very fine-grained mudstones and siltstones interpreted to be part of the Great Valley Sequence (Evans et al., 2005; Hickman et al., 2005).

The thicknesses of blocks 9 and 10 gives a minimum thickness of 224 m and if we assume the apparent thickness of block 11 to be the maximum possible thickness of that block, total maximum thickness of the Lower Arkose is 331 m.

2-4 SUMMARY OF LITHOLOGIC CHARACTERIZATION

On the basis of grain composition, and wireline and image log data, we divided the arkosic section in the SAFOD borehole from 1920 mmd to 3157 mmd into three distinct lithologic units: the upper arkose, the clay-rich zone and the lower arkose. The upper arkose extends from 1920 mmd (1878.95 m vertical depth) to 2530 mmd (2241.92 m vertical depth) with a combined thickness of 156.4-381.4 m (Figure 2.20). It is more feldspathic than the lower two units with fewer clay grains. There are five different structural blocks within the upper arkose which exhibit similar compositions. We infer intraformational faults separating the different dip regimes which define the structural blocks. The fracture and bedding orientations for each structural block can be found in Appendices B and C.

The clay-rich zone extends from 2530 mmd (2241.92 m vertical depth) to 2680 mmd (2330.97 m vertical depth) and is characterized by high gamma ray and porosity values, with low density and velocity values. Borehole instability in the low-velocity zone did not permit data collection by the FMS tool, so we have few data for fracture or bedding orientations. Without bedding or fracture data, we cannot calculate the true thickness of the clay-rich zone, but it should fall in the range of 28.7 – 121.3 m thick (Figure 2.20). Compositionally, the clay-rich zone is dominated by clay-sized particles and clay minerals with similar amounts of feldspar and accessory minerals as the lower arkose. There are elevated amounts of fuchsite and calcite in the clay-rich zone compared to the other two lithologic units.

The lower arkose extends from 2680 mmd (2330.97 m vertical depth) to 3157 mmd (2613.51 m vertical depth) with a thickness of 224-331 m (Figure 2.20). The lower arkose is the more fine-grained of the two arkosic units. There is a higher percentage of clay mineral matrix and cement present. Both fuchsite and volcanic clasts are present in the lower arkose but are very rare in the upper arkose. The lower arkose can be divided into at least two different structural units, the last 107 m of the lower arkose were drilled during phase two and image logs are not available for that portion of the section.

The compositional and structural differences between the upper arkose, clay-rich zone and lower arkose indicate that these are, in fact, different rock units. To illustrate the compositional difference between the three lithologic units graphically, Figure 2.20 compares the three major components of the system, quartz, feldspar, and clay minerals, normalized to 100%. The implications of these differences are discussed in the Discussion/Analysis portion of this report.

The complete table of framework percentages of point counts can be found in Appendix A. Tables of fractures and bedding can be found in Appendix B.

2-5 ANALYSIS OF RESULTS

By examining the results of a variety of datasets we can work towards a better understanding of the important elements of the geologic history of the arkosic sedimentary rocks. We use cuttings, core, wireline logs and image logs results to interpret the depositional environment, diagenesis, and deformational history of the arkosic section.

Significance of the Three Lithologic Units

Fundamentally, the upper arkose, clay-rich zone and lower arkose differ in framework composition (Figure 2.20), alteration and deformational features. We have established these compositional differences in the methods and results sections; here we discuss the causes of these differences.

The disparate types of feldspar alteration and presence/absence of laumontite can be attributed to the difference in present depths of the units with the lower arkose deeper than the upper arkose. Therefore the feldspars in the lower arkose have undergone more progressive alteration from illite to muscovite. Because diagenetic alteration is highly dependent on pore fluid composition, diagenetic differences in the three units may be a result of compartmentalized fluid regimes within the entire section.

Given the clay-rich composition of the clay-rich zone, compartmentalization could be caused by the clay-rich zone working as an impermeable layer between the two arkosic units. This would explain the change in chlorite characteristics from the upper arkose to the lower arkose seen in optical analyses as well as detailed XRD analyses (Solum et al., 2006). A change in oxidation state may result in a change from the chloritized biotite of the upper arkose to fine-grained chlorite as a constituent of the lower arkose (Dapples, 1979). Furthermore, the upper arkose contains more calcite than the lower arkose; those rocks may have been altered by fluids supersaturated with carbonate ions.

Along with differences in diagenesis, the upper arkose, clay-rich zone and lower arkose also show evidence of differences in depositional characteristics. Volcanic clasts

and fuchsite are present in the lower arkose but not in the clay-rich zone or the upper arkose. Additionally, the ratio of quartz to feldspar to clay minerals is different for each lithologic unit. If cuttings analysis permitted plotting of sandstone composition in the traditional QFL ternary diagram, we suspect that the three units would plot in disparate regions of the diagram. However, this does not necessarily mean that the three units are unrelated in their depositional history. Here we discuss some possibilities for the genesis of the three lithologic units and how they may be related.

1) The three units could represent progressive deposition from one source area. The arkosic section could be a unroofing sequence where volcanics and fuchsite-rich rocks are eroded and deposited first in the lower arkose followed by the exhumation and weathering of the granitic pluton, resulting in a more feldspathic unit – the upper arkose. In this scenario, the clay-rich unit may represent a long period of tectonic quiescence and little sedimentary input. Or the clay-rich unit could have been deposited as an overbank deposit after a channel avulsion. This interpretation is based on the assumption that nearly horizontal bedding in the arkosic section is right-side-up rather than overturned. In that case the lower arkose would be older than the clay-rich zone which is in turn older than the upper arkose.

2) Another hypothesis is that the clay-rich zone is associated with a fault zone which has offset two units derived from the same source. The lower and upper arkoses may still be an unroofing sequence which has subsequently been faulted. Reflection seismic data did not image a fault zone in that location (Hole et al., 2001; Catchings and Rymer, 2002; Bleibinhaus et al., in review), which could be a consequence of a steeply

dipping fault similar to others in the vicinity of the SAFOD site. The orientation of the possible fault zone could not be determined from the electrical image logs. Without knowing the orientation of the possible fault zone, it is difficult to ascertain whether the fault is a normal fault, thrust fault or strike-slip fault. The lower and upper arkoses would have different age relationships depending on the history of faulting and simple superposition principles may not apply to the SAFOD arkoses.

3) It is also possible that the clay-rich zone is a fault zone which has offset two units derived from two very different sources. The difference in composition between the upper and lower arkoses could be the result of juxtaposition of two units from different basins and different ages. The complexity of the SAF zone could make it possible to have a fault-bounded block of rocks normally found on the east side of the fault stranded on the west side of the fault. This is seen at Mustang Ridge, where Franciscan serpentinite sits on both sides of the fault (Rymer, 1981), in the northern portions of the fault where Salinian granite sits on the east side of the SAF (Ross, 1984). The lower arkose could be a similar fault-bound block which at some point in the history of the SAF became juxtaposed against the Salinian Block on the west side of the fault.

Interpretation of the stratigraphic and age relationships between the three units is complicated by the amount of faulting in the arkosic section. With a total of 12 possible faults identified, the entire arkosic section has been offset and deformed to such a degree that it may be impossible to precisely determine original depositional or stratigraphic relationships. It is possible that portions of the stratigraphic section have been repeated through faulting or that there is section missing from the whole. As a result, each unit

could be either thicker or thinner than it appears in the borehole. The data do indicate that there is a compositional difference between the three lithologic units, but to draw conclusions about the significance of the three units beyond that result is not applicable in this situation.

Depositional Environment

Image logs would have been the best dataset for determining the depositional setting of the arkosic rocks because even small scale sedimentary structures can be seen with the millimeter resolution of the image logs. However, with the low quality of the SAFOD Image logs we could not find any conclusive sedimentary structures.

In the absence of sedimentary structures we can use our observations about the nature of the sedimentary rocks to draw some conclusions about depositional environment. Arkoses are generally considered to be proximal deposits due to the instability of feldspars (i.e. Scholle, 1979). Feldspars are far less resistant to abrasion and chemical weathering than quartz, thus it is unlikely that a clastic sedimentary rock containing 11-21 % feldspar will be very far traveled. Furthermore, the angularity of clasts in the spot core and conglomeratic intervals observed in the Image logs indicate that the arkosic rocks are texturally immature.

We also observe abrupt changes in grain size of the sediments over short distances. In 11 m of core the arkose grades from a pebble/cobble conglomerate to coarse sandstone to fine-grained sandstone to siltstone (Figure 2.6). No sedimentary structures are found in the spot core to indicate a paleohorizontal and collection of logs in

the cored interval was unsuccessful, so we do not know the bedding orientation of the spot core. Therefore, we cannot make any assertions about whether this is a fining upwards or downwards sequence. The fact that there is such a rapid change in grain size indicates that the rocks were deposited in a setting which experienced sudden shifts in depositional energy. A similar cyclicity is seen in the image logs through the rest of the arkose, although it is not as clearly defined as in the hard rock samples.

Given the overall coarse-grained nature of the arkosic section and the lack of microfossils, we cannot determine if the arkoses were deposited in a marine or terrestrial setting. The presence of conglomerates with angular clasts means that it is unlikely that the rocks were deposited too far from a highland; if they are marine sediments they likely represent the most proximal portion of the marine sequence.

Clasts in the arkoses are almost entirely granitic, with no more than 2.00% volcanic clasts in the lower arkose. There may be sedimentary clasts present in the conglomerates, but there were not any observed in the spot core and it would be difficult to identify primary vs. secondary sedimentary clasts in the cuttings samples. The primarily granitic composition implies that the arkoses were shed from a granitic highland with a small volcanic input.

Based on the range of grain sizes, the somewhat regular bed spacing, the angularity of clasts observed in image logs and core, and the overall textural immaturity associated with unaltered feldspars, we interpret the arkoses to have been deposited in a subaerial or subaqueous fan setting weathered from a granitic source terrane. Fine-grained, laminated intervals likely represent channel avulsions or overbank deposits.

Overall, there are more sandstone and siltstone intervals than conglomerate in the arkosic section which is an indication of longer periods of quiescence than high energy depositional environments. Changes in depositional energy could represent water depth changes, but that is difficult to interpret without lateral controls or micropaleontological indicators. The arkoses could also be the most proximal portion of a fluvial system, where the clasts have not been far-traveled. Chaotic intervals in the image logs may represent slump or slope failure deposits, both of which could be present in a fluvial or marine fan setting.

The lower arkose has more fine-grained intervals than the upper arkose but both units contain conglomerate, sandstone and siltstone. Although the two units differ compositionally and diagenetically, the depositional characteristics are alike enough, and the data are limited enough, that we interpret the two units to have been deposited in similar depositional environments.

Diagenetic History

The diagenetic history of the arkosic rocks is not easy to determine from the datasets examined in this study. This could be a case of poor luck in where the spot core was collected (because alteration in the core is generally less than that in the cuttings) and lack of quality data in the image logs, or the diagenetic history of the arkosic rocks is not straightforward.

There are several different cements observed in the cuttings samples, although none appear to be pervasive through the entire arkose. Calcite, laumontite, secondary

quartz, iron-oxide and clay cements were all observed to some degree in the cuttings as well as the core samples.

Iron-oxide cements are most commonly observed as grain coatings and interstitial cements (Figure 2.5c and 2.16f). These cements were likely developed in a redoximorphic stage, one of the initial stages of burial where the equilibrium between ferric and ferrous iron shifts towards an oxidation state (Dapples, 1979). The most likely way the iron-oxide cements were produced was from the oxidation of biotite and amphiboles derived from a granitic source (Dapples, 1979). This reaction is common in arkosic sandstones because biotite is rarely stable enough to remain long after deposition (i.e. Scholle, 1979; Carozzi, 1993). Iron-oxides can also be produced in the later stages of diagenesis where the oxidation of remaining biotite results in hematite and muscovite (Dapples, 1979).

Calcite cements were rarely observed; the majority of calcite grains are either discrete calcite crystals or feldspar altering to calcite. Very few calcite veins or grains cemented with calcite were counted overall. The spot core also showed very little evidence of these cementing mechanisms as a pervasive trend. Interestingly, calcite veins observed in the spot core thin sections all occur near cataclasite zones. In that area calcite could be a local deformational feature rather than a diagenetic feature.

Quartz overgrowths are very rarely observed with quartz veins ranging from 0.21%-0.44% of sample counted in the cuttings (Figure 2.14). There is some evidence of local dissolution along grain boundaries in the spot core, however (Figure 2.21). In the absence of extensive cementation, we interpret this to be the primary mechanism which

has produced the overall induration of the SAFOD arkoses. The compaction features observed in the quartz and feldspar grains are not as well developed as stylolites but there are instances of convex-concave contacts and quartz indentor grains (Figure 2.21), similar to those features seen in deeply buried clastic sedimentary rocks (i.e. Liu, 2002) .

Altered feldspars vary in abundance through the arkosic section and several factors could control the amount of altered feldspar present. First we will consider the diagenetic conditions under which feldspars alter to illitic material.

The three stages of diagenesis in which clay minerals form are: eogenesis, mesogenesis and telegenesis. Eogenesis occurs in the shallow subsurface, mesogenesis involves the reactions occurring with resulting burial and telegenesis involves the uplift of the sediments. It is thought that conditions do not exist during eogenesis that will produce illite; illite will either be introduced to sediments as a detrital fraction (as in the depositional matrix) or it forms during mesogenesis (Worden and Morad, 2003). Worden and Morad (2003) consider three primary reactions which could produce illite during mesogenesis:

1) kaolinite + Potassium feldspar (K-spar), which occurs between 70º C and 150ºC
2) dioctahedral smectite + source of K^+: 60ºC -130ºC
3) feldspar + moderate pH: 90ºC-110ºC.

The full reactions are below:

1) $Al2Si2O5(OH)4 + KAlSi3O8 \rightarrow KAl3Si3O10(OH)2 + 2SiO2 + H2O$

kaolinite k-spar illite quartz water

2) smectite + K^+ → S/I → I/S → I

This is a progressive reaction that produces mixed layer phases of illite and smectite. Because the SAFOD drilling mud is montmorillinite (smectite) based, the amount of formational smectite has not been precisely determined (Solum et al., 2006). For the purposes of this chapter we will not discuss this reaction specifically, only after more detailed X-ray diffraction, SEM, and TEM studies are conducted will we have a better understanding of how much the amount of illite can be attributed to the reaction.

3) $3KAlSi_3O_8 + H_2O + 2H^+ \rightarrow KAl_3Si_3O_{10}(OH)_2 + 6SiO_2 + 2K^+$

k-spar water acidity illite quartz potassium ion

The acidity called for in this reaction can be explained by the presence of organic acid-rich formation waters (Worden and Morad, 2003) or by the migration of a CO2 gas phase into the structure (i.e. Barclay and Worden, 2000). An organic-rich setting in the SAFOD subsurface is supported by the observed presence of methane in the borehole post-drilling (S.Hickman, pers comm., 2006).

Additionally, Aargard et al. (1990) propose a reaction incorporating Sodium-plagioclase that could produce illite:

4) $2KAlSi_3O_8 + 2.5Al_2Si_2O_5(OH)_4 + Na^+ \rightarrow NaAlSi_3O_8 + 2KAl_3Si_3O_{10}(OH)_2 +$

K-feldspar kaolinite sodium ion albite illite

$2SiO_2 + 2.5\ H_2O + H^+$

quartz water hydrogen ion

This is the albitization of K-feldspar which occurs at temperatures greater than or equal to 130˚C. The reaction is controlled by the ionic activity of Na+ and the pH of the system (Aargard et al., 1989).

However, illite may be formed from the alteration of plagioclase in ways other than the albitization of k-feldspar. Huang (1992) simulated the diagenesis of arkoses to examine under what conditions illite forms and found that Na-feldspar produces similar results as K-feldspar as long as the solution contains potassium ions.

The mechanism for altering feldspar to illitic material is reasonably well established. In the SAFOD arkose, it is likely that kaolinite and K-feldspar (or Na-feldspar) alter to illite as in reactions 1 and 3. There are only trace amounts of kaolinite found in thin sections of the SAFOD cuttings, implying that any kaolinite present has been reacted to form illite, although it is possible that kaolinite can be washed away in the cuttings preparation process. The reactions and results mentioned above have been exclusively for studies on diagenesis of sandstones, however Shaw and Conybeare (2003) present evidence that similar reactions occur in mudstones as well as interlayered mudstone and sandstones. The SAFOD rocks vary from conglomerate to siltstone but degree of alteration does not seem to be related to rock type, with the exception of within

the fault zones where the amount of alteration is elevated (Bradbury et al., in review; Solum et al., 2006).

In order to understand the fluid composition and initial mineralogy of the sedimentary rocks, it is necessary to study what morphologies of illite (or mixed layer illite/smectite) are present (Huang, 1992). Other workers have been examining the morphology of SAFOD clay minerals using SEM and TEM methods and have found mixed layer illite-smectite forms as films and fibers along shear surfaces along with fibrous to columnar laumontite forming in the pores of rock chips collected during coring (Solum et al., 2006; Schleicher et al., 2005; Schleicher et al., submitted). The investigation of authigenic clay mineral morphology in the SAFOD cuttings and core is an ongoing endeavor by these workers.

If the illite in the SAFOD arkoses formed at 70-150˚C (reaction 1), then these rocks may have been buried slightly deeper than the depth at which they were encountered. From the temperatures measured in the borehole we calculate an average geothermal gradient of 38.48ºC/km (Figure 2.22). This gradient is approximately 3°C greater than the average geothermal gradient in the area (Page et al., 1998; Blythe et al., 2004), and may have interesting implications with regard to the heat flow paradox of the SAF (Lachenbruch and Sass, 1980). Using the measured geothermal gradient, 70ºC-150ºC corresponds to depths of 1.3 km-3.4 km (Figure 2.23). This overlaps with the current depth of the arkoses but may be as much as 0.8 km deeper than the deepest extent of the arkoses today. The implications of these reactions will be discussed below.

Other reactions to consider in the diagenetic history of the arkoses are those that produce authigenic mica and alter feldspar to coarse muscovite. The feldspars of the lower arkose are often altered to coarse-grained muscovite and there are veins filled with authigenic muscovite in the phase one spot core (Figures 2.5d and 2.16h). If a rock is rich in aluminum and potassium but poor in magnesium and iron and continues to be buried to low metamorphic grade temperature and pressure, illite will continue to acquire potassium and may become pure muscovite (Worden and Morad, 2003). The reaction converting illite to muscovite can occur at temperatures as low as 100ºC (Merino, 1975), although conditions of formation are highly dependent on fluid chemistry (Montoya and Hemley, 1975). Authigenic muscovite can also form from degraded detrital muscovite once the rocks enter the well-ordered mica stability field (Dapples, 1979). Hoffman and Hower (1979) similarly found that the composition of authigenic mineral assemblages are largely dependent on pore fluid compositions, although they assign a temperature gradient of 200-300ºC to authigenic muscovite development. Authigenic muscovite has not been observed to form at temperatures less than 100ºC (Merino, 1975; Boyd and Lewis, 1995). So while it is difficult to precisely pinpoint the temperature at which the authigenic muscovite formed in the SAFOD arkoses, we can assume that the minimum temperature of development is 100ºC. This corresponds to a depth of 2.08 km (Figure 2.23).

The other mineral which may be significant in the diagenetic history is the zeolite mineral laumontite. Laumontite is associated with low-grade metamorphism, the exact boundary conditions of which are debated. The zeolite facies has often been considered

to be the transition from deep-diagenesis to metamorphism (Coombs et al., 1959) but in reality the precipitation of zeolite minerals is complex, based largely on pore fluid composition and pressure as well as rock temperatures and pressures (Ghent, 1979). The presence of laumontite in the SAFOD arkoses is complicated by the fact that laumontite is often found in altered granites. Laumontite could be introduced as a detrital fraction in the SAFOD arkoses from the granitic source terrane which fed deposition. It is possible that the lower arkose has a slightly different provenance than the upper arkose, which would explain the presence of laumontite as a detrital component. There are laumontite veins and cements observed in the spot core, implying an authigenic component as well. Merino (1975) found laumontite cements in close association with authigenic muscovite in the Temblor Formation of central California. This formation contains arkosic sandstones that resemble the SAFOD arkoses. There it was concluded that the laumontite and muscovite formed approximately coevally (Merino, 1975). Here, in the absence of better information with regards to laumontite formation, we will consider the laumontite to have formed at temperatures at or greater to 100ºC.

Age of the Rocks and Thermal History

In order to identify possible surface rock units that are correlatable to the arkosic section, it is important to constrain the age of the arkosic rocks. Arkosic composition is nonunique in California and by applying age bounds on the SAFOD arkoses we are better equipped to investigate formations possibly equivalent to the SAFOD arkoses.

Because there are no direct measures of the age of the rocks from micropaleontology or geochronological analyses, we can use zircon and apatite fission-track studies performed by other workers (Kirschner and Garver, written comm.; Blythe et al., 2004; Kirschner et al., 2006) to constrain the age of the SAFOD rocks. We combine these fission-track analyses with other tectonic studies of the area and our diagenetic analyses to approximate the burial and uplift history of the SAFOD arkoses.

In 2006, J. Garver and D. Kirschner performed zircon fission-track analyses (ZFT) on three zircon samples with 15 zircons per sample separated from phase two arkosic SAFOD cuttings (Kirschner et al., 2006). The annealing temperature of zircon is ~240ºC (Hurford and Carter, 1991), as rocks cool to temperatures less than 240ºC, spontaneous fission of the uranium in zircon will cause measurable damage to the crystal lattice of the mineral (Wagner and Van der Haute, 1992). These damaged areas are called fission tracks, the length and extent of which are proportionate to the amount of time since the zircons cooled beyond the annealing temperature. In the case of sedimentary rocks, we are not dating the time at which the sedimentary rocks cooled past 240ºC but rather when the detrital zircons derived from a source rock cooled through the annealing temperature. These analyses allow us to interpret the provenance and burial and exhumation history of the sedimentary rocks. For example, if the analyses show several different cooling ages for different zircons, we may interpret several different sources of the sedimentary rocks; whereas if the cooling population data are tightly clustered, there may be a single source terrane that fed the deposition of the arkoses (Naeser, 1979; Hurford and Carter, 1991).

Table 2.4 shows the results from preliminary ZFT analyses of the Phase 2 SAFOD cuttings. The zircons are similar in age, passing the Chi-squared statistical test which evaluates the likelihood that the zircon ages cluster in one population. This homogeneity implies that the zircons collected in the arkoses are likely derived from a single source terrane or from a source region with a homogeneous thermal history. Garver and Kirschner conclude that the source rock of the arkoses (likely the granitic source) cooled through 240ºC during the late Cretaceous, between 64 and 70 Ma. Another important result from the ZFT analyses is the constraint on depth of burial of the arkosic section. The zircons do not show evidence of being reset, or buried to temperatures exceeding 240ºC, which would anneal the crystal structure again. Therefore, we know that the sedimentary rocks have not likely been buried to depths corresponding to those temperatures since deposition. We predict that temperatures would equal or exceed the zircon annealing temperature of 240ºC at 5.7 km depth in the SAFOD borehole (Figure 2.23). Assuming a constant geothermal gradient over time, this implies that the arkosic rocks have not been buried to a depth greater than 5.7 km, or 3.1 km more than ZFT samples 37-61 and 37-62 (Table 2.4) since deposition.

The Maastrichtian/Paleocene cooling age of the zircons recovered from the arkoses serves as a maximum age for the SAFOD arkoses. These data eliminate the possibility that the SAFOD arkoses are associated with the Great Valley sequence on the northeast side of the SAF because sedimentary rocks cannot be older than their constituents. Kidder et al. (2003) calculate a late Cretaceous exhumation rate of >2-3 mm/yr for the Salinian Block. Using this rate of exhumation, we estimate that the

granitic body which supplied the zircons in the SAFOD arkoses could have reached the surface 1.9-2.8 m.y. after passing through the zircon annealing temperature. Therefore, a Paleocene age of 62.1-61.2 Ma for the arkoses is a possibility.

2-6 DISCUSSION

We use the interpretations and analyses we have discussed to this point to identify features which may be helpful in correlating an equivalent unit exposed at the surface to the SAFOD arkoses. This correlation is important for modeling the evolution of the San Andreas fault in central California, because other sedimentary correlation studies in the past have successfully established amounts of offset on different strands of the SAF (Nilsen and Clarke, 1975; Nilsen, 1984; Graham et al., 1989). When looking for a correlatable unit, we must consider all of the possibilities of the relationships between the upper arkose, clay-rich unit, and lower arkose as well as the tectonic history of the SAF in the vicinity of the SAFOD site.

315-320 km of Neogene offset on the San Andreas fault has been well established (Figure 2.24). Ross (1970) correlated similar diorite and gabbro units at the Logan, Gold Hill and Eagle Rest Peak areas. This correlation calculates the offset on the San Andreas to be between 160 km and 321 km. Clarke (1973) and Clarke and Nilsen (1973) correlated the Eocene Butano sandstone of the Santa Cruz Mountains to the Point of Rocks formation of the San Joaquin Basin, a calculated offset of approximately 315 km (although the margin of error is relatively large, 10's of kilometers). Graham et al. (1989) used detailed sedimentological analysis to correlate the Upper Oligocene/Lower Miocene

Vacqueros Formation of the La Honda Basin to the Temblor Formation of the southern Temblor Mountains/San Joaquin Basin. The Oligocene/Miocene correlation of Graham et al. (1989) agrees with the 315 km offset of the Clarke and Nilsen (1973), Eocene correlation. The flaws in these analyses, however, are 1) both the Eocene and Miocene outcrops are several kilometers lateral distance from the San Andreas fault plane and so need to be projected into the fault zone, and 2) the boundaries of the basins are diffuse and not well-defined. This produces merely an approximation of fault offset. However, the Matthews (1976) analysis of the Miocene Pinnacles and Neenach volcanics verified the 315 km of offset suggested by others. These Miocene volcanic units were essentially erupted along the plane of the fault and are not regional in extent. Therefore these two units serve as a kind of discrete piercing point to evaluate the offset of the San Andreas fault.

The tectonic history of the SAF is almost always interpreted to be reasonably simple in central California, with the majority of offset occurring along the modern trace of the SAF (Irwin, 1990; Wright, 2000). However, the presence of the SAF-parallel Buzzard Canyon fault (Figures 2.2 and 2.3) potentially adds a measure of complexity to the offset history of the San Andreas system near the SAFOD site. Formations equivalent to the SAFOD arkoses would be found in much different locations depending on how offset has been distributed across the faults encountered at the SAFOD site. Here we evaluate three hypotheses for the evolution of the San Andreas fault system in the vicinity of the SAFOD site.

Three Hypotheses for the Evolution of the

San Andreas Fault System

A) The majority of dextral offset has occurred along the modern trace of the San Andreas fault with only a small component of offset on the Buzzard Canyon fault (Figure 2.25a). In this case, a formation equivalent to the SAFOD arkoses would be located ~315 km to the southeast. With a small amount of offset on the BCF, there would likely be rocks similar to the SAFOD arkoses somewhere relatively nearby to the northwest (Figure 2.25a). The nearby rocks could be either at the surface or the as deeply buried as the SAFOD arkoses.

B) The 315 km offset could have been distributed more evenly across both the Buzzard Canyon and the modern San Andreas fault (Figure 2.25b). The SAFOD arkoses could be a stranded portion of an offset basin, where equivalent formations would be found both to the southeast and the northwest (Figure 2.25b).

C) The Buzzard Canyon fault could have been the major fault of the system until recently, where the majority of offset has occurred along the BCF rather than the modern SAF (Figure 2.25c). In this case, the SAFOD arkoses would be rocks associated with the east-side of the fault with equivalent units ~315 km to the northwest (Figure 2.25c). Rocks similar to the SAFOD arkoses would therefore also be found at the surface or in the subsurface somewhere nearby to the southeast after being transported a small distance along the modern SAF (Figure 2.25c).

Here we discuss the validity of each hypothesis and whether they pass tests designed around the correlation of the SAFOD arkoses to surface or subsurface units.

The possible tectonic history of the SAFOD arkoses as determined by each hypothesis is also discussed.

Hypothesis 1

The implication of the first hypothesis is that the SAFOD arkoses are Salinian-derived. The age of Salinian granite matches the interpreted thermal history of the source terrane for the SAFOD arkoses well. Zircon-fission track cooling ages of detrital zircons in the arkoses are younger than U/Pb geochronology that dates Salinian magmatism occurring between 130 and 70 Ma (Kistler and Champion, 2001; Barth et al., 2003; Kidder et al., 2003; Barbeau et al., 2005). 40Ar/39Ar cooling ages of biotite of 76-75 Ma in the Salinas Valley, northwest of SAFOD, further verify the U/Pb ages of the Salinian Block (Barth et al., 2003). The youngest cooling ages from those studies are similar to the oldest ZFT cooling ages, but the majority of the ZFT ages cluster around 64 Ma. There are numerous lines of evidence which show that from ~80-65 Ma the Salinian block was rapidly uplifted from 25 km depth (Barbeau et al., 2005). The ZFT ages represent when the zircons passed through the annealing temperature, which corresponds to a depth of 5.7 km. It makes sense that at 64 Ma that a Salinian source was 5.7 km below the surface. Therefore, the age and exhumation history of the Salinian block in central California closely matches the ZFT cooling ages of the SAFOD arkoses, which is good evidence that the SAFOD arkoses may be Salinian-derived.

If the SAFOD arkoses are deposited from Salinian granite and have not been transported far along the BCF, they may have a similar tectonic history to the Salinian

granite/granodiorite found in the SAFOD borehole. In that case, the burial and exhumation history constructed through apatite fission track-data from the granite in the SAFOD borehole could help to constrain the age of the SAFOD arkoses.

Blythe et al. (2004) published findings from apatite fission-track analyses of the granite and granodiorites of the pilot hole drilled in 2002. The theory behind apatite fission-track (AFT) analysis is similar to zircon fission-track analysis. It examines when apatite minerals cooled or heated beyond the apatite annealing temperature of 110ºC (Wagner and Van der Haute, 1992). In this case, the cooler annealing temperature of the apatites allows study of exhumation and burial events in the shallower subsurface. Through these analyses Blythe et al. were able to identify three notable events in the thermal history of the granites.

1) Slow cooling through the partial annealing zone (PAZ) from 80-31 Ma. The PAZ is defined as the zone where fission tracks anneal slowly, between 60-110ºC (Gleadow and Fitzgerald, 1987). By 31 Ma, the granites had cooled completely through the PAZ to temperatures of 40-50ºC.

2) Reheating of the granites by 48-58ºC between 31 and 8-4 Ma. This is interpreted to correspond to burial by 1.3-1.5 km of sediments.

3) Cooling by 30-47ºC from 8-4 Ma to present-day. This amount of cooling indicates between 0.8 and 1.3 km of exhumation, assuming a geothermal gradient of 35ºC/km (the temperature data we have from phase one and two drilling of the SAFOD mainhole were not available at the time of the publication of Blythe et al., 2004 and temperature measurements of the pilot hole failed, therefore a typical geothermal gradient was

assumed). The age of initiation of uplift in the Plio/Pleistocene agrees well with measured uplift rates and the interpreted tectonic evolution of the central coast ranges (Page et al., 1998).

If hypothesis one is true, then the uplift and burial events of Blythe et al. (2004) would similarly apply to the SAFOD arkoses, with one exception. Because the arkoses are deeper than the granite and buried beneath more sediment, burial of the arkoses likely began before the granite.

The best approximations we can make on the uplift and burial history of the arkoses beyond the AFT and ZFT data come from the clay alteration reactions which have occurred. The illitization of k-feldspar occurs between 70ºC and 150ºC. The depths which correspond to these temperatures are 1.30 km – 3.4 km, which means the reactions could occur at the depth where the arkoses are today. Authigenic muscovite forms at >100ºC, corresponding to a depth of 2.08 km (Figure 2.23). Authigenic muscovite is only observed in the lower arkose which sits at 2.33 km vertical depth, the upper arkose has limited feldspar alteration with almost no evidence of authigenic muscovite. The upper arkose extends from 1.87 km to 2.2 km vertical depth; the lack of authigenic muscovite may indicate a difference in fluid chemistry at that level than in the lower arkose. In that case, where authigenic clay mineral development is more dependent on fluid chemistry than temperature or pressure (Montoya and Hemley, 1975) then we cannot draw absolute conclusions about how much deeper the arkoses have been buried beyond their present-day depth.

The granitic rocks in the pilot hole analyzed by Blythe et al. (2004) show evidence of slow cooling from 80-31 Ma, then at 31 Ma burial of the granites began. If the SAFOD arkoses were derived from Salinian granite similar to that in the borehole, then 31 Ma serves as a minimum age of the SAFOD arkoses. The simplest model for the emplacement of the SAFOD arkoses is that they were deposited sometime in the Paleocene or Eocene, after the exhumation of the nearby Salinian granite but before the subsequent burial of that granite. By the early Oligocene both the granite and arkoses have been buried and continue to be buried further after initiation of the Neogene San Andreas fault system. Dextral offset along the San Andreas fault results in the modern location of both the granite and the SAFOD arkoses.

Correlative Units on the Northeastern Side of the San Andreas Fault (Hypothesis 1)

If a unit that is correlative to the SAFOD arkoses is exposed at the surface, this hypothesis implies it should be found ~315 km to the southeast of the SAFOD site (Figure 2.25a). The SAFOD arkoses should also be Paleocene/Eocene in age under this tectonic hypothesis. Paleocene and Eocene sedimentary rocks commonly outcrop in central California (i.e. Dibblee, 1971, 1973, 1980; Nilsen and Clarke, 1975; Graham, 1978; Bent, 1988; Graham et al., 1989; Seiders and Cox, 1992; Sims, 1990, 1993; Dibblee et al., 1999) mostly as marine fan deposits formed in major basins in the Salinian block (Nilsen and Clarke, 1975; Nilsen, 1984; Graham et al., 1989) (Figure 2.26). When restoring the slip in the San Andreas system, however, few of these basins restore to

locations near the SAFOD site. One candidate formation, the Eocene Tejon Formation of the San Emigdio Mountains approximately 280-290 km to the southeast, can be eliminated as a possibility because there are significant differences in the lithology of the SAFOD site from the Tejon Formation. The Tejon Formation is composed of the basal Uvas conglomerate member, 0-120 m thick, the Liveoak Shale Member, 0-600 m thick, the Metralla Sandstone Member, 0-600 m thick and the Reed Canyon Siltstone Member, 0-60 m thick (Nilsen, 1984). This formation grossly resembles the SAFOD arkoses, but the conglomerate is rich in large gabbro clasts derived from the mafic basement upon which the Tejon formation lies (Nilsen, 1984). The SAFOD arkoses do not contain any grains which appear to have been derived from gabbro, thus we can eliminate the Tejon Formation as a possibility.

There are Paleocene conglomerates with compositions which could potentially resemble the SAFOD arkoses. Seiders and Cox (1992) extensively studied Paleocene conglomerates of the Salinian Block in order to reconstruct the Paleocene tectonic history of the SAF. The rock unit which is most similar to the SAFOD arkoses is the San Francisquito Formation which is composed of granite rich conglomerates interbedded with arkosic sandstones and mudstones. The San Francisquito Formation crops out in Cajon Pass, the Liebre Mountain block, and the Pinyon Ridge block (Figure 2.27). The Cajon Pass, Liebre Mountain and Pinyon Ridge outcrops have all been palinspastically restored to locations close in proximity to the SAFOD site (Figure 2.27). However, there is not enough lithologic data on these units to precisely correlate them to the SAFOD arkoses, but basic published descriptions grossly resemble the SAFOD arkoses. These

description data are enough to imply that hypothesis one has not been eliminated as a possibility for the evolution of the San Andreas fault.

Correlative Units of the Southwestern Side of the San Andreas Fault (Hypothesis 1)

Rocks older than Miocene in age are not mapped at the surface in the immediate vicinity of the SAFOD site (Dibblee, 1971; Sims, 1990; Thayer and Arrowsmith, 2005). The closest Paleocene/Eocene sedimentary rocks similar to the SAFOD arkoses on the southwestern side of the SAF are thick sequences of unnamed marine sedimentary rocks in the La Panza and Sierra Madre Ranges approximately 50 km to the southwest of the SAFOD site (Jennings and Strand, 1958). The rocks consist of interbedded arkosic sandstones, siltstones, clay shale, and granitic conglomerates ranging in age from Upper Cretaceous to Middle Eocene (Chipping, 1972; Vedder and Brown, 1968; Dibblee, 1973). The unnamed unit has been estimated to be between 600-9100 m thick, but this encompasses the entire age sequence, the unit is not subdivided into different age units due to the paucity of fossils encountered (Dibblee, 1973). A complex series of folds and faults could result in similar rocks in the subsurface adjacent to the San Andreas fault.

It is possible that the SAFOD arkoses are part of a small, localized basin that is not exposed at the surface on the northwestern side of the fault. Small scale, subsidiary basins were commonly formed along the Salinian block (Vedder et al., 1982; Grove, 1993). Well control in that region is very limited, rocks similar to the SAFOD arkoses could be at similar depths in other localities on the northwestern side of the fault.

Without a correlative unit found on the northwestern side of the fault, however, doubt could be cast on the validity of hypothesis one.

Hypothesis 2

If 315 km of offset were distributed between the Buzzard Canyon and San Andreas faults in some nearly equal proportion, we cannot determine if the SAFOD arkoses are depositionally related to the granite/granodiorite in the borehole. Therefore, the uplift and burial history of the granitic rocks in the borehole cannot be applied to the SAFOD arkoses. Only the maximum early Paleocene age derived from the zircon-fission track cooling ages is applicable. If hypothesis 2 is true, the SAFOD arkoses could potentially be younger than Paleocene/Eocene in age.

The distribution of possible correlative units is also less constrained with respect to distance from the SAFOD site. However, there is at least one compelling possible correlative basin to the SAFOD arkoses. The Eocene Butano sandstone of the Santa Cruz Mountains and the Point of Rocks Formation of the San Joaquin Basin are nearly identical to each other in provenance, sedimentary characteristics, and depositional environment (Clarke, 1973; Clarke and Nilsen, 1973). The Butano sandstone is part of the La Honda Basin, approximately 200 km to the northwest of the SAFOD site (Figure 2.28), and the Point of Rocks Formation is part of the southern San Joaquin Basin approximately 100 km to the southeast of the SAFOD site (Clarke and Nilsen, 1973; Graham et al., 1989). The offset between these two basins is one line of evidence to show that the Neogene San Andreas system has experienced 315 km dextral offset. The

Butano/Point of Rocks Formation is composed of well indurated arkosic conglomerate, sandstone and siltstone sequences 100s-1000s m thick (Critelli and Nilsen, 1996); similar to the SAFOD arkoses. Furthermore, the Butano Sandstone in the Santa Cruz Mountains has been divided into three members, a 980 m thick thin-thick bedded upper sandstone, a 75-230 m thick siltstone member, and a 460+ m thick sandstone interbedded with pebble conglomerate (Clark, 1981) (Figure 2.28). The three members of the Butano Sandstone are similar in lithology and thickness to the SAFOD arkoses.

Additionally, the Miocene Vaqueros Formation of the La Honda Basin and the Miocene Temblor Formation of the San Joaquin Basin have been robustly correlated (Graham et al., 1989) and are grossly similar to the SAFOD arkoses. However, basaltic clasts are commonly found in the Vacqueros Formation (Clark, 1981; Berggren and Aubert, 1983), a clast composition not observed in the SAFOD arkoses.

If the SAFOD arkoses were once part of the San Joaquin/La Honda Basin system, then the offset history of the Buzzard Canyon and San Andreas faults would indeed be quite complex. It would be difficult to determine the timing and offset on each fault because the SAFOD arkoses would correlate to rocks on each side of the fault system to the northwest and the southeast. There could potentially have been a complex interplay across the two fault traces where the SAFOD arkoses were being transported back and forth dextrally. The amount of faulting, fracturing and deformation observed in the SAFOD arkoses could be a result of a complex faulting history between the Buzzard Canyon and San Andreas faults.

Hypothesis 3

The constraints on the age of the arkoses is similar in hypothesis 3 as in hypothesis 2, where we cannot use the history of the SAFOD granite to constrain a minimum age for the SAFOD arkoses. Therefore, with hypothesis 3, the rocks could be younger than Paleocene/Eocene in age. We predict that a small amount of offset on the modern San Andreas fault would result in rocks similar to the SAFOD arkoses somewhere nearby on the southeastern side of the SAF.

At the surface, there are not any Tertiary sedimentary rocks which resemble the SAFOD arkoses, the majority of Tertiary sedimentary rocks are associated with the Miocene Monterey Formation (Dibblee, 1971, 1980; Sims, 1990; Dibblee et al., 1999). The Miocene Monterey Formation is a term liberally applied to argillaceous Miocene shales on the northeastern side of the SAF (i.e. Dibblee, 1973, Sims, 1990) which do not resemble the SAFOD arkoses. There are exposures of the Miocene Temblor Formation approximately 20 km southeast of the SAFOD site (Sims, 1990) but they are only 10's of meters thick and are volcanic-rich in composition, not similar to the SAFOD arkoses. In the subsurface, there are no reports of rocks similar to the SAFOD arkoses in well logs (Payne, 1964).

At this point, we do not have evidence which supports hypothesis 3 but there is not necessarily evidence that invalidates hypothesis 3. We cannot conclusively favor one hypothesis over another, especially because correlating the SAFOD arkoses to other similar sedimentary rocks is not easily accomplished.

Problems with Correlation

There are several factors which make a straightforward correlation between the SAFOD arkoses and another similar sedimentary rock unit unlikely.

1) The SAFOD arkoses are heavily faulted and composed of at least 11 distinct structural blocks. A precise correlation depends on the thickness of a sedimentary sequence and we cannot measure a true thickness of the entire arkosic section with the amount of faulting present. The largest zone of uninterrupted stratigraphy is block 9 which is 158.9 meters thick (Table 2.3), so that could serve as an absolute minimum in thickness for a correlation, but the SAFOD arkoses are likely thicker than that. Furthermore, faulting results in an unclear stratigraphic relationship between the upper arkose, clay-rich zone and the lower arkose.

2) It is difficult to compare our compositional data with those of other published studies because of the inherent limitations of a borehole study for this type of a correlation. Our compositional data are derived from drill cuttings while most sedimentological studies are based on whole rock and outcrop analysis. For instance, it is common practice to use the Gazzi-Dickinson method in analyzing the composition of sandstones. However, we cannot accurately quantify the amount of lithics in the SAFOD arkoses. The amount of lithics can be crucial in distinguishing one sandstone from another. Without that corner of the ternary diagram we are limited in our comparison to other sandstones. There is a similar problem with comparing the SAFOD arkoses to studies where conglomerate compositions are determined. Conglomerate studies usually involve clast counts where pebbles or cobbles of a predefined size are counted using a randomizing methodology.

We are unable to isolate the compositional components that are derived from larger conglomeratic clasts from those originally a part of the sand fraction.

In order to better constrain a correlation between the SAFOD arkoses and therefore the evolution of the San Andreas fault system in the vicinity of the SAFOD site, more work is needed. Tighter constraints on the age of the SAFOD arkoses would assist this work immensely, either through palynological analyses of fine grained intervals or geochronological analysis of volcanic clasts in the phase one core. More detailed surface mapping on the southwest side of the fault would also be helpful, along with more detailed study of the Buzzard Canyon fault to analyze whether there is evidence that the fault has been a more significant component of the SAF system in the past.

2-7 CONCLUSIONS

We utilized wireline logs, cuttings microscopy, core samples, and electrical image logs to fully characterize the SAFOD arkosic rocks. As a whole, the 1230 m of arkosic rock between the modern day San Andreas fault to the northeast and the Buzzard Canyon fault to the southwest is heavily faulted with at least 12 faults and 11 fault-bound structural blocks. The arkosic section consists of three distinct lithologic units: the upper arkose, the clay-rich zone and the lower arkose. The upper arkose is 156.4 m – 381.4 m thick interrupted by intraformational faults which separate five distinct structural blocks with different bedding orientations and fracture densities. The five blocks are coarse-grained quartzofeldspathic conglomerates and sandstones with rare clay-rich grains. Feldspar altered to illitic material and iron-oxide alteration products are abundant. The

clay-rich zone is a 28.7 m – 121.3 m thick low-velocity zone with anomalously high gamma ray signatures. It is characterized by abundant clay-rich grains composed of high birefringent clay minerals such as illite and smectite. A 27 m thick block of well bedded, coarser grained rock is incorporated into the clay-rich zone, from 2565-2595 mmd. The lower arkose has more variable log signatures than the upper arkose, with generally higher velocities and lower porosities. It is 224 m – 331 m thick and is finer-grained with a high abundance of clay-rich grains than the upper arkose. The lower arkose contains more volcanic clasts than the upper arkose, perhaps reflecting a slightly different provenance.

We interpret the arkosic section to have been deposited in either a sub-aerial or sub-aqueous fan setting, perhaps as part of a transtentional sub-basin system common to the Salinian block. Fission-track cooling ages of 64-70 Ma constrain the maximum age of the SAFOD arkoses to be earliest Paleocene. Diagenetic mineral assemblages of authigenic muscovite and laumontite indicate that at the modern day geothermal gradient of 38.48° C/km the arkoses have not been likely buried more than 0.8 km deeper than the depth they are today.

We present three models for the evolution of the San Andreas fault system in the vicinity of the SAFOD site which predict where sedimentary rock units equivalent to the SAFOD arkoses maybe located. The first hypothesis is that the majority of the 315 km of Neogene San Andreas fault slip has occurred along the modern trace of the San Andreas fault. This hypothesis predicts that the SAFOD arkoses are depositionally related to granite/granodiorite encountered in the SAFOD borehole and therefore have a similar

uplift and burial history. Apatite fission-track cooling ages of Blythe et al. (2004) show that the granite/granodiorite began to be buried at 31 Ma, effectively shutting off the potential depositional source for the SAFOD arkoses, which limits the age of the arkoses to 31-64 Ma. Furthermore, this hypothesis predicts that rocks equivalent to the SAFOD arkoses would be located ~315 km to the southeast. We identify the San Francisquito Formation of Cajon Pass, Pinyon Ride or the Liebre Mountain block ~300 km to the southeast as a unit with similar composition to the SAFOD arkoses which may possibly be correlative.

The second hypothesis is that slip has been distributed nearly equally across the Buzzard Canyon and San Andreas faults. This hypothesis predicts that the SAFOD arkoses would be a stranded sliver of an offset basin with correlative units possibly located both to the northwest and the southeast. This negates using apatite fission-track data from the granite in the borehole to constrain the age of the SAFOD arkoses, therefore we can only assign a maximum age 64 Ma for the arkoses. Possible correlative units may be the Eocene Butano Sandstone or the Miocene Vaqueros Formations of the La Honda Basin to the northwest and the Eocene Point of Rocks Formation or Miocene Temblor Formation of the San Joaquin Basin to the southeast.

The third hypothesis is that the majority of slip has occurred along the Buzzard Canyon fault with only a small component of slip occurring along the modern San Andreas fault. This predicts that a correlative unit would be found nearly 315 km to the northwest with a small offset portion to the southeast of the SAF. We have not found

anything which resembles the SAFOD arkoses near the SAFOD site on the east side of the fault. Therefore, we do not have any evidence to support or invalidate hypothesis 3.

Difficulties in comparison of results and the sheer number of faults in the arkosic section prevent drawing any conclusive correlations at this time. With better age constraints and direct lithologic comparison between the SAFOD arkoses and units identified as candidates for correlation we may be able to more robustly constrain the evolution of the San Andreas fault system in the vicinity of the SAFOD site.

References

Aagaard, P., Egeberg, P.K., Saigal, G.C., Morad, S., and Bjorlykke, K., 1990, Diagenetic albitization of detrital K-feldspars in Jurassic, lower Cretaceous and Tertiary clastic reservoir rocks from offshore Norway, II. Formation water chemistry and kinetic considerations: Journal of Sedimentary Petrology, v. 60, no. 4, p. 575-581.

Almeida, R., Chester, J.S., Chester, F.M., Kirschner, D.L., Moore, D.E., and Waller, T.D., 2005, Mesoscale structure and lithology of the SAFOD Phase I and Phase II core samples: EOS trans. American Geophysical Union, 86(52), Fall Meeting Supplement, Abstract T21A-0454.

Barbeau, D.L., Ducea, M.N., Gehrels, G.E., Kidder, S., Wetmore, P.H., and Saleeby, J.B., 2005, U-Pb detrital-zircon geochronology of northern Salinian basement and cover rocks: Geological Society of America Bulletin, v. 117, no. 3/4, p. 466-481.

Barclay, S.A., and Worden, R.H., 2000, Effects of reservoir wettability on quartz cementation in oil fields, *in* Worden, R.H. and Morad, S.A., eds., Quartz Cementation in Sandstone, International Association of Sedimentologists Special Publication no. 29, p. 103-117.

Barth, A.P., Wooden, J.L., Grove, M., Jacobson, C.E., Pedrick, J.N., 2003, U-Pb zircon geochronology of rocks in the Salinas Valley region of California: A reevaluation of the crustal structure and origin of the Salinian block: Geology, v. 31, no. 6, p. 517-520.

Bent, J.V., 1988, Paleotectonics and provenance of Tertiary sandstones of the San Joaquin Basin, California: *in* Graham, S.A., ed, Studies of the Geology of the San

Joaquin Basin, Pacific Section Society of Sedimentary Geology, v. 60, p. 109-127.

Berggren, W.A., and Aubert, J., 1983, Paleogene benthic foraminiferal biostratigraphy and paleobathymetry of the central Coast Ranges of California: *in* Brabb, E.E., ed., Studies in Tertiary Stratigraphy of the California Coast Ranges, Geological Survey Professional Paper 1213, p. 4-19.

Bleibinhaus, F., Hole, J.A., Ryberg, T., and Fuis, G.S., in review, Structure of the California Coast Ranges and San Andreas Fault at SAFOD from seismic waveform inversion and reflection imaging: Journal of Geophysical Research-Solid Earth.

Blythe, A.E., d'Alessio, M.A., Burgmann, R., 2004, Constraining the exhumation and burial history of the SAFOD pilot hole with apatite fission track and (U-Th)/He thermochronometry: Geophysical Research Letters, v. 31, doi: 10.1029/2003GL019407.

Boness, N.L., and Zoback, M.D., 2006, A multi scale study of the mechanisms controlling shear velocity anisotropy in the San Andreas Fault Observatory at Depth: Geophysics, v. 71, no. 5, doi: 10.1190/1.2231107.

Boyd, R.J., and Lewis, D.W., 1995, Sandstone diagenesis related to varying burial depth and temperature in Greymouth Coalfield, South Island, New Zealand: New Zealand Journal of Geology and Geophysics, v. 38, p. 333-348.

Carozzi, A.V., 1993, Sedimentary Petrography, New Jersey, PTR Prentice Hall, 263 p.

Catchings, R.D., and Rymer, M., 2002, High resolution seismic velocities and shallow structure of the San Andreas fault zone at Middle Mountain, Parkfield, California: Bulletin of the Seismological Society of America, v. 92, p. 2493-2503.

Chipping, D.H., 1972, Early Tertiary paleogeography of central California: American Association of Petroleum Geologists Bulletin, v. 56, no. 3 p. 480-493.

Clark, J.C., 1981, Stratigraphy, Paleontology, and Geology of the Central Santa Cruz Mountains, California Coast Ranges: Geological Survey Professional Paper 1168, 51 p.

Clarke, S.H., 1973, The Eocene Point of Rocks sandstone: provenance, mode of deposition, and implications for the history of offset along the San Andreas fault in central California [PhD thesis]: Berkeley, California, University of California, 302 p.

Clarke, S.H., and Nilsen, T.H., 1973, Displacement of Eocene strata and implication for the history of offset of the San Andreas fault, central and northern California, *in* Kovach, R.L. and Nur, A. eds., Proceedings of the Conference on Tectonic Problems of the San Andreas Fault System: Stanford University Publications in Geological Sciences, v. 13, p. 358-367.

Coombs, D.S., Ellis, A.J., Fyfe, W.S., and Taylor, A.M., 1959, The zeolite facies, with comments on the interpretation of hydrothermal synthesis: Geochimica et Cosmochimica, v. 17, p. 53-107.

Critelli, S., and Nilsen, T.H., 1996, Petrology and diagenesis of the Eocene Butano Sandstone, La Honda Basin, California: Journal of Geology, v. 104, p. 295-315.

Dapples, E.C., 1979, Diagenesis of sandstones, *in* Larsen, G., Chilinger, G.V., eds., Developments in Sedimentology 8: Diagenesis in Sediments, Elesevier, p. 91-127.

Dibblee, T.W., Jr., 1971, Geologic maps of 17 15-minute quadrangles along the San Andreas fault in the vicinity of King City, Coalinga, Panoche Valley and Paso Robles, with index map: U.S. Geological Survey Open-File Report 71-87, scale 1:62,500.

Dibblee, T.W., Jr., 1973, Stratigraphy of the Southern Coast Ranges near the San Andreas Fault from Cholame to Maricopa, California: U.S. Geological Survey Professional Paper 764, 45 p.

Dibblee, T.W., Jr., 1980, Geology along the San Andreas fault from Gilroy to Parkfield, *in* Streitz, R., and Sherburne, R., eds.., Studies of the San Andreas fault zone in northern California: California Division of Mines and Geology Special Paper 140, p. 3–18.

Dibblee, T.W., Graham, S.E., Mahony. T.M., Blissenbach, J.L., Mariant, J.J., and Wentworth, C.M., 1999, Regional geologic map of San Andreas and related faults in Carrizo Plain, Temblor, Caliente, and La Panza Ranges and vicinity, California: A digital database: U.S. Geological Survey Open File Report, 99-14.

Dickinson, W.R., and Butler, R.F., 1998, Coastal and Baja California paleomagnetism reconsidered: Geological Society of America Bulletin, v. 110, no. 10, p. 1268-1280.

Dickinson, W.R., Ducea, M., Rosenberg, L.I., Greene, H.G., Graham, S.A., Clark, J.C., Weber, G.E., Kidder, S., Ernst, G.W., and Brabb, E.E., 2005, Net dextral slip, Neogene San Gregorio-Hosgri fault zone, coastal California: Geologic evidence

and tectonic implications: The Geological Society of America Special Paper 391, 43 p.

Ekstrom, M.P., Dahan, C.A., Chen, M.Y., Lloyd, P.M., and Rossi, D.J., 1986, Formation imaging with microelectrical scanning arrays: Society of Professional Well Log Analysts Twenty-Seventh Annual Logging Symposium.

Engelder, J.T., 1974, Cataclasis and the generation of fault gouge: Geological Society of America Bulletin, v. 85, p. 1515-1522.

Erzinger, J., Wiersberg, T., and Zimmer, M., 2006, Real-time mud gas logging and sampling during drilling: Geofluids, v. 6, no. 3, p. 225-233.

Evans, J.P., Moore, D.E., Kirschner, D., and Solum, J.G., 2005, Lithologic characterization of the deep portion of the SAFOD drillhole: EOS Trans., AGU, 86(52), Fall Meeting Supplement, Abstract T21A-0450.

Ghent, E.D., 1979, Problems in zeolite facies geothermometry, geobarometry and fluid compositions, in Scholle, P.A. and Schluger, P.R., eds., Society of Sedimentary Geology Special Publication no. 26, p. 81-87.

Gleadow, A.J.W., and Fitzgerald, P.G., 1987, Uplift history and structure of the Transantarctic mountains – New evidence from fission-track dating of basement apatites in the Dry Valleys area, Southern Victoria Land, Earth Planetary Science Letters, v. 82, p. 1-14.

Graham, S.A., 1978, Role of Salinian Block in the evolution of the San Andreas fault system, California: American Association of Petroleum Geologists, v. 62, no. 11, p. 2214-2231.

Graham, S.A., Stanley, R.G., Bent, J.V., and Carter, J.B., 1989, Oligocene and Miocene paleogeography of central California and displacement along the San Andreas fault: Geological Society of America Bulletin, v. 101, p. 711-730.

Grove, K., 1993, Latest Cretaceous basin formation within the Salinian terrane of west-central California: Geological Society of America Bulletin, v. 105, p. 447-463.

Hickman, S., Zoback, M., Ellsworth, B., 2005, Structure and composition of the San Andreas Fault Zone at Parkfield: Initial results from SAFOD Phases 1 and 2: EOS trans. American Geophysical Union, 86(52), Fall Meeting Supplement, Abstract T23E-05.

Hoffman, J., and Hower, J., 1979, Clay mineral assemblages as low grade metamorphic geothermometers: application to the thrust faulted disturbed belt of Montana,

USA, *in* Scholle, P.A. and Schluger, P.R., eds., Society of Sedimentary Geology Special Publication no. 26, p. 55-79.

Hole, J.A., Catchings, R.D., St Clair, K.C., Rymer, M.J., Okaya, D.A., and Carney, B.J., 2001, Steep-dip seismic imaging of the shallow San Andreas Fault near Parkfield: Science, v. 294, p. 1513-1515.

Hole, J.A., Ryberg, T., Fuis, G.S., Bleibinhaus, F., and Sharma, A.K., 2006, Structure of the San Andreas fault zone at SAFOD from a seismic refraction survey: Geophysical Research Letters, v. 33, no. 7, doi: 10.1029/2005GL025194.

Huang, W.L., 1992, Illitic-clay formation during experimental diagenesis of arkoses, *in* Houseknecht, D.W. and Pittman, E.D., eds., Origin, Diagenesis, and Petrophysics of Clay minerals in Sandstones: Society of Sedimentary Geology Special Publication no.47, p. 49-63.

Hurford, A.J., and Carter, A., 1991, The role of fission track dating in discrimination of provenance, *in* Morton, A.D., Todd, S.P., and Haughton, P.D.W., eds., Developments in Sedimentary Provenance Studies: Geological Society Special Publication no. 57, p. 67-78.

Jennings, C.W., and Strand, R.G., 1958, Geologic Map of California, San Luis Obisbo sheet, Cal. Division of Mines and Geology, scale 1:250,000.

Kidder S., Ducea, M.N., Gehrels, G.E., Patchett, P.J., and Vervoot, J., 2003, Tectonic and magmatic development of the Salinian Coast Ridge Belt, California: Tectonics, v. 22, 1058 doi: 10.1029/2002TC001409.

Kirschner, D., Evans, J.P., Chester, J., Chester, F., Garver, J., Solum, J., Hickman, S., and Moore, D.E., 2006, Results of elemental, stable isotope, organic matter, and fission-track analyses of SAFOD drill-hole cuttings and core material: EOS trans. American Geophysical Union 87(52), Fall Meeting Supplement, Abstract T21C-0434.

Kistler, R.W., and Champion, D.E., 2001, Rb-Sr whole rock and mineral ages, K-Ar, 40Ar/39Ar, and U-Pb mineral ages, and strontium, lead, neodymium, and oxygen isotopic compositions for granitic rocks from the Salinian Composite Terrane, California: U.S. Geological Survey Open-file Report 01-453, 84 p.

Lachenbruch, A.H., and Sass, J.H., 1980, Heat flow and energetics of the San Andreas fault zone: Journal of Geophysical Research, v. 85, p. 6185-6223.

Liu, K.W., 2002, Deep burial diagenesis of the silisclastic Ordovician Natal Group, South Africa: Sedimentary Geology, v. 154, p. 177-189.

Matthews, V., III, 1976, Correlation of the Pinnacles and Neenach volcanic formations and their bearing on the San Andreas fault problem: American Association of Petroleum Geologists Bulletin, v. 60, p. 2128–2141.

Merino, E., 1975, Diagenesis of Tertiary sandstones from Kettleman North Dome, California: diagenetic mineralogy: Journal of Sedimentary Petrology, v. 45, p. 320-336.

Montoya, J.W., and Hemley, J.J., 1975, Activity relations and stabilities in alkali feldspar and mica alteration reactions: Economic Geology, v. 70, p. 577-583.

Moore, D.M., and Reynolds, R.C., 1989, X-Ray Diffraction and the Identification and Analysis of Clay Minerals, Oxford University Press, 378 p.

Morad, S., Bergan, M., Knarud, R., and Nystuen, J.P., 1990, Albitization of detrital plagioclase in Triassic reservoir sandstones from the Snorre Field, Norwegian North Sea: Journal of Sedimentary Petrology, v. 60, no. 3, p. 411-425.

Naeser, C.W., 1979, Thermal history of sedimentary basins: fission-track dating of subsurface rocks, *in* Scholle, P.A. and Schluger, P.R., eds., Society of Sedimentary Geology Special Publication no. 26, p. 109-112.

Narr, W., and Suppe J., 1991, Joint spacing in sedimentary rocks: Journal of Structural Geology, v. 13, no. 9, p. 1037-1048.

Nilsen, T.H., 1984, Offset along the San Andreas fault of Eocene strata from the San Juan Bautista area and western San Emigdio Mountains, California: Geological Society of America Bulletin, v. 95, p. 599-609.

Nilsen, T.H., and Clarke, S.H., 1975, Sedimentation and Tectonics in the Early Tertiary Continental Borderland of Central California: U.S. Geological Survey Professional Paper 925, 64 p.

Page, B.M., Thompson, G.A., and Coleman, R.G., 1998, Late Cenozoic tectonics of the central and southern Coast Ranges of California: Geological Society of America Bulletin, v. 110, no. 7, p. 846-876.

Payne, M.B., 1964, San Andreas Fault Cross Section Parallel Along the East Side of the Fault from Bitterwater Valley to Parkfield, California: American Association of Petroleum Geologists, Cross Section No. 5.

Powell, R.E., 1993, Balanced palinspastic reconstruction of pre-late Cenozoic paleogeography, southern California: Geologic and kinematic constraints on

evolution of the San Andreas fault system, *in* Powell, R.E., Weldon, R.J., II, and Matti, J.C., eds.., The San Andreas fault system: Displacement, palinspastic reconstruction, and geologic evolution: Geological Society of America Memoir 178, p. 1-106.

Rider, M. H., 1996, The geological interpretation of well logs, 2nd edition, Gulf Publishing Company, Houston, TX, 280 p.

Ross, D.C., 1970, Quartz gabbro and anorthositic gabbro: Markers of offset along the San Andreas fault in the California Coast Ranges: Geological Society of America Bulletin, v. 81, no. 12, p. 3647–3661.

Ross, D. C., 1984, Possible correlations of basement rocks across the San Andreas, San Gregorio-Hosgri, and Rinconada-Reliz-King City faults, California: U.S. Geological Survey Professional Paper 1317, 37 p.

Rymer, M.J. 1981, Geologic map along a 12 kilometer segment of the San Andreas fault zone, southern Diablo Range, California: U.S. Geological Survey Open-File Report 81-1173, scale 1:12,000.

Rymer, M. J., Catchings, R. D., and Goldman, M. R., 2003, Structure of the San Andreas fault zone as revealed by surface geologic mapping and high-resolution seismic profiling near Parkfield, California: EOS trans. American Geophysical Union, 85(47), Fall Meeting Supplement, Abstract T-11F-08.

Schleicher, A.M., van der Pluijm, B.A., Warr, L.N., Tourscher, S., and Solum, J.G., 2005, The origin and significance of fracture coatings in the SAFOD mudrock samples: EOS trans. American Geophysical Union, 86(52), Fall Meeting Supplement, Abstract T21A-0455.

Schleicher, A.M., van der Pluijm, B.A., Solum, J.G., Warr, L.N., 2006 (submitted), The origin and significance of clay minerals on surfaces, in fractures and in veins from SAFOD borehole samples (Parkfield, California): Journal of Geophysical Research, submitted.

Scholle, P.A., 1979, A Color Illustrated Guide to Constituents, Textures, Cements, and Porosities of Sandstones and Associated Rocks: American Association of Petroleum Geologists Memoir 28, 201 p.

Seiders, V.M., and Cox, B.F., 1992, Place of Origin of the Salinian Block, California, as Based on Clast Compositions of Upper Cretaceous and Lower Tertiary Conglomerates: U.S. Geological Survey Professional Paper 1526, 80 p.

Shaw, H.F., and Conybeare, D.M., Patterns of clay mineral diagenesis in interbedded mudrocks and sandstones: an example from the Paleocene of the North Sea: *in* Worden, R.H. and Morad, S., eds., clay mineral cements in sandstones: International Association of Sedimentologists Special Publication no. 34, p. 129-146.

Sims, J.D., 1990, Geologic map of the San Andreas Fault in the Parkfield 7.5-minute Quadrangle, Monterey and Fresno counties, California: Miscellaneous Field Studies Map, 2115, MF-2115.

Sims, J.D., 1993, Chronology of displacement on the San Andreas fault in central California: Evidence from reversed positions of exotic rock bodies near Parkfield, CA, *in* Powell, R.E., Weldon, R.J.I., and Matti, J.C., eds., The San Andreas Fault System: Displacement, Reconstruction, and Geologic Evolution, Geological Society of America Memoir 178, p. 231-256.

Solum, J.G., Hickman, S.H., Lockner, D.A., Moore, D.E., van der Pluijm, B.A., Schleicher, A.M., and Evans, J.P., 2006, Mineralogical characterization of protolith and fault rocks from the SAFOD main hole: Geophysical Research Letters, v. 33, doi: 10.1029/2006GL027285.

Tembe, S., Lockner, D.A., Solum, J.G., Morrow, C.A., Wong, T., Moore, D.E., 2005, Strength of the San Andreas Fault Zone: Insight from cuttings and core: EOS trans. American Geophysical Union, 86(52), Fall Meeting Supplement, Abstract T24B-03.

Thayer, M., and Arrowsmith, R., 2005, Fault zone structure of Middle Mountain, Central California: EOS trans. American Geophysical Union, 86(52), Fall Meeting Supplement, Abstract T21A-0458.

Thompson, L.B., ed., 2000, Atlas of Borehole Imagery: American Association of Petroleum Geologists Discovery Series 4, Tulsa OK.

Vedder, J.G., and Brown, R.D., 1968, Structural and stratigraphic relations along the Nacimiento fault in the southern Santa Lucia Range and San Rafael Mountains, California, *in* Dickinson, W.R. and Grantz, A., eds., Proceedings of Conference on Geologic Problems of the San Andreas Fault System: Stanford University Publications of the Geological Sciences, v. 11, p. 243-258.

Vedder, J.G., Howell, D.G., and McLean, H., 1982, Stratigraphy, sedimentation and tectonic accretion of exotic terranes, southern Coast Ranges, California, *in* Watkins, J.S. and Drake, C.L., eds.., Studies in continental geology: American Association of Petroleum Geologists Memoir No. 34, p. 471-496.

Wagner, G.A., and Van der Haute, P., 1992, Fission track dating: Dordrecht and Boston, Kluwer, 285 p.

Whidden, K.J., Lund, S.P., Bottjer, D.J., Champion, D., and Howell, D.G., 1998, Paleomagnetic evidence that the central block of Salinia (California) is not a far-travelled terrane: Tectonics, v. 17, no. 3, p. 329-344.

Winter, H., Adelhardt, S., Jerak, A., and Kuchenhoff, H., 2002, Characterization of cataclastic shear-zones of the KTB deep drill hole by regression analysis of drill cuttings data: Geophysical Journal International, v. 150, p. 1-9.

Worden, R.H., and Morad, S., 2003, Clay minerals in sandstones: controls on formation, distribution and evolution, *in* Worden, R.H. and Morad, S., eds., Clay mineral cements in sandstones: International Association of Sedimentologists Special Publication no. 34, p. 3-42.

Wright, T.A., 2000, The evolving San Andreas fault system: Nascent tectonic succession of California?, *in* Bokelmann, G. and Kovach, R.L., (eds.), Proceedings of the 3rd Conference on Tectonic Problems of the San Andreas Fault System, Stanford University Publications, p. 144-149.

Table 2.1: Wireline log values for three lithologic units

	porosity (ratio)	density (g/cm3)	velocity (km/sec)	gamma ray (API)
Upper Arkose	0.01-0.44 **0.10**	2.13-2.72 **2.56**	3.20-5.76 **4.57**	77.73-258.45 ← range **129.08** ← average value
Clay-rich Zone	0.02-0.46 **0.19**	2.05-2.70 **2.52**	2.69-7.08 **4.25**	73.45-266.56 **152.54**
Lower Arkose	0.01-0.44 **0.08**	1.95-2.79 **2.53**	3.66-6.40 **5.04**	72.49-259.63 **112.48**

Wireline logs values for the three lithologic units: upper arkose, clay-rich unit and lower arkose. Upper values in each box are the range of values found in that units while the bold value beneath the range is the average value for that unit. Porosity is neutron porosity, a measure of bound water in the formation and is reported as a ratio, or phi. Density is the bulk density of the formation, measured in g/cm^3, velocity is compressional or p-wave (V_p) velocity of the formation, measured in microseconds/foot and converted to km/sec. Gamma Ray is the measure of natural radioactivity in the formation from Potassium, Thorium and Uranium. Values are reported in API, which stands for American Petroleum Industry, indicating that the measurements are based on an industry standard.

Table 2.2: Wireline data values for individual structural blocks

	porosity (ratio)	density (g/cm3)	velocity (km/sec)	gamma ray (API)
BLOCK 1	0.01-0.37 **0.11**	2.17-2.68 **2.55**	3.20-5.65 **4.53**	77.73-172.91 ← range **121.80** ← average
BLOCK 2	0.02-0.34 **0.12**	2.26-2.67 **2.57**	3.45-5.68 **4.48**	82.61-154.38 **125.05**
BLOCK 3	0.02-0.29 **0.14**	2.40-2.65 **2.56**	3.53-5.66 **4.31**	84.02-163.40 **133.06**
BLOCK 4	0.01-0.33 **0.09**	2.13-2.70 **2.57**	3.48-5.66 **4.61**	86.40-257.27 **135.51**
BLOCK 5	0.01-0.44 **0.10**	2.25-2.72 **2.57**	3.73-5.76 **4.96**	79.54-258.45 **135.70**
BLOCK 6	0.02-0.46 **0.27**	2.05-2.65 **2.48**	2.69-7.08 **4.00**	77.15-255.33 **183.43**
BLOCK 7	0.02-0.32 **0.12**	2.41-2.70 **2.58**	2.89-5.03 **4.48**	73.45-213.99 **127.41**
BLOCK 8	0.02-0.42 **0.18**	2.19-2.68 **2.53**	2.89-5.59 **4.27**	80.51-266.56 **148.73**
BLOCK 9	0.01-0.44 **0.09**	2.03-2.77 **2.53**	3.67-6.03 **5.03**	72.95-259.63 **114.68**
BLOCK 10	0.02-0.35 **0.08**	1.95-2.79 **2.52**	3.66-6.40 **5.07**	72.49-224.50 **109.55**

Wireline log ranges and average values for each individual structural block (see Figure 2.17 for index of blocks). Upper values in each box are the range of values measured in that block, the lower bold value is the arithmetic mean value for the block. Wireline logs measurements are collected every 15 cm. See Table 2.1 for explanation of wireline log properties.

Table 2.3: True thicknesses of structural blocks

Block 2	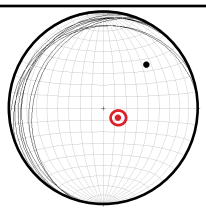	average pole to bedding = 124/75 α = 53.2° y = 75 m	True Thickness: **44.9 m**
Block 3	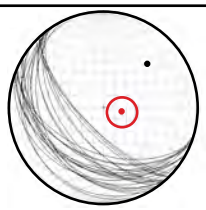	average pole to bedding = 104/74 α = 47.9° y = 30 m	True Thickness: **20.1 m**
Block 4	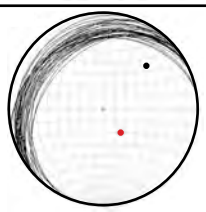	average pole to bedding = 143/65 α = 62.0° y = 40 m	True Thickness: **18.8 m**
Block 5	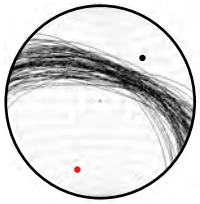	average pole to bedding = 199/26 α = 66.2° y = 180 m	True Thickness: **72.6 m**
Block7	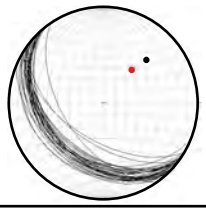	average pole to bedding = 041/52 α = 16.9° y = 30 m	True Thickness: **28.7 m**
Block 9	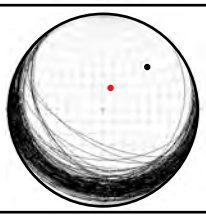	average pole to bedding = 018/70 α = 37.4° y = 200 m	True Thickness: **158.9 m**
Block 10 **(and Block 11)**	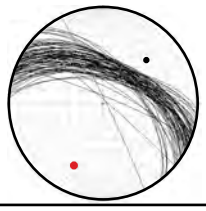	average pole to bedding = 205/29 α = 67.5° y = 170 m	True Thickness: **65.1 m**

Thickness calculations for blocks 2-10 from bedding orientation data derived from electrical image logs. Blocks 1, 6, and 8 were excluded due to a lack of clear bedding data. The technique for determining block thickness is detailed in figure 2.18. α = angle between bedding and borehole bearing, y = apparent thickness

Table 2.4: Zircon fission-track data values

Sample	Measured Depth (ft)	Measured Depth (m)	n	$\chi 2$	Age	2σ	$+2\sigma$	U ± 2se (ppm)
37-59	10240	3123.2	15	90.4	**64.3**	-4.2	4.5	252.7 ± 25.3
37-61	10280	3135.4	15	78.7	**70.1**	-4.6	4.9	237.7 ± 24.4
37-62	10310	3144.55	15	91.3	**66.1**	-4.8	5.1	200.5 ± 22.8

Results from zircon fission-track analysis performed on zircons collected from the arkosic section of the SAFOD borehole. Results pass chi-squared distribution statistical test, indicating that age populations for each sample cluster around one age, rather than the bimodal age populations sometimes found in detrital zircons. This is interpreted to indicate a source terrane for the arkoses that is either composed of a single lithology or several source rocks with similar thermal histories. Analyses conducted and interpreted by J. Garver and D. Kirschner, 2006.

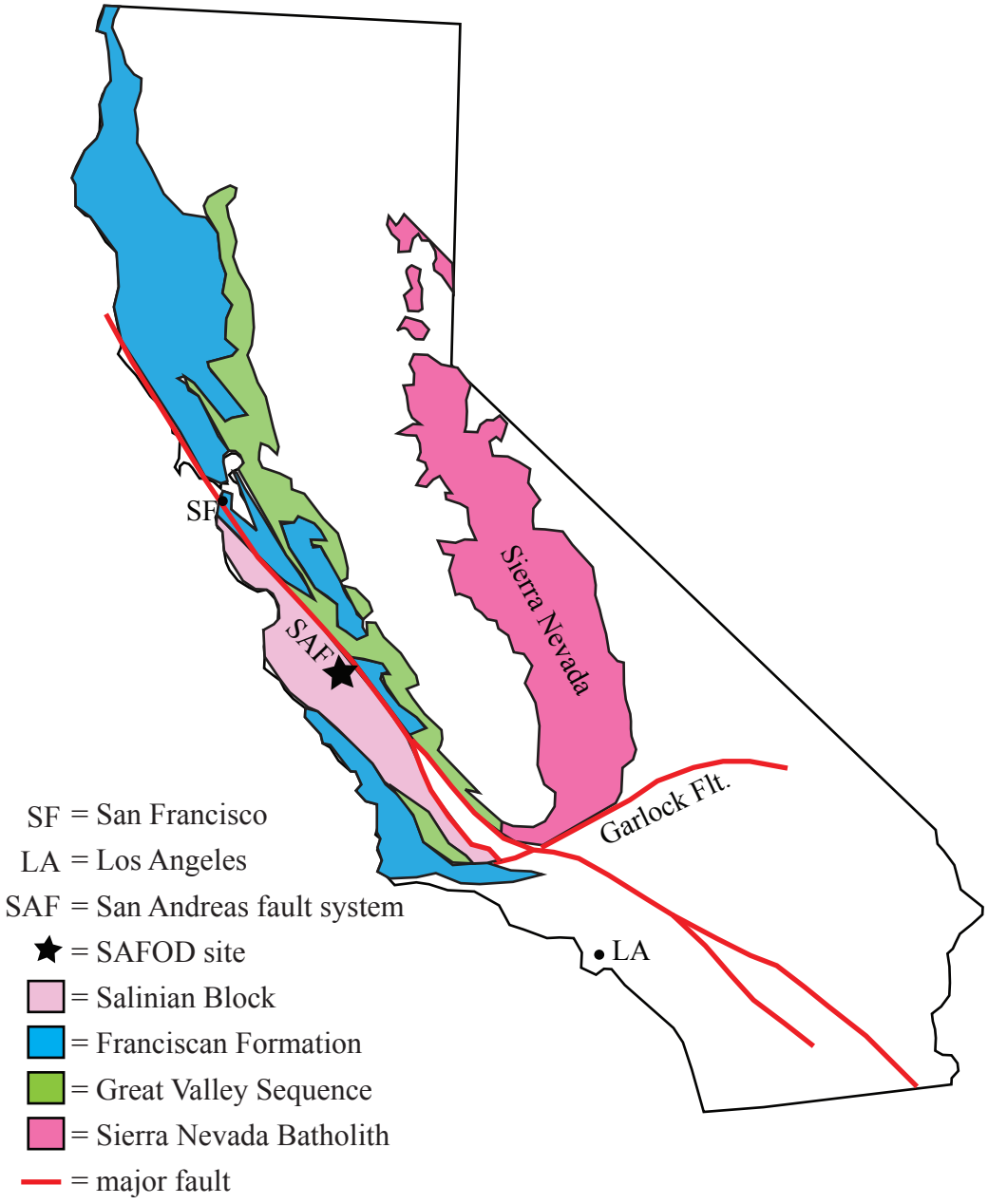

Figure 2.1: Map of the state of California showing the location of the SAFOD site and major basement terranes of central California. In the vicinity of the SAFOD site the Salinian Block, a Mesozoic plutonic complex, is located on the southwest side of the San Andreas fault and the Jurassic Franciscan Formation and Cretaceous Great Valley Sequence are located on the northeastern side of the SAF.

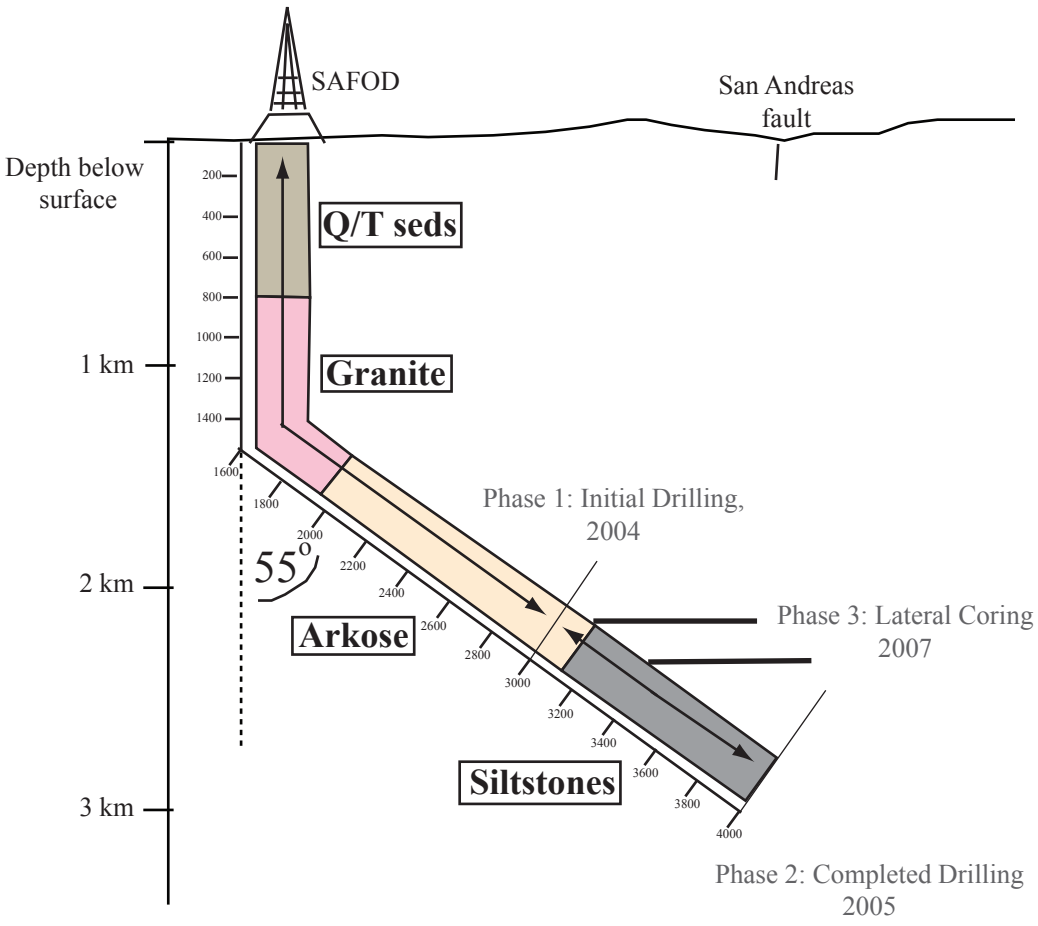

Figure 2.2: Schematic of the SAFOD drilling borehole showing the different lithologies encountered. From the surface to 800 m are Quaternary/Upper Tertiary sedimentary rocks, 800-1920 meters measured depth are granite and granodiorites of the Salinian Block, 1920-3150 mmd are well-indurated arkosic conglomerate/sandstones/siltstones, and 3150-3990 mmd are siltstone/mudstones of the Cretaceous Great Valley Sequence. An actively creeping strand of the San Andreas fault was encountered at approximately 3310 mmd.
During phase one, the borehole was drilled to 3050 mmd, during phase two the borehole was completed at 3990 mmd (3.0 km vertical depth). Phase three will take place summer 2007 and will collect multiples lateral cores of the fault zone.

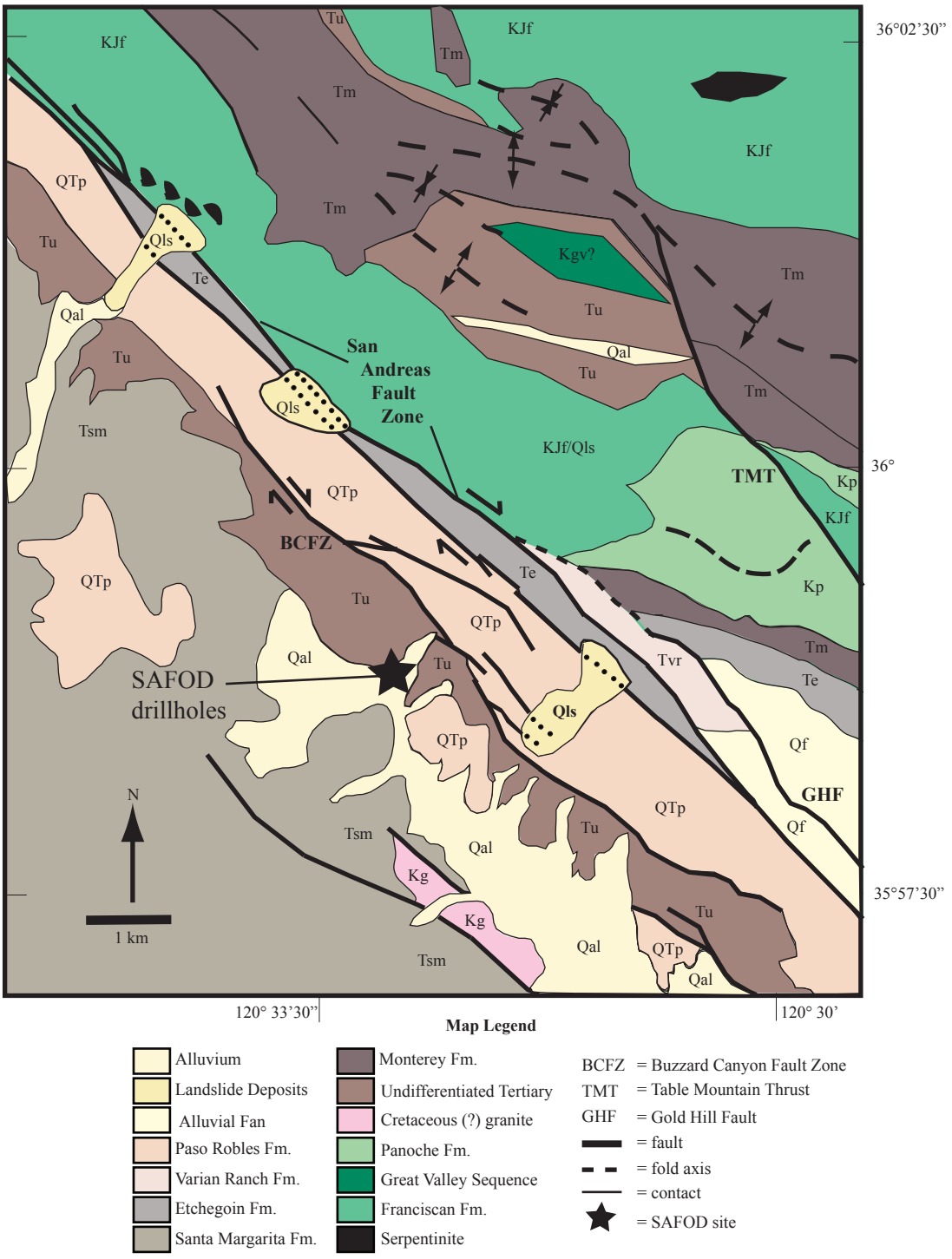

Figure 2.3: Geologic map of the SAFOD site, based on Walrond and Gribi (1963), Dickinson (1966), Dibblee (1971), Durham (1974), Sims (1990), and Thayer and Arrowsmith (2005). Figure modified from Bradbury et al., in review.

237.9 mmd

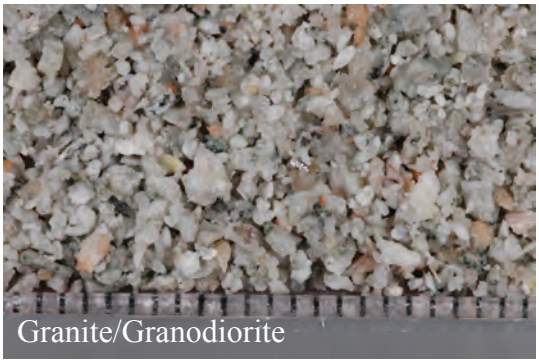

1207.8 mmd

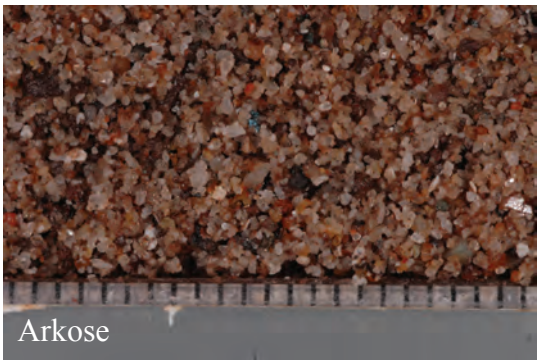

2141.1 mmd

3714.9 mmd

Figure 2.4: Photographs of cuttings after initial on-site washing, but before subsequent preparation. There is one representative photograph from the four main lithologies encountered in the SAFOD borehole, each photograph was taken under exactly the same conditions. Differences in the appearance of each photograph are due entirely to compositional differences between each lithological unit. Each tick mark on the scale at bottom of the photographs is in millimeters.

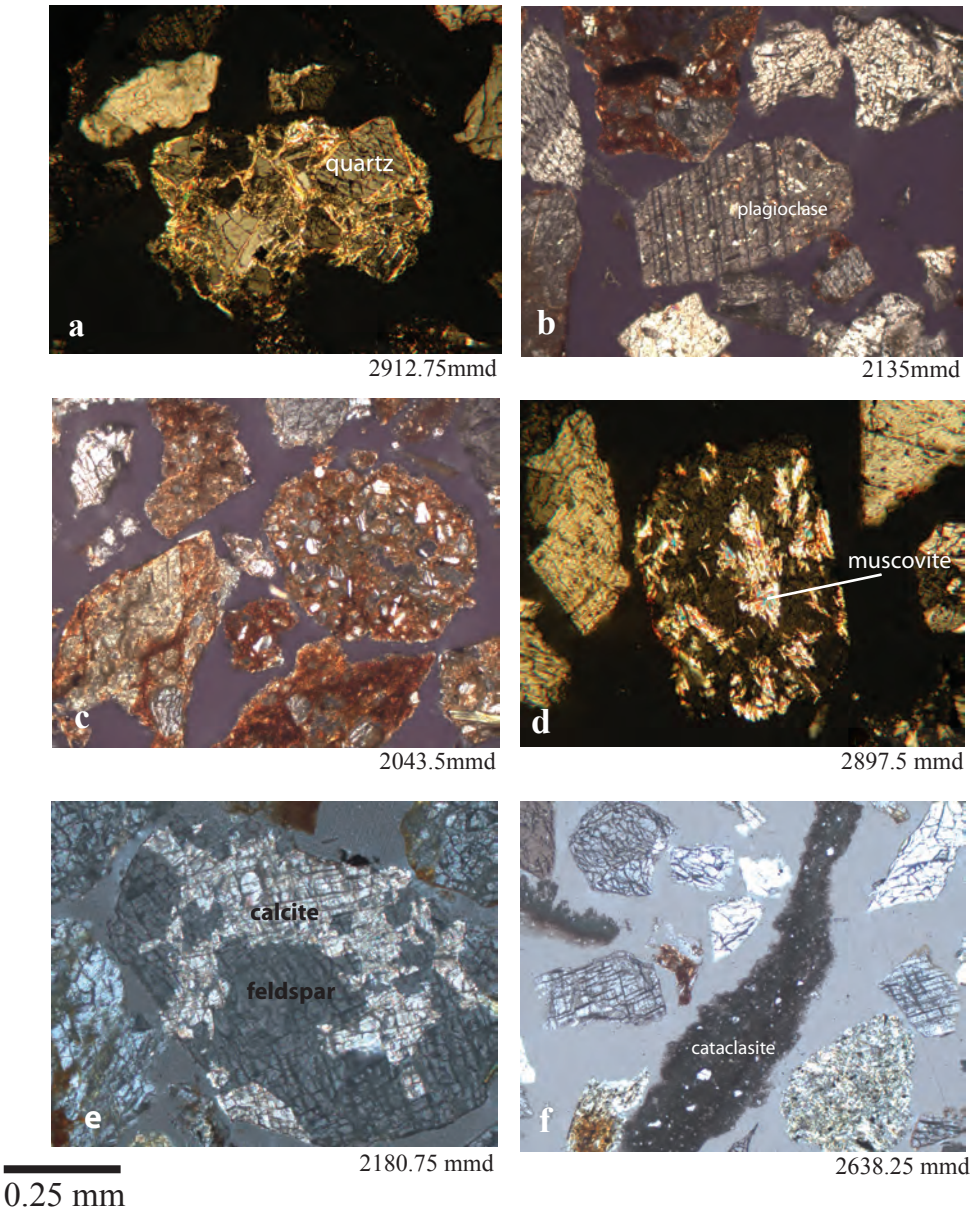

Figure 2.5: Photomicrographs showing characteristic features from cuttings samples. Depths of the samples (meters) are noted at the lower right-hand corner of the photographs. All photographs were taken in cross polarized light. Differences in color are due to different cameras taking the photos or a difference in light levels. Scale bar applies to all photomicrographs.

a: High birefrigence clay minerals fills space between quartz crystals. b: Altered plagioclase in center of photo shows alteration typical in the Upper Arkose. The grain is still easily recognizable as plagioclase with small areas of sericite formation. c: Grains displaying iron-oxide rich matrix/cement. The grain in the upper right of the photo shows depositional related iron-oxides (matrix) while the iron-oxides in the grain in the lower left look post-depositional, either a staining effect or an iron-oxide rich cement.

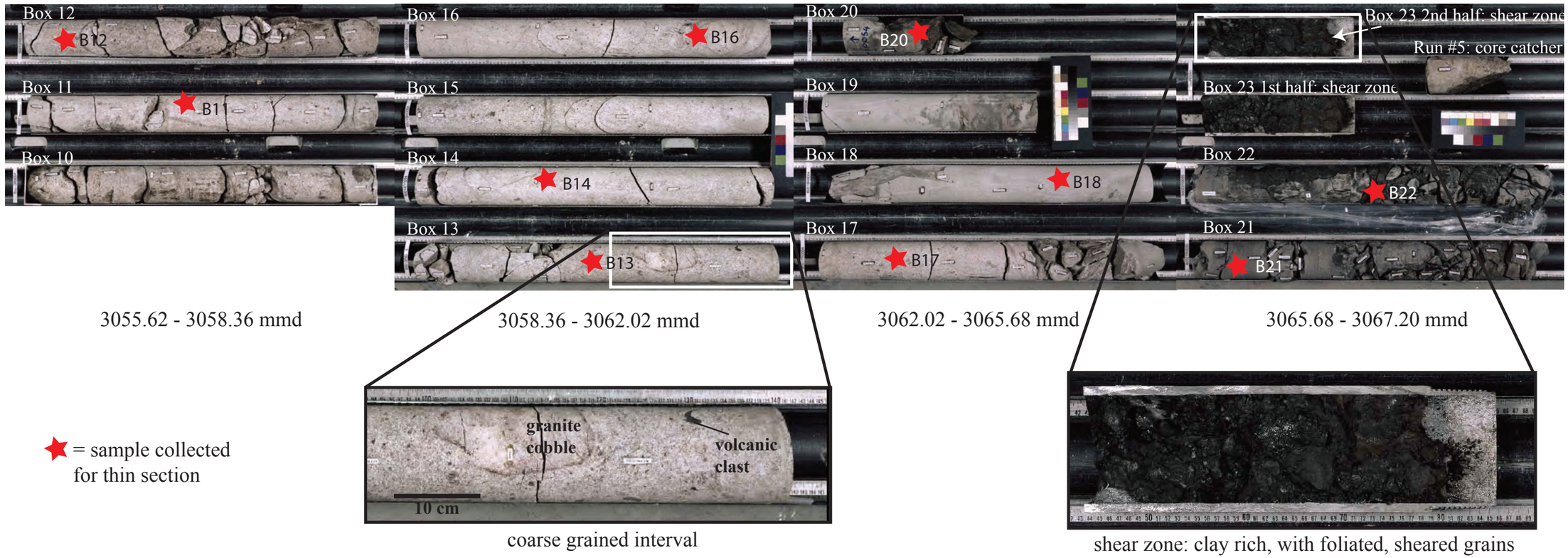

Figure 2.6: Photographs of the phase one core, runs four and five (runs 1-3 are in the granodiorite farther up in the borehole). Core is indexed by box number, smaller box numbers correspond to shallower depths. Core is 10.16 cm in diameter and each box is approximately 1 m long. Core grades from coarse-grained sandstones and matrix-supported granule-pebble conglomerate (boxes 10 - 16) to fine grained sandstone (box 17) to siltstone (boxes 18-20) to very fine-grained siltstone/mudstone (boxes 21 and 22) and into a clay-rich shear zone (Box 23). The small piece of rock to the right labelled run #5 is from a failed fifth coring attempt. Sample comes from the "core catcher" which is a basket attached to the coring bit. That sample is a fine-grained iron-oxide stained sandstone. Red stars indicate where a sample was made into a thin section for our study (the samples in boxes 12, 14, 17, 20, and 22 were made into multiple thin sections in order to capture interesting features of the sample). The nomenclature used for labelling samples is of the form MHP1-B11, as in "Main Hole Phase One Box 11", here the stars are labelled with a condensed form of the sample number, i.e. B11. Core sample descriptions can be found in Table 3.2.

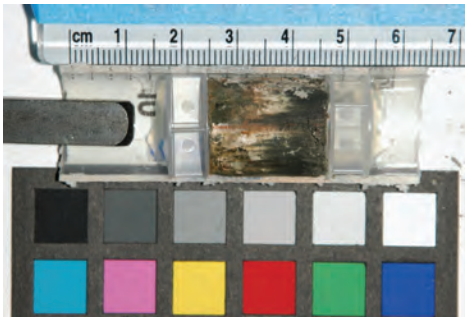

Sidewall core #69: whole core photo
Depth = 3121.15 mmd

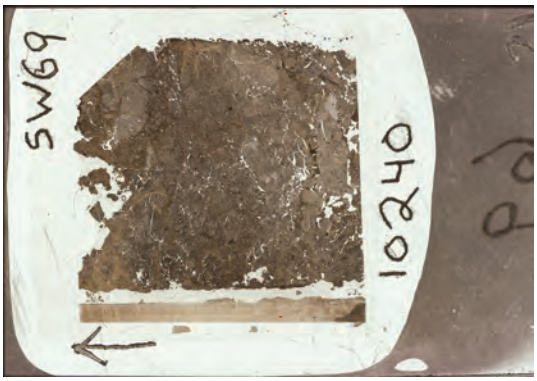

Sidewall core #69: slide scan

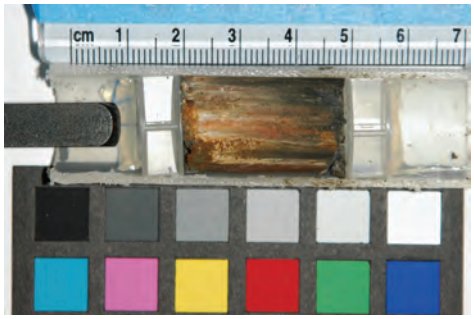

Sidewall core #71: whole core photo
Depth = 3084.58 mmd

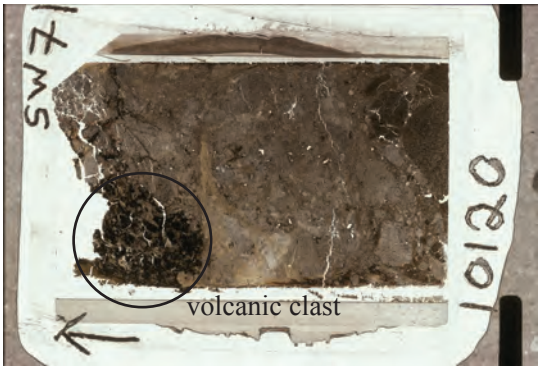

Sidewall core #71: slide scan

Figure 2.7: Photographs of two sidewall cores collected in the arkosic section. Sidewall cores 69 and 71 were made into thin section, two other cores were collected in similar zones but were archived without being sliced for thin section. SW #69 has extensive iron-oxide cementation with angular coarse grained quartz and feldspar. Feldspars are often altered, in places near total replacement by illite and muscovite have occurred. SW #71 is fine-grained than #69 with similarly altered feldspars and a large volcanic clast which shows evidence of mineral alignment within a fine-grained devitrified matrix.

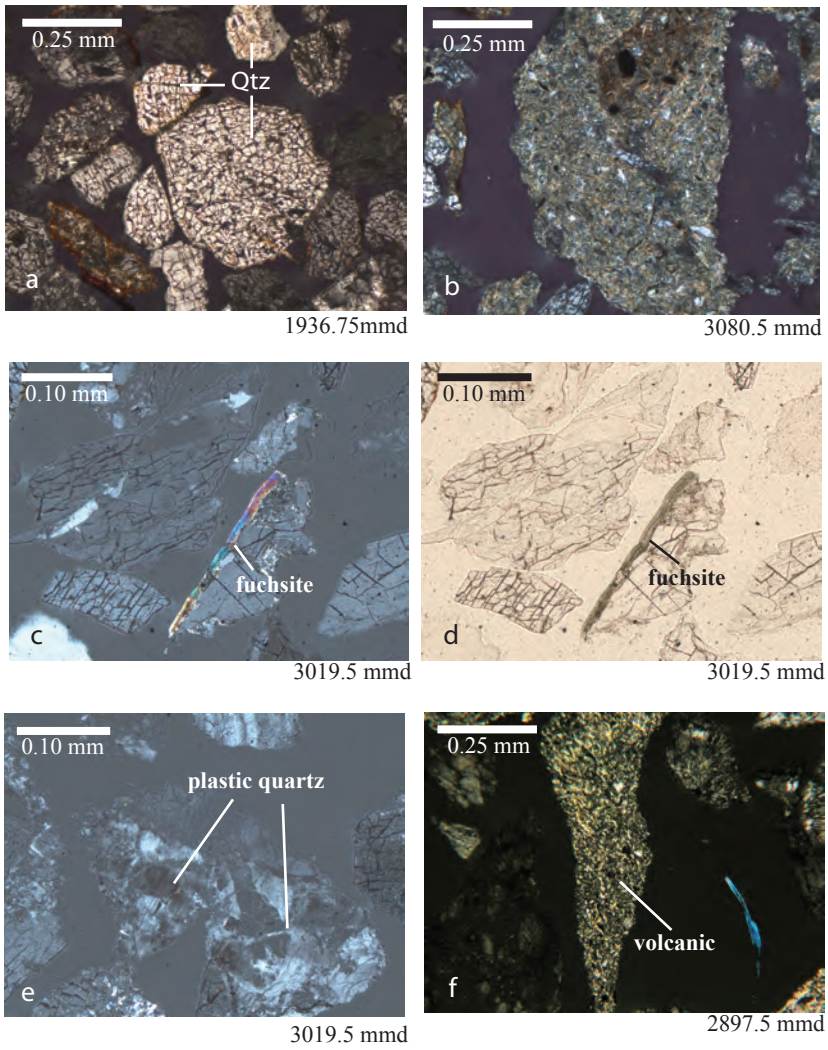

Figure 2.8: Examples of features commonly observed in cuttings. Photomicrographs are all taken with cross-polarized light except photo b which is taken with plane-polarized light. Photos c, d and e taken with a blue filter.

a) Concoidally fractured quartz grains. Fractured texture is drilling induced. b) clay-rich grain from the lower arkose, several compositions of clay mineral present in the grain. Greenish color is due to the presence of fine-grained chlorite. c) fuchsite in cross-polarized light. Interference colors are higher order than in chlorite. d) the same fuchsite grain in plane-polarized light, notice distinct green color. e) plastically deformed quartz grain. f) devitrified volcanic grain from the lower arkose. Photo light levels have been altered digitally in order to see features in the grain. Petrographically, volcanic grains are typically very dark.

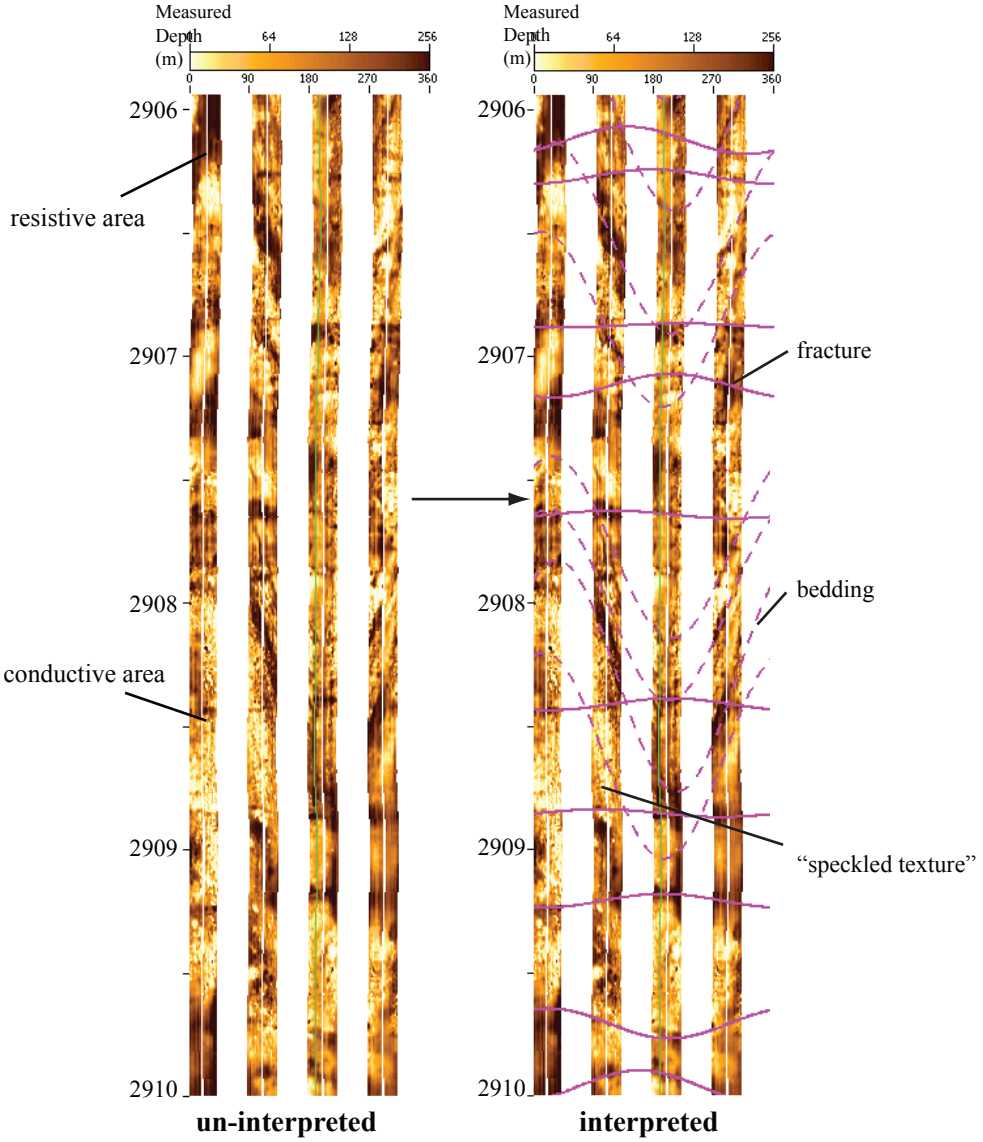

Figure 2.9: Image logs from a sandstone interval in the lower arkose. These images are an example of good quality data where bedding can be identified along with a set of bedding perpendicular fractures. Dark areas are more electrically resistive and light areas are more conductive. These logs have been dynamically normalized so that the scale of resistivity vs. conductivity is not numeric but instead the highest and lowest resistivities create maximum and minimum values and a scale on which the logs can be based. Here fractures (indicated by solid sinusoids in the interpreted section) are somewhat regularly spaced, open-mode, conductive features. Beds (indicated by dashed sinusoids in interpreted section) are steeply dipping to the NE.

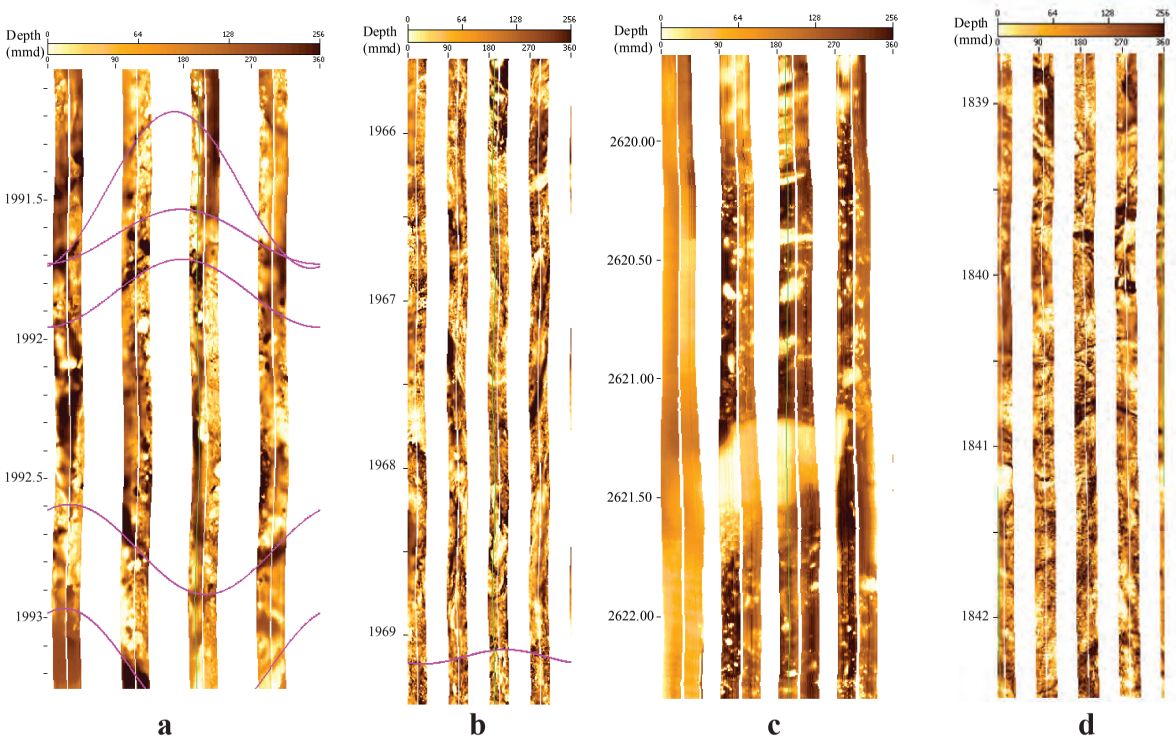

Figure 2.10: Examples of different lithologies or image log "facies". Each example is displayed in a 1:1 aspect ratio but at different scales to highlight features. a) conglomeratic interval in the upper arkose. Notice the abundance of resistive clasts, likely granitic in composition. b) Chaotic interval in the upper arkose with good image clarity but no discernable bedding or fractures. This interval is interpreted to be a slump fold or similar soft sediment deformation due to the lack of brittle deformation features which would be present in post-lithification deformation. c) An example of poor image quality in the clay-rich zone. Image may represent a brecciated or cataclastic zone but the clast/matrix features are more likely a result of blurring from poor data. The majority of the clay-rich zone images have these characteristics. d) An uninterpreted image of granite in the borehole above the arkoses. Image quality is very good, granite is highly fractured.

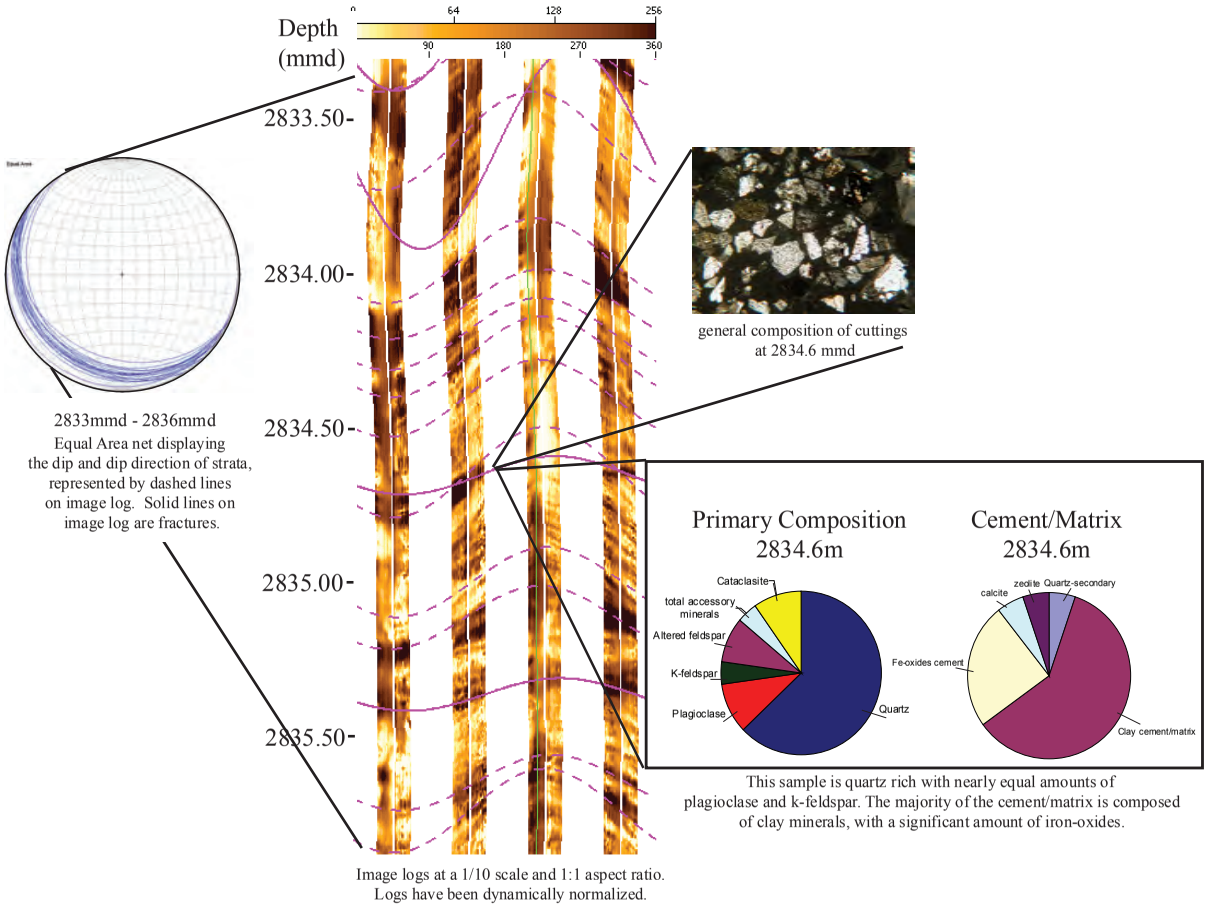

Figure 2.11: A composite image from a two meter interval in the Lower Arkose. Here the rocks are laminated fine-grained sandstone/siltstones. Solid purple lines on image log are interpreted fractures while dashed purple lines are interpreted bedding planes. Image quality in this interval is some of the best in the entire arkosic interval.

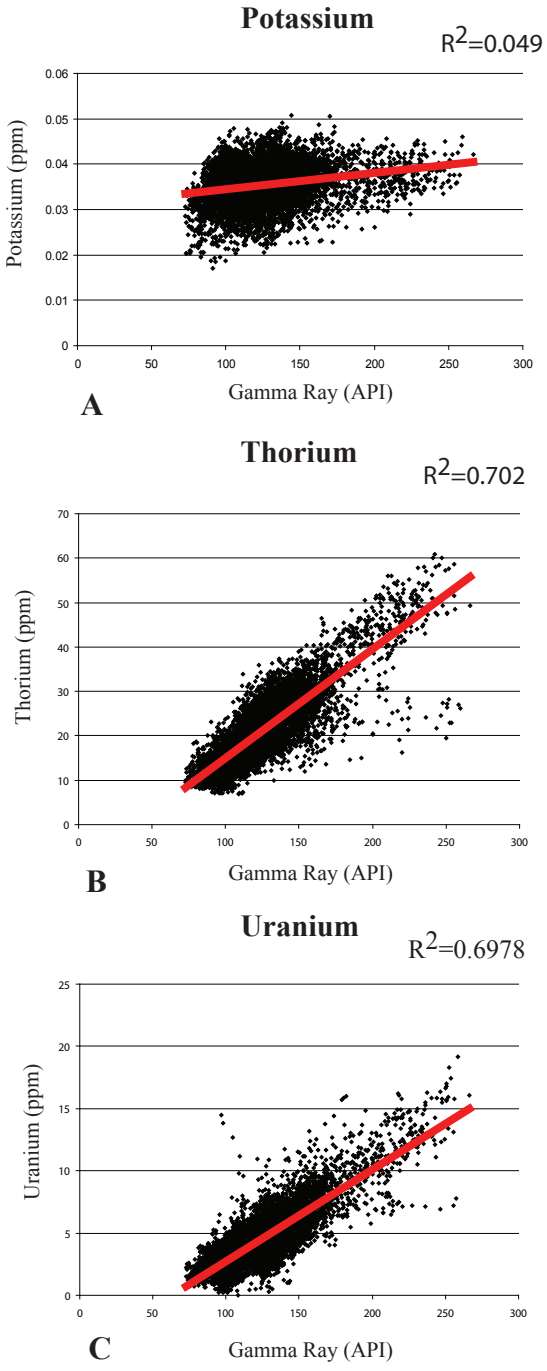

Figure 2.12: Spectral Gamma Ray values collected using a Hostile Environment Gamma Ray Sonde (HNGS) tool are resolved into the three most common components of naturally occurring radioactivity: Potassium, Thorium and Uranium. The stronger linear correlation between Gamma Ray and Thorium and Uranium implies that Potassium is not the dominant naturally radioactive element in the rocks encountered in the SAFOD borehole from 1920 mmd to 3050 mmd.

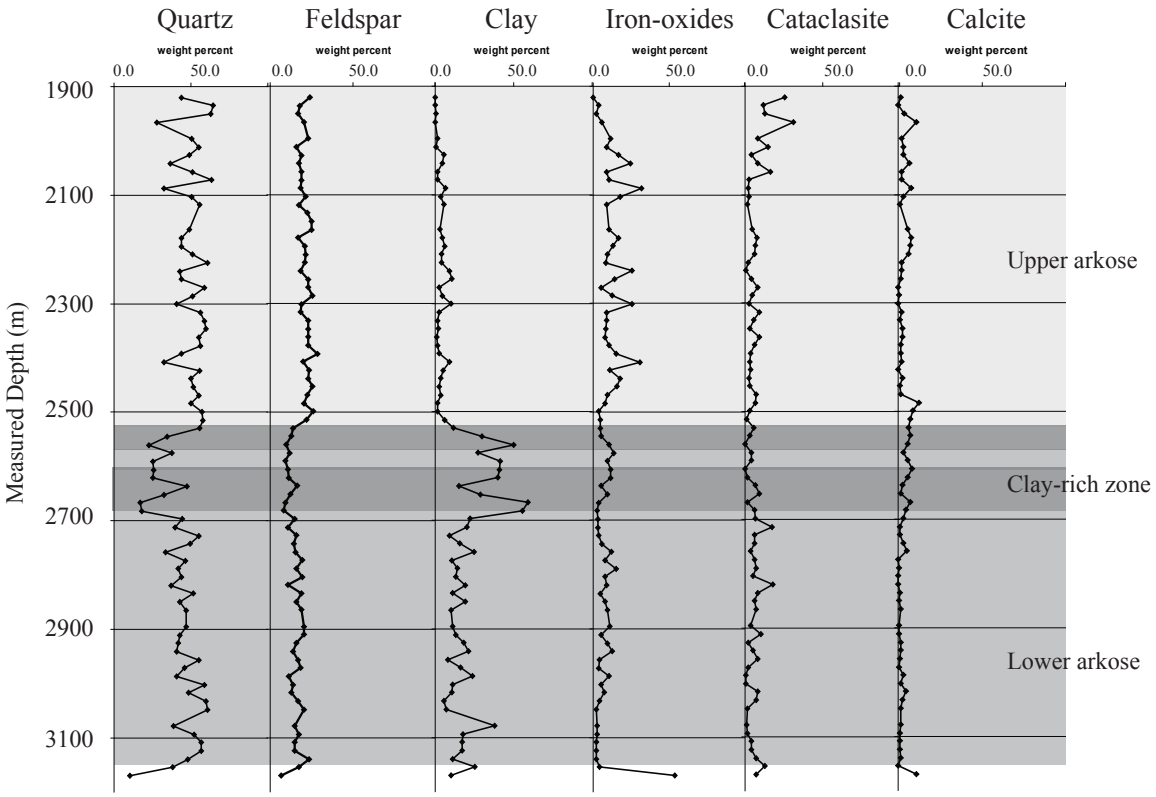

Figure 2.13: Composition of arkosic section derived from petrographic point counts. Graph is divided into the three different lithologic units: upper arkose, clay-rich zone and lower arkose.

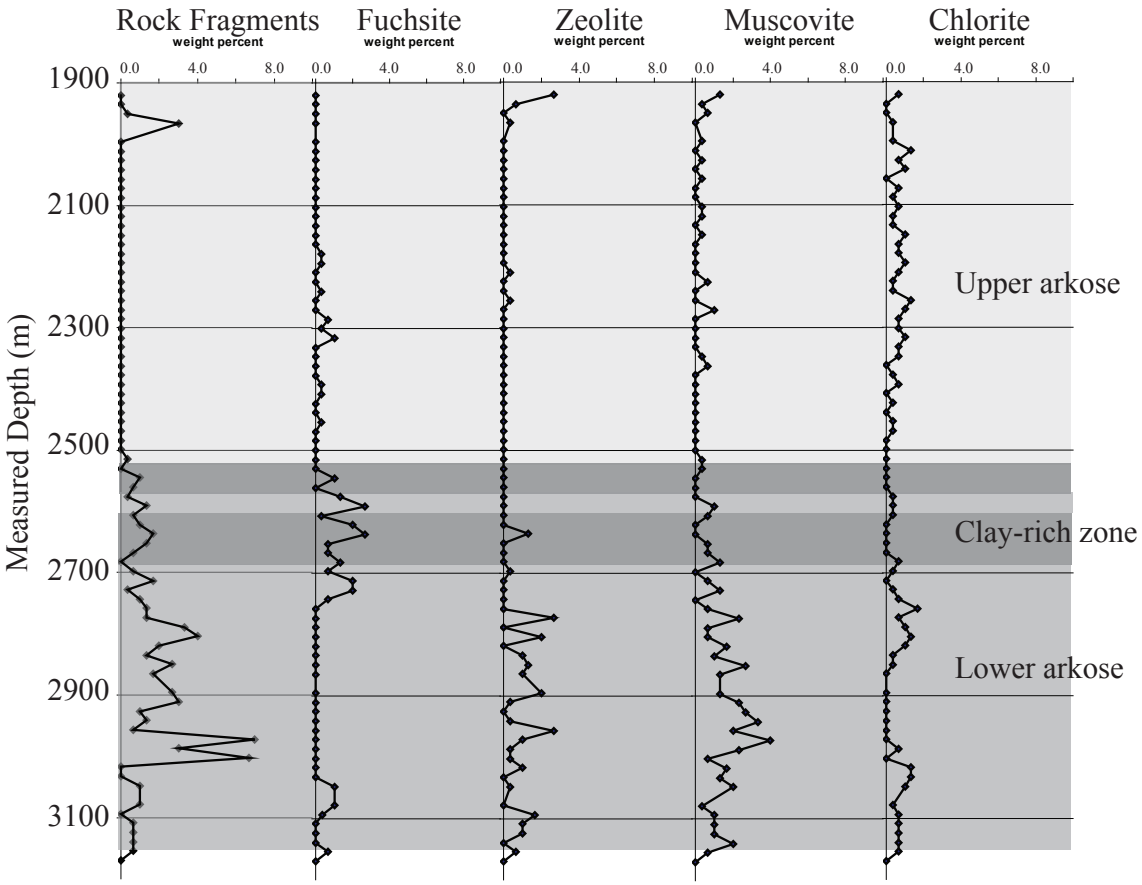

Figure 2.14: Minor compositional components which make up less than 10% of any given sample, but which are still significant components. If plotted against the other components of the system, these would look insignificant in scale, thus they are plotted separately. Graphs have been split into the three lithologic units: upper arkose, clay-rich zone and lower arkose.

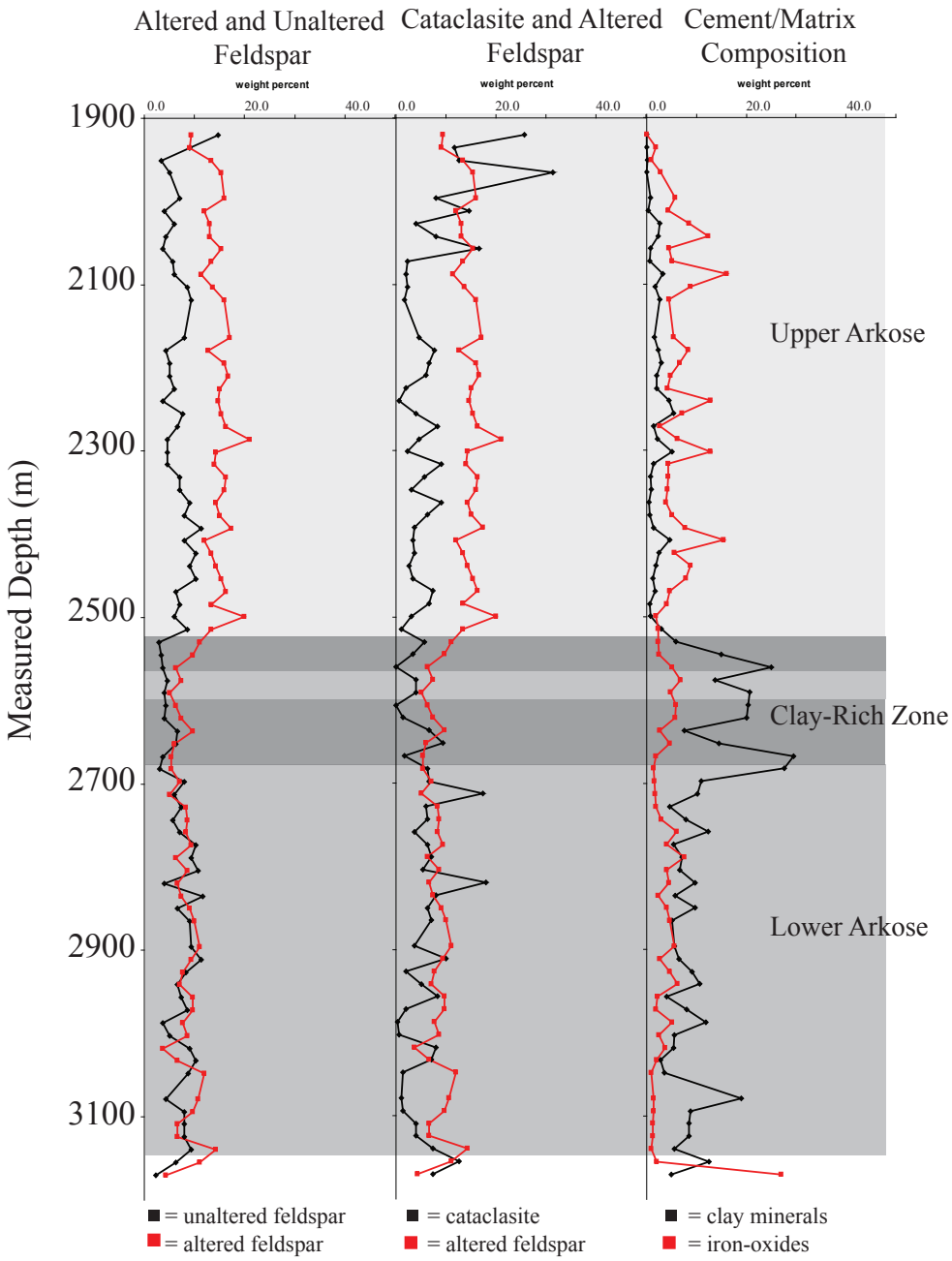

Figure 2.15: Comparison of alteration, diagenetic and deformational features of the arkosic section.

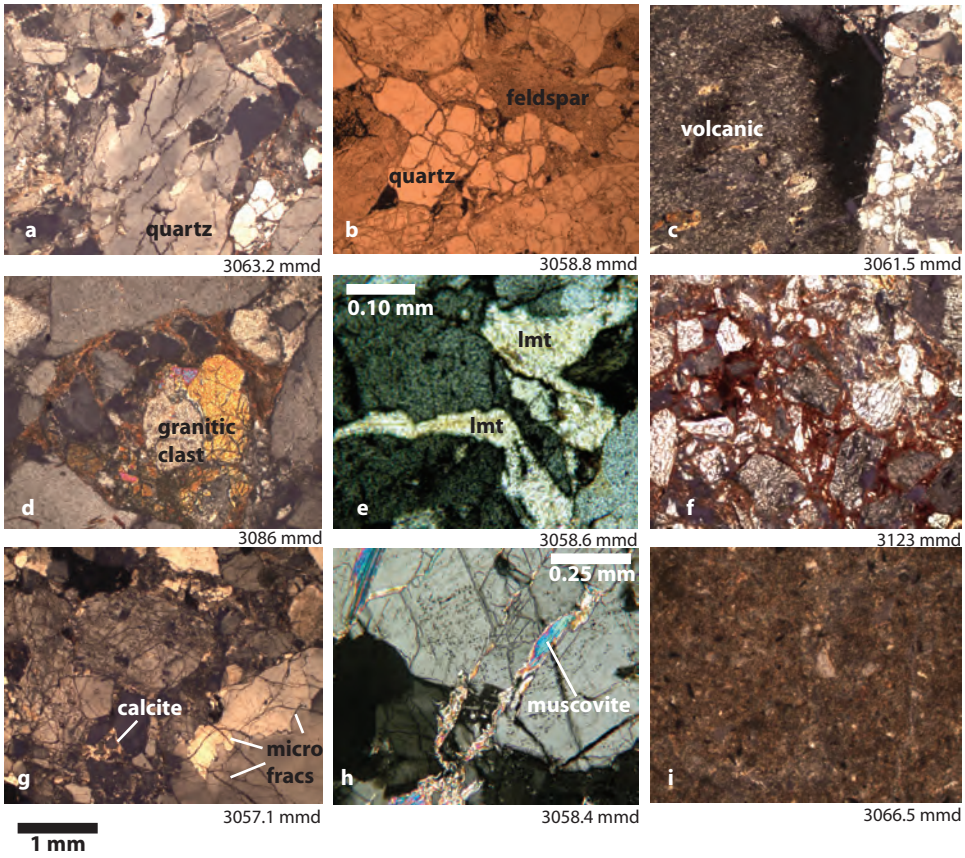

Figure 2.16: Photomicrographs of Phase one spot core and Phase two sidewall cores. All photos except photo b are taken in cross-polarized light, photo b is taken in plane-polarized light. Scale bar applies to all photomicrographs except e and h. Depths are based on the distance from the lower end of the core to the sample collected.

a) Fractured/brittlely damaged quartz grain b) Quartz grain broken apart with individual slivers remaining in place, the beginning of grain size reduction.
c) Fine-grained, devitrified volcanic clast takes up left half of photo. Opaque mineral at center of photo and edge of volcanic clast is not identifiable in reflected light.
d) Altered granitic clast with amphibole beginning to oxidize. From sidewall core #69.
e) Veins filled with the zeolite mineral laumontite. f) An example of iron-oxide cementation in sidewall core #71. g) Localized calcite cementation in lower left-hand corner of photo. Grains are extremely fractured in this portion of the core.
h) Post-depositional muscovite vein formation in quartz grain. i) Siltstone portion of spot core, grains are texturally immature with little to no mineral alignment. Closely resembles fine-grained cuttings.

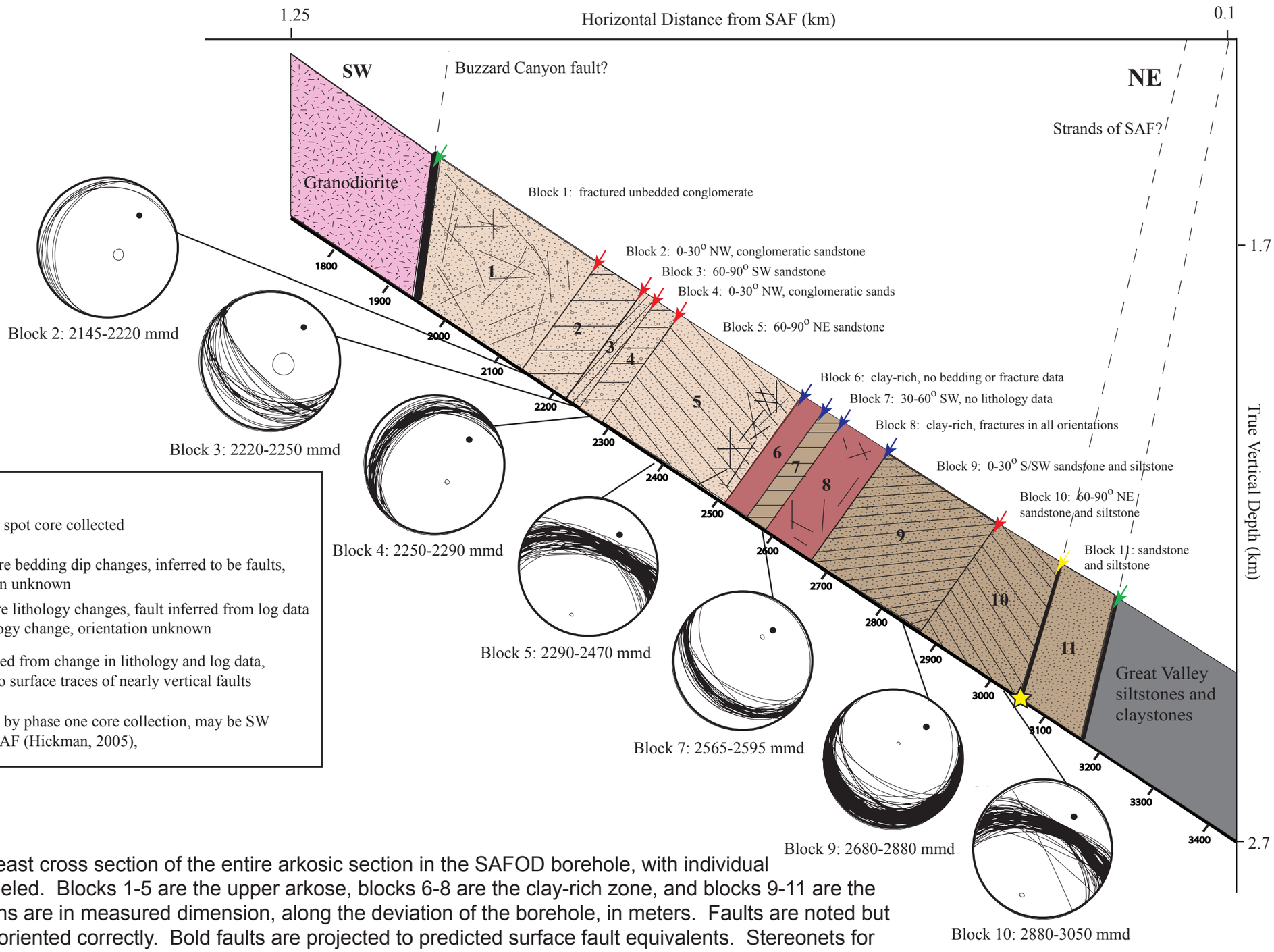

Southwest to northeast cross section of the entire arkosic section in the SAFOD borehole, with individual structural blocks labeled. Blocks 1-5 are the upper arkose, blocks 6-8 are the clay-rich zone, and blocks 9-11 are the lower arkose. Depths are in measured dimension, along the deviation of the borehole, in meters. Faults are noted but are not necessarily oriented correctly. Bold faults are projected to predicted surface fault equivalents. Stereonets for each block are equal area nets with bedding plotted as great circles, black point is the trend/plunge of the borehole. Apparent dips of bedding are shown schematicallywithin each block.

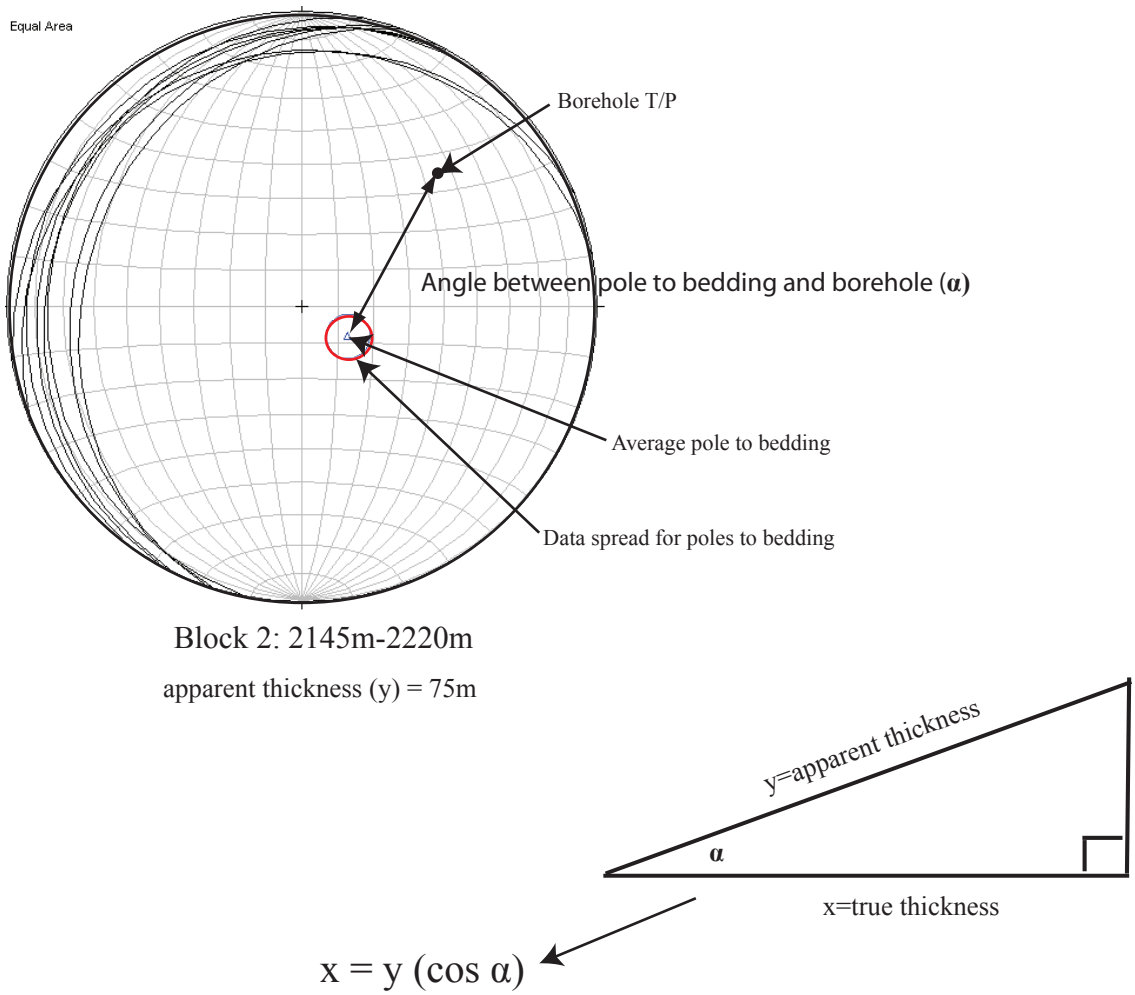

Figure 2.18: Schematic illustrating the calculation to determine the thickness bedded intervals in each fault block. Using the perpendicular to bedding (the pole) allows us to calculate the true thickness through the pythagorean relationship shown in the right triangle above.

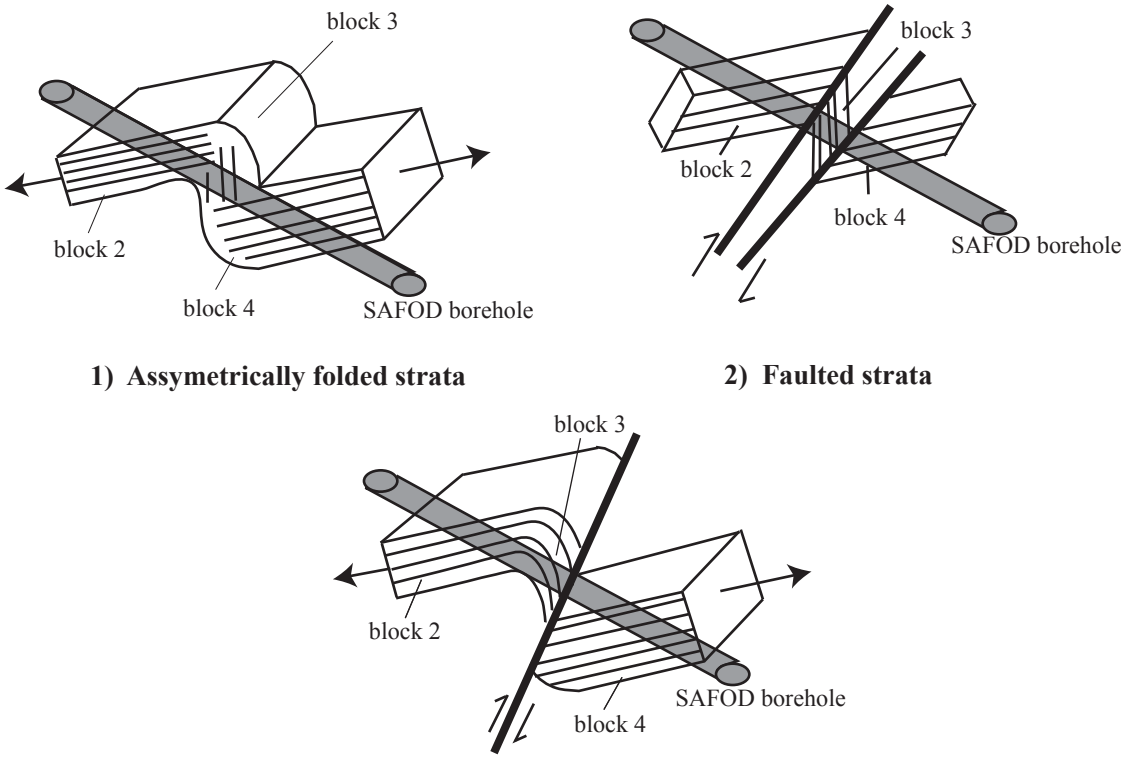

Figure 2.19: Three hypotheses to explain the orientation of bedding in blocks 2, 3 and 4. Dips of faults are purely hypothetical because there are no data to suggest their true orientation.

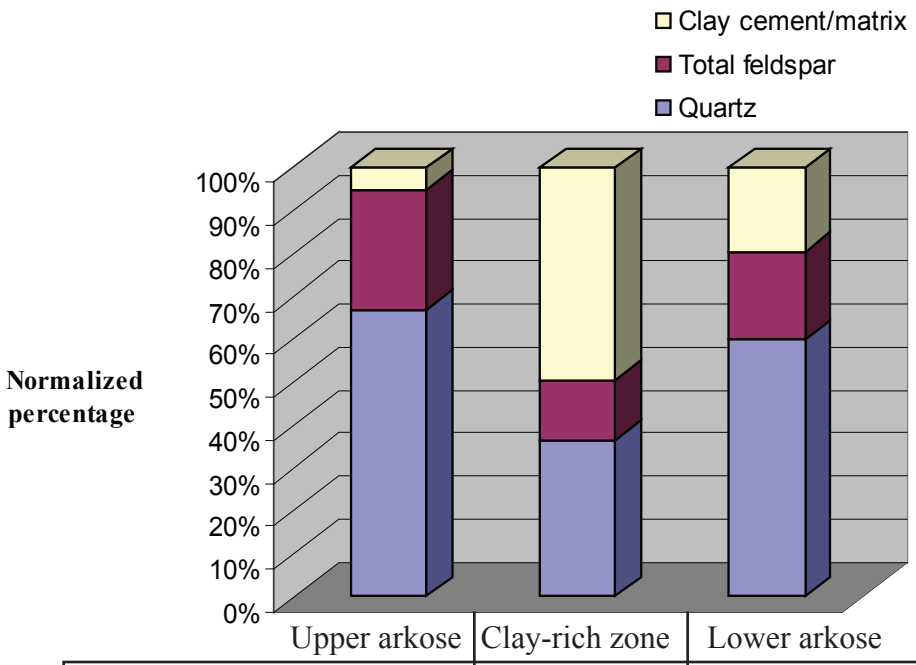

	Upper arkose	Clay-rich zone	Lower arkose
Thickness : (meters)	**156.4-381.4**	**28.7-121.3**	**224-331**

Figure 2.20: Comparison of major compositional components in the three lithologic units. These would typically be plotted on a ternary diagram but because point counts were performed using cuttings samples, we cannot classify the clay fraction in the "lithic" category as in traditional sandstone classifications. Therefore, the components are plotted in a bar diagram to illustrate the differences between the units. Total thicknesses are calculated from bedding measurements (Figure 2.18 and Table 2.3) and minimum and maximum thicknesses for blocks where bedding was not measured (Blocks 1, 6, 8, and 11).

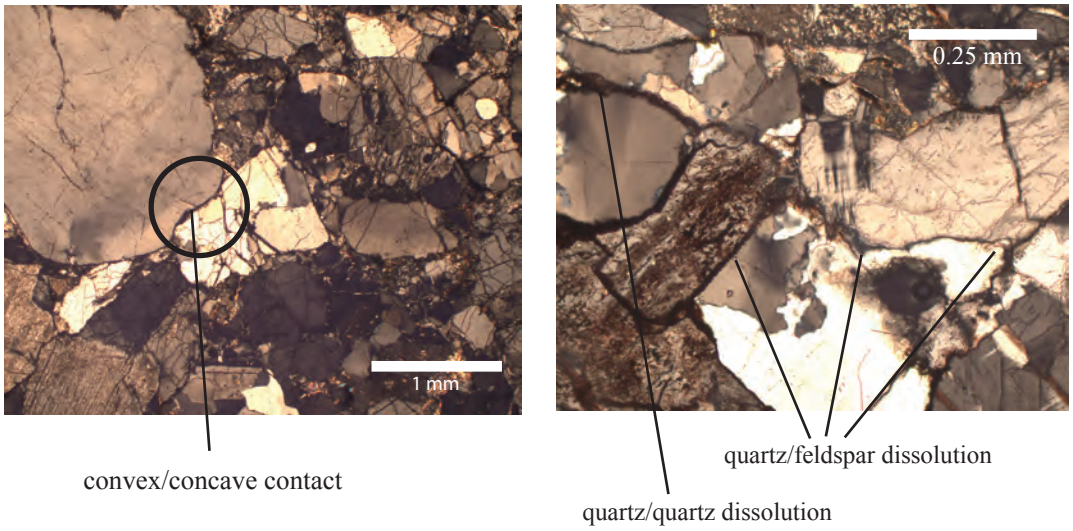

Figure 2.21: Examples of beginning stage of mineral dissolution in the SAFOD phase one spot core. Advanced dissolution fabrics such as stylolites were not observed. Both photmicrographs are from core samples from approximately 3050 mmd.

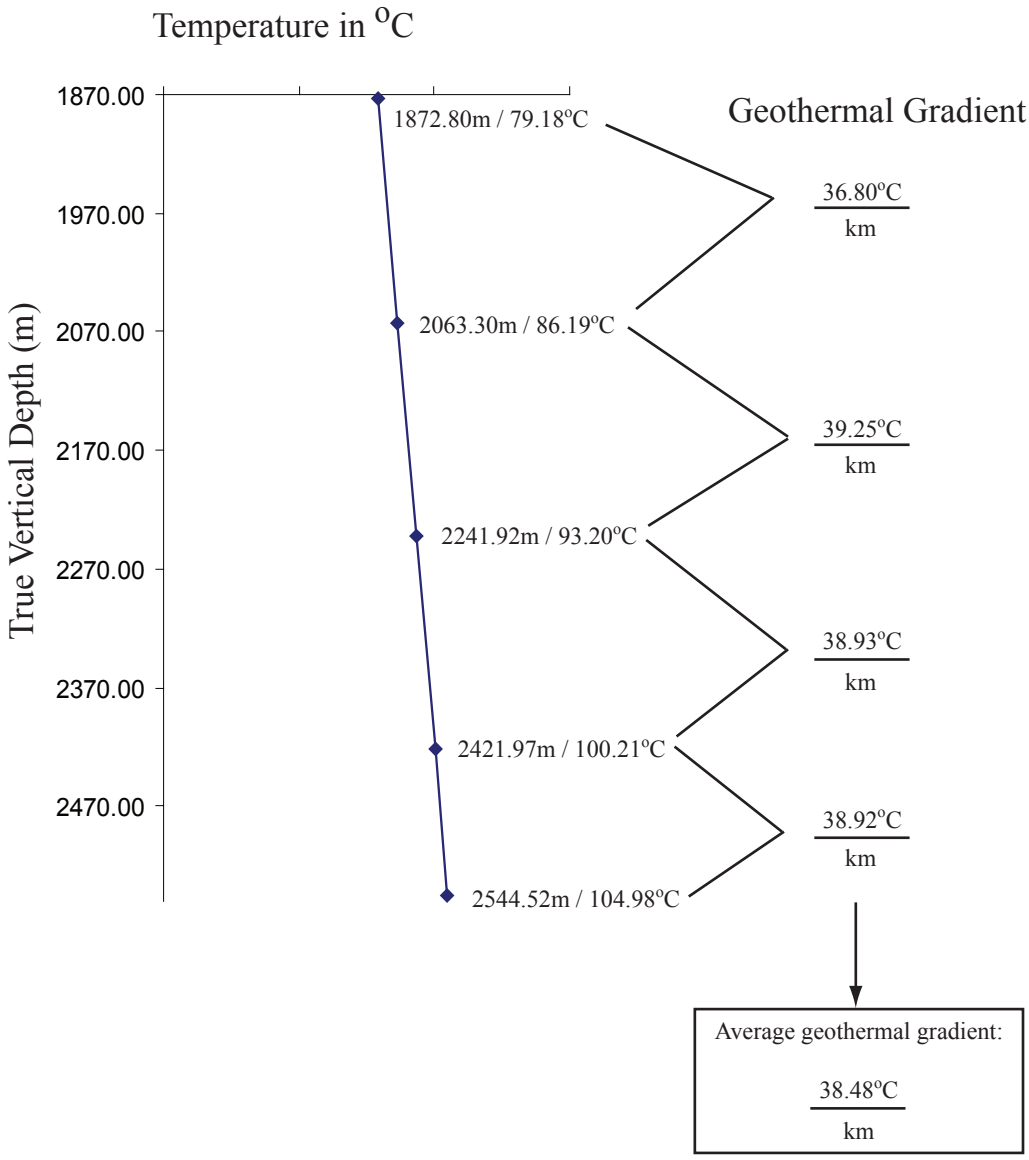

Figure 2.22: Empirically determined temperature gradient. Data are derived from temperatures measured every 3.3 m in the borehole and recorded in degrees Farenheit. Here we convert the temperatures to degrees Celsius and measured depth to true vertical depth in meters. Vertical depths are measured as part of the directional survey performed during drilling of the SAFOD borehole. Temperatures are measured using a temperature tool.

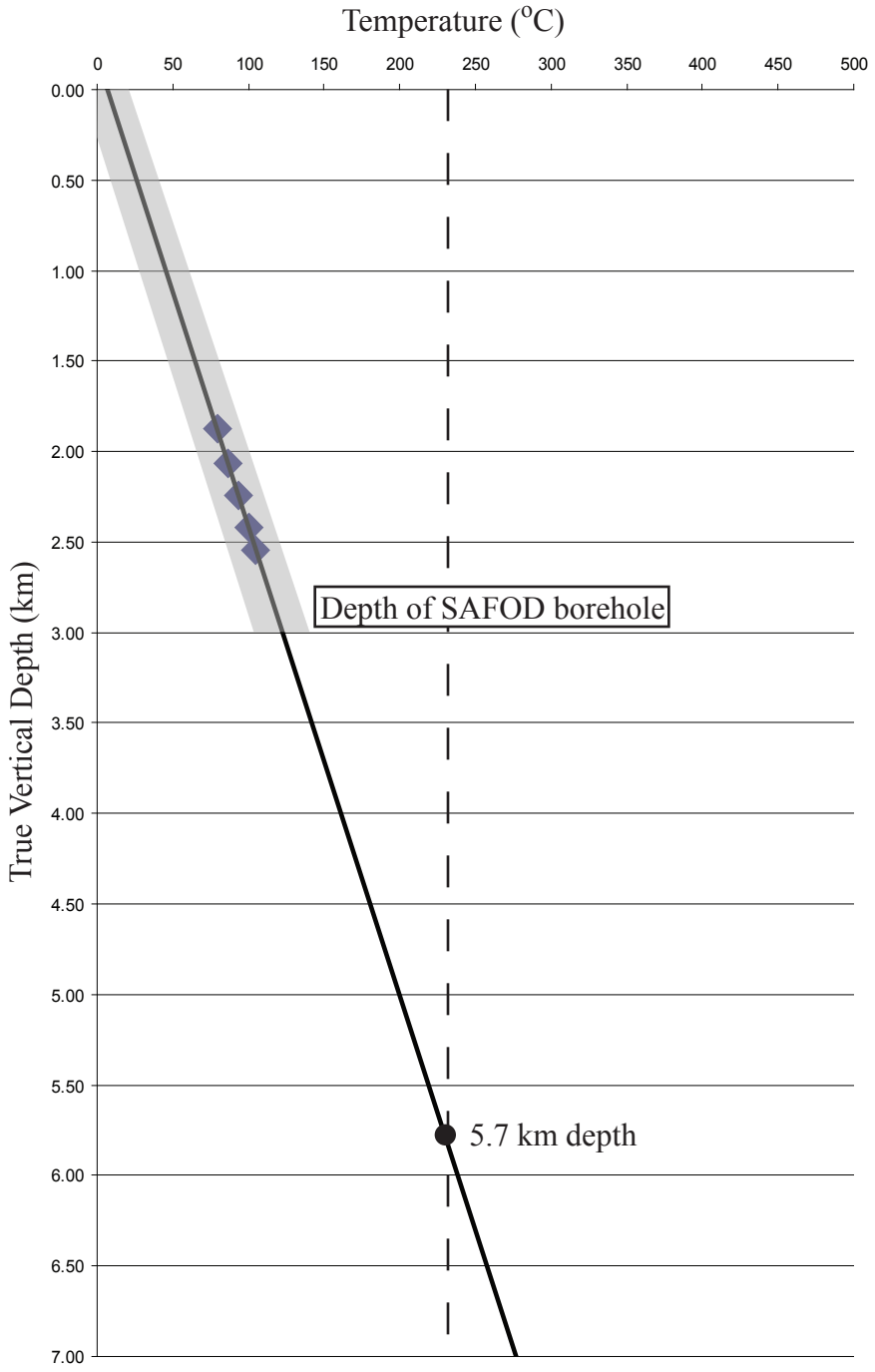

Figure 2.23: Approximate subsurface temperature gradient based on the average calculated geothermal gradient in Figure 2.22, five data points here are those from Figure 2.22. This gradient is used to predict the depths where certain temperatures might be encountered below the borehole. For instance, the annealing temperature of zircon, 240° C, corresponds to a depth of 5.7 km.

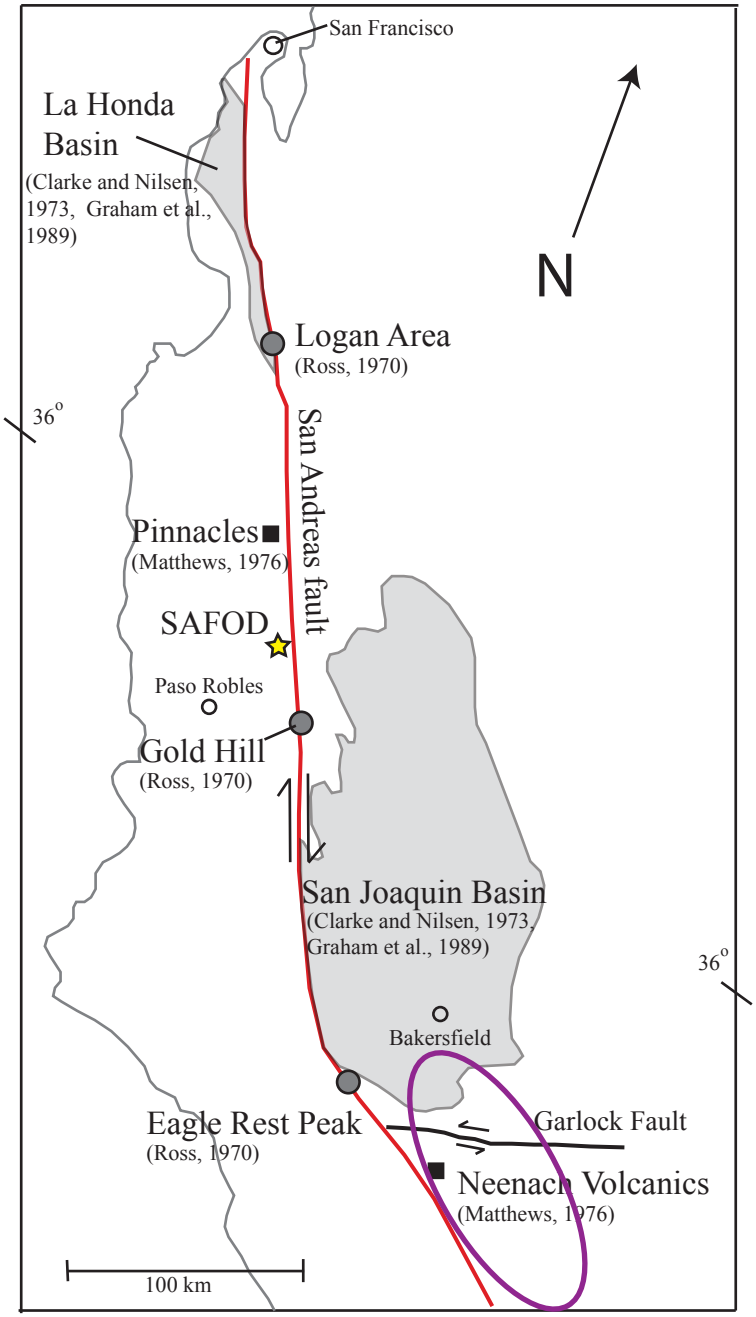

Figure 2.24: Schematic map showing offset units along the San Andreas fault zone. Location of SAFOD drilling site marked by star. Offset points such as Eagle Rest Peak not to scale although basin outlines are to scale. Map modified after Irwin, 1990. Dark ellipse near bottom of map represents the area that is approximately 315 km southeast of the SAFOD site on the opposite side of the SAF.

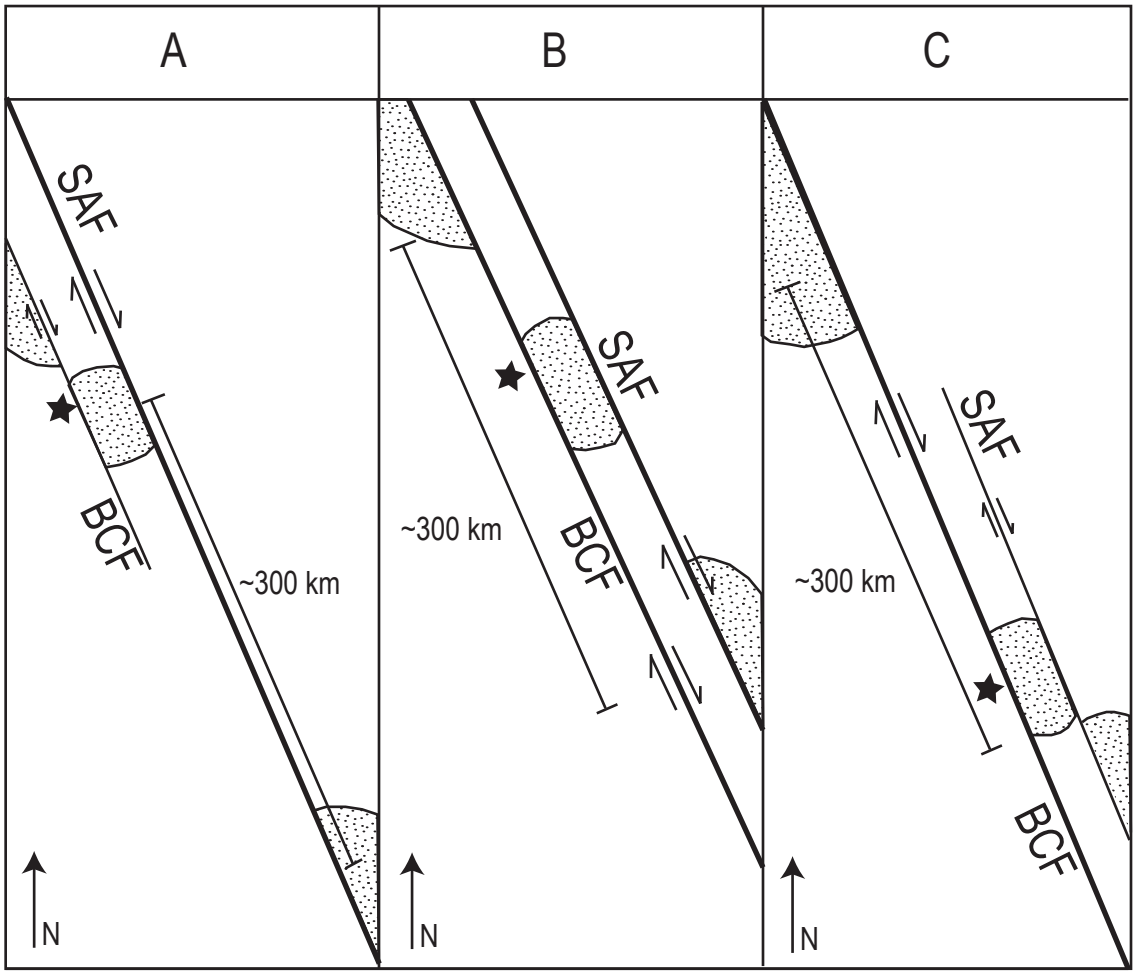

★ = SAFOD site BCF = Buzzard Canyon fault SAF = San Andreas fault

Majority of 315 km slip is along the modern San Andreas fault, Buzzard Canyon fault has a small amount of slip	315 km distributed over both the Buzzard Canyon fault and the modern San Andreas fault	Majority of 315 km slip is along the Buzzard Canyon fault, modern San Andreas fault has a small amount of slip

Location of Sedimentary Rocks Equivalent to the SAFOD Arkoses

~300 km SE and/or small distance NW of SAFOD	Both NW and SE of SAFOD total offset ~300 km	~300 km NW and/or small distance SE of SAFOD

Figure 2.25: Three hypotheses for the tectonic evolution of the San Andreas fault system in the vicinity of the SAFOD site. A sedimentary rock unit correlative to the SAFOD arkoses would be found in a different location depending on which hypothesis is correct. Stippled unit represents the SAFOD arkoses and the equivalent sedimentary rocks.

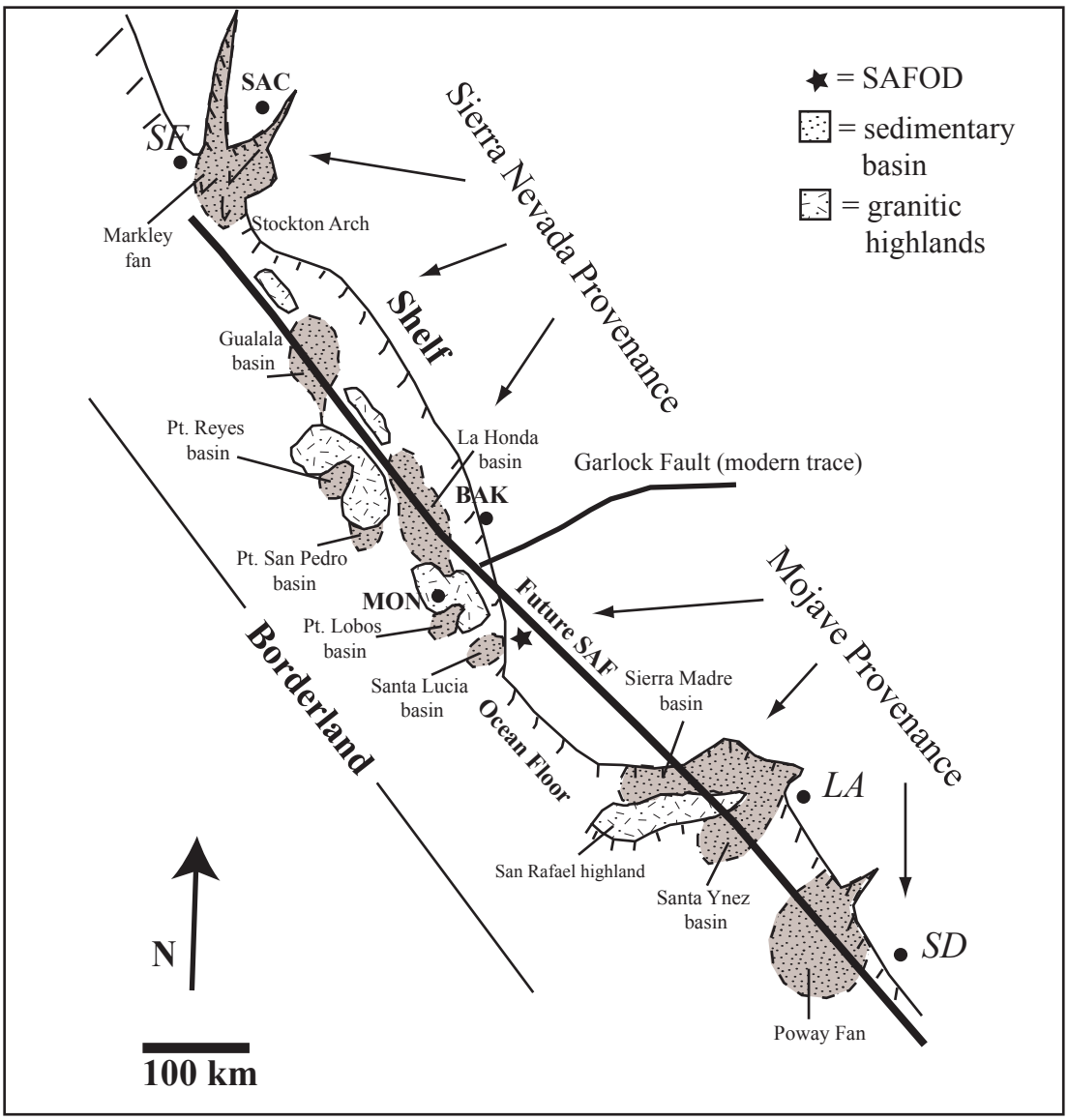

Figure 2.26: Coastal California Paleocene paleogeography model of Nilsen and Clarke, 1975. Based on regional sedimentology, stratigraphy and tectonic models. Modern San Andreas fault is shown for reference. SF = San Francisco, SAC = Sacramento, BAK = Bakersfield, MON = Monterey, LA = Los Angeles, SD = San Diego. Modified after Nilsen and Clarke, 1975 their figure 7.

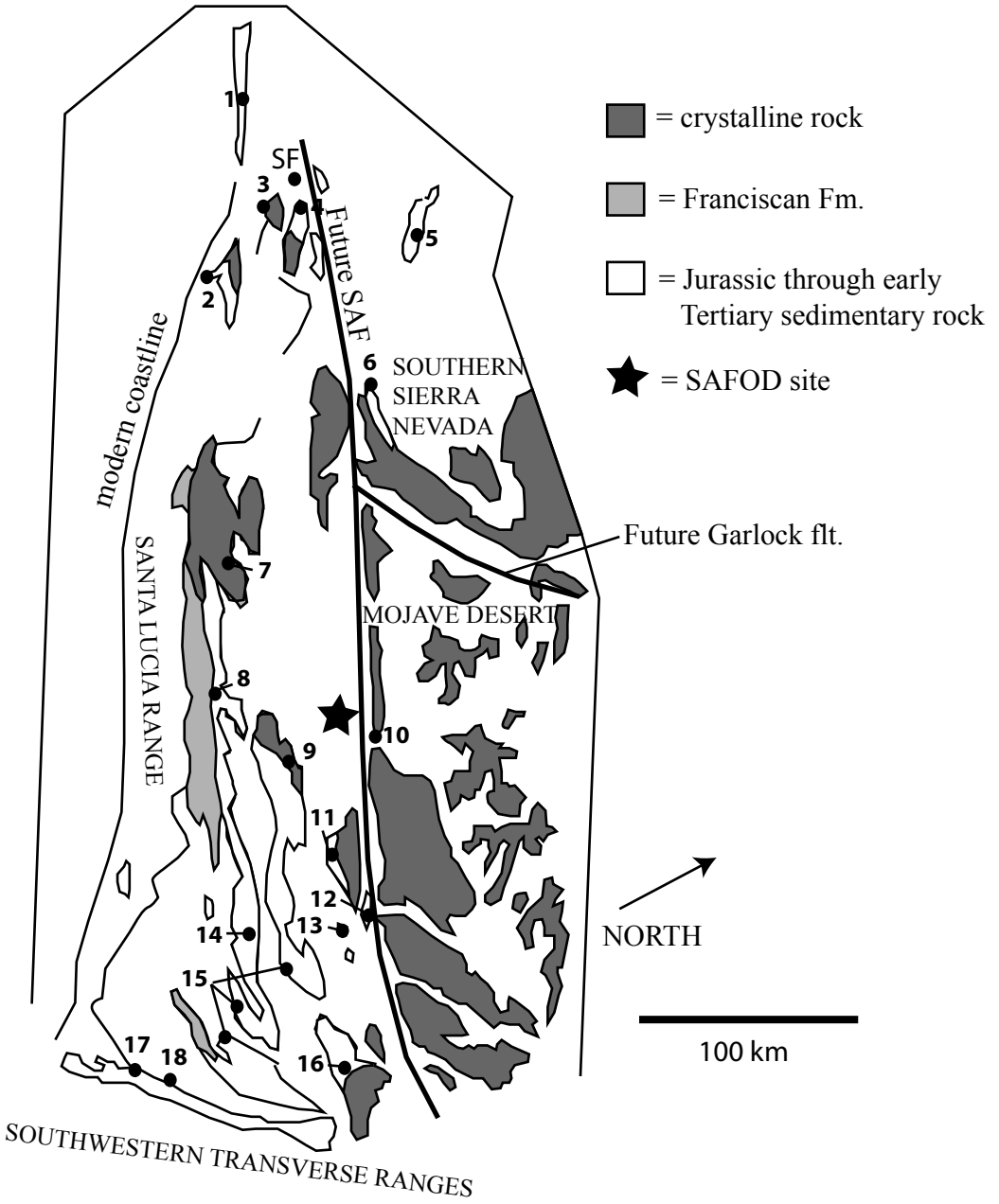

Figure 2.27: Map of crystalline and sedimentary rock outcrops of central California (Transverse ranges mark the southernmost extent of map), palinspastically restored to pre- to early tertiary paleogeography. Modified after Cox and Seiders, 1993 and based on Powell, 1993.
1) Gualala 2) Point Reyes 3) Point San Pedro 4) Santa Cruz Mountains (La Honda Basin) 5) Temblor Range (San Joaquin Basin) 6) Tejon Fm. (San Emigdio Mtns.) 7) Arroyo Seco 8) Central Santa Lucia Mtns. 9) La Panza Range 10) Cajon Pass 11) Liebre Mountain Block 12) Pinyon Ridge Block 13) Caliente Range 14) Stanley Mtn. Area 15) Central San Rafael Mtns. 16) Frazier Mtn. block 17) Santa Ynez 18) San Marcos Pass
Approximate location of SAFOD marked with black star. In present day, SAFOD is north of the La Panza Range and east of the Santa Lucia Range.

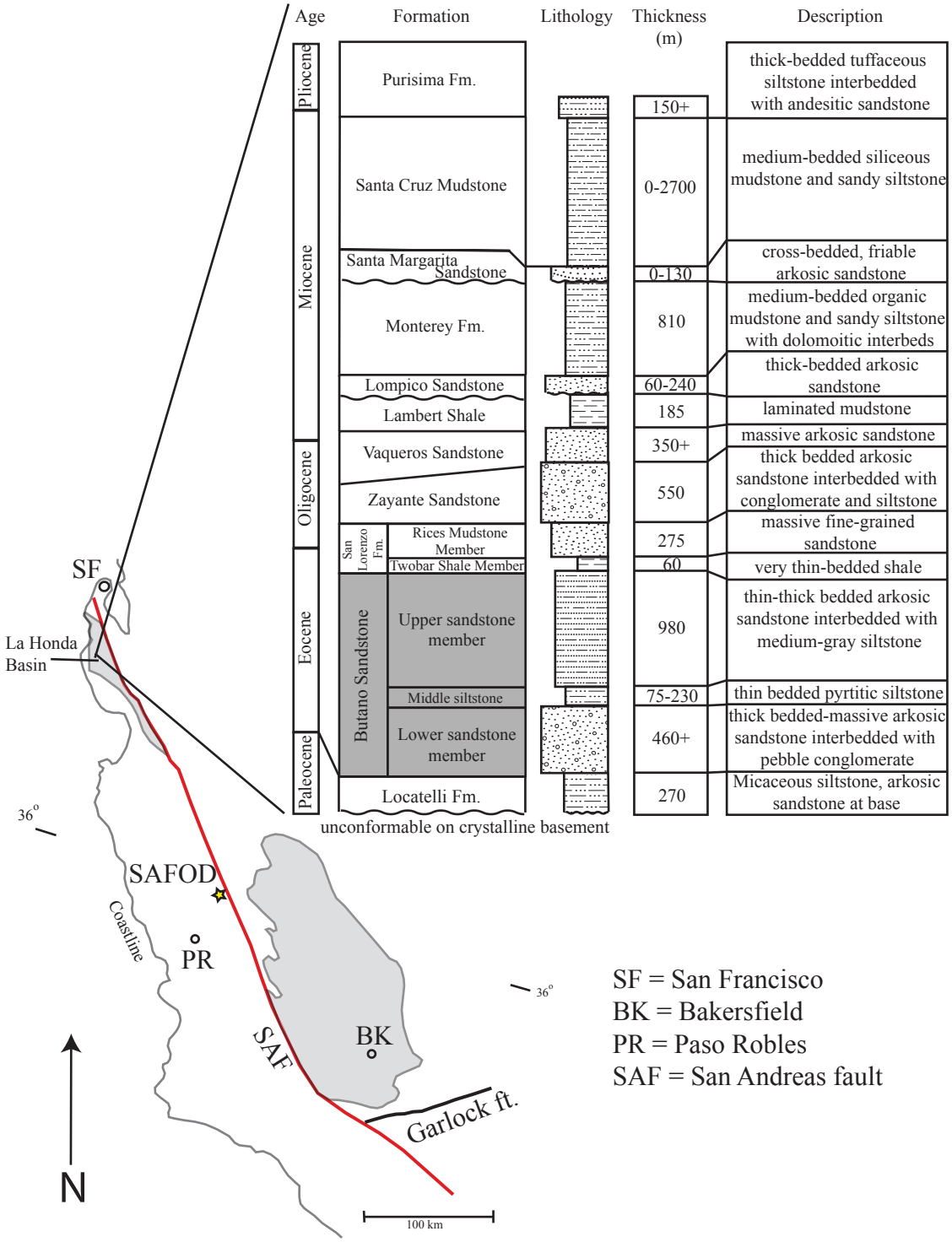

Figure 2.28: Simplified stratigraphic column from the La Honda Basin in the Santa Cruz Mountains of California. Map in lower left corner is from Figure 2.24, this thesis, modified after Irwin, 1990. Stratigraphic column modified after Clark, 1981.

CHAPTER 3

PHYSICAL PROPERTIES, MICROSTRUCTURES, AND DEFORMATIONAL FEATURES OF THREE SUBSIDIARY FAULTS ENCOUNTERED IN THE SAN ANDREAS FAULT OBSERVATORY AT DEPTH (SAFOD) BOREHOLE, CENTRAL CALIFORNIA

ABSTRACT

The San Andreas Fault Observatory at Depth (SAFOD) project provides a unique opportunity to examine fault rocks from active zones of seismicity in the subsurface. We characterize the physical properties, microstructures, and composition of three of the major fault zones out of 12 total identified in an arkosic section of rocks 500-100 meters west of the San Andreas fault encountered in the SAFOD borehole during. Fault zone A is the largest fault. It is correlated to the Buzzard Canyon fault, was drilled at 1920 meters measured depth (mmd) and is approximately 45 m wide, separates Salinian granodiorite on the southwest from the arkosic section on the northeast and contains fine-grained quartzofeldspathic cataclasites and abundant calcite. Fault zone B was encountered in the SAFOD borehole at 2530 mmd, is the medium offset fault localized in a clay-rich sedimentary unit between the upper and lower arkoses and is a diffuse >65 mmd wide low-velocity, high gamma, clay-rich fault zone with numerous sheared clay-filled veinlets. Fault zone B may correlate to a fault mapped at the surface by Thayer and Arrowsmith (2005) on the west flank of Middle Mountain with a dip of 70°SW, parallel to the Buzzard Canyon and San Andreas faults. Fault zone C is the smallest fault and

was cored during phase one drilling at 3067 mmd. It is brittley damaged with little textural or mineralogic evidence of fluid driven alteration and is an intraformational fault within the lower arkose and may be a small fault within the active San Andreas fault zone. These faults zones each have different characteristics, fault zone A contains abundant calcite and iron-oxide alteration and fault zone B has numerous clay-filled veins, features consistent with extensive subsurface fluid flow. Fault zone C does not show evidence of alteration resulting from extensive fluid flow. Generally, textures, degree of alteration and composition observed in the three fault zones are very similar to those observed in exhumed strike-slip fault zones.

3-1 INTRODUCTION

The San Andreas Fault Observatory at Depth (SAFOD) project consists of a 3 km deep (4 km measured depth) inclined borehole drilled across the San Andreas fault (SAF) 5 km north of Parkfield, California. The primary objective of SAFOD is to study active-fault processes at the depth of earthquake nucleation. By necessity, fault studies have often centered around inactive exhumed faults or active faults at or near the surface (i.e. Flinn, 1977; Chester and Logan, 1986; Chester et al., 1993; Little, 1995; Schulz and Evans, 2000; Evans et al., 2000; Wibberly and Shimamoto, 2003; Faulkner et al., 2003; Chester et al., 2005a and b). The SAFOD project provides the unique opportunity to study the San Andreas fault in the subsurface and other subsidiary faults encountered in the SAFOD borehole.

Faults can be difficult to identify in borehole studies because: 1) even fault zones with relatively large offsets can have slip surfaces too narrow to detect with most subsurface methods, 2) fault-related rocks and other fine-grained rocks often have similar physical properties, making it difficult to distinguish between a clay-gouge along a fault zone and a sedimentary shale layer and 3) the only method of examining whole fault zones is by recovery of core. It is very difficult to obtain core of faulted rock. Brittle fault zones have been shown to have gouge zones on the scale of centimeters wide (i.e. Flinn, 1977; Chester and Logan, 1986), a small area when examining the extent of the 4 km long SAFOD borehole. Studies of exhumed faults show that a fault zone proper, composed of fault core containing one or more slip surface, primary damage zone and secondary damage zone (i.e., Sibson, 1977; Forster and Evans, 1991; Scholz and Anders, 1994; Chester et al., 1993), is typically wider and more extensive than the primary slip surface alone (Chester et al., 2005a). Projecting the exhumed fault architecture model to the subsurface, we can examine the entire fault zone even if a primary slip surface is too small to be precisely identified in a borehole study. Furthermore, we can maximize the return on our analyses by using several datasets to evaluate subsurface fault zones, filling the gaps in understanding that may result when utilizing datasets individually.

In this study, we use petrography of cuttings and core collected during the first phase of SAFOD drilling in combination with borehole-based geophysical logs and electrical resistivity image logs to characterize three subsidiary fault zones with different amounts of displacement. These three zones were identified as faults in previous studies (Solum et al., 2006; Boness and Zoback, 2006; Bradbury et al., in review). Identification of faults was based on abrupt decreases in compressional and shear velocities (Boness

and Zoback, 2006), juxtaposition of two distinctly different lithologic units (Boness and Zoback, 2006; Solum et al., 2006; Bradbury et al., in review), changes in clay mineralogy (Solum et al., 2006), and increases in cataclasite and grain-scale alteration (Bradbury et al., in review). Over a 1230 meters measured depth (mmd) section of the borehole, a total of 12 faults were inferred from changes in lithology, bedding orientations, amount of deformational features observed and geophysical indicators such as low velocity, high gamma ray and porosity (Chapter 2, this thesis) (Figure 3.1). We focus on faults located at 1920 mmd, 2530 mmd, and 3067 mmd (Figure 3.1). The three faults were selected because data coverage is most complete in those areas but also because each is distinctly different in character and scale of offset based on disparity of rock types juxtaposed across the fault plane. We characterize in detail the style and extent of deformation in each fault zone and compare these features to models of fault zone architecture developed from surface outcrop studies (i.e. Chester et al., 1993). Our primary goals are to gain a better understanding of how the character of fault zone constituents may change with exhumation and how the faults of the SAF system have evolved.

We also use the information obtained here as another step towards establishing a structural framework for the subsurface of the SAFOD site. Subsequent studies at the SAFOD site will rely heavily on subsurface structural models, therefore understanding the nature and distribution of subsidiary faults in the SAFOD borehole is very important to the success of future studies.

These small-scale studies are important for addressing the mechanical paradox of the SAF. The orientations of the maximum horizontal stress along the San Andreas fault

has consistently been shown to be at an anomalously high angle to the SAF plane (Mount and Suppe, 1987; Zoback et al., 1987; Townend and Zoback, 2004), indicating that the fault moves under very low shear stresses (Zoback et al, 1987; Townend and Zoback, 2000). Preliminary results from shear wave anisotropy studies in the SAFOD borehole show that the maximum horizontal stress continues to be nearly orthogonal to the SAF plane through the borehole (Hickman and Zoback, 2004) but the stresses are rotated to a shallower angle within the active San Andreas fault zone at 3295 mmd (Boness et al., 2005; Zoback et al., 2005; Boness and Zoback, 2006). The lack of a heat anomaly along the strike of the fault (Lachenbruch and Sass, 1980, 1992; Williams et al., 2004) also indicates that the fault has a low shear strength. These observations have led to the hypothesis that the SAF is anomalously weak while the surrounding crust is strong (i.e. Zoback et al., 1987; Hickman, 1991), but the reason for this behavior remains unkown. Hypotheses proposed to explain this behavior include the presence of inherently weak minerals in the fault zone (Moore and Byerlee, 1992; Reinen et al., 1994; Moore and Rymer, 2006), locally high pore pressures in the fault zone (Rice, 1992; Byerlee, 1990), or a set of dynamic slip weakening processes (Heaton, 1990). By providing direct observations of fault materials, we can constrain the processes in the fault zone and thus contribute to the larger study of the mechanical paradox of the San Andreas fault.

Description of Fault Zones from Previous Studies

Lithologic and structural characterization of the rocks encountered in the SAFOD borehole has been conducted using several different approaches. Solum et al. (2006)

examined the bulk mineralogy of the borehole through X-ray diffraction with an emphasis on the mineralogical properties of fault zones. Solum et al. (2006) divided the borehole into six lithologic units based on distinct mineral assemblages and a total of five shear zones at 1360, 1926, 2545, 3067 and 3300 mmd identified using variations in clay mineral phases present. Bradbury et al. (in review) conducted a broad microscopic reconnaissance of cuttings from both the SAFOD pilot and main boreholes and inferred the presence of six shear zones at 1050, 1600, 2300, 2700, 3050, and 3500 mmd based on the abundance of cataclastically deformed cuttings and the nature and abundance of alteration phases observed. Boness and Zoback (2006) evaluate the physical properties of the borehole through wireline and image logs, also identifying five shear zones at similar depths as Solum et al. (2006) and Bradbury et al. (in review) based on decreases in velocity, increases in gamma ray and/or increases in porosity measured by a variety of borehole based geophysical tools. Petrographic and geophysical datasets show that 12 different faults divide disparate dip domains within the 1230 mmd long arkosic section (Chapter 2, this thesis). The arkosic section is a well-indurated sequence of rocks up to 500-600 m thick that is composed of granite-rich conglomerate, sandstone and siltstone (Chapter 2, this thesis). Here we focus on three of those 12 faults. We refer to the fault at 1920 mmd as fault zone "A" (FZA), the fault at 2530 mmd as fault zone "B" (FZB) and the fault at 3069 mmd as fault zone "C" (FZC) (Figure 3.1).

Fault zone A, at 1920 mmd, separates Salinian granodiorite on the southwest from arkosic sedimentary rocks on the northeast (Figure 3.1). Bradbury et al. (in review) suggests that FZA is equivalent to the nearly vertical Buzzard Canyon fault (BCF) mapped at the surface by Thayer and Arrowsmith (2005) and M. Rymer (written com.,

2005). The steep southwest dip of FZA is inferred by Bradbury et al. (in review) by connecting the surface trace of the BCF with the fault in the borehole because the lithologic transition from Salinian granodiorite to arkosic sedimentary rocks is not observed in the 2.2 km deep vertical SAFOD pilot hole drilled in 2002. Fault zone A is a quartz and feldspar rich fault zone with 1-6 weight % clay minerals (Solum et al., 2006), with anomalously low resistivities and velocities (Boness and Zoback, 2006) with no increase in gamma ray (Boness and Zoback, 2006).

Fault zone B, beginning at 2530 mmd and extending to somewhere between 2565-2680 mmd, is a zone significantly richer in clay minerals than the arkosic rocks on either side (see Chapter 2, this thesis). Solum et al. (2006) define it as a fault zone due to the abundance of mixed layer phases of illite-smectite (9-14 weight %), a mineral phase they associate with faulting. Boness and Zoback (2006) assign the fault zone a slightly deeper depth of 2550 mmd, because that depth corresponds to porosity and gamma ray peaks and a decrease from ~5 km/sec to 2-3 km/sec in Vp.

Fault zone C, at 3067 mmd, is a shear zone that was cored during SAFOD phase one coring in the arkosic sedimentary rocks. It is an approximately 61 cm wide (in the inclined borehole measured dimension); clay-rich zone composed of sheared grains with smectite and mixed layer illite-smectite coatings (Schleicher et al., 2006). Tembe et al., (2005) show that fault gouge from FZC has a lower coefficient of friction ($\mu = 0.42$-0.5) than cuttings collected from that depth ($\mu \sim 0.6$) but similar to other shear zones. It is suspected that FZC may be the southwestern active strand of the SAF and may be generating a cluster of microearthquakes (Hickman and Zoback, 2004; Hickman et al., 2005). Because FZC may be one of three active strands of the SAF and it provides an

opportunity for whole-rock analysis, FZC was extensively studied by other workers (i.e. Tembe et al., 2005; Solum et al., 2006; Schleicher et al., submitted). The objective of our study of FZC is to characterize the damage zone of the fault because it has not been the focus of other efforts.

3-2 METHODS

In Chapter 2, we describe in detail our sampling and processing procedures for cuttings, core, wireline logs and image logs. Here we use the same datasets to interpret the structural features of the three major fault zones located in the SAFOD arkoses. Some results from that chapter, such as cuttings composition, will be referenced in this chapter but with applications to the structural framework rather than the objectives of chapter two. Nomenclature from Chapter 2 for the classification of lithologic units, for example differentiation between the upper arkose, clay-rich zone and lower arkose, will be preserved in this chapter. In this section, we will discuss any methodologies utilized in this paper which differ from Chapter 2.

We analyzed petrographic thin sections of cuttings at 3 m intervals through FZA, 1920 mmd to 1935.48 mmd, quantifying deformational features such as cataclasite, calcite, zeolite, and iron-oxide alteration. A similar petrographic method was employed through FZB, examining thin sections of cuttings every 3 m from 2545.08 mmd to 2560.32 mmd although thin sections of cuttings from 2530 mmd to 2545 mmd were not available for this study. Aside from the interval between 2545-2560 mmd, petrographic thin sections were analyzed every 15 m through FZB.

We analyzed porosity, density, gamma ray, spectral gamma ray and Vp logs through both fault zones A and B. The Vp log is the only log that is not continuous through the entire arkosic section. Intervals where velocity was not measured successfully, if present, are noted in each individual fault zone analysis.

Electrical image logs are available through the entire arkosic section but the data are poor in quality through portions of FZA and all of FZB (Chapter 2, this thesis). However, intervals of very good data quality allow us to make both bedding and fracture interpretations above and below both FZA and FZB. We use the image logs to map out the distribution and character of fracture sets in the rocks adjacent to the fault zones. Fracture densities are defined based on a relative scale for the arkosic section where the interval with the most fractures over a 10 meter interval is the highest fracture density and the interval with least fractures per 10 meters is the lowest fracture density (Table 3.1).

FZC is the only fault zone where whole rock samples are available. The phase one spot core collected from 3055.62 mmd to 3067.9 mmd is 11.3 m long. FZC is located at the deepest portion of the core making 11 m of damage zone available for analysis. Neither wireline logs nor image logs are available through the cored interval. Image logs are good in quality to 3030 mmd, 39 m southwest of FZC and the various wireline logs end measurements at different depths depending on the tool's location along the drill string. Despite the lack of geophysical data, FZC is the fault zone that is most directly comparable to exhumed exposures of faults simply because whole rock samples were recovered.

3-3 RESULTS

Fault Zone A

Fault zone A, at 1920 mmd, separates granodiorite from arkosic sedimentary rocks (Boness and Zoback, 2006; Solum et al., 2006; Bradbury et al., in review; Chapter 2, this thesis). This is apparent in both image logs, which show distinctly fractured granite changing to less distinct, disorganized rock, and in cuttings samples which contain similar amounts of quartz and feldspar on both sides of the 1920 mmd transition, but show the disappearance of amphiboles and biotite below 1920 mmd. There is a subtle change in physical properties in the wireline logs (Boness and Zoback, 2006) (Figure 3.2), that could be attributed to the change from granodiorite to sedimentary rock rather than the presence of fault rocks.

Several lines of evidence lead us to believe the contact between the granodiorite and sedimentary rocks is a fault. The change in character of the rocks is abrupt, occurring over centimeters. The steep dip of the contact inferred by Bradbury et al., (in review) and seismic data (Bleibinhaus et al., 2006) and the age interpreted for the deeper arkosic sedimentary rocks (Chapter 2) which is younger than the granodiorite in the borehole would be highly unusual for a depositional contact. It implies a >90° of northeastward tilting of the crystalline fault block and we consider that to be unlikely.

At 1920 mmd cataclasite composes 25.67 weight % of the sample but by 1929.38 mmd there is only 6.09 weight % cataclasite observed (Figure 3.2). However, by 1965.96 mmd, 31.13 weight % of the sample is cataclasite. The cataclasite is very fine grained with small round porphyroclasts of quartz entrained in fine-grained nearly

isotropic matrix (Figure 3.3). The lack of color in the cataclasite grains in either cross- or plane-polarized indicates that there are no clay minerals present in the matrix (Figure 3.3). This quartz-rich cataclasite is similar to that observed in other quartz-rich faults zones such as the Punchbowl fault in the Transverse Ranges of California, where crystalline basement rock is faulted against the Miocene Punchbowl Formation (i.e. Chester and Logan, 1986).

Fracture density analysis from image logs show a fracture density of 25 fractures per 10 m from 1940 mmd to 1950 mmd (Figure 3.4). Image logs from 1920 mmd to 1935 mmd were blurry due to bad data retrieval, so fractures could not be interpreted above 1935 mmd. The fractures are random in orientation. The less faulted parts of the upper arkose has a fracture density of 5-10 fractures/10m (Figure 3.4). By 1960 mmd fracture density has dropped to low levels. The high fracture density from 1935 mmd to 1950 mmd corresponds to an increase in cataclasite to 11-12 weight % of sample, although the sample with the largest amount of cataclasite and calcite, 1965.96 mmd, corresponds to a low fracture density with only 2 fractures/10 m. This is an interesting observation in that it indicates that the 31.13 weight % cataclasite and 10.67 weight % calcite at 1965.96 mmd is not associated with imageable fractures. We interpret 1965.96 mmd to be an area of localized deformation, perhaps the zone where the majority of slip has been accommodated. Due to the elevated amount of cataclasite and high fracture density we interpret 1920-1965.96 mmd to be the damage zone of FZA. The rock below 1965.96 mmd has a moderate fracture density (Figure 3.4) with moderate amounts of cataclasite (Figure 3.2), implying that the amount of deformation is not symmetrical, there is more deformation above 1965.96 mmd than below.

Fault Zone B

Between 2530 mmd to 2680 mmd is a zone containing high concentrations of clay minerals and clay-sized particles. FZB is associated with this clay-rich zone and may be a fault zone within the larger clay-rich zone or may encompass the entire clay-rich zone. Boness and Zoback (2006) defined this zone as a thin 15m fault zone from 2550 mmd to 2565 mmd with sandstone and shale units below until 2680 mmd. Their interpretation is based on the dramatic increases in gamma ray and porosity and decreases in velocity and density measured between 2550-2565 (Figure 3.5), and a return to typical values for sandstone from 2565-2595 mmd. From 2595-2680 mmd the gamma ray and porosity increases and velocity decreases, but these changes are less pronounced than between 2550-2565 mmd. Solum et al. (2006) observed the characteristically fault-related mixed layer phase clay minerals from 2550 mmd to 2720 mmd, although they only define the fault zone proper to be between 2545-2560 mmd.

We define the clay-rich zone to extend from 2530 mmd to 2680 mmd with a small block of sandstone at 2565 mmd to 2595 mmd (Chapter 2, this thesis). This definition is based on the amount of clay observed in the cuttings samples, where the amount of clay jumps from 11weight % at 2529.84 mmd to 30weight % at 2545.08 mmd (there are no samples analyzed between these two depths). It is at 2530 mmd that the image logs are no longer interpretable and this continues until 2680 mmd. We attribute the poor quality of data to the poor condition of the borehole. This entire section the borehole is greatly enlarged, at times beyond the maximum extent of the caliper tool (plate 1). The only area where the data are somewhat clear (but still relatively poor quality) is from 2565 to 2595

mmd. The poor condition of the borehole is likely due to the very soft, easily erodable lithologies in that zone. This interpretation is verified by the cuttings composition, which show 40-60% of cuttings to be clay-rich in nature with little discrete quartz or feldspar.

In Chapter two we suggested the rocks in FZB are a separate lithologic unit from the upper and lower arkoses, possibly an overbank deposit or deeper-water mudstone with a localized narrower fault zone. 150 meters is especially thick for a fault zone, but geometries involved with deviated boreholes can exaggerate the width of features (figure 3.9). Here we examine the evidence for and against the presence of a fault in the clay-rich unit.

The clay-rich unit lacks a significant cataclasite component and has a maximum of 9.33 weight % cataclasite at 2651.76 mmd (Figure 3.5). Amounts of calcite vary, but are generally higher than in other parts of the arkosic section. The highest levels of calcite are found in the area that Boness and Zoback (2006) and Solum et al. (2006) defined as a fault zone. Calcite noticeably increases when there is also an increase in iron-oxides. Both calcite and iron-oxides peak at 2257.27 mmd with 13.48 weight % and 16.29 weight % of sample, respectively.

While image logs are uninterpretable through the clay-rich zone, the image quality is quite good above and below. The highest fracture density of the entire arkosic section is from 2500-2510 mmd: 26 fractures/10m (Figure 3.4). The fracture density stays high until the beginning of the poor data section at 2530 mmd. Below the clay-rich zone, fracture density is moderate, a trend which persists for the majority of the lower arkose rock volume. The fractures in the high density zone immediately above the clay-

rich zone are generally discrete electrically conductive features without systematic orientation.

Although very few grains of distinct cataclasite were observed, there is still evidence of deformation in cuttings from the clay-rich zone. The majority of cataclasite observed is foliated with a component of iron-oxide alteration (Figure 3.6a), a feature not observed in the cataclasite from FZA. Some grains are filled with anastamozing clay or iron-oxide filled fractures (Figures 3.6a and b). In some cases, veins display cross-cutting relations showing several episodes of deformation (Figure 3.6c). Sigmoidally sheared veins in a fine-grained matrix are also observed (Figure 3.6d). The material filling veins may be clay minerals, but the isotropic character of the vein fill may indicate the presence of ultracataclasite.

These deformational features are not observed in cuttings below 2565 mmd where the majority of clay-rich grains are similar to those in figure 3.4e. The undeformed clay-rich grains of figure 3.6e share similar compositonal and morphological characteristics with the clay-rich grains observed from 2530-2565 mmd, but without deformational features like those in figures 3.6a-d.

Based on the fracture densities and observed deformational features, in combination with the wireline log signatures identified by Boness and Zoback, (2006), we interpret FZB to extend from 2530-2565 mmd. The similarity of composition and character of the clay-rich fraction between the 2530 zone and the 2595 zone supports the hypothesis that these zones belong to a larger lithologic unit. We believe that FZB formed within a clay-rich lithologic unit and therefore produced a fine-grained fault zone with clay-rich veins and micro-shears and few quartz-rich cataclasites or easily

identifiable ultracataclasites. Similar features were observed by Isaacs (2005) and Ohtani et al. (2001) in core collected from the fine-grained Mozumi and Nojima fault zones (respectively) of Japan.

Fault Zone C

Our analysis of FZC is quite different than that of FZA and FZB because the primary dataset are whole-rock samples from the phase one spot core. No useable image logs were recovered from the cored interval. Wireline logs data were collected through the cored interval the following year, but we do not use those data because hole conditions between 2004 and 2005 may have changed drastically.

A 10.16 cm diameter core was collected from 3055.62 mmd to 3067 mmd during phase one in the summer of 2004. A complete description of the mesoscopic structure and lithology of the core can be found in Almeida et al., 2005 and on the SAFOD website: www.safod.icdp-online.org. The 61 cm wide clay-rich shear zone at the bottom end of the cored interval has been the topic of numerous studies (i.e. Tembe et al., 2005; Solum et al., 2006; Schleicher et al., submitted), but the rest of the core has not been studied. We examined 16 petrographic thin sections constructed from discrete pieces of the core. Several thin sections are constructed from the same sample but different faces or orientations. An index of samples and their lithologic description from hand sample analysis can be found in Table 3.2. Sample numbers inversely reflect distance from the shear zone; samples with larger numbers are closer to the shear zone and are therefore northeast and deeper samples with smaller numbers (Table 3.2)

The greatest amount of damage is observed in the coarse-grained samples, MHP1_B11-MHP1_B17. The fine-grained samples, despite their proximity to FZC, show little detectable deformation (Figure 3.7a). Clasts within the siltstone matrix are angular (Figure 3.7a) but do not show grain-scale fracturing or dilation as in the coarse-grained samples. There is little evidence for fluid flow and alteration through the fine-grained samples both in thin section and in hand sample (Figure 3.7a). Hand samples are particularly indurated and nonfissile in habit, so much so that the samples did not need to be epoxied during thin section construction.

The coarse-grained portions of the core consistently show evidence for episodes of dilatancy which have produced grain scale brecciation (Figures 3.7b and c). The grains in figures 3.7b and c have undergone repeated fracturing and grain size reduction, but there is little evidence for the rotation required for cataclasis (i.e. Engelder 1974; Sibson, 1977). The fractured and brecciated quartz grains display symmetric extinction in cross-polarized light, implying that after the fracturing which broke the grain apart occurred, the individual pieces of that grain have not been rotated from original orientation.

In some areas of the core, this grain-scale brecciation is accompanied by iron-oxide infill and cementation (Figure 3.7d) while in other areas there is little evidence at all for fluid flow and alteration. For the most part, feldpars are unaltered (Figure 3.7e) and iron-oxides cements and veins are localized (Figure 3.7f). Calcite is rarely found in the core. The few places calcite is observed it is very localized, cementing two to three fine sand sized grains together (Figure 3.8a). The most pervasive cementation is iron-

oxide, which is relatively common through the entire arkosic section and is not confined to the core or to fault zones.

The localization of the iron-oxide alteration is more apparent in penetrative fractures which cut an entire rock volume, such as the fracture observed in the MHP1_B16 hand sample (Table 3.2). In thin section that fracture is filled with a combination of a cataclastic matrix stained red from iron-oxide content and highly fractures angular grains of wall rock (Figure 3.8b). The fracture is a grossly linear feature, but microscopically the fracture varies in width and orientation and anastamozes through the thin section (Figure 3.8b and d). There are similar, but more diffuse, deformational features in MHP1_B14 (Figure 3.8c). There the cataclastic matrix texture is not localized within a fracture but is spread throughout the sample, but in places abruptly transitions into less deformed rock. In the case of MHP1_B14, the cataclastic matrix is not as strongly stained with iron-oxides as in the fracture fill.

Fracture analysis shows an elevated fracture density for the 100 meters above FZC (FIG 3.4). There are three 10 m intervals where the fracture density is considerably higher than the rest of the lower arkose section. This zone of high fracture density is wider than for that associated with FZA and FZB and may be a product of more complex distributed deformation than a direct result of FZC alone.

3-4 DISCUSSION/ANALYSIS

The three fault zones examined here are drastically different from each other in scale and composition. The entirety of FZA is, at most, 45 meters wide in the measured

dimension and is composed of quartz and relatively unaltered feldspar with high levels of quartz-rich cataclasite. FZA is the fault with the largest amount of offset because two distinctly different lithologies, granodiorite on the southwest and arkose on the northeast, are juxtaposed across the fault zone. FZB, at least 35 meters wide in the measured dimension, developed in a clay-rich lithologic unit and is composed of sheared and deformed clay minerals with high levels of calcite but very little cataclasite. FZB juxtaposes the upper arkose on the southwest against the clay-rich unit and lower arkose to the northeast and is considered to have an amount of offset intermediate between FZA and FZC. FZC, with a primary slip surface 61 cm wide in the measured dimension and a damage zone at least 11 m wide in the measured dimension but perhaps wider, is brittlely deformed with little evidence of fluid flow in the damage zone. Lithologies on either side of FZC are very similar, both part of the lower arkose, therefore FZC has the smallest amount of offset of the three studied faults.

Compositionally, the setting of FZA is very similar to the Punchbowl fault of Southern California. The Punchbowl fault is an extinct, exhumed trace of the SAF which has been extensively studied in macro- and microscopically (i.e. Chester and Logan, 1986; Chester and Chester, 1998; Schulz and Evans, 1998). In some locations, the Punchbowl fault juxtaposes the Miocene/Pliocene Punchbowl Formation, composed of arkosic conglomerates, sandstones and siltstones, against crystalline basement rocks (Chester and Logan, 1986). There, the fault zone is relatively simple, composed of a main gouge zone, a damage zone and undamaged country rock (Chester and Logan, 1986; Chester and Chester, 1998). Microfractures in the Punchbowl fault zone have been

observed to follow a preferred orientation and increase in density with proximity to the ultracataclasite layer in the fault core (Wilson et al., 2003).

Due to the limits of the data, we cannot precisely determine the width of the different components of FZA. We interpret a zone of localized deformation at 1965.96 mmd where the highest levels of cataclasite and calcite were observed. In the Punchbowl fault zone, calcite cementation was only observed immediately adjacent to the fault core (Chester and Logan, 1986). There appears to be a larger amount of deformation from 1920-1965.96 mmd, above the zone of localized deformation at 1965.96 mmd than below, implying an asymmetric fault zone. Fault zone width may be related to composition, with quartzofeldspathic fault zones such as FZA undergoing a certain amount of strain weakening associated with extreme deformation localization (Chester and Logan, 1986; Faulkner et al., 2003).

With exhumation, the rock in and around a fault zone will become more fractured due to unloading processes (i.e. Chester and Logan, 1986). The width of the Buzzard Canyon fault at the surface is unknown and we have established the subsurface width of FZA to be at least 45 m wide in the measured dimension. The correlation of FZA to the Buzzard Canyon fault predicts a dip of approximately 80º to the southwest (Bradbury et al., in review), similar to the 83ºSW dip of the active San Andreas fault plane. This implies that the fault intersects the borehole at an angle slightly less than 90º, which would produce a fault zone width which is slightly exaggerated (Figure 3.9). Therefore, the true width of FZA is likely a little less than 45 meters wide.

Fault Zone B provides an opportunity to study a deep clay-rich fault zone in the subsurface. Clay-rich fault zones at the surface are quickly eroded and degraded, limiting

the ability to study in situ fault rock structure (i.e. Isaacs, 2005). Other fine-grained fault zones have been drilled in the past (for example, the Chelungpu fault zone in Taiwan, see www.chelungpu.icdp-online.org), but not to as great of depth as FZB.

There are two possible interpretations of the nature of the relationship between the clay-rich zone from 2530-2680 mmd and FZB: 1) The entire clay-rich zone, 2530-2680 mmd, is a fault zone which separates the upper and lower arkoses or 2) FZB extends from 2530-2565 mmd and developed in an already clay-rich, fine-grained lithologic unit. Fault zones that develop in fine-grained rock and contain significant amounts of phylosilicates undergo strain hardening, which could result in the distribution of deformation over a wider area (Faulkner et al., 2003). An example of this process is found in the Carboneras fault of southeastern Spain, a right-lateral fault which has experienced 40 km of offset (Faulkner et al., 2003). The Carboneras fault zone is approximately 1 km wide with several gouge zones interspersed with blocks of damaged country rock (Faulkner et al., 2003). The structure of FZB may be similar, where deformation is distributed over a 35 m and an 85 m wide zone (2530-2565 mmd) with a 28.7 m thick block of country rock (Chapter 2) incorporated from 2565-2595 mmd. Deformation of clay-rich grains was only observed in the first clay-rich block (2530-2565 mmd) but because samples are widely spaced in the lower clay-rich block we cannot rule out the possibility that more deformation occurred in that block.

The incorporation of wall rock into a fault zone is a rare occurrence (Chester et al., 2005a), a block as large as 28.7 m thick may simply be a depositional feature. The gamma ray and porosity log values are higher and velocity values lower from 2530-2565 mmd than in the clay-rich zone below, 2595-2680 mmd. This could indicate that the

zone from 2530-2565 mmd contains both clay-rich country rock and fault gouge while 2595-2680 mmd contains clay-rich country rock without any fault gouge. In FZB it is difficult to differentiate between the physical properties of clay-rich rock and fault gouge. To what degree are changes in wireline logs a result of the presence of clay fault-gouge versus clay-rich rock?

Thus, the location and width of fault core and damage zone is uncertain. Our preferred interpretation is that the 30 meters of high fracture density from 2500-2530 mmd is part of the damage zone of FZB with the fault core located somewhere within 2530-2565 mmd. There may be another gouge zone within 2595-2680 mmd but at this time there is little evidence for that. We favor the interpretation that the block of sandstone at 2565-2595 mmd is a coarse-grained constituent of the larger clay-rich zone where FZB developed. This interpretation implies a width of at least 65 m in the measured dimension for FZB.

The measured width of the fault zone can provide some information about the expected geometry of that fault zone. If FZB dips in an orientation normal to the borehole, the measured thickness of the fault would be equal to the true thickness (Figure 3.8). A fault dipping to the northwest or southeast would appear artificially wider than the true thickness (Figure 3.9). Because the width of FZB is within reason and not overly wide, we believe that the orientation of FZB could be close to borehole perpendicular, much like the Buzzard Canyon fault (FZA) and the SAF (Figure 3.10). If FZB is oriented normal to the borehole in the subsurface, when projected to the surface that would correlate to a fault plane dipping 70°SW on the west side of Middle Mountain. Thayer and Arrowsmith (2005) mapped a fault trace very near that location (slightly more

southwest of where we projected FZB) (Figure 3.10) although no fault plane strike/dip or slip vectors were observed. There are not any faults identified in seismic surveys of the SAFOD site which correlate to the surface fault or FZB (Hole et al., 2001; Catchings and Rymer, 2002; Bleibinhaus et al., 2006) although seismic resolution is low below 1 km depth in that portion of the survey (Hole et al., 2001). The best way to determine conclusively if FZB correlates to the fault mapped at the surface by Thayer and Arrowsmith (2005) would be to conduct more detailed surface fault studies.

At fault zone C the same lithologies exist on both sides of the fault plane: arkosic conglomerates, sandstones and siltstones. It does not fall into the structural category of either the Carboneras or Punchbowl faults. It does, however, display many of the same characteristics as exhumed faults: grain-scale brecciation and dilation, cataclastic matrix as fracture fill, and extensive microfractures. Few data from FZC support extensive fluid flow. Feldspar alteration is very rarely observed and calcite and quartz cements are nearly absent. This may be due to the lack of porosity generally observed at this depth; the arkoses immediately above FZC are characterized by high velocities and low porosities (Figure 3.10). It is feasible that as a fault zone is exhumed form a depth of 2.5 km, porosity would be enhanced by unloading processes, allowing for fluid flow and subsequent alteration. This has important implications for the mechanics of the San Andreas fault, if fault processes occur during earthquakes that are not fluid-assisted, what role does pore pressure play in the strength of the SAF? We are not asserting that fluids are completely absent in the fault processes that have occurred in FZC, but there is much less textural and mineralogical evidence of fluid flow than expected.

3-5 CONCLUSIONS

The composition and structure of three fault zones encountered in the SAFOD Main borehole at 1920 mmd, 2530 mmd, and 3069 mmd were studied using wireline and image logs, and petrography of cuttings and core. The physical properties of the three faults zone are distinctly different from each other. Fault zone A, 1920 mmd, which may correlate to the Buzzard Canyon fault, is at least 45 meters wide and is quartzofeldspathic in composition with high levels of quartz-rich cataclasite and peaks of zeolite and calcite. Fault zone B, at 2530 mmd and at least 65 meters wide, was developed in a clay-rich lithologic unit and is not associated with quartz-rich cataclasite. Fault zone C, 3069 mmd, consists of a 61 cm wide clay-rich shear zone with a damage zone at least 11 meters wide. Fault zone C is quartz and feldspar rich with extensive damage observed in the coarse intervals of the damage zone. While damage and gouge zones were not strictly defined for each fault zone, given the low resolution of the datasets, elements of both portions of a fault zone were identified for Fault zones A, B, and C, implying that the model for fault architecture developed at the surface is applicable to subsurface fault zones.

References

Bleibinhaus, F., Hole, J.A., Ryberg, T., and Fuis, G.S., submitted, Structure of the California Coast Ranges and San Andreas fault at SAFOD from seismic waveform inversion and reflection imaging: Journal of Geophysical Research.

Boness, N.L., and Zoback, M.D., 2005, Shear velocity anisotropy in and near the San Andreas fault: Implications for mapping stress orientations: EOS trans. American Geophysical Union, 86(52), Fall Meeting Supplement, Abstract T23E-03.

Boness, N.L., and Zoback, M.D., 2006, A multi scale study of the mechanisms controlling shear velocity anisotropy in the San Andreas Fault Observatory at Depth: Geophysics, v. 71, no. 5, doi: 10.1190/1.2231107.

Bradbury, K.K., Barton, D.C., Solum, J.G., Draper, S.D., Evans, J.P., in review, Mineralogic and textural analyses of drill cuttings from the San Andreas Observatory at Depth [SAFOD] boreholes: Initial interpretations of fault zone composition and constraints on geologic models: submitted to Geosphere, 2006.

Byerlee, J., 1990, Friction, overpressure and fault normal compression: Geophysical Research Letters, v. 17, p. 2109-2112.

Catchings, R.D., and Rymer, M., 2002, High-resolution seismic velocities and shallow structure of the San Andreas fault zone at Middle Mountain, Parkfield, California: Bulletin of the Seismological Society of America, v. 92, p. 2493-2503.

Chester, F.M., and Logan, J.M., 1986, Implications for mechanical properties of brittle faults from observations of the Punchbowl Fault zone, California: Pure and Applied Geophysics, v. 124, nos. 1/2, p. 79-106.

Chester, F.M., Evans, J.P., and Biegel, R.L., 1993, Internal structure and weakening mechanisms of the San Andreas Fault: Journal of Geophysical Research, v. 98, no. B1, p. 771-786.

Chester, F.M., and Chester, J.S., 1998, Ultracataclasite structure and friction processes of the Punchbowl fault, San Andreas system, California: Tectonophysics, v. 295, p. 199-221.

Chester, F.M., Chester, J.S., Kirschner, D.L., Schulz, S.E., and Evans, J.P., 2005a, Structure of large-displacement, strike-slip fault zones in the brittle continental crust, *in* Karner, G.D., Taylor, B., Driscoll, N.W., and Kohlstedt, D.L., eds, Rheology and Deformation in the Lithosphere at Continental Margins, Columbia University Press, New York.

Chester, J.S., Chester, F.M., and Kronenberg, A.K., 2005b, Fracture surface energy of the Punchbowl fault, San Andreas system: Nature, v. 437, p. 133-136.

Engelder, J.T., 1974, Cataclasis and the generation of fault gouge: Geological Society of America Bulletin, v. 85, p. 1515-1522.

Evans, J.P., Shipton, Z.K., Pachell, M.A., Lim, S.J., Robeson, K., 2000, The structure and composition of exhumed faults, and their implications for seismic processes, *in* Bokelmann, G. and Kovach, R.L., (eds), Proceedings of the 3rd Conference on

Tectonic Problems of the San Andreas Fault System, Stanford University Publications, p. 67-81.

Faulkner, D.R., Lewis, A.C., and Rutter, E.H., 2003, On the internal structure and mechanics of large strike-slip fault zones: field observations of the Carboneras fault in southeastern Spain: Tectonophysics v. 367, p. 235-251.

Flinn, D., 1997, Transcurrent faults and associated cataclasis in Shetland: Journal of the Geological Society of London, v. 133, p. 231-248.

Forster, C.B., and Evans, J.P., 1991, Hydrology of thrust faults and crystalline thrust sheets – Results of combined field and modeling studies: Geophysical Research Letters, v. 18, p. 979-982.

Heaton, T.H., 1990, Evidence for and implication of self-healing pulses of slip in earthquake rupture: Physical Earth Planetary International, v. 64, p. 1-20.

Hickman, S.H., 1991, Stress in the lithosphere and the strength of active faults: Review of Geophysics Supplemental, v. 29, p. 759-775.

Hickman, S.H., and Zoback, M.D., 2004, Stress orientations and magnitudes in the SAFOD pilot hole from observations of borehole failure: Geophysical Research Letters, v. 31, doi: 10.1029/2004GL020043.

Hickman, S., Zoback, M., Ellsworth, B., 2005, Structure and composition of the San Andreas Fault Zone at Parkfield: Initial results from SAFOD Phases 1 and 2: EOS trans. American Geophysical Union, 86(52), Fall Meeting Supplement, Abstract T23E-05.

Hole, JA, Catchings, RD, St Clair, KC, Rymer, MJ, Okaya, DA, and Carney, BJ, 2001, Steep-dip seismic imaging of the shallow San Andreas Fault near Parkfield: Science, v. 294, p. 1513-1515.

Isaacs, A.J., 2005, Characterizing deformation, damage parameters, and clay composition in fault zones: Insights from the Chelungpu thrust, Taiwan and Mozumi right-lateral fault, Japan: [Masters Thesis], Utah State University, Logan, UT, 206 p.

Lachenbruch, A.H., and Sass, J.H., 1980, Heat flow and energetics of the San Andreas fault zone: Journal of Geophysical Research, v. 85, p. 6185-6223.

Lachenbruch, A.H., and Sass, J.H., 1992, Heat flow from Cajon Pass, fault strength, and tectonic implications: Journal of Geophysical research, v. 97, no. B4, p. 4995-5015.

Little, T.A., 1995, Brittle deformation adjacent to the Awatere strike-slip fault in New Zealand: Faulting patterns, scaling relationships, and displacement partitioning: Geological Society of America Bulletin, v. 107, p. 1255-1271.

Moore, D.E., and Byerlee, J., 1992, Relationships between sliding behavior and internal geometry of laboratory fault zones and some creeping and locked strike-slip faults of California: Tectonophysics, v. 211, p. 305-316.

Moore, D.E., and Rymer, M.J., 2006, Discovery of talc in SAFOD serpentinite cuttings: Possible implications for the origin of creep in the San Andreas fault: EOS trans., American Geophysical Union, 87(52), Fall Meeting Supplement, Abstract S32A-06.

Mount, V.S., and Suppe, J., 1987, State of stress near the San Andreas fault: implications for wrench tectonics: Geology, v. 15, p. 1143-1146.

Ohtani, T., Tanaka, H., Fujimoto, K., Higuchi, T., Tomida, N., and Ito, H., 2001, Internal structure of the Nojima Fault zone from the Hirabayashi GSJ drill core: The Island Arc, v. 10, p. 392-400.

Reinen, L.A., Weeks, J.D., and Tullis, T.E., 1994, The frictional behavior of lizardite and antigorite serpentinites: Experiments, constitutive models and implications for natural faults: Pure and Applied Geophysics, v. 143, no. 1/2/3, p. 317-358.

Rice, J.R., 1992, Fault stress states, pore pressure distributions, and the weakness of the San Andreas fault, *in* Evans, B. and Wong, T.-F., eds, Fault mechanics and transport properties in rocks, Academic, San Diego, p. 475-503.

Schleicher, A.M., van der Pluijm, B.A., Solum, J.G., Warr, L.N., 2006 (submitted), The origin and significance of clay minerals on surfaces, in fractures and in veins from SAFOD borehole samples (Parkfield, California): Journal of Geophysical Research.

Scholz, C.H., and Anders, M.H., 1994, The permeability of faults, in The Mechanical Involvement of Fluids in Faulting: Geological Survey Open-file Report 94-228, p. 191-231.

Schulz, S.E., and Evans, J.P., 2000, Mesoscopic structure of the Punchbowl Fault, southern California and the geologic and geophysical structure of active strike-slip faults: Journal of Structural Geology, v. 22, p. 913-930.

Sibson, R.H., 1977, Fault rocks and fault mechanisms: Journal of the Geological Society of London, v. 133, p. 191-213.

Solum, J.G., Hickman, S.H., Lockner, D.A., Moore, D.E., van der Pluijm, B.A., Schleicher, A.M., and Evans, J.P., 2006, Mineralogical characterization of protolith and fault rocks from the SAFOD main hole: Geophysical Research Letters, v. 33, doi: 10.1029/2006GL027285

Tembe, S., Lockner, D.A., Solum, J.G., Morrow, C.A., Wong, T., Moore, D.E., 2005, Strength of the San Andreas Fault Zone: Insight from cuttings and core: EOS trans. American Geophysical Union, 86(52), Fall Meeting Supplement, Abstract T24B-03.

Thayer, M., and Arrowsmith, R., 2005, Fault zone structure of Middle Mountain, Central California: EOS trans. American Geophysical Union, 86(52), Fall Meeting Supplement, Abstract T21A-0458.

Thurber, C. Roecker, S., Zhang, H., Baher, S., and Ellsworth, W., 2004, Fine-scale structure of the San Andreas fault zone and location of the SAFOD target earthquakes: Geophysical Research Letters, v. 31, doi: 10.1029/2003GL019398.

Townend, J., and Zoback, M.D., 2000, How faulting keeps the crust strong: Geology, v. 28, no. 5, p. 399-402.

Townend, J., and Zoback, M.D., 2004, Regional tectonic stress near the San Andreas fault in central and southern California: Geophysical Research Letters, v. 31, doi: 10.1029/2003/GL018918.

Wibberly, C., and Shimamoto, T., 2003, Internal structure and permeability of major strike-slip fault zones: the Median Tectonic Line in W. Mie Prefecture, SW Japan: Journal of Structural Geology, v. 25, p. 59-78.

Williams, C.F., Grubb, F.V., and Galanis, S.P., Jr, 2004, Heat flow in the SAFOD pilot hole and implications for the strength of the San Andreas fault: Geophysical Research Letters, v. 31, doi: 10.1029/2003GL019352.

Wilson, J.E., Chester, J.S., and Chester, F.M., 2003, Microfracture analysis of fault growth and wear processes, Punchbowl Fault, San Andreas system, California: Journal of Structural Geology, v. 25, p. 1855-1873.

Zoback, M.D., Zoback, M.L., Mount, V.S., Suppe, J., Eaton, J.P., Healy, J.H., Oppenheimer, D., Reasenberg, P., Jones, L., Raleigh, C.B., Wong, I.G., Scotti, O., and Wentworth, C., 1987, New evidence on the state of stress of the San Andreas fault system: Science, v. 238, p. 1105-1111.

Table 3.1: Fracture density ranges

Fracture Density	**# fractures / 10m**
Low	0 - 5
Moderate	5 - 15
High	15 - 20
Very High	> 20

Fracture density ranges are derived from interpreted electrical image logs through the arkosic section. Ranges are for arkosic section only and do not apply to other lithologies in the SAFOD borehole.

Table 3.2: Mesoscopic description of core samples

Core Sample	Measured Depth (m)	Lithologic Description
MHP1_B11	3057.14	Moderate to coarse grained arkosic sandstone
MHP1_B12	3058.06	Granule-pebble sandstone/conglomerate, contains a sub-angular red-stained volcanic lithic
MHP1_B13	3058.67	Similar to B12, pervasive red staining
MHP1_B14	3060.15	Very fractured arkosic pebble conglomerate, subangular, fractured clasts
MHP1_B16	3061.72	Coarse sandstone, fracture filled with oxidized material
MHP1_B17	3062.33	Very coarse, granule sandstone, high %age of k-feldspar
MHP1_B18	3063.24	Well sorted, fine-grained sandstone
MHP1_B20	3064.46	Siltstone, very dark in color, surface is naturally polished with hematite coating
MHP1_B21	3065.07	Very fine-grained sandstone
MHP1_B22	3066.29	Siltstone matrix with light-colored fine sand grains

Lithologic descriptions of core samples. Nomenclature of core sample numbers is as follows: Main Hole Phase 1 = MHP1, core box 14 = B14. Core boxes reference the archived core box, each box is approximately 1 m in length. Box numbers increase in depth and proximity to cored fault gouge at 3067 mmd.

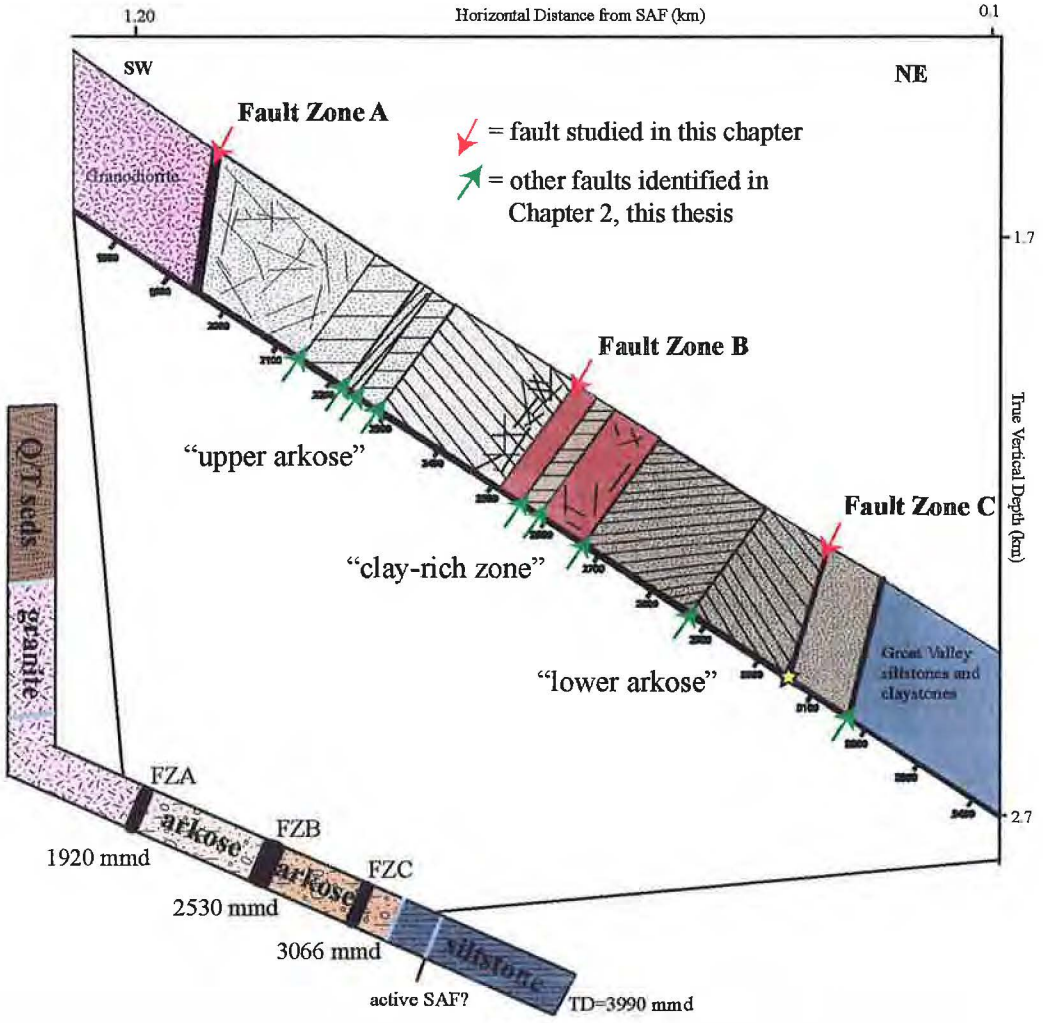

Figure 3.1: Schematic of the SAFOD borehole with a closer view of the structure of the arkosic section (1920-3150 meters measured depth). The arkosic section is composed of 11 distinctly different structural blocks separated by faults. Twelve faults in total are interpreted in Chapter 2 of this thesis. The three faults which are the focus of this study are fault zones A, B, and C (red arrows on arkosic section). Fault zone A (FZA) is located at 1920 mmd, separating Salinian granite/granodiorite from arkosic sedimentary rocks. Fault zone B (FZB) is located in a clay-rich zone at 2530 mmd and separates upper and lower arkosic units. Fault zone C (FZC) was cored at the end of phase one at 3060 mmd and is hypothesized to be an active southwestern strand of the San Andreas fault (Hickman et al., 2005, Solum et al., 2006).

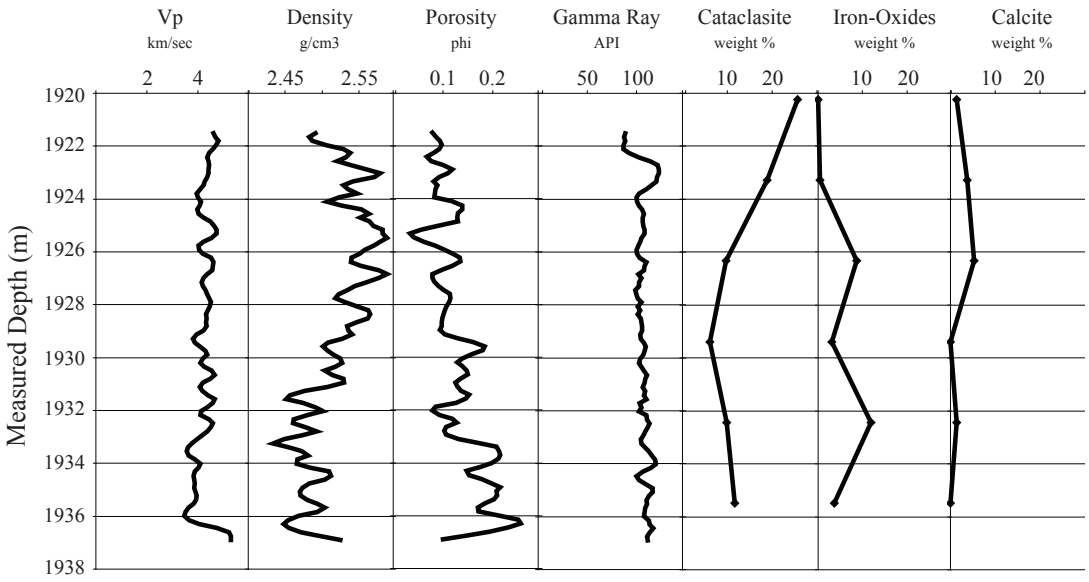

Figure 3.2: Fault zone A wireline and composition logs. Data are derived from wireline log values and cuttings thin section petrography.
Vp = compressional velocity measured in km/sec, converted from us/ft
Density = bulk density of rock measured in g/cm^3, Porosity = neutron porosity a measure of amount of water in formation, measured as a ratio, or phi
Gamma Ray = a measure of nature radioactivity in the formation, measured in API units, which is an industry standard measurement, Cataclasite, iron-oxides and calcite are deformational features observed in cuttings thin sections and quantified through petrographic point counts.
Thin sections samples are more widely spaced than wireline logs, therefore compositional curves are smoother than wireline curves.

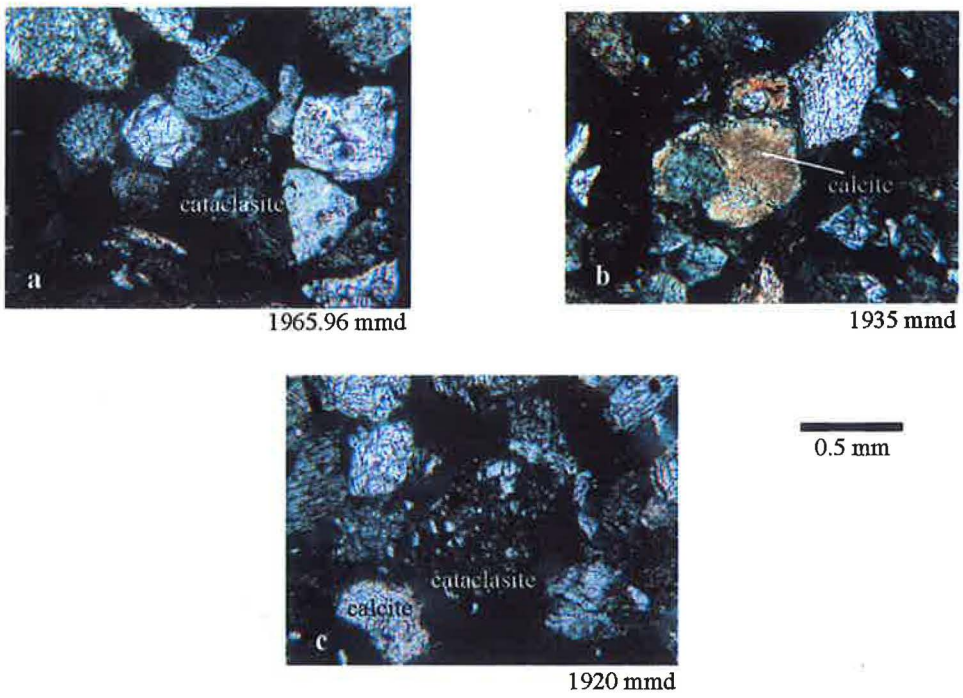

Figure 3.3: Examples of deformational features observed in fault zone A Photomicrographs taken under cross-polarized light with a blue filter. Scale bar applies to all photomicrographs.

a) fine-grained cataclasite with well-rounded quartz and feldspar grains (white grains in fine-grained dark matrix) b) example of microcrystalline calcite c) slightly coarser-grained cataclasite but with evidence of beginnings of cataclastic flow (alignment of quartz grains).

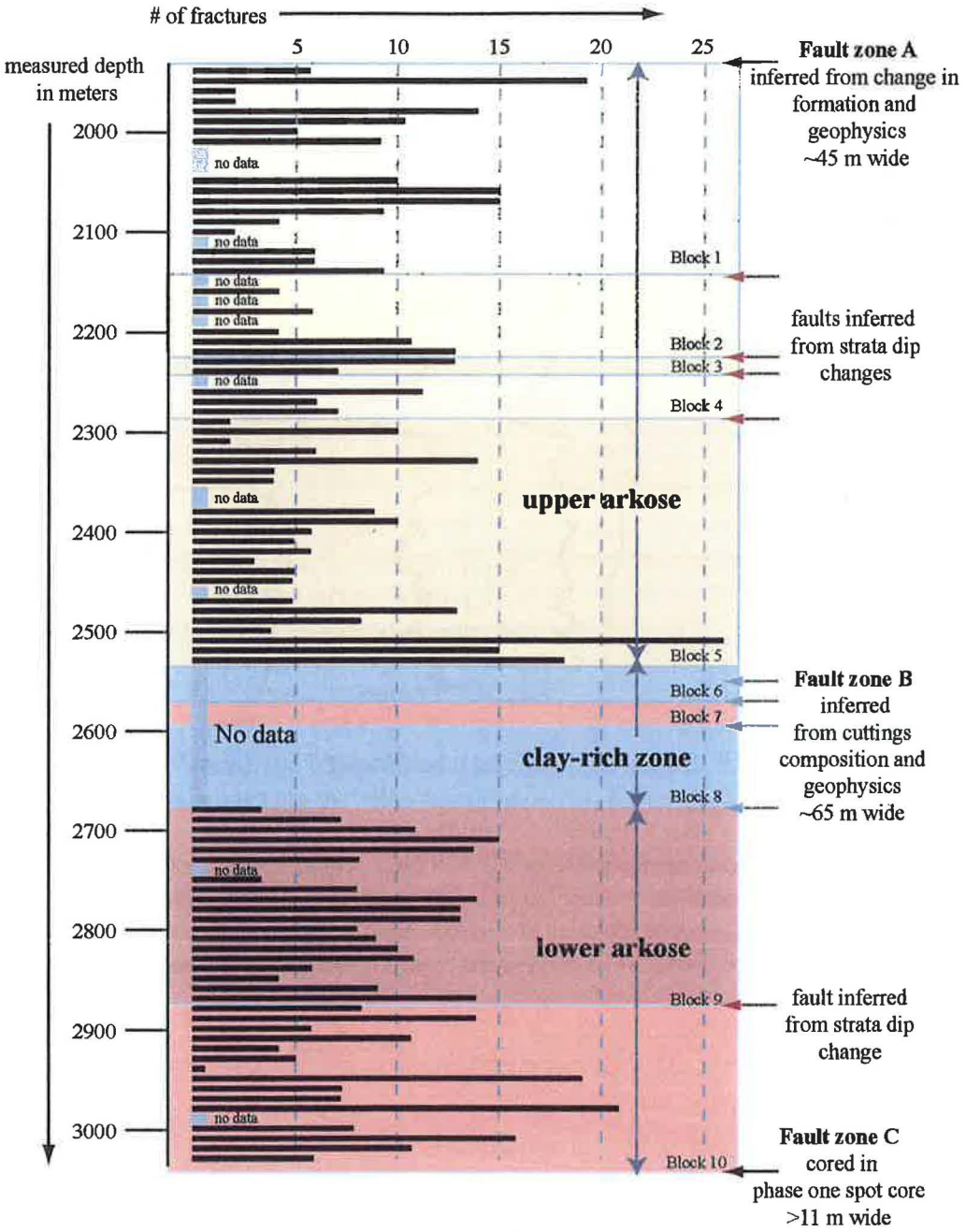

Figure 3.4: Fracture densities for entire Arkosic section beginning at 1920 mmd derived from image log analysis. Bins are 10 meters wide so that fracture density is plotted at # of fractures per 10 meters. Gray bars indicate where data are too poor to interpret fractures properly. Section has been divided into structural blocks (Chapter 2). Block 11 (beneath block 10) is missing because image log data were not available for that interval.

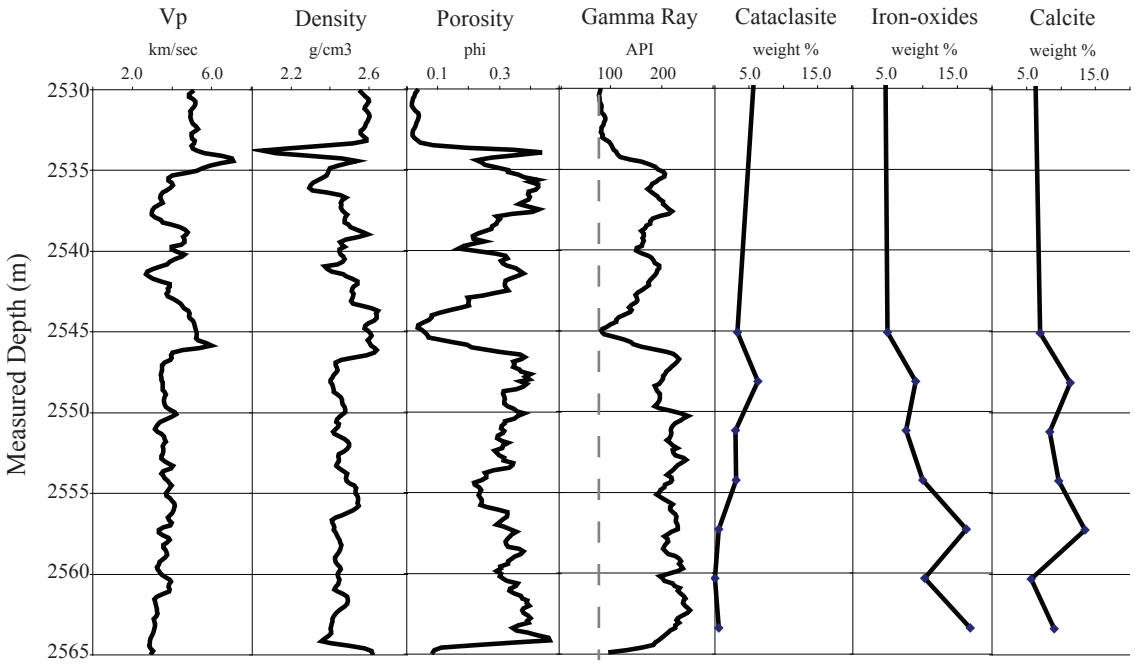

Figure 3.5: Wireline and compositional logs for fault zone B, from 2530-2565 mmd. Wireline log headings are the same as in Figure 3.1, for detailed description of each physical property, see Figure 3.1. Defomational features were only evaluated at the 3.3 meter interval below 2545 mmd, above that depth, samples were analyzed every 15 meters. That is why the compositional curves are linear above 2545 mmd. The point where the compositional curves intersects the x-axis corresponds to the measured value of those deformational features at 2529 mmd.

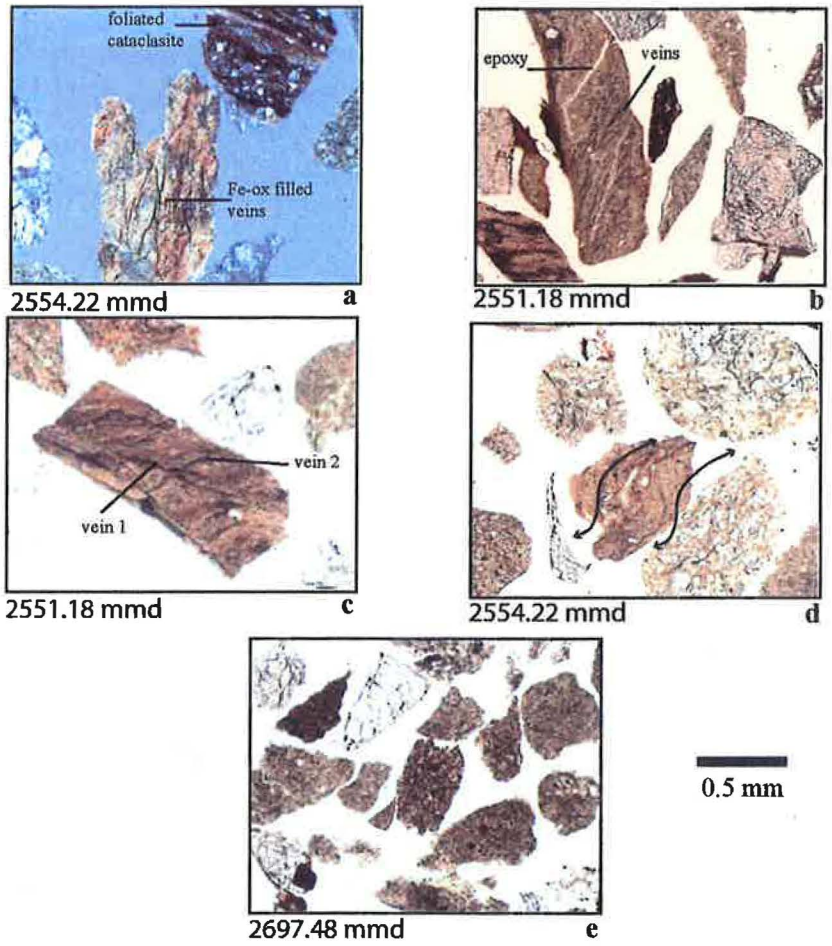

Figure 3.6: Photomicrographs of clay-rich grains from Fault Zone B. Scale bar applies to all photos. All photos taken under plane-polarized light except photo a which is taken under cross-polarized light. The bright, washed out color in photos c, d, and e result from high light levels designed to display the dark features of the grains.

a) Upper right corner is a foliated cataclasite grain stained by iron-oxides, center grain contains numerous anastamozing iron-oxide filled veins. b) Large grain on left side contains clay-filled veins, light colored areas are cracks in the grain where the slide epoxy shows. Grain in lower left corner has a foliated fabric. c) Large grain in center contains several clay-filled veins. Vein 1 is cross-cut by vein 2, showing different episodes of deformation. d) Grain in center of photo displays a sense of shear apparent in the sigmoidal shape of clay-filled veins. e) Undeformed clay-rich grains of similar composition to the grains of photos a-d but without veins or shear fabrics. This photo was taken further down in the clay-rich zone than photos a-d.

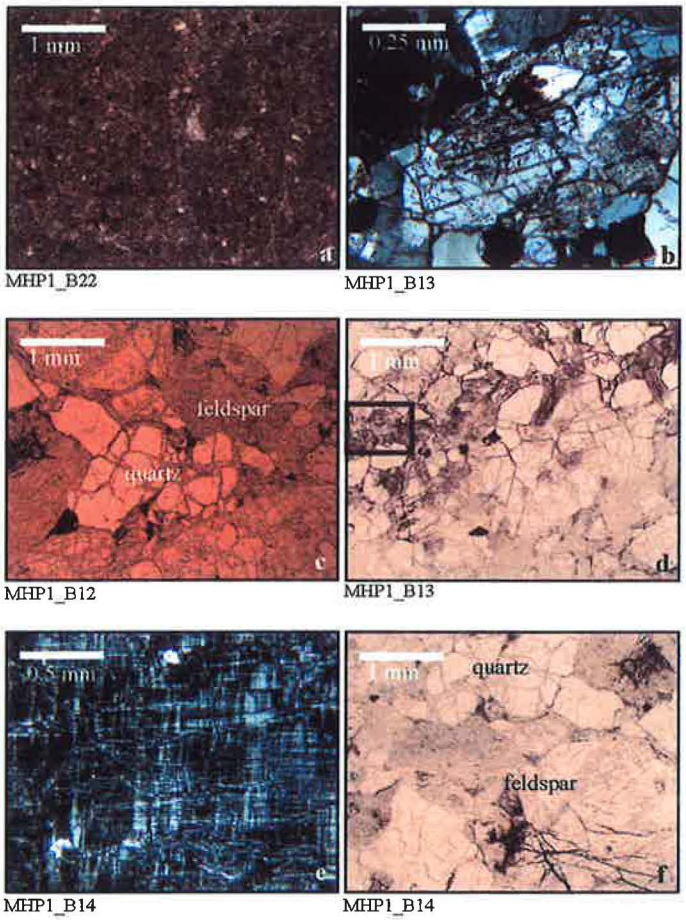

Figure 3.7: Photomicrographs from fault zone C. Photos a, c, d, and f are under plane-polarized light, photos b and e are under cross-polarized light. Differences in color between a/c and d/f due to blue filter applied to photos d and f.

a) Fine-grained, texturally immature, undeformed sample. Clay-rich in composition, similar to clay-rich cuttings samples. b) Fractured feldspar grain, fractures are filled with iron-oxide c) Micro-fractured quartz grain and heavily fractured feldspar d) Brecciated quartz and feldspar grains locally cemented with iron-oxides. Black box show approximate outline of photo b e) Unaltered, brittley fractured microcline grain. Representative of majority of feldspar in phase one core. f) Localized iron-oxide infiltration into fractured feldspar grains. Fractures are in feldspar grains with fractured quartz at top of photo.

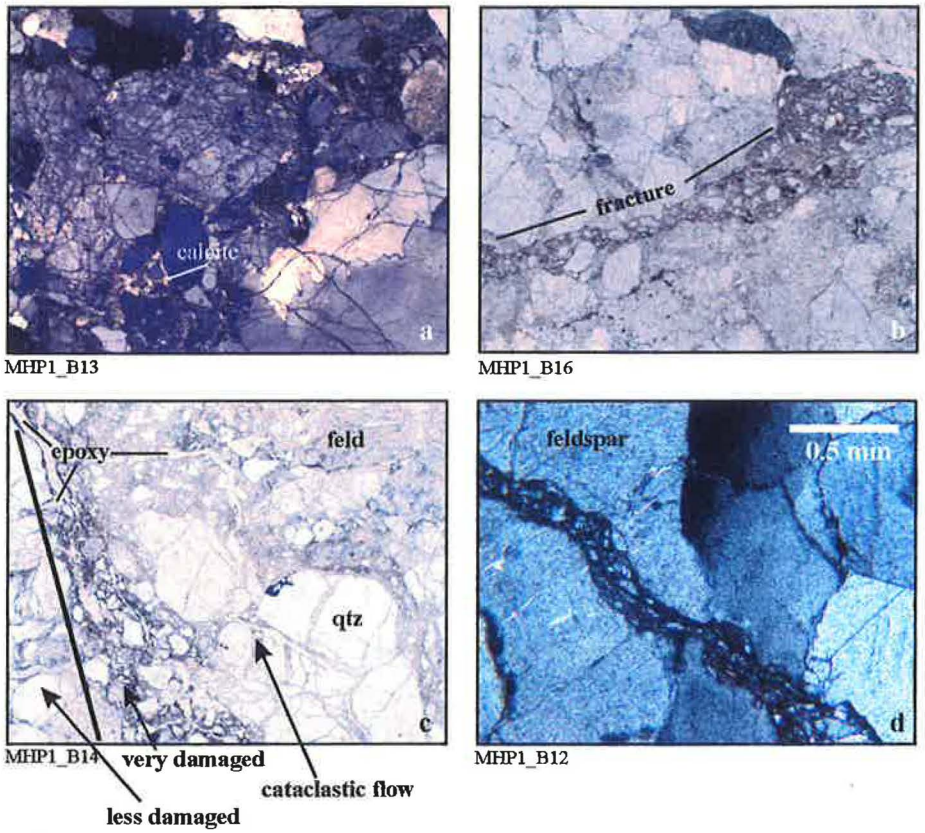

Figure 3.8: Photomicrographs of damage zone of fault zone C. Photos a and d are under cross-polarized light, photos b and c are under plane-polarized light. Scale bar below photos apply to all except photo d.

a) photo displaying localized calcite cementation b) mesoscale fracture stretches the length of the hand sample. Fracture is filled with iron-oxide rich cataclasite with angular grains entrained. Fracture widens at right side of photo but narrows significantly to the left, through the photo and beyond the fractures becomes quite narrow. c) diffuse area of deformation with similar iron-oxide rich cataclasite as in photo b. Notice zones of cracking in the thin section where epoxy shows through, those are not veins. Black line on left delineates boundary between zone of intense damage (right) from less damaged zone (left). Grain scale fracture filled with cataclasite implies a certain amount of flow occurring in this sample.
d) another example of a cataclasite-filled fracture with distinct fracture boundaries.

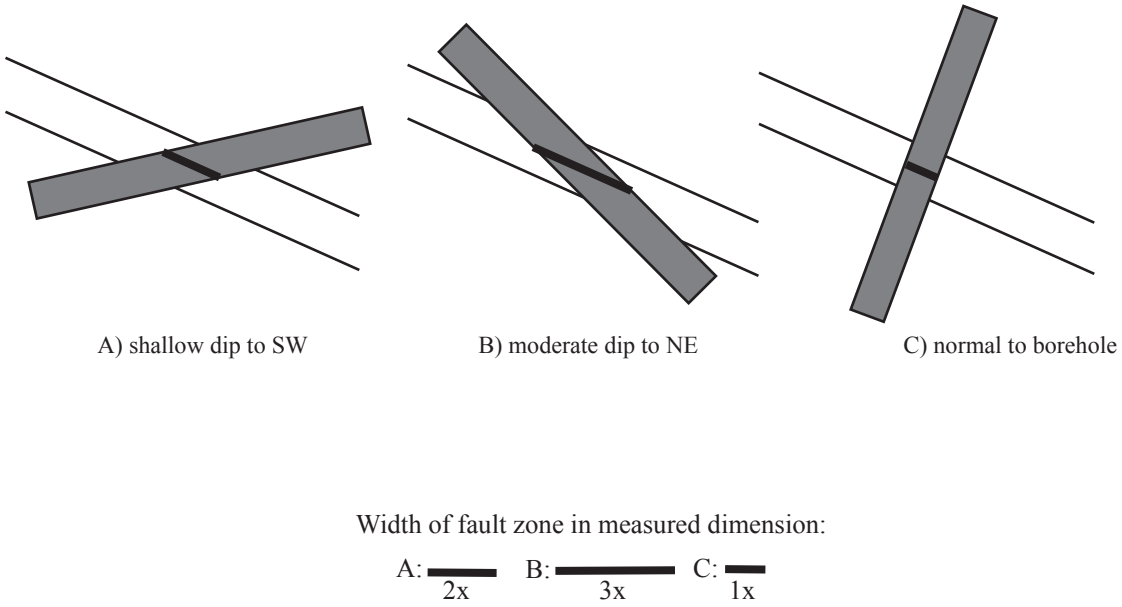

Figure 3.9: Three possible orientations of FZB and the resulting measured width. All dimensions are equal in each scenario, i.e. the fault zone (in gray) is the same sized polygon in each case, rotated to different angles. Parallel black lines represent the borehole trend while the thick black line represents what is measured in the borehole. This schematic shows that if the fault zone is normal to the borehole, the measured width is equal to the true width of the fault zone. If the fault dips shallowly to the SW, the measured width can be twice the true width and if the fault dips to the NE the measured width can be three times the true width. This illustrates the difficulty of evaluating the structure of a fault zone without constraints on orientation.

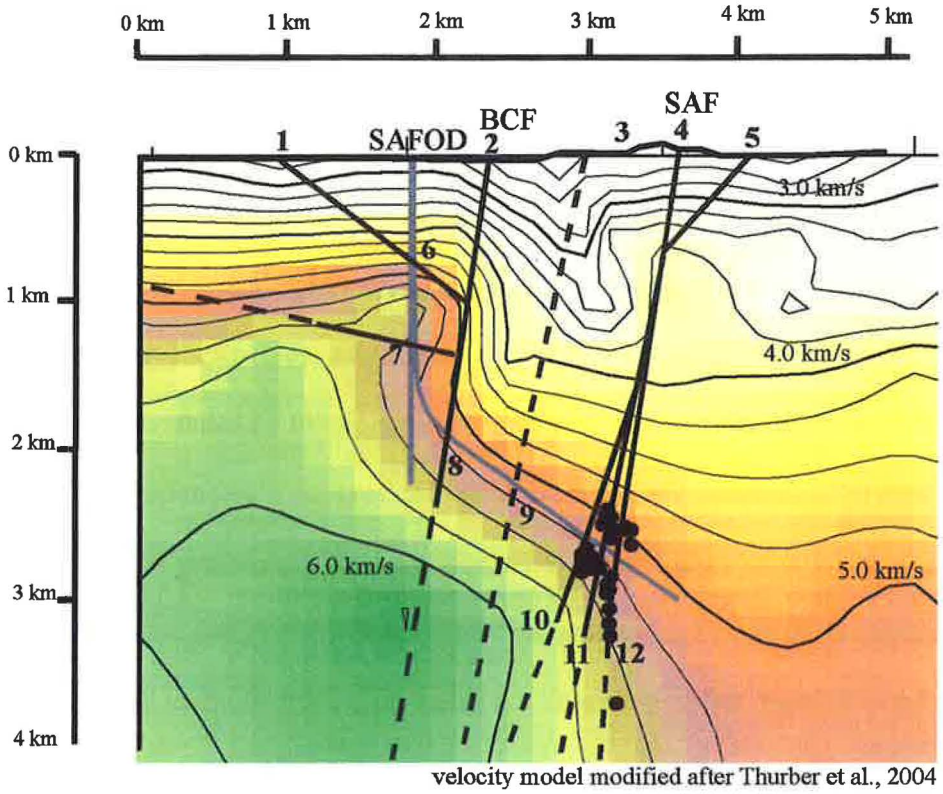

Figure 3.10: Schematic of surface and subsurface fault zones at the SAFOD site with subsurface velocity model of Thurber et al., 2004 in background. Description of data source for each fault is detailed with fault number below.

1) Fault mapped by Thayer and Arrowsmith, 2005 **2)** Buzzard Canyon fault, mapped by M. Rymer (unpublished) and Thayer and Arrowsmith, 2005 **3)** Fault mapped by Thayer and Arrowsmith (2005), possible correlation to FZB **4)** Surface trace of San Andreas fault, mapped by Dibblee, 1971 and Thayer and Arrowsmith, 2005 **5)** Fault mapped by Thayer and Arrowsmith, 2005 **6)** Fault interpreted from wireline logs and lithology change from Quaternary/Tertiary sedimentary rocks to Salinian granite **7)** Fault interpreted from wireline logs and lithology change from granite to granodiorite, orientation interpreted by Bradbury et al., in review from correlation between Pilot and Main Boreholes **8)** FZA, interpreted from lithology change from granodioriteto arkosic sedimentary rocks, dip interpreted by Bradbury et al., in review, the same lithology change is not observed in the PilotHole, implying that the fault must dip steeply to the southwest, FZA is correlated to Buzzard Canyon Fault **9)** FZB, interpreted from wireline logs and compositional data (Solum et al., 2006, Boness and Zoback, 2006, Bradbury et al., in review, this report), unknown orientation **10)** FZC, cored in 2005, no lithology change, interpreted to be a possible SW active strand of SAF (Hickman et al., 2005, Solum et al., 2006) **11)** Fault interpreted by Draper et al. (Chapter 2), lithology change from arkosic sedimentary rocks to fine-grained Great Valley Sequence (Evans et al., 2005) **12)** Location of borehole deformation due to a creeping fault plane, interpreted to be an active strand of the SAF. Correlation to the surface trace implies a dip of 83°SW (Bradbury et al., in review).

CHAPTER 4

SUMMARY/CONCLUSIONS

We use cuttings and core petrographic microscopy, electrical image logs, and borehole-based geophysical logs to examine the lithologic and structural character of arkosic sedimentary rocks on the southwest side of the San Andreas fault plane. This arkosic section is bounded by lithology breaks interpreted to be fault zones and is at least 500 meters thick, extending from 1920 meters measured depth (mmd) to 3150 mmd. At 1920 mmd, Salinian granodiorite changes abruptly to a well-indurated 409.1 m – 833.7 m thick block of arkosic sedimentary rocks. This is interpreted to be a fault relationship and has been correlated to the Buzzard Canyon fault, a little studied fault parallel to the modern SAF, at the surface (Bradbury et al., in review). At the bottom of the arkosic section, 3150 mmd, there is an abrupt change from feldspathic sandstones and siltstones to dark gray siltstones/claystones of the Great Valley Sequence to the end of the SAFOD borehole at 3990 mmd. Between those two major fault boundaries, the structure and lithology of the arkosic section is complex.

We divided the section into three distinct lithologic units based on difference in cuttings composition, sedimentary character derived from electrical image logs, and wireline log character.

The Upper Arkose

The upper arkose, from 1920 mmd to 2530 mmd, is a 156.4 m – 381.4 m thick section and is coarse-grained with several unbedded conglomerate intervals, composed primarily of quartz and feldspar with extensive iron-oxide alteration. We interpret the iron-oxide alteration to be the result of the degradation of plutonic minerals such as biotite and amphibole. Rock fragments are almost exclusively granitic and indicate a homogeneous plutonic source region. Fracture densities vary dependent on proximity to subsidiary fault zones. The upper arkose has been further sub-divided into five distinct structural blocks which have different bedding orientations. Block one is a massive texturally immature conglomerate with a generally moderate to high fracture density. Blocks two and four are conglomeratic sandstones dipping shallowly to the northwest with block three, dipping steeply to the southwest, sandwiched in between. Block five is a finer-grained sandstone with beds dipping steeply to the northeast. Block five gets progressively more fractured with depth and closer proximity to a fault zone at 2530 mmd. It is most likely that intraformational faults separate the individual blocks although the changes in bedding orientations could be the result of folding as well.

The fault zone at 1920 mmd is composed of fine-grained quartzofeldspathic cataclasite with high concentrations of calcite compared to background levels in the upper arkose country rock. The fault zone is at least 45 meters wide in the arkosic section with a zone of localized deformation at ~1965 mmd where the abundance of cataclasite is the highest but the fracture density is the lowest.

The Clay-rich Zone

The clay-rich zone, from 2530-2680 mmd and 28.7 m – 121.3 m thick, is characterized by compressional velocities as low as 2 km/sec and anomalously high gamma ray values. The zone is composed of abundant clay-sized particles and clay minerals with a comparatively large amount of fuchsite, a chromium bearing muscovite. Image log data recovery is generally low through the clay-rich zone due to the instability of the borehole through the section. The exception is the coarser grained interval from 2565-2595 mmd where bedding trends can be measured and the abundance of clay decreases. In that coarse-grained interval compressional velocity increases and gamma ray decreases to values similar to those measured in the lower arkose. Then at 2595 mmd the rocks become clay-rich again, corresponding to a decrease in velocity and increase in gamma ray.

From 2530 to 2565 mmd, we interpret a clay-rich fault zone referred to as fault zone B in chapter 3. Well developed deformation textures and microstructures such as clay-filled veins and sigmoidally sheared veinlets are observed, corresponding to the initial dramatic decrease in velocity and increase in porosity and gamma ray. We suggest a correlation of fault zone B to a fault mapped by Thayer and Arrowsmith (2005) on the west flank of Middle Mountain at the surface. Verification of this correlation requires more mapping and observation of the surface fault. If that unnamed fault does correlate to fault zone B it would dip approximately 70° to the southwest, a similar dip to the Buzzard Canyon and San Andreas faults.

The Lower Arkose

The lower arkose, 260-3150 mmd, is 224-331 m thick. It is finer-grained than the upper arkose with more clay-sized particles and clay minerals and less feldspar observed overall. Fewer conglomeratic intervals were observed in image logs in the lower arkose than the upper arkose.

The lower arkose is divided into three main blocks (9, 10 and 11) with different bedding orientations. In block 9 bedding dips 0-30° to the southwest, in block 10 bedding dips 60-90° to the northeast. Bedding orientations are unknown in block 11 because image logs were not collected in that zone.

Alteration of feldspar is more advanced in the lower arkose than the upper arkose. Many feldspars are nearly completely replaced by coarse muscovite as opposed to the fine-grained sericite/illite in the upper arkose. We interpret this to be a result of different diagenetic conditions, where temperatures are higher and pore fluids have a different composition in the lower arkose than the upper arkose. Despite the advanced degree of alteration, neither the upper or lower arkose shows evidence for having been buried more than 0.8 km deeper than the depth at which they were encountered in the borehole. This is verified by the results of detrital zircon fission-track analysis performed on zircons separated in cuttings from block 11. The separated zircons show no evidence of crystal lattice annealing since initial cooling of the source rocks at 64-70 Ma, indicating that the arkoses have not reached temperatures of 240°C after deposition.

Within the lower arkose is fault zone C, at 3067 mmd. Fault zone C is composed of extensively damaged rock, with many examples of grain-scale brecciation and grain-size reduction caused by repeated microfracturing. Interestingly, there is little evidence

of pervasive alteration caused by extensive fluid flow in the damage zone of FZC. Feldspars are generally unaltered and there is little cementation or veining observed. We believe that the lack of alteration is a result of the porosity reduction caused by deep burial and that alteration could occur as the fault zone is uplifted and unloading increases the porosity of the rocks.

Depositional Environment

The presence of conglomerates, sandstones and siltstones in close proximity to one another with abrupt changes in depositional energy, along with the general textural immaturity of the arkoses indicates that the arkoses were deposited as the most proximal portion of either a subaqueous or subaerial fan system. The clay-rich intervals could represent overbank deposits or extended periods of depositional or tectonic quiescence. The abundance of granitic rock fragments indicate that the fan system was likely derived from Salinian plutonics.

Based on zircon fission-track analysis, our reconstruction of the diagenetic history, and tectonic interpretations of the Salinian block we interpret a maximum Paleocene/Eocene age for the SAFOD arkoses. Paleocene/Eocene Salinian-derived transtensional basins are commonly found in California.

Tectonic History of SAFOD Arkoses

The evolution of the San Andreas fault system in the vicinity of the SAFOD site may be determined through the correlation of the SAFOD arkoses to equivalent sedimentary units found either at the surface or in the subsurface. If the majority of slip

occurred along the modern SAF, then equivalent units may be found ~315 km to the southeast of the SAFOD site. We identify possible units in outcrop in the Cajon Pass, Pinyon Ridge Block and Liebre Mountain Block approximately 300 km to the southeast of the SAFOD site reported in other published papers. If 315 km of slip has been distributed across the Buzzard Canyon and San Andreas faults, the SAFOD arkoses could be a stranded sliver of an offset basin such as the San Joaquin and La Honda Basins. The SAFOD arkoses are grossly lithologically similar to the Eocene Butano and Miocene Vacqueros Formations of the La Honda Basin to the northwest and the Eocene Point of Rocks and Miocene Temblor Formations of the San Joaquin Basin to the southeast. If the majority of slip has occurred on the Buzzard Canyon fault with only a small component of slip along the modern San Andreas fault, an equivalent unit may be located ~300 km to the northwest and a short distance to the southeast. We do not find any evidence to support this third hypothesis, but do not completely rule out the validity of the hypothesis.

More complete tectonic interpretation is needed for this area and can be carried out through a robust correlation study between the SAFOD arkoses and those candidates identified above.

Potential Future Studies

This thesis study has documented the lithology and structure of the arkosic section and suggested sedimentary rock units in California which are potentially equivalent to the SAFOD arkoses. There are several potential studies that can build upon the work detailed here, including but not limited to those discussed below.

1) More complete age constraints on the SAFOD arkoses are needed through palynological analsysis of fine-grained intervals or geochronological studies of volcanic clasts in the phase one core. This would help to correlate the SAFOD arkoses to another equivalent unit and to constrain provenance. Also, determining the exact chemical signature of the volcanics may pinpoint the origin and age of the volcanic source in the lower arkose.

2) Field observations of the Buzzard Canyon fault and other faults in the vicinity of the SAFOD site are needed. Locations of faults have been mapped, but there are no data collected for the slip vectors or orientations of the faults planes. Furthermore, an analysis of fault architecture and fault zone width, if possible, would be helpful for further modeling of the geometry of the subsurface of the SAFOD site.

3) More detailed work studying the fluid chemistries of pore fluids and fault-related fluid phases would be interesting. Determining the distribution of mineral assemblages is a necessary first step, but we believe this work shows that there have been episodes of fluid compartmentalization causing differential alteration and it would be interesting to see if that persists today. Authigenic mineral phases observed in the core may indicate to certain extent the chemistry of pore fluids in the past and present.

4) Well records from central California extend to several miles deep in some places and provide a key to understanding how the top of the Salinian basement changes regionally. The presence of the arkoses generates the question of whether there are other units similar to the SAFOD arkoses in the subsurface in other parts of central California. By integrating those well records into a regional subsurface model, we can may be able to constrain the validity of different hypotheses for the evolution of the San Andreas fault.

APPENDICES

APPENDIX A

CUTTINGS COMPOSITION DATA FROM PETROGRAPHIC POINT COUNTS

UPPER ARKOSE VALUES

Measured Depth in ft	Measured Depth in m	Vertical depth (m)	Quartz	Plagioclase	K-feldspar	Total unaltered feldspar
6300.00	1920.24	1872.80	44.00	10.33	4.33	14.67
6350.00	1935.48	1883.01	64.33	3.67	5.33	9.00
6400.00	1950.72	1893.10	62.67	3.33	0.00	3.33
6450.00	1965.96	1903.19	28.00	4.33	0.67	5.00
6550.00	1996.44	1923.42	50.33	3.00	4.00	7.00
6600.00	2011.68	1933.51	55.33	2.67	1.33	4.00
6650.00	2026.92	1943.49	49.00	2.33	3.67	6.00
6700.00	2042.16	1953.30	36.67	2.33	2.00	4.33
6750.00	2057.40	1962.91	51.00	2.33	1.33	3.67
6800.00	2072.64	1972.39	63.33	3.67	2.00	5.67
6850.00	2087.88	1981.76	34.33	3.67	2.00	5.67
6900.00	2103.12	1991.02	49.67	3.67	2.00	5.67
6950.00	2118.36	2000.17	32.67	2.33	3.67	6.00
7000.00	2135.00	2009.32	50.67	4.67	4.00	8.67
7050.00	2150.25	2018.49	55.67	5.00	4.33	9.33
7100.00	2164.08	2027.57	49.00	4.33	3.66	7.99
7150.00	2179.32	2036.55	44.00	1.66	2.66	4.32
7200.00	2194.56	2045.47	44.00	3.00	2.00	5.00
7250.00	2209.80	2054.39	51.00	2.33	2.66	4.99
7300.00	2225.04	2063.30	61.00	1.66	4.33	5.99
7350.00	2240.28	2072.21	43.00	1.66	2.00	3.66
7400.00	2255.52	2081.14	44.00	4.00	3.66	7.66
7450.00	2270.76	2090.09	58.66	2.33	4.33	6.66
7500.00	2286.00	2099.11	51.00	3.00	1.66	4.66
7550.00	2301.24	2108.18	40.66	2.33	2.33	4.66
7600.00	2316.48	2117.18	56.33	2.33	2.33	4.66
7650.00	2331.72	2126.08	58.66	4.66	2.33	6.99
7700.00	2346.96	2134.99	60.00	4.66	2.33	6.99
7750.00	2362.20	2143.93	55.00	4.00	5.00	9.00
7800.00	2377.44	2152.92	56.33	3.33	4.66	7.99
7850.00	2392.68	2162.00	43.66	4.66	6.66	11.32
7900.00	2407.92	2171.12	32.33	2.33	5.66	7.99
7950.00	2423.16	2180.14	55.66	4.00	6.33	10.33
8000.00	2438.40	2188.99	50.00	4.66	4.33	8.99
8050.00	2453.64	2197.72	51.33	6.33	4.00	10.33
8100.00	2468.88	2206.36	55.33	2.66	3.66	6.32
8150.00	2484.12	2215.18	50.00	3.00	4.00	7.00
8200.00	2499.36	2224.15	57.00	3.66	2.33	5.99
8250.00	2514.60	2233.07	57.66	4.33	4.33	8.66
8300.00	2529.84	2241.92	55.66	1.33	1.66	2.99
Upper arkose averages			50.22	3.49	3.24	6.73

CLAY-RICH ZONE

Measured Depth in ft	Measured Depth (m)	Vertical depth (m)	Quartz	Plagioclase	K-feldspar	Total unaltered feldspar
8350.00	2545.08	2250.93	34.66	0.66	2.66	3.32
8400.00	2560.32	2259.98	22.66	1.00	2.66	3.66
8450.00	2575.56	2268.99	37.66	2.33	2.33	4.66
8500.00	2590.80	2277.92	25.00	1.66	2.33	3.99
8550.00	2606.04	2286.84	25.66	1.33	3.00	4.33
8600.00	2621.28	2295.81	25.33	1.00	3.00	4.00
8650.00	2636.52	2304.91	47.33	2.66	4.00	6.66
8700.00	2651.76	2314.17	32.33	2.33	4.00	6.33
8750.00	2667.00	2323.48	17.00	1.00	2.66	3.66
8800.00	2682.24	2332.84	18.00	1.00	2.00	3.00
Clay-rich zone averages			28.56	1.50	2.86	4.36

LOWER ARKOSE

Measured Depth (ft)	Measured Depth (m)	Vertical depth (m)	Quartz	Plagioclase	K-feldspar	Total unaltered feldspar
8850.00	2697.5	2342.00	44.33	5.00	3.00	8.00
8900.00	2712.7	2350.98	39.66	3.33	2.66	5.99
8950.00	2728.0	2359.87	55.33	5.00	2.33	7.33
9000.00	2743.2	2368.75	49.33	3.66	2.00	5.66
9050.00	2758.4	2377.62	33.33	3.33	3.66	6.99
9100.00	2773.7	2386.48	46.33	4.00	6.33	10.33
9150.00	2788.9	2395.31	41.66	4.33	5.00	9.33
9200.00	2804.2	2404.15	43.66	5.66	5.00	10.66
9250.00	2819.4	2413.05	37.33	2.00	2.00	4.00
9300.00	2834.6	2421.97	51.33	8.00	3.66	11.66
9350.00	2849.9	2430.88	43.00	3.33	3.33	6.66
9400.00	2865.1	2439.77	47.00	4.33	4.66	8.99
9500.00	2895.6	2457.29	46.66	4.66	4.66	9.32
9550.00	2910.8	2466.01	43.00	6.66	4.66	11.32
9600.00	2926.1	2474.78	41.66	4.00	4.33	8.33
9650.00	2941.3	2483.65	40.66	5.00	1.66	6.66
9700.00	2956.6	2492.64	55.00	4.33	3.00	7.33
9750.00	2971.8	2501.75	46.00	5.33	3.33	8.66
9800.00	2987.0	2510.96	40.66	1.00	2.66	3.66
9850.00	3002.3	2520.25	59.00	1.66	3.33	4.99
9900.00	3017.5	2529.54	48.66	7.33	1.66	8.99
9950.00	3032.8	2538.91	59.66	5.00	5.33	10.33
10000.00	3048.0	2548.24	60.67	3.67	5.00	8.67
10100.00	3078.5	2567.13	38.67	3.67	0.67	4.33
10150.00	3093.7	2576.54	52.00	2.67	5.33	8.00
10200.00	3109.0	2585.81	56.67	3.33	4.67	8.00
10250.00	3124.2	2594.00	56.67	3.33	4.67	8.00
10300.00	3139.4	2603.49	48.00	3.67	5.67	9.33
10350.00	3154.7	2611.86	38.33	3.67	2.67	6.33
Lower rkose averages			48.12	4.13	3.66	7.79

UPPER ARKOSE

Measured Depth in m	Vertical depth (m)	Muscovite	Chlorite	Opaque	Cataclasite	Altered feldspar
1920.24	1872.80	1.33	0.67	0.00	25.67	9.33
1935.48	1883.01	0.33	0.00	0.67	11.67	9.00
1950.72	1893.10	0.67	0.00	0.33	12.67	13.33
1965.96	1903.19	0.00	0.33	0.00	31.33	15.33
1996.44	1923.42	0.33	0.33	0.66	8.00	16.00
2011.68	1933.51	0.00	1.33	0.00	14.67	12.00
2026.92	1943.49	0.33	0.67	0.00	4.00	13.00
2042.16	1953.30	0.00	1.00	0.33	8.00	13.00
2057.40	1962.91	0.33	0.00	0.00	16.67	15.33
2072.64	1972.39	0.00	0.67	0.67	2.33	13.33
2087.88	1981.76	0.00	0.33	0.33	6.67	12.67
2103.12	1991.02	0.33	0.67	0.33	2.67	16.00
2118.36	2000.17	0.33	0.33	0.00	2.00	11.33
2135.00	2009.32	0.00	0.33	0.33	2.33	13.67
2150.25	2018.49	0.33	1.00	0.00	1.67	16.00
2164.08	2027.57	0.00	0.66	0.33	4.66	17.00
2179.32	2036.55	0.00	0.66	0.33	7.66	12.66
2194.56	2045.47	0.00	1.00	0.33	6.66	16.00
2209.80	2054.39	0.00	0.66	0.33	6.00	16.66
2225.04	2063.30	0.66	0.33	0.67	2.00	15.00
2240.28	2072.21	0.00	0.33	0.00	0.66	14.66
2255.52	2081.14	0.00	1.33	0.00	4.00	15.33
2270.76	2090.09	1.00	1.00	0.00	8.33	16.33
2286.00	2099.11	0.00	0.66	0.00	4.66	21.00
2301.24	2108.18	0.00	0.66	0.33	2.33	14.33
2316.48	2117.18	0.00	1.00	0.66	9.00	14.00
2331.72	2126.08	0.00	0.66	0.00	5.66	16.33
2346.96	2134.99	0.33	0.66	0.00	3.00	16.00
2362.20	2143.93	0.66	0.00	0.00	9.00	14.33
2377.44	2152.92	0.00	0.33	0.00	6.33	15.00
2392.68	2162.00	0.00	0.66	0.33	3.66	17.33
2407.92	2171.12	0.00	0.00	0.00	3.33	12.00
2423.16	2180.14	0.00	0.33	0.00	3.66	13.33
2438.40	2188.99	0.00	0.00	0.00	2.66	14.33
2453.64	2197.72	0.00	0.33	0.00	3.33	15.33
2468.88	2206.36	0.00	0.33	0.00	7.33	16.33
2484.12	2215.18	0.00	0.00	0.33	6.66	13.33
2499.36	2224.15	0.00	0.00	0.00	3.00	20.00
2514.60	2233.07	0.33	0.00	0.00	1.00	13.33
2529.84	2241.92	0.33	0.00	0.00	5.66	11.00
	Averages	0.19	0.48	0.18	6.76	14.51

CLAY-RICH ZONE

Measured Depth (m)	Vertical depth (m)	Muscovite	Chlorite	Opaque	Cataclasite	Altered feldspar
2545.08	2250.93	0.00	0.00	0.00	3.33	9.66
2560.32	2259.98	0.00	0.00	0.00	0.00	6.33
2575.56	2268.99	0.00	0.33	0.00	4.00	7.33
2590.80	2277.92	1.00	0.33	0.00	4.00	5.00
2606.04	2286.84	0.66	0.33	0.33	0.00	6.33
2621.28	2295.81	0.00	0.00	0.00	1.33	7.33
2636.52	2304.91	0.00	0.00	0.00	6.66	9.66
2651.76	2314.17	0.66	0.00	0.66	9.33	6.00
2667.00	2323.48	0.66	0.00	0.00	1.66	5.33
2682.24	2332.84	1.33	0.66	0.00	6.33	5.33
	Averages	0.43	0.17	0.10	3.66	6.83

LOWER ARKOSE

Measured Depth (m)	Vertical depth (m)	Muscovite	Chlorite	Opaque	Cataclasite	Altered feldspar
2697.5	2342.00	0.00	0.33	0.00	6.66	7.00
2712.7	2350.98	0.66	0.00	0.00	17.33	5.00
2728.0	2359.87	1.33	0.33	0.33	6.00	8.33
2743.2	2368.75	0.00	0.66	0.00	6.33	8.66
2758.4	2377.62	0.66	1.66	0.66	3.66	8.33
2773.7	2386.48	2.33	0.66	0.33	6.33	9.33
2788.9	2395.31	0.66	1.00	0.33	7.00	6.33
2804.2	2404.15	0.66	1.33	0.66	5.33	8.66
2819.4	2413.05	1.66	1.00	0.00	18.00	6.66
2834.6	2421.97	1.00	0.33	0.00	8.00	7.33
2849.9	2430.88	2.66	0.33	0.00	6.33	9.00
2865.1	2439.77	1.33	0.00	1.33	7.00	10.00
2895.6	2457.29	1.33	0.00	0.00	3.66	11.00
2910.8	2466.01	2.33	0.00	0.66	10.00	9.33
2926.1	2474.78	2.66	0.00	1.66	2.00	7.66
2941.3	2483.65	3.33	0.00	0.00	5.00	7.00
2956.6	2492.64	2.00	0.00	0.00	8.33	9.66
2971.8	2501.75	4.00	0.00	0.33	2.00	9.66
2987.0	2510.96	2.33	0.66	1.00	0.33	7.66
3002.3	2520.25	0.66	0.00	0.33	0.66	8.66
3017.5	2529.54	1.66	1.33	0.66	8.00	3.66
3032.8	2538.91	1.33	1.33	0.33	7.00	6.66
3048.0	2548.24	2.00	1.00	0.00	1.33	12.00
3078.5	2567.13	0.33	0.33	2.00	1.00	10.67
3093.7	2576.54	1.00	0.67	1.00	1.33	9.67
3109.0	2585.81	1.00	0.67	0.00	4.00	6.67
3124.2	2594.00	1.00	0.67	0.00	4.00	6.67
3139.4	2603.49	2.00	0.67	2.00	7.33	14.33
3154.7	2611.86	0.67	0.67	0.67	12.67	11.00
	Averages	1.73	0.46	0.57	5.62	8.81

UPPER ARKOSE

Measured Depth in m	Vertical depth (m)	Total feldspar	Unknown	Quartz-secondary	Clay cement/matrix
1920.24	1872.80	24.00	0.00	0.33	0.00
1935.48	1883.01	18.00	0.00	0.33	0.00
1950.72	1893.10	16.67	0.33	0.33	0.33
1965.96	1903.19	20.33	0.33	0.00	0.00
1996.44	1923.42	23.00	0.00	0.66	1.66
2011.68	1933.51	16.00	0.00	0.00	0.67
2026.92	1943.49	19.00	0.00	0.00	5.33
2042.16	1953.30	17.33	0.33	0.33	4.67
2057.40	1962.91	19.00	0.00	0.00	1.67
2072.64	1972.39	19.00	0.00	0.00	1.33
2087.88	1981.76	18.33	0.00	0.00	2.67
2103.12	1991.02	21.67	0.00	0.33	3.33
2118.36	2000.17	17.33	0.33	0.67	6.33
2135.00	2009.32	22.33	0.00	0.00	3.33
2150.25	2018.49	25.33	0.33	0.33	5.33
2164.08	2027.57	24.99	0.33	0.66	3.00
2179.32	2036.55	16.98	0.00	0.00	4.66
2194.56	2045.47	21.00	0.33	0.00	6.00
2209.80	2054.39	21.65	0.00	0.00	4.00
2225.04	2063.30	20.99	0.00	0.00	4.00
2240.28	2072.21	18.32	0.33	0.00	9.00
2255.52	2081.14	22.99	0.00	0.66	10.66
2270.76	2090.09	22.99	0.00	0.00	2.66
2286.00	2099.11	25.66	0.00	0.33	4.33
2301.24	2108.18	18.99	0.33	0.33	10.33
2316.48	2117.18	18.66	0.00	0.00	2.66
2331.72	2126.08	23.32	0.00	0.33	1.66
2346.96	2134.99	22.99	0.00	0.00	2.00
2362.20	2143.93	23.33	0.00	0.00	1.00
2377.44	2152.92	22.99	0.00	0.33	1.33
2392.68	2162.00	28.65	0.00	1.33	2.66
2407.92	2171.12	19.99	0.66	0.33	9.33
2423.16	2180.14	23.66	0.00	0.33	5.00
2438.40	2188.99	23.32	0.00	0.00	3.66
2453.64	2197.72	25.66	0.00	0.00	2.33
2468.88	2206.36	22.65	0.00	0.00	3.33
2484.12	2215.18	20.33	0.33	0.00	1.33
2499.36	2224.15	25.99	0.00	0.00	1.66
2514.60	2233.07	21.99	0.00	0.33	6.00
2529.84	2241.92	13.99	0.00	0.00	11.66
	Averages	21.24	0.10	0.21	3.77

CLAY-RICH ZONE

Measured Depth (m)	Vertical depth (m)	Total feldspar	Unknown	Quartz-secondary	Clay cement/matrix
2545.08	2250.93	12.98	0.00	0.33	30.00
2560.32	2259.98	9.99	0.00	0.00	50.00
2575.56	2268.99	11.99	0.00	0.00	27.33
2590.80	2277.92	8.99	0.00	0.00	41.33
2606.04	2286.84	10.66	0.00	0.66	40.66
2621.28	2295.81	11.33	0.00	0.33	40.00
2636.52	2304.91	16.32	0.00	0.66	15.00
2651.76	2314.17	12.33	0.00	0.33	29.00
2667.00	2323.48	8.99	0.00	0.00	59.00
2682.24	2332.84	8.33	0.00	0.33	55.33
	Averages	11.19	0.00	0.26	38.77

LOWER ARKOSE

Measured Depth (m)	Vertical depth (m)	Total feldspar	Unknown	Quartz-secondary	Clay cement/matrix
2697.5	2342.00	15.00	0.00	1.00	22.00
2712.7	2350.98	10.99	0.00	1.33	20.33
2728.0	2359.87	15.66	1.33	2.00	9.33
2743.2	2368.75	14.32	0.00	2.00	15.66
2758.4	2377.62	15.32	0.00	1.66	24.66
2773.7	2386.48	19.66	0.00	1.33	10.66
2788.9	2395.31	15.66	0.00	0.33	14.33
2804.2	2404.15	19.32	0.00	1.66	13.33
2819.4	2413.05	10.66	0.00	1.00	19.33
2834.6	2421.97	18.99	0.00	1.00	11.33
2849.9	2430.88	15.66	0.00	0.33	19.33
2865.1	2439.77	18.99	0.33	0.33	10.33
2895.6	2457.29	20.32	0.00	1.00	11.00
2910.8	2466.01	20.65	0.00	0.66	13.00
2926.1	2474.78	15.99	0.33	0.00	18.33
2941.3	2483.65	13.66	0.00	0.00	21.33
2956.6	2492.64	16.99	0.00	0.00	8.00
2971.8	2501.75	18.32	0.00	0.33	16.00
2987.0	2510.96	11.32	0.00	0.33	23.66
3002.3	2520.25	13.65	0.66	0.00	11.00
3017.5	2529.54	12.65	0.00	2.33	10.66
3032.8	2538.91	16.99	0.66	0.00	5.66
3048.0	2548.24	20.67	0.00	0.33	7.00
3078.5	2567.13	15.00	0.00	0.00	38.00
3093.7	2576.54	17.67	0.33	1.00	17.67
3109.0	2585.81	14.67	0.00	0.33	17.00
3124.2	2594.00	14.67	0.00	0.33	17.00
3139.4	2603.49	23.67	0.33	0.00	11.00
3154.7	2611.86	17.33	0.00	0.00	25.00
	Averages	16.60	0.13	0.44	15.79

UPPER ARKOSE

Measured Depth in m	Vertical depth (m)	Fe-oxide cement/matrix	Calcite	Zeolite	Miscellaneous
1920.24	1872.80	0.00	1.33	2.67	0.00
1935.48	1883.01	3.67	0.00	0.67	0.00
1950.72	1893.10	2.00	3.67	0.00	0.00
1965.96	1903.19	5.67	10.67	0.33	0.00
1996.44	1923.42	11.33	2.00	0.00	1.00
2011.68	1933.51	8.67	3.00	0.00	0.33
2026.92	1943.49	17.00	3.33	0.00	0.00
2042.16	1953.30	24.67	6.67	0.00	0.00
2057.40	1962.91	9.00	2.33	0.00	0.00
2072.64	1972.39	10.33	2.33	0.00	0.00
2087.88	1981.76	33.33	4.00	0.00	0.00
2103.12	1991.02	15.67	4.33	0.00	0.00
2118.36	2000.17	32.00	8.00	0.00	0.00
2135.00	2009.32	17.67	3.00	0.00	0.00
2150.25	2018.49	9.00	1.00	0.00	0.00
2164.08	2027.57	10.66	5.66	0.00	0.00
2179.32	2036.55	16.66	8.00	0.00	0.00
2194.56	2045.47	13.33	7.00	0.00	0.00
2209.80	2054.39	9.66	6.00	0.33	0.00
2225.04	2063.30	8.33	2.00	0.00	0.00
2240.28	2072.21	25.66	2.33	0.00	0.00
2255.52	2081.14	14.33	1.66	0.33	0.00
2270.76	2090.09	5.33	0.00	0.00	0.00
2286.00	2099.11	12.33	0.33	0.00	0.00
2301.24	2108.18	25.66	0.00	0.00	0.00
2316.48	2117.18	8.66	2.00	0.00	0.00
2331.72	2126.08	8.66	1.00	0.00	0.00
2346.96	2134.99	8.33	2.66	0.00	0.00
2362.20	2143.93	7.66	2.66	0.00	0.00
2377.44	2152.92	10.33	1.66	0.00	0.00
2392.68	2162.00	15.33	1.66	0.00	0.00
2407.92	2171.12	31.00	2.00	0.00	0.00
2423.16	2180.14	11.00	0.00	0.00	0.00
2438.40	2188.99	17.66	2.66	0.00	0.00
2453.64	2197.72	15.66	1.00	0.00	0.00
2468.88	2206.36	9.33	1.66	0.00	0.00
2484.12	2215.18	8.00	12.66	0.00	0.00
2499.36	2224.15	3.66	8.66	0.00	0.00
2514.60	2233.07	4.66	7.00	0.00	0.00
2529.84	2241.92	4.66	6.33	0.00	0.00
	Averages	12.66	3.56	0.11	0.03

CLAY-RICH ZONE

Measured Depth (m)	Vertical depth (m)	Fe-oxide cement/matrix	Calcite	Zeolite	Miscellaneous
2545.08	2250.93	5.00	7.00	0.00	0.00
2560.32	2259.98	10.33	5.66	0.00	0.00
2575.56	2268.99	13.66	3.00	0.00	0.00
2590.80	2277.92	9.66	5.66	0.00	0.00
2606.04	2286.84	11.66	8.33	0.00	0.00
2621.28	2295.81	11.33	5.66	0.00	0.00
2636.52	2304.91	5.33	2.66	1.33	0.00
2651.76	2314.17	9.33	1.33	0.00	0.00
2667.00	2323.48	3.66	7.33	0.00	0.00
2682.24	2332.84	2.66	4.66	0.00	0.00
	Averages	8.26	5.13	0.13	0.00

LOWER ARKOSE

Measured Depth (m)	Vertical depth (m)	Fe-oxide cement/matrix	Calcite	Zeolite	Miscellaneous
2697.5	2342.00	3.00	3.33	0.33	0.00
2712.7	2350.98	3.33	1.00	0.00	0.33
2728.0	2359.87	3.66	1.00	0.00	0.00
2743.2	2368.75	6.00	3.00	0.00	0.33
2758.4	2377.62	12.00	5.00	0.00	0.00
2773.7	2386.48	8.00	0.00	2.66	0.00
2788.9	2395.31	15.00	0.66	0.00	0.00
2804.2	2404.15	8.00	0.00	2.00	0.00
2819.4	2413.05	9.00	0.00	0.00	0.00
2834.6	2421.97	4.66	1.00	1.00	0.00
2849.9	2430.88	8.00	0.33	1.33	0.00
2865.1	2439.77	9.33	1.33	1.00	0.00
2895.6	2457.29	11.00	0.33	2.00	0.00
2910.8	2466.01	5.33	0.66	0.33	0.00
2926.1	2474.78	9.33	1.33	0.00	0.00
2941.3	2483.65	12.33	1.66	0.33	0.33
2956.6	2492.64	4.33	1.00	2.66	0.00
2971.8	2501.75	3.66	0.66	1.00	0.00
2987.0	2510.96	10.33	3.33	0.33	0.00
3002.3	2520.25	5.00	1.66	0.33	0.00
3017.5	2529.54	7.33	4.66	1.00	0.00
3032.8	2538.91	4.00	2.66	0.00	0.00
3048.0	2548.24	2.00	1.33	0.33	0.33
3078.5	2567.13	2.67	1.33	0.00	0.33
3093.7	2576.54	2.67	1.00	1.67	0.00
3109.0	2585.81	2.33	1.00	1.00	0.00
3124.2	2594.00	2.33	1.00	1.00	0.00
3139.4	2603.49	2.00	1.33	0.00	0.00
3154.7	2611.86	4.00	0.00	0.67	0.00
	Averages	5.79	1.31	0.76	0.05

UPPER ARKOSE

Measured Depth in m	Vertical depth (m)	Volcanic rock	Igneous minerals	Walnut shells	Fuchsite
1920.24	1872.80	0.00	0.00	0.00	0.00
1935.48	1883.01	0.00	0.33	0.00	0.00
1950.72	1893.10	0.33	0.00	0.00	0.00
1965.96	1903.19	3.00	0.00	0.00	0.00
1996.44	1923.42	0.00	0.33	0.33	0.00
2011.68	1933.51	0.00	0.00	0.00	0.00
2026.92	1943.49	0.00	0.00	1.33	0.00
2042.16	1953.30	0.00	0.00	0.00	0.00
2057.40	1962.91	0.00	0.00	0.00	0.00
2072.64	1972.39	0.00	0.00	0.00	0.00
2087.88	1981.76	0.00	0.00	0.00	0.00
2103.12	1991.02	0.00	0.00	1.00	0.00
2118.36	2000.17	0.00	0.00	0.00	0.00
2135.00	2009.32	0.00	0.00	0.00	0.00
2150.25	2018.49	0.00	0.00	0.00	0.00
2164.08	2027.57	0.00	0.00	0.00	0.00
2179.32	2036.55	0.00	0.00	0.66	0.33
2194.56	2045.47	0.00	0.00	0.00	0.33
2209.80	2054.39	0.00	0.00	0.00	0.00
2225.04	2063.30	0.00	0.00	0.00	0.00
2240.28	2072.21	0.00	0.00	0.00	0.33
2255.52	2081.14	0.00	0.00	0.00	0.00
2270.76	2090.09	0.00	0.00	0.00	0.00
2286.00	2099.11	0.00	0.00	0.00	0.66
2301.24	2108.18	0.00	0.00	0.00	0.33
2316.48	2117.18	0.00	0.00	0.00	1.00
2331.72	2126.08	0.00	0.00	0.00	0.00
2346.96	2134.99	0.00	0.00	0.00	0.00
2362.20	2143.93	0.00	0.00	0.66	0.00
2377.44	2152.92	0.00	0.33	0.00	0.00
2392.68	2162.00	0.00	0.00	1.66	0.33
2407.92	2171.12	0.00	0.00	0.66	0.33
2423.16	2180.14	0.00	0.33	0.00	0.00
2438.40	2188.99	0.00	0.00	0.00	0.00
2453.64	2197.72	0.00	0.00	0.00	0.33
2468.88	2206.36	0.00	0.00	0.00	0.00
2484.12	2215.18	0.00	0.00	0.33	0.00
2499.36	2224.15	0.00	0.00	0.00	0.00
2514.60	2233.07	0.33	0.00	0.66	0.00
2529.84	2241.92	0.00	0.33	1.33	0.00
	Averages	0.09	0.04	0.22	0.10

CLAY-RICH ZONE

Measured Depth (m)	Vertical depth (m)	Volcanic rock	Igneous minerals	Walnut shells	Fuchsite
2545.08	2250.93	1.00	0.00	4.66	1.00
2560.32	2259.98	0.66	0.33	0.33	0.00
2575.56	2268.99	0.33	0.00	0.33	1.33
2590.80	2277.92	1.33	0.00	0.00	2.66
2606.04	2286.84	0.66	0.00	0.00	0.33
2621.28	2295.81	1.00	0.00	1.66	2.00
2636.52	2304.91	1.66	0.00	0.33	2.66
2651.76	2314.17	1.33	0.33	2.33	0.66
2667.00	2323.48	0.66	0.33	0.00	0.66
2682.24	2332.84	0.00	0.00	1.00	1.33
	Averages	0.86	0.10	1.06	1.26

LOWER ARKOSE

Measured Depth (m)	Vertical depth (m)	Volcanic rock	Igneous minerals	Walnut shells	Fuchsite
2697.5	2342.00	0.66	0.33	2.33	0.66
2712.7	2350.98	1.66	0.00	1.33	2.00
2728.0	2359.87	0.33	0.33	1.00	2.00
2743.2	2368.75	1.00	0.33	0.33	0.66
2758.4	2377.62	1.33	0.00	0.00	0.00
2773.7	2386.48	1.33	0.33	0.00	0.00
2788.9	2395.31	3.33	0.00	0.00	0.00
2804.2	2404.15	4.00	0.00	0.00	0.00
2819.4	2413.05	2.00	0.00	0.00	0.00
2834.6	2421.97	1.33	0.00	0.00	0.00
2849.9	2430.88	2.66	0.00	0.00	0.00
2865.1	2439.77	1.66	0.00	0.00	0.00
2895.6	2457.29	2.66	0.00	0.00	0.00
2910.8	2466.01	3.00	0.00	0.33	0.00
2926.1	2474.78	1.00	1.00	4.66	0.00
2941.3	2483.65	1.33	0.00	0.00	0.00
2956.6	2492.64	0.66	0.00	1.00	0.00
2971.8	2501.75	7.00	0.00	0.66	0.00
2987.0	2510.96	3.00	0.33	2.33	0.00
3002.3	2520.25	6.66	0.00	0.33	0.00
3017.5	2529.54	0.00	0.33	0.66	0.00
3032.8	2538.91	0.00	0.00	0.33	0.00
3048.0	2548.24	1.00	0.67	0.33	1.00
3078.5	2567.13	1.00	0.67	0.33	1.00
3093.7	2576.54	0.00	0.33	0.00	0.33
3109.0	2585.81	0.67	1.33	0.00	0.00
3124.2	2594.00	0.67	0.67	0.00	0.00
3139.4	2603.49	0.67	0.67	0.00	0.00
3154.7	2611.86	0.67	0.33	0.00	0.67
	Averages	1.79	0.30	0.52	0.14

APPENDIX B

BEDDING DATA DERIVED FROM ELECTRICAL IMAGE LOGS

Measured Depth (m)	True Dip (deg)	True Dip Direction (azimuth)	Apparent Dip (deg)	Apparent Dip Direction (azimuth)
2064.53	69.51	358.69	68.64	178.43
2064.85	68.25	359.69	69.34	180
2065.07	69	1.92	67.68	181.57
2083.21	67.67	11.61	64.52	190.96
2083.56	72.55	10.56	60.29	187.83
2161.22	15.6	337.26	62.44	21.91
2162.07	14.22	349.63	63.82	25.43
2165.45	14.91	296.8	52.51	18.78
2166.15	8.78	307.86	54.44	26.61
2167.76	12.46	299.11	52.95	21.91
2168.67	26.98	289.43	50.25	3.13
2176.23	14.77	281.81	48.68	19.57
2177.03	23.45	288	49.66	7.83
2192.07	53.04	29.98	73.15	211.3
2192.97	55.03	30.27	71.14	211.3
2194.51	55.55	24.27	71.45	206.09
2195.24	54.39	27.86	72.03	209.35
2196.45	55.75	18.91	72.37	201.52
2228.95	67.12	226.77	15.11	250.43
2229.11	69.59	226.76	17.32	246.52
2229.26	71.28	226.11	18.64	242.61
2229.39	71.11	224.03	17.89	236.74
2231.02	43.44	211.1	11.66	62.61
2233.96	60.69	232.13	13.62	281.74
2234.11	59.49	230.06	11.47	281.74
2234.65	48.36	228.87	9.96	344.35
2235.21	46.9	230.41	11.56	347.48
2237.90	51.62	233.33	12.14	322.83
2239.13	50.52	201.59	13.51	109.57
2239.85	45.14	203.36	14.18	86.09
2240.94	45.92	202.62	14.34	90
2241.20	37.52	199	21.32	72
2241.58	33.43	202.36	23.19	61.04
2241.92	35.06	199.92	22.73	66.52
2242.57	26.05	197.77	30.48	56.35
2247.21	34.73	216.16	19.23	42.26
2248.00	36.55	209.77	18.39	54.78
2249.13	32.52	231.57	23.31	20.35
2249.71	33.8	241.95	26.04	7.83
2249.83	30	235.96	26.9	18.78
2251.61	26.7	217.54	27.59	39.13

Measured Depth (m)	True Dip (deg)	True Dip Direction (azimuth)	Apparent Dip (deg)	Apparent Dip Direction (azimuth)
2252.92	29.06	230.45	26.31	25.04
2253.28	34.21	210.07	20.77	51.65
2257.11	16.14	251.95	41.27	25.04
2257.37	14.99	236.49	40	31.3
2259.75	18.73	320.75	59.69	17.22
2261.88	16.6	316.73	57.83	19.13
2262.16	11.22	311.92	55.33	25.04
2263.55	28.88	296.49	53.47	2.73
2263.74	24.68	295.11	52.41	7.83
2264.30	22.56	295.11	52.12	10.54
2264.56	12.7	284.56	50	23.48
2264.93	31.4	307.99	59.77	1.57
2266.79	24.12	346.81	70.64	18.78
2267.63	29.29	318.69	63.48	6.26
2268.24	25.75	329.83	66.04	12.52
2269.15	31.99	327.53	68.68	6.26
2271.83	34.56	320.38	66.43	1.57
2272.33	39.16	314.57	65.77	355.3
2273.08	34.67	320.73	66.84	1.57
2274.12	21.97	320.71	60.63	14.09
2276.04	30.49	328.34	67.91	7.83
2277.13	27.72	349.42	73.51	17.22
2277.54	29.22	330.07	67.85	9.39
2278.95	23.94	330.19	64.77	14.09
2279.29	25.29	325.83	63.88	11.74
2279.60	28.24	321.49	63.59	7.83
2279.82	22.62	331.48	64.22	15.65
2280.10	31.68	322.15	65.61	4.7
2280.39	26.64	323.21	63.49	9.78
2280.73	27.93	336.67	69.29	12.52
2281.30	26.84	347.91	72.18	17.22
2282.09	23	332.94	64.95	15.65
2283.04	13.81	327.08	58.65	23.48
2284.55	21.97	335.55	65.3	17.22
2284.92	19.88	334.47	63.76	18.78
2285.53	32.74	320.31	65.49	3.13
2286.42	22.06	329.74	63.62	15.65
2288.96	20.57	313.49	57.19	14.09
2289.54	15.91	305.77	53.65	18.78
2290.28	36.25	309.02	61.08	356.09
2297.10	57.66	14.34	72.5	197.22
2298.37	56.45	17.6	72.72	200.35
2302.69	64.6	354.91	73.86	178.04
2302.94	64.41	359.73	71.62	181.96
2304.07	60.36	4.39	73.07	187.83
2306.62	55.84	16.48	73.43	199.57
2307.65	54.72	16.01	74.68	199.57

Measured Depth (m)	True Dip (deg)	True Dip Direction	Apparent Dip (deg)	Apparent Dip Direction (azimuth)
2310.52	63.75	6.35	69.44	187.83
2310.83	64.94	5.21	68.83	186.26
2311.25	71.47	5.53	62.92	183.13
2311.47	71.72	7.34	61.86	184.7
2311.90	70.05	11.75	61.55	189.78
2312.22	71.68	5.68	62.59	183.13
2312.65	64.74	12.21	66.15	192.52
2312.99	77	3.62	58.95	178.04
2313.28	76.22	5.17	58.77	180
2314.00	73.28	11.41	58.46	187.83
2314.30	74.54	12.04	56.98	187.83
2314.71	74.48	12.02	57.03	187.83
2319.15	70.48	19.65	58.21	197.61
2319.42	76.94	20.04	51.95	195.65
2321.14	62.83	18.29	65.79	198.78
2321.39	65.92	19.35	62.45	198.78
2321.61	64.11	20.37	63.95	200.35
2321.98	62.59	18.24	65.81	198.78
2322.62	65.03	19.9	62.88	199.57
2323.54	64.77	17.4	63.72	197.22
2323.98	63.79	11.95	66.41	192.52
2324.28	66.62	9.89	64.54	189.39
2324.78	59.98	11.96	69.93	194.09
2325.10	63.39	17.3	65.15	197.61
2325.30	63.94	17.5	64.59	197.61
2325.44	64.24	15.52	64.9	195.65
2325.96	65.64	16.05	63.54	195.65
2326.33	66.01	18.2	62.59	197.61
2326.52	66.8	18.45	61.87	197.61
2327.58	64.76	12.31	65.73	192.52
2327.76	70.97	12.3	59.98	189.78
2328.21	71.95	10.79	59.72	187.83
2329.42	68.87	10.82	62.76	189.39
2330.19	70.21	19.15	58.78	197.22
2333.05	67.25	25.77	60.49	205.04
2333.60	65.18	25.34	62.48	205.04
2334.05	65.84	19.21	63.18	198.78
2334.53	66.03	20.08	62.71	199.57
2335.04	66.22	22.11	61.94	201.52
2335.90	65.86	27.8	61.21	207.39
2340.25	58.41	20.28	69.54	201.91
2344.99	58.99	29.09	67.65	209.74
2367.69	59.73	39.2	66.18	219.13
2368.10	59.87	30.91	66.32	211.3
2368.91	65.58	45.07	60.66	225.39
2369.26	64.2	39.1	61.75	219.13
2370.39	64.85	40.59	61.13	220.7
2394.83	51.19	33.62	75.47	214.43

Measured Depth (m)	True Dip (deg)	True Dip Direction	Apparent Dip (deg)	Apparent Dip Direction (azimuth)
2395.23	54.84	30.24	72.08	211.3
2396.12	56.71	28.73	70.36	209.74
2396.52	61.74	17.83	67.44	198.78
2399.73	64.89	36.04	62.18	216
2401.26	79.07	16.52	52.19	190.96
2405.76	59.13	25.65	68.79	206.61
2407.24	57.62	18.15	71.56	200.35
2408.07	58.69	9.29	72.97	192.52
2408.62	72.15	10.7	60.11	187.83
2410.95	62.19	23.07	65.59	203.48
2411.34	56.36	17.85	72.4	200.35
2411.72	57.14	19.95	71.19	201.91
2412.87	58.44	22.12	69.59	203.48
2413.35	56.13	26.98	71.08	208.17
2425.39	71.71	20.98	56.59	198.78
2427.38	58.99	32.57	66.97	212.87
2441.47	49.91	17.17	77.57	201.52
2445.49	71.62	7	60.37	183.91
2446.00	58.5	13.35	70.02	195.65
2446.65	59.27	26.76	66.36	207.39
2449.45	65.27	20.08	61.88	199.57
2451.89	67.93	30.02	57.58	209.35
2454.59	61.4	29.18	63.81	209.35
2456.62	56.43	26.21	69.11	207.39
2457.20	56.45	30.63	68.48	211.3
2457.93	55.88	14.57	71.91	197.61
2458.42	58.57	24.49	67.11	205.43
2460.71	55.24	28.26	69.56	209.35
2462.67	56.29	26.2	69.03	207.39
2463.51	56.21	26.2	69.06	207.39
2476.07	52.32	202.46	12.19	109.57
2476.80	68.4	212.26	14.12	197.61
2477.52	68.81	224.36	15.2	242.61
2477.77	67.9	224	14.26	242.61
2490.11	61.49	246.17	25.75	297.39
2490.75	43.99	250.92	27.1	338.48
2494.79	85.16	223.12	31.57	228.91
2495.20	84.24	207.9	31.14	199.57
2631.79	28.94	217.86	24.15	37.17
2631.96	29.63	198.26	26.55	58.7
2632.07	25.77	207.02	28.16	46.96
2687.69	20.31	183.25	37.86	57.83
2688.10	32.53	195.16	25.77	68.23
2691.19	45.83	182.82	27.83	102.67
2692.92	39.38	229.5	15.74	12.35
2693.08	43.8	221.45	9.48	26.64
2693.18	59.97	213.06	8.34	183.25
2693.27	62.59	207.26	13.55	170.25

Measured Depth (m)	True Dip (deg)	True Dip Direction	Apparent Dip (deg)	Apparent Dip Direction (azimuth)
2693.55	49.91	203.54	12.2	109.17
2695.22	39.93	197.87	19.94	80.58
2695.31	37.82	198.25	20.98	75.38
2704.85	37.4	230.35	18.38	16.79
2704.99	40	227.67	15.3	17.57
2705.31	39.7	232.01	17.06	9.78
2712.12	10.88	197.61	43.69	44.84
2716.16	34.72	208.26	20.71	55.23
2716.28	23.14	198.75	33.09	52.64
2716.43	22.22	215.16	32.05	40.94
2716.70	36.77	191.27	25.88	77.33
2717.00	27.04	203.46	28.82	52.64
2718.18	18.68	196.42	37.72	50.04
2718.62	22.67	195.89	34.48	53.94
2719.03	27.04	202.12	29.48	53.94
2719.65	29.1	169.75	40.01	73.43
2719.97	18.72	204.65	36.63	46.14
2720.34	16.82	180.88	42.2	53.94
2720.86	21.95	196.75	34.91	52.64
2721.19	17.66	161.36	46.66	59.13
2721.46	24.39	181.7	37.03	63.03
2721.60	18.16	195.73	38.14	50.04
2722.25	10.8	182.98	45.91	47.44
2722.52	13.57	177.67	44.74	51.34
2722.94	16.29	179.43	42.58	53.94
2723.81	15.47	197.41	40.11	47.44
2724.56	23.3	190.97	34.71	57.83
2724.89	19.22	208.3	35.32	44.84
2726.69	15.45	150.66	49.86	57.83
2727.28	17.43	170.57	43.97	57.83
2727.52	20.27	192.63	36.83	53.94
2728.66	22.03	169.06	42.42	64.33
2728.96	25.9	163.13	43.52	70.83
2729.67	16.7	173.19	43.82	56.53
2729.95	13.7	225.08	40.64	37.04
2737.13	16.24	171.4	44.74	56.53
2742.47	14.33	178.04	44.23	52.64
2742.76	15.46	153.35	49.4	57.83
2749.40	25.08	219.89	29.35	38.34
2750.44	29.23	210.36	25.95	48.74
2750.81	27.04	192.79	31.88	61.73
2751.02	31.25	197.29	27.27	64.33
2751.16	24.37	200.05	32.17	53.94
2751.39	24.38	185.81	36.05	61.73
2754.11	4.77	174.03	50.67	43.54
2758.35	12.7	169.98	46.55	52.64
2759.26	20.26	208.6	34.33	46.14
2775.09	23.84	135.89	55.74	69.11

Measured Depth (m)	True Dip (deg)	True Dip Direction	Apparent Dip (deg)	Apparent Dip Direction (azimuth)
2775.42	23.09	155.6	47.9	68.33
2776.09	25.58	164.5	43.74	70.67
2777.67	21.66	163.11	45.29	65.21
2778.09	19.04	164.47	45.62	61.3
2778.62	18.4	167.91	44.9	59.74
2786.95	17.49	201.92	38.26	46.96
2787.41	13.71	211.96	41.24	41.09
2789.84	25.24	194.67	32.67	56.74
2790.16	29.02	200.57	27.87	56.74
2790.80	23.68	206.83	31.54	46.96
2795.48	12.56	184.59	44.31	48.03
2795.68	23.35	194.03	33.94	55.05
2796.09	19.77	176.1	41.19	58.18
2796.39	21.72	192.61	35.59	53.94
2796.56	20.73	180.76	39.3	57.83
2796.71	14.83	200.53	40.41	44.84
2796.82	19.79	193.82	36.99	51.34
2796.97	28.93	171.27	38.84	72.13
2797.26	22.4	200.71	33.32	50.04
2797.94	21.33	215.83	32.79	39.64
2798.23	14.43	210.49	39.89	41
2798.82	13.22	205.65	41.37	42.24
2798.91	13	197.09	42.25	44.84
2799.09	26.61	180.87	35.64	65.63
2799.22	25.36	190.58	33.16	59.13
2799.30	24.63	183.56	35.83	61.73
2799.38	22.71	183.76	37.01	59.13
2799.55	18.66	194.41	37.65	50.04
2799.69	14.93	188.98	41.64	48.74
2813.26	10.41	216.01	43.58	39.13
2814.73	12.53	171.24	46.19	51.34
2815.15	12.29	198	42.77	44.84
2826.74	12.43	205.91	41.76	43.54
2827.26	6.08	216.36	47.78	39.64
2828.12	8.71	205.26	45.61	42.24
2828.27	11.3	208.98	42.96	42.24
2828.46	12.24	205.79	42.24	43.54
2828.61	9.7	195.59	45.36	44.84
2830.19	19.38	235.55	35.9	30.54
2830.51	19.64	223.76	34.66	37.04
2830.59	18.89	221.67	35.35	38.34
2831.18	16.85	205.45	38	46.14
2831.65	17.02	235.93	38.03	31.84
2831.83	13.83	215.75	40.36	40.94
2831.94	10.48	214.22	43.72	40.94
2832.18	17.62	216.91	36.55	40.94
2832.50	13.99	226.47	40.29	37.04
2833.30	22.74	238.02	33.14	26.64

Measured Depth (m)	True Dip (deg)	True Dip Direction	Apparent Dip (deg)	Apparent Dip Direction (azimuth)
2833.57	13.09	238.87	41.95	33.14
2833.96	16.77	224.93	37.44	37.04
2834.10	22.31	212.21	32.08	44.84
2834.19	21.27	217.54	32.87	40.94
2834.27	18.55	209.85	35.93	44.84
2834.40	19.3	217.24	34.84	40.94
2834.64	15.92	201.42	39.17	47.44
2835.00	23.08	204.95	32.15	50.37
2835.11	24.59	216.52	29.57	42.24
2835.65	28.82	205.26	26.79	55.23
2835.74	17.55	204.02	37.32	47.44
2838.18	3.79	184.61	50.84	42.24
2842.74	13.35	249.49	43.28	29.35
2842.93	4.24	214.58	50.04	39.64
2843.30	6.96	215.83	47.41	39.64
2843.45	4.44	226.35	49.99	38.34
2844.25	9.62	169.49	48.44	48.74
2844.76	11.31	181.06	45.54	48.74
2845.13	11.87	194.22	43.56	46.14
2845.25	14.74	184.29	42.57	51.34
2845.44	14.66	192.83	41.27	48.74
2845.56	19.39	179.98	40.33	57.83
2845.77	14.78	193.09	41.13	48.74
2845.96	30.52	186.72	31.46	70.18
2846.09	34.55	181.81	31.88	79.28
2846.50	16.81	190.89	39.85	51.15
2846.69	18.43	170.79	43.37	58.96
2846.93	21.55	189.43	36.49	56.62
2847.22	20.68	221.87	33.49	37.04
2847.68	17.8	227.69	36.61	34.44
2848.08	21.08	238.62	34.82	26.64
2848.26	19.65	240.95	36.46	26.64
2849.22	14.36	310.46	55.81	21.44
2849.72	14.14	291.91	51.26	21.44
2849.92	10.13	288.72	51.3	26.64
2851.54	5.57	15.98	58.9	36.31
2853.39	10.69	356.88	62.16	30.85
2853.99	13.77	22.53	67.18	34.75
2855.75	23.66	353.87	72.03	21.48
2858.14	19.43	125.67	57.44	62.08
2881.73	56.93	23.75	69.72	205.43
2882.53	54.14	18.13	73.6	201.52
2885.64	60.91	22.28	66.04	203.04
2885.72	59.4	24.41	66.99	205.38
2886.61	60.02	2.66	73.4	186.64
2886.83	59.44	11.97	70.26	194.45
2887.63	51.54	20.07	75.38	203.82
2889.99	53.24	35.08	71.85	215.74

Measured Depth (m)	True Dip (deg)	True Dip Direction	Apparent Dip (deg)	Apparent Dip Direction (azimuth)
2892.52	72.57	31.97	53.08	210.54
2892.92	66.5	27.39	59.71	206.64
2893.15	68.72	17.39	60.06	195.65
2893.81	76.16	26.22	50.41	202.74
2894.55	67.78	13.01	62.4	191.74
2897.19	53.6	17.88	74.18	201.52
2897.67	59.82	15.83	68.69	197.61
2898.18	55.49	22.79	71.08	204.97
2898.38	57.2	17	70.83	199.57
2898.67	64.69	19.13	63.12	198.84
2899.11	53.19	25.04	72.92	207.39
2902.30	53.44	29.81	72.1	211.3
2902.68	59.27	8.52	71.89	191.74
2903.18	63.6	10.11	67.35	191.05
2903.79	51.38	26.96	74.6	209.35
2905.08	54.2	26.1	71.92	208.09
2905.48	56.6	19.04	71.03	201.52
2906.00	57.5	31.55	67.93	212.25
2906.52	59.53	25.12	66.78	206.01
2906.85	65.67	11.94	64.85	191.74
2907.78	60.63	26.86	65.56	207.39
2908.01	60.75	20.56	66.71	201.52
2908.30	54.97	33.76	70.35	214.44
2908.62	60.94	14.08	68.33	195.65
2910.73	56.65	25.98	69.64	207.39
2911.53	54.27	25.39	72.12	207.39
2912.37	56.09	40.39	69.25	220.22
2912.51	54.53	48.63	71.39	227.25
2913.23	59.02	22.09	68.74	203.48
2914.26	55.2	36.91	70.84	217.17
2915.38	63.4	21.32	64.71	201.52
2917.78	62.95	25.31	63.97	205.43
2924.77	63.03	33.17	62.48	213.14
2925.02	62.3	29.13	63.62	209.24
2925.17	60.51	28.82	65.42	209.24
2925.35	62.13	27.78	63.83	207.94
2925.68	63.14	19.94	64.38	200.14
2925.79	66.01	22.19	61.06	201.44
2926.19	64.83	19.18	62.89	198.84
2926.52	62.92	15.68	65.72	196.25
2926.72	66.85	14.61	62.41	193.65
2926.88	69.66	17.1	58.93	194.95
2927.02	66.09	10.15	64.64	189.78
2927.24	69.22	5.46	63.9	183.91
2927.68	68.62	19.25	59.16	197.55
2946.97	64.34	21.54	64.24	201.52
2963.80	26.61	245.32	30.53	16.79
2965.07	78.08	249.63	36.98	274.49

Measured Depth (m)	True Dip (deg)	True Dip Direction	Apparent Dip (deg)	Apparent Dip Direction (azimuth)
2967.91	58	265.1	37.67	315.88
2968.06	52.65	254.89	28.15	321.34
2968.40	44.79	261.74	32.62	337.74
2968.90	51.32	259.83	31.66	325.25
2972.03	87.03	40.22	40.2	220.61
2973.39	65.15	229.28	14.9	256.53
2973.49	65.06	233.72	17.25	268.44
2973.61	63.93	235.28	17.44	274.49
2976.43	87.16	63.71	45.96	254.35
2977.27	63.66	26.53	64.7	206.64
2977.59	60.78	26.69	67.43	207.39
2978.00	61.01	30.9	66.67	211.3
2979.17	83.66	21.49	46.64	194.57
2988.90	60.88	47.2	67.22	226.82
2989.07	61.14	50.48	67.32	229.94
2989.30	58.81	51.94	69.78	230.87
2991.05	55.74	38.93	71.84	219.13
2992.95	53.32	29.38	74.96	211.3
2993.22	52.78	34.05	75.09	215.22
2993.64	59.93	12.84	72.54	195.61
2993.82	58.56	6.94	75.97	191.45
2993.98	59.74	5.66	75.49	189.89
2994.54	57.93	21.59	72.02	203.74
2995.09	55.58	34.81	72.46	215.6
2995.48	55.83	37.11	72.23	217.58
2995.87	59.07	47.37	69.12	226.82
2996.52	52.69	18.64	77.8	202.89
2996.74	55.81	17.27	75.24	200.81
2997.35	67.47	3.51	69.7	184.16
3000.01	64.08	39.54	63.62	219.54
3000.20	66.18	37.58	61.57	217.46

APPENDIX C

FRACTURE DATA DERIVED FROM ELECTRICAL IMAGE LOGS

Measured Depth (m)	True Dip (deg)	True Dip Direction (azimuth)	Apparent Dip (deg)	Apparent Dip Direction (azimuth)
1975.493	87.5	229.1	41.66	237.23
1975.828	83.59	5.42	54.66	178.43
1976.892	52.79	277.81	48.53	320.87
1979.226	43.8	230.57	13	330.65
1981.078	50.92	229.12	11.98	295.83
1981.492	50.44	231.67	13.73	300.52
1981.708	59.59	218.74	12.04	234.78
1982.127	49.92	223.86	7.82	294.26
1983.184	85.42	153.17	65.31	140.87
1983.857	49.72	235.51	16.37	305.22
1984.591	71.69	198.23	27.29	180
1993.191	84.05	24.89	48.66	201.91
2002.394	82.05	211.59	33.67	209.74
2007.489	86.46	18.33	47.6	192.52
2010.684	84.88	15.48	49.82	189.39
2011.563	70.56	38.79	61.27	219.13
2012.78	76.19	38.4	55.76	219.13
2039.795	14.61	335.53	58.28	20.35
2044.324	66.42	265.66	45.12	300.52
2045.241	61.64	231.2	17	270.78
2045.98	23.27	225.91	28.24	26.61
2046.171	26.6	222.09	24.56	28.17
2046.361	10.56	230.14	40.63	31.3
2049.262	78.19	210.64	27.82	205.04
2054.875	43.93	255.13	29.32	333.39
2055.094	85.57	284.54	70.35	295.83
2057.639	35.74	260.37	33.78	349.04
2057.839	35.41	256.26	31.56	350.61
2058.068	60.3	240.95	22.17	291.13
2058.634	88.77	220.77	37.12	223.83
2059.587	66.31	239.43	24.46	277.04
2060.56	12.57	286.9	48.85	20.35
2061.238	61.87	254.75	33.53	300.52
2062.015	84.57	38.22	43.58	219.13
2062.259	36.55	297.76	55.56	350.61
2063.115	46.26	276.92	45.15	333.39
2068.18	68.03	290.31	64.27	314.61
2068.386	34.9	230.06	18.55	10.96
2071.281	87.26	340.78	65.66	151.83
2072.244	77.37	190.78	34.72	169.04
2072.62	44.03	221.06	7.69	9.39
2085.028	27.8	214.92	24.48	37.57
2086.14	88	198.64	39.24	187.83
2090.158	25.81	284	46.49	2.61

Measured Depth (m)	True Dip (deg)	True Dip Direction (azimuth)	Apparent Dip (deg)	Apparent Dip Direction (azimuth)
2099.379	53.47	22.57	75.21	205.04
2111.525	53.91	264.73	38.18	320.87
2119.668	25.95	243.28	31.4	14.09
2121.431	30.43	272.65	41.82	357.39
2122.094	64.65	245.97	27.53	289.57
2122.289	80.14	258.72	46.6	281.74
2127.303	88.57	273.65	63.33	286.43
2130.727	52.22	238.21	17.13	316.17
2132.416	89.28	7.02	46.47	173.74
2133.199	86.42	16.88	44.38	187.83
2134.004	23.09	275.57	44.38	7.83
2134.306	46.12	242.6	20.88	333.91
2139.803	27.35	207.21	25.87	46.96
2141.04	61.99	218.89	9.76	228.52
2141.327	45.62	230.07	12.19	344.35
2141.482	46.55	191.41	19.83	101.74
2142.391	51.34	236.97	16.19	315.65
2142.754	67.22	173.5	39.52	136.17
2143.12	76.13	155.31	58.84	133.04
2159.163	21.05	359.38	71.19	23.48
2160.138	67.64	77.46	69.99	256.7
2164.293	31.64	196.16	25.97	62.61
2164.631	18.14	252.81	39.89	20.87
2173.3	16.38	246.83	39.92	25.04
2174.707	20.3	6.44	71.52	26.61
2176.935	21.4	33.78	75.22	36
2178.403	53.63	27.03	73.03	208.7
2194.646	27.85	229.68	27.37	26.09
2195.472	62.86	271.96	46.21	313.04
2199.132	65.84	74.54	69.08	253.57
2199.874	40.49	255.11	30.13	346.96
2200.547	41.02	245.95	24.31	350.22
2200.918	33.5	132.52	58.66	78.26
2202.541	78.76	142.51	71.8	127.17
2202.833	72.68	141.74	69.08	121.3
2202.873	32.96	190.24	28.29	70.43
2203.277	86.49	156.26	65.24	142.43
2203.684	87.58	333.48	71.12	145.57
2205.378	79.84	164.65	54.58	142.43
2206.922	29.12	314.64	61.74	4.7
2207.621	58.24	187.71	25.46	129.91
2209.688	28.24	295.6	52.89	2.61
2211.738	71.42	170.31	45.36	137.74
2212.652	41.04	202.17	17.25	75.65
2214.499	54.64	204.46	11.11	127.83
2214.641	56.68	209.19	7.84	146.09
2215.744	47.17	194.16	19.59	100.17
2217.42	46.41	185.47	26.03	100.17
2218.03	35.26	165.89	40.06	82.96

Measured Depth (m)	True Dip (deg)	True Dip Direction (azimuth)	Apparent Dip (deg)	Apparent Dip Direction (azimuth)
2218.997	57.09	135.7	65.9	103.7
2219.198	19.96	166.92	43.71	60.65
2220.278	66.16	160.66	50.53	125.22
2222.957	77.81	179.44	42.11	152.61
2223.252	78.66	185.29	38.57	159.65
2223.524	69.73	186.05	32.07	148.7
2224.717	82.88	207.59	30.61	197.22
2225.512	35.09	206.1	20.61	57.91
2226.882	40.97	221.85	13.47	27.39
2227.1	21.38	136.46	53.96	64.57
2227.651	18.38	151.52	48.84	60.65
2228.82	21.19	142.33	51.72	64.57
2228.962	21.88	201.9	33.42	48.91
2230.564	67.91	172.87	41.48	135
2232.604	66.68	153.39	56.61	122.09
2236.851	74.11	155.66	58.74	131.09
2237.207	51.56	184.62	26.68	113.48
2252.426	18.07	213.89	36.24	40.7
2253.808	21.64	226.61	32.88	32.87
2254.507	33.36	194.4	26.33	68.87
2254.908	23.72	198.68	32.53	53.22
2255.85	13.06	321.51	58.05	23.48
2256.76	5.94	315.85	55.06	31.3
2258.672	10.48	31.45	64.32	37.09
2260.262	70.01	258.01	38.06	294.26
2261.161	36.84	118.05	67.45	78.26
2269.957	76.08	261.38	44.02	289.57
2270.826	80.51	66.16	52.57	253.57
2274.694	60.12	21.55	68.3	202.74
2278.022	60.96	189.77	25.5	137.74
2278.103	63.5	172.21	40.63	129.63
2279.312	19.12	277.73	45.54	15.65
2285.266	76.79	25.3	51.39	201.91
2293.419	22.88	358.81	71.5	23.48
2301.405	55.65	21.16	72.28	203.48
2301.791	22.68	160.41	44.71	65.74
2302.698	59.9	239.79	19.06	295.83
2303.788	84.68	52.74	43.7	239.48
2304.654	54.05	8.74	77.19	194.09
2305.596	75.59	31.39	51.27	209.74
2308.111	48.29	22.83	79.5	206.61
2313.694	85.08	351.46	59.78	161.22
2314.799	68.6	10.74	62.93	189.39
2315.317	83.66	224.79	30.33	231.65
2316.488	86.77	230.94	35.1	241.04
2317.001	76.85	224.76	23.88	234.78
2319.879	69.07	226.65	17.09	247.3
2322.535	53	274.87	45.38	327.13
2326.897	70.95	14.99	59.02	192.52

Measured Depth (m)	True Dip (deg)	True Dip Direction (azimuth)	Apparent Dip (deg)	Apparent Dip Direction (azimuth)
2326.912	78.27	25.56	49.03	201.91
2327.087	82.15	4.35	53.81	175.3
2327.346	83.23	183.8	42.51	162.78
2327.717	82.64	232.88	31.85	247.3
2327.831	79.5	240.84	33.06	262.96
2328.149	76.77	27.73	50.14	205.04
2328.53	67.31	34.66	58.88	214.43
2329.096	29.76	275.14	43.3	0
2329.251	35.06	276.97	43.92	352.17
2345.548	82.4	347.13	64.53	159.65
2345.919	27.5	284.89	48.15	3.13
2346.02	50.26	284.01	51.16	333.39
2371.659	34.25	287.34	49.92	353.74
2372.726	67.76	172.57	41.09	134.61
2374.58	87.64	5.48	48.91	172.85
2374.857	88.78	357.44	52.93	163.75
2375.817	18.42	193.05	37.14	50.09
2383.003	10.25	118.81	55.71	50.09
2384.77	10.92	108.01	57.67	50.09
2385.596	72.15	85.56	70.73	266.09
2385.639	28.32	140.03	52.64	73.57
2385.713	70.02	75.78	67.08	256.7
2385.809	19.18	37.02	72.41	37.57
2385.83	71.12	64.95	61.24	247.3
2386.772	6.58	307.71	53.3	29.74
2388.972	54.03	256.6	30.8	317.74
2389.929	60.94	12.1	70.46	194.09
2392.248	76.99	173.38	46.31	147.13
2393.815	33.75	236.53	23.23	10.96
2394.936	56.4	302.35	66.83	333.39
2394.999	31.41	3.21	80.52	20.35
2395.116	64.22	282.56	55.38	316.17
2402.827	15.28	229.32	37.92	32.87
2403.98	78.72	41.19	48.61	222.26
2405.573	65.61	280.14	54.28	313.04
2414.511	66.48	22.52	61.61	201.91
2415.197	56	34.14	70.71	214.43
2415.832	58.7	23.96	69.02	205.04
2417.653	55.74	138.77	61.47	103.3
2420.092	85.26	269.68	58.1	286.43
2421.928	78.38	20.15	50.69	195.65
2431.016	44.93	156.89	45.73	95.48
2433.475	44.08	134.16	60.83	89.22
2433.714	32.44	155.96	45.51	78.26
2434.56	39.71	149.59	49.92	87.65
2437.994	20.59	239.65	36.18	23.48
2438.491	83.7	208.54	29.97	200.35
2443.371	65.07	35.3	59.99	215.22
2444.725	72.38	351.94	67.79	170.22

Measured Depth (m)	True Dip (deg)	True Dip Direction (azimuth)	Apparent Dip (deg)	Apparent Dip Direction (azimuth)
2446.652	14.21	250.8	43.76	25.43
2456.177	79.32	91.07	68.36	275.87
2465.845	48.22	19.17	78.29	203.48
2467.861	89.45	214.79	34.15	213.26
2472.047	82.32	23.37	44.72	197.61
2472.428	89.79	233.59	38.08	244.57
2472.781	80.16	247.29	37.37	271.96
2473.475	84.55	54.43	43.65	242.61
2476.401	79.48	223.89	25.11	232.83
2476.624	61.89	165.52	44.2	121.3
2478.032	87.79	221.61	33.31	225
2479.243	70.36	44.03	55.31	225
2479.497	71.1	38.88	54.21	219.13
2483.536	62.74	125.58	75.81	103.7
2485.583	70.56	49.3	56.7	230.87
2486.779	59.65	59.77	70.05	237.83
2487.78	65.77	44.53	61.09	224.84
2488.684	78.95	30.17	48.01	207.94
2489.081	69.96	191.51	27.74	156.52
2493.35	89.92	263.26	56.02	277.83
2498.199	61.54	237.39	18.93	289.57
2498.684	72.35	234.6	24.15	262.17
2499.959	44.39	219.57	9.79	25.43
2500.15	34.81	196.61	23.57	66.52
2500.559	85.8	82.97	58.94	273.91
2501.179	82.96	256.37	46.26	277.83
2502.263	67.43	234.54	20.4	270
2502.797	86.96	204.94	34.87	195.65
2503.256	58.97	167.63	40.99	119.35
2504.018	39.08	199.06	19.65	72.39
2505.029	75.04	246.37	33.57	275.87
2505.845	88.27	41.93	37.97	225
2506.431	87.74	93.25	64.75	283.7
2507.882	27.9	277.11	45.04	1.96
2508.631	57.51	199.5	14.8	135
2508.865	75.6	190.56	31.9	162.39
2509.208	87.9	12.01	44.55	180
2509.891	31.51	157.52	44.44	77.07
2510.244	39	163.41	40.76	88.04
2510.648	34.36	150.94	48.08	80.98
2510.998	27.67	164.33	41.74	70.83
2511.087	34.59	171.98	36.21	80
2511.331	26.63	175.37	37.35	66.52
2511.496	80.36	262.36	48.68	285.92
2511.537	37.63	180.53	30.49	82.93
2511.986	18.9	139.35	52.2	60.65
2517.257	50.51	269.81	41.15	328.7
2518.435	58.43	47.15	68.03	226.34
2520.071	71.21	239.37	25.88	271.96

Measured Depth (m)	True Dip (deg)	True Dip Direction (azimuth)	Apparent Dip (deg)	Apparent Dip Direction (azimuth)
2520.495	62.58	165.79	44.13	123.26
2521.008	87.41	346	61.22	154.57
2521.184	62.93	181.43	31.48	133.04
2524.221	44.29	231.49	14.8	354.13
2525.438	55.29	244.95	22.72	313.04
2525.839	83.54	278.99	63.53	295.43
2526.088	88.13	282.08	68.76	293.48
2527.77	37.3	223.77	17.88	23.48
2528.052	40.91	228.96	16.16	7.83
2528.57	47.06	244.29	22.27	334.57
2528.984	27.26	181.04	35.02	64.88
2529.205	41.27	203.16	16.57	70.43
2529.479	28.65	244.94	31.21	11.22
2530.19	39.75	220.69	14.76	27.39
2530.792	66.52	70.68	67.39	250.43
2531.057	77.04	83.78	65.99	268.04
2531.173	43.2	197.81	17.81	84.13
2531.422	43.5	192.21	21.14	90
2531.925	51.72	198.87	14.56	113.48
2544.229	82.01	169.49	51.63	148.7
2545.748	14.85	169	43.81	52.83
2549.426	76.05	179.99	40.16	152.61
2551.171	56.48	238.55	18.26	301.3
2557.876	46.86	237.89	17.8	334.57
2558.654	41.69	234.06	17.74	354.13
2562.784	27.56	236.46	29.62	17.21
2562.994	26	245.62	33.45	13.24
2563.215	28.3	224.16	26.52	27.79
2563.919	34.3	236.63	24.4	7.94
2564.729	29.47	180.58	33.66	67.5
2566.662	32.42	227.42	22.88	21.18
2566.886	34.12	220.09	20.14	30.44
2567.15	36.14	227.12	19.48	17.21
2567.277	40.2	221.74	14.46	22.5
2567.62	40.61	228.66	16.06	6.62
2568.384	38.33	202.58	18.46	64.57
2568.887	54.73	235.99	15.85	309.13
2569.601	52.06	189.42	21.63	113.48
2571.803	37.44	215.64	16.34	38.54
2572.184	43.78	220.85	10.51	19.85
2572.453	38.75	226.31	16.58	14.56
2572.593	38.29	226.73	17.06	14.56
2572.88	35.81	224.14	18.67	22.5
2573.157	40.33	218.29	13.36	31.76
2573.479	42.07	218.82	11.67	29.12
2573.629	45.82	218.32	7.94	27.39
2574.041	43.66	214.71	10.14	43.68
2576.535	67.84	125.11	78.32	107.61
2577.028	25.41	99	68.25	60.88

Measured Depth (m)	True Dip (deg)	True Dip Direction (azimuth)	Apparent Dip (deg)	Apparent Dip Direction (azimuth)
2577.864	30.66	230.49	25.01	19.85
2578.27	27.19	211.07	26.94	42.35
2578.699	26.21	216.15	27.86	37.06
2580.228	65.28	145.28	61.22	115.43
2580.868	74.85	142.61	68.28	123.26
2581.127	76.9	146.11	66.6	127.17
2582.773	44.74	157.98	44.17	95.87
2585.118	40.32	215.21	13.1	41.09
2585.88	57.85	210.97	6.53	168.26
2587.312	55.62	215.72	2.14	195.88
2587.952	38.43	210.11	15.87	51.62
2588.123	45.06	218.54	8.65	27.79
2588.432	38.48	217.04	15.14	35.74
2588.981	40.01	224.93	14.9	15.65
2589.222	29.85	219.62	23.86	33.09
2589.535	33.91	212.38	19.97	43.68
2590.569	39.21	230.88	17.73	5.87
2591.181	37.79	223.61	16.75	21.52
2591.795	34.71	228.49	20.75	17.21
2591.948	32.91	225.21	21.66	23.82
2592.374	36.48	223.82	18.09	22.5
2604.094	15.69	151.93	48.72	55.59
2611.94	61.69	147.68	58.02	113.48
2618.943	25.42	228.93	29.48	27.39
2626.446	42.99	217.72	10.41	37.17
2626.774	41.2	217.69	12.31	37.17
2628.097	43.82	220.93	10.01	23.48
2628.668	35.64	222.92	18.13	27.39
2628.884	38.29	222.72	15.51	25.43
2629.689	35.44	205.33	19.77	58.7
2633.685	30.36	206.49	23.65	51.34
2634.013	22.5	200.09	31.92	50.04
2634.274	15.99	239.72	38.35	27.94
2646.972	40.4	211.93	12.48	54.78
2648.021	36.82	216.03	15.41	41.09
2660.484	32.71	254.1	30.73	359.61
2664.31	41.94	281.33	45.61	342.45
2665.679	82.36	72.13	55.47	260.22
2666.418	29.16	244.11	27.28	11.74
2679.087	30.56	285.39	46.9	359.35
2680.756	85.59	222.15	32.88	224.84
2684.48	76.9	34.5	49.98	213.26
2685.844	37.92	182.69	29.58	86.09
2687.088	35.62	195.57	23.63	73.43
2687.38	41.83	191.9	22.58	90
2689.788	45.93	198.41	16.8	98.39
2690.344	44.24	205.54	13.01	83.56
2690.522	39.47	196.23	20.79	82
2690.888	41	198.27	18.89	83.56

Measured Depth (m)	True Dip (deg)	True Dip Direction (azimuth)	Apparent Dip (deg)	Apparent Dip Direction (azimuth)
2692.783	52.32	215.12	2.87	113.23
2693.385	50.85	224.84	5.35	334.57
2693.911	42.99	219.64	10.14	34.75
2695.051	63.73	203.15	16.93	163.21
2695.846	45.44	181.82	28.71	101.52
2696.252	53.68	181.09	30.02	118.27
2698.627	49.28	161.79	43.86	105.27
2699.618	28.11	171.51	38.37	72.78
2700.987	12.71	197.31	41.82	46.14
2701.365	31.78	180.26	33.32	76.03
2701.589	48.93	200.74	14.97	105.42
2701.645	47.86	206.13	11.49	95.27
2702.973	24.97	267.75	40.42	9.78
2703.794	74.53	211.65	21.76	199.57
2706.798	70.87	260.46	39.98	295.43
2708.467	70.73	230.28	19.44	252.39
2708.604	77.11	209.42	24.75	196.01
2709.519	65.57	235.29	18.1	273.71
2710.403	73.5	232.84	23.1	254.35
2710.72	77.49	235.04	27.66	254.35
2711.19	76.11	64.57	55.57	249.5
2711.594	84.6	52.54	43.55	238.7
2711.779	82.75	232.19	31.44	244.57
2712.341	89.87	54.91	39.36	244.57
2712.625	30.32	211.04	23.85	48.91
2713.143	40.11	262.68	34.13	346.3
2715.498	20.02	227.5	34.14	33.26
2721.368	66.08	60.03	62.81	240.65
2721.505	72.74	59.39	56.38	242.61
2721.622	79.26	60.23	50.61	246.52
2721.721	78.06	60.74	51.9	246.52
2721.843	86.06	54.53	42.24	242.61
2721.919	88.73	54.93	39.87	244.57
2731.221	15.17	231.16	39.24	34.44
2731.381	19.42	223.14	34.63	37.04
2743.768	30.34	243.27	28.47	13.7
2744.494	36.63	141.44	54.87	84.73
2745.409	30.45	160.57	43.95	77.7
2753.715	12.77	182.02	44.52	50.04
2758.467	30.63	150.17	49.38	78.26
2758.988	23.79	185.9	36.01	61.73
2759.427	16.77	221.15	37.34	38.66
2759.788	10.19	191.84	45.16	46.14
2759.996	27.6	154.31	47.32	74.35
2760.418	10.64	81.16	62.27	47.44
2760.88	17.71	184.06	40.52	55.23
2762.544	7.22	177.28	48.51	46.14
2763.473	18.49	176.57	41.55	58.7
2765	16.73	224.47	37.26	37.04

Measured Depth (m)	True Dip (deg)	True Dip Direction (azimuth)	Apparent Dip (deg)	Apparent Dip Direction (azimuth)
2765.391	10.68	142.04	52.33	52.64
2765.754	30.97	147.88	50.63	78.63
2766.689	13.5	219.77	40.66	39.64
2767.723	55.11	147.53	57.52	107.61
2768.495	33.16	158.28	45.6	82.17
2769.089	34.56	160.51	44.35	84.13
2770.28	34.16	205.05	22.69	61.73
2770.415	34.62	160.9	44.23	84.13
2770.903	37.18	133.99	59.99	84.13
2773.915	10.93	222.25	43.53	39.64
2774.342	6.19	95.58	58.25	46.14
2775.894	19.1	120.37	59.85	61.73
2778.85	52.52	265.51	36.96	326.74
2779.069	20.54	139.69	53.65	64.57
2779.308	15.81	194.92	40.69	48.91
2779.518	53.61	198.69	16.54	119.35
2780.065	47.47	264.42	35.51	334.62
2780.23	49	266.45	37.19	332.28
2780.72	37.37	247.91	26.49	358.04
2780.819	31.24	246.61	29.32	9.78
2785.17	48.16	218.25	6.48	43.04
2786.021	4.39	217.29	50.29	39.13
2788.144	69.44	28.62	56.56	207.39
2788.568	10.13	178.85	47.3	47.25
2789.391	86.66	263.87	52.81	281.74
2791.428	76.43	79.17	62.51	264.13
2791.632	31.39	177.15	35.4	74.35
2791.71	29.69	180.39	34.65	70.43
2791.784	82.49	76.62	56.16	266.09
2793.303	88.77	66.62	45.29	260.22
2793.468	84.92	57.71	44.51	246.52
2802.823	22.97	246.27	35.21	19.57
2803.288	36.62	234.93	21.13	9.78
2804.522	76.01	219.98	21.79	223.04
2804.918	87.11	36.3	38.83	215.22
2805.342	73.66	205.89	22.34	185.87
2805.469	73.1	233.65	23.46	258.26
2805.48	39.14	225.15	15.85	21.52
2805.68	68.76	218.48	14.8	219.13
2808.622	38.37	230.68	17.78	11.74
2809.056	19.79	236.63	35.37	27.39
2812.576	36.91	216.27	17.13	43.04
2812.665	16.44	100.36	62.85	54.78
2815.883	16.02	230.78	38.62	33.26
2816.546	1.52	279.58	53.5	37.04
2818.233	13.06	222.26	40.84	37.87
2819.699	19.42	198.36	36.23	50.37
2820.273	87.97	237.66	38.14	250.18
2820.334	89.9	234.96	38.87	244.98

Measured Depth (m)	True Dip (deg)	True Dip Direction (azimuth)	Apparent Dip (deg)	Apparent Dip Direction (azimuth)
2821.111	7.57	46.66	61.45	40.22
2821.657	35.09	173.15	36.41	83.17
2823.244	54.91	158.28	48.43	111.52
2830.816	12.34	134.68	54.07	54.78
2833.138	9.58	118.69	56.5	50.87
2833.595	35.15	129.66	61.34	80.58
2834.651	36.78	208.53	18.96	60.43
2835.36	39.71	208.56	16.42	65.63
2836.937	29.41	180.8	34.63	72.39
2840.293	12.42	149.75	50.7	54.78
2841.723	30.03	142.1	53.68	76.3
2848.256	20.06	242.87	36.46	25.34
2850.117	83.31	28.63	43.59	204.04
2850.417	78.85	54.37	49.22	239.13
2850.562	78.92	49.24	47.93	232.64
2851.268	7.43	269	49.22	31.3
2852.838	18.44	0.23	68.96	26.64
2859.541	23.05	7.36	74.2	26.64
2860.1	16.39	59.29	69.46	45
2860.915	9.13	217.23	44.93	39.44
2861.906	9.63	37.07	63.74	38.66
2862.228	60.66	246.76	24.18	301.3
2862.556	29.42	307.68	58.67	3.91
2863.343	5.81	75.16	58.72	43.04
2864.489	22.29	218.38	31.65	39.54
2865.385	72.01	216.5	18.27	211.3
2867.222	76.81	200.2	28.67	178.04
2867.549	19.46	182.71	39.25	57.23
2875.799	68.38	230.65	17.05	258.26
2878.113	66.84	33.71	58.24	213.26
2878.639	66.87	228.18	14.05	255.36
2878.868	67.11	214.37	12.65	198.35
2878.962	63.97	211.2	11.17	178.83
2879.053	61.04	205.99	12.65	153.06
2879.172	58.95	211.22	7.7	156.18
2882.589	42.09	202.43	17.9	78.26
2883.3	52.72	210	7.79	109.57
2883.79	58.42	204.77	12.53	140.87
2884.166	59.89	209.22	9.7	156.52
2884.484	43.42	186.25	27.23	93.91
2886.168	37.19	221.07	17.89	35.22
2888.431	46.08	223.29	9.45	21.52
2888.723	55.58	230.77	9.44	309.13
2889.337	51.39	220.63	3.75	23.48
2889.675	48.46	217.83	6.65	48.91
2889.919	43.24	216.41	11.98	48.91
2890.468	50	233.96	12.6	336.52
2891.321	41.12	235.12	18.05	3.91
2891.875	86.1	201.91	35.28	188.2

Measured Depth (m)	True Dip (deg)	True Dip Direction (azimuth)	Apparent Dip (deg)	Apparent Dip Direction (azimuth)
2893.412	67.83	18.99	60.44	197.61
2899.683	48.02	210.64	9.83	80.22
2904.143	45.26	224.94	10.59	17.61
2906.127	54.01	241.98	18.41	318.91
2906.274	47.86	228.11	9.89	358.04
2906.879	51.96	219.18	2.91	40.58
2907.122	39.43	225.16	16.08	25.43
2907.646	56.09	225.54	5.44	297.39
2908.415	46.93	221.48	8.16	26.01
2908.857	57.61	224.74	5.55	279.78
2909.213	46.16	225.01	9.79	12.49
2909.711	74.51	213.38	20.26	203.48
2909.965	46.87	244.72	21.5	338.48
2910.142	68.12	262.11	39.91	301.3
2910.282	50.3	226.87	7.83	346.47
2919.706	57.52	34.84	68.34	215.22
2920.371	60.05	27.44	66.64	208.09
2921.214	78.42	0.45	59.86	174.13
2922.662	76.88	57.72	51.99	242.43
2923.668	52.36	48.72	74.06	226.96
2925.156	78.57	261.21	45.25	287.61
2925.631	60.6	276.2	48.37	318.91
2927.427	84.46	70.98	50.64	262.2
2929.401	71.25	207.65	19.68	185.87
2940.351	74.32	241.09	28.15	269.48
2940.998	89.32	19.23	40.69	187.83
2941.471	77.61	207.27	25.49	191.74
2941.948	25.83	264.71	39.47	9.36
2942.258	83.54	205.88	31.57	193.7
2943.645	70.23	10.37	62.05	188.32
2944.001	70.04	37.37	56.14	217.17
2944.633	46.94	253.97	27.59	333.99
2944.841	39.77	256.48	30.26	348.26
2945.288	23.41	226.39	30.6	33.29
2945.873	50.9	246.14	21.54	324.78
2948.984	1.84	94.45	54.4	41.09
2955.712	48.04	154.84	49.24	101.97
2955.794	82.23	86.85	62.6	274.68
2958.572	71.37	66.02	60.81	248.48
2966.891	52.67	34.36	74.27	215.22
2967.125	56.48	23.45	71.87	205.43
2967.432	62.5	29.13	65.01	209.35
2967.625	81.98	249.57	39.77	270.52
2968.288	62.49	20.1	66.85	200.81
2969.393	78.16	359.41	61.65	173.76
2970.162	79.08	238.93	31.36	258.26
2970.653	64.9	37.23	62.18	217.17
2973.718	59.58	17.12	70.71	199.13
2974.186	72.2	219.46	19.33	219.64

Measured Depth (m)	True Dip (deg)	True Dip Direction (azimuth)	Apparent Dip (deg)	Apparent Dip Direction (azimuth)
2974.29	77.4	27.03	51.06	203.82
2974.686	58.13	34.98	69.09	215.38
2974.889	71.24	241.12	26.52	271.37
2975.202	53.91	265.83	36.99	322.13
2975.41	49.25	266.61	36.52	329.93
2975.608	61.18	251.8	28.37	301.82
2976.538	55.15	23.04	73.55	205.43
2979.83	44.52	245.63	21.26	340.43
2980.449	42.37	288.22	49.95	344.35
2980.612	66.02	267.25	42.77	305.22
2980.988	59.68	32.8	68.05	213.26
2991.308	52.82	245.09	19.52	316.96
2991.412	45.64	233.03	11.67	350.22
2991.524	38.62	239.95	19.47	1.96
2996.469	83.12	254.9	43.8	274.49
2997.175	61	42.66	66.89	222.56
2997.914	88.97	339.66	68.18	150.33
3000.36	63.86	248.28	26.08	292.37
3000.457	68.76	249.26	29.71	285.09
3000.762	88.29	45.93	39.77	228.9
3001.168	56.81	160.19	48.6	116.7
3001.376	49.2	139.37	60.63	99.78
3002.085	34.63	135.04	57.35	83.08
3002.865	74.72	148.28	67	129.02
3003.17	70.86	186.21	35.31	152.95
3004.633	68.66	281.39	54.47	311.1
3006.119	52.72	26.83	76.22	209.35
3007.287	62.24	281.74	51.49	318.38
3007.538	51.68	44.22	76.2	223.52
3007.94	60.58	351.66	81.27	178.96
3011.224	85.97	146.74	74.65	137.34
3012.306	70.27	274.24	49.75	304.86
3016.451	63.14	250.99	27.71	296.7
3016.68	63.2	31.07	65	211.21
3016.827	71.3	215.17	19.48	204.97
3017.378	66.03	166.6	47.71	131.09
3018.021	74.14	27.79	54.73	205.43
3020.835	79.69	258.49	43.57	281.74